Doctoral Dissertation

博士論文

General Framework and Industrial Application of Two-Inertia System Control with Effective Use of Load-Side Information

（負荷側情報を有効に用いた2慣性系の制御の一般的枠組とその産業応用）

by

37-167084 **Shota Yamada**
（山田 翔太）

Dissertation Submitted to

Department of Electrical Engineering and Information Systems

for the Degree of

Doctor of Philosophy

at

The University of Tokyo

November 30th 2018

Supervisor:
Professor Hiroshi Fujimoto

Abstract

The controlled plants dealt with in this paper range from ball-screw driven stages and precise positioning stages of machine tools, industrial robots, welfare robots, electric vehicles, HDDs, rolling mills, etc. In these plants, since the industrial demand for the responsiveness is increasing, the resonances of the mechanical systems have to be carefully considered not to be excited for higher control performance. Conventionally, these plants have been modeled into a two-inertia system composed of three elements of a motor side, a transmission part, and a load side. A number of studies on two-inertia system have been actively conducted for more than 30 years.

The reason why the two-inertia system has been actively studied for over 30 years largely depends on its versatility. Also, in systems with multiple resonance modes, the primary resonance mode mainly limits the control bandwidth. Therefore, they are often modeled and handled as a two-inertia system, which expresses the first-order resonance characteristics. All the control methods proposed in this paper are targeted for two-inertia model and therefore they can be applied to various controlled objects used in industry.

Along with the development of robotics, industrial robots (collaborative robots) that can work in cooperation with human beings in the same production line are attracting attentions, and also in the field of welfare, human-support robots that can care for the elderly and people with disabilities are highly demanded. Robots operating in the same environment as human beings are required human-friendly motion control that does not cause harm to people. Therefore, in industry, force control that enables human-friendly motion control is currently required.

Conventionally, in the fields of machine tools, industrial and welfare robots and the like, semi-closed control (feedback control of motor-side information by a motor-side encoder) has been generally applied. However, in the semi-closed control, the control accuracy on the load side required for final positioning deteriorates due to the deformation of the transmission mechanism with low rigidity. Furthermore, since the transmission mechanisms such as gears and ball screws have not only low rigidity but also nonlinear elements such as backlash, the control accuracy on the load side even deteriorates. Therefore, in order to improve the accuracy, there is an increasing adoption of full-closed control, which feeds back not only the motor-side but also the load-side information by using a

load-side encoder.

The rapid developments of high-resolution with cost reduction of the encoder in industry have increased adoption of full-closed control. As a rotary encoder for general industrial robots, a high-resolution encoder such as 20 bits is being used. As for cost, the 1 million pulse encoder has become the price of about one tenth of 10 years ago. For this reason, now high-resolution encoders are used not only in the field of precise positioning but also in various fields. Furthermore, since the environmental resistance performance of the encoder has been improved, it is expected that optical high-resolution encoders will be applied even in automobile field in the near future. Along with the spread of high-resolution encoders in industry, a control method that effectively utilizes higher-order state quantities such as acceleration and jerk will be required in the future.

Due to two industrial trends such as higher accuracy demand and lower cost of high-resolution encoder, the number of the industrial devices with high-resolution encoders on the load side are increasing. However, despite the industrial trend, it is hard to say that the research on control methods that effectively use load-side high-resolution encoder information has been sufficiently conducted. Therefore, in this dissertation, novel control methods that effectively use load-side high-resolution encoder information are proposed. In consideration of recent attentions for force control, control methods for not only the load-side position and acceleration but also the joint torque and the external torque are proposed. The advantages of the proposed methods are validated through simulations and experiments.

In chapter 1 and chapter 2, research background and experimental setups are described, respectively. Four experimental setups, precision positioning stage, motor bench, industrial robot module, and in-wheel motor driven electric vehicle are used for quantitative evaluation. All setups are modeled as two-inertia system and control methods for two-inertia systems are applied.

In chapter 3, studies on load-side position control conducted from the three viewpoints, vibration suppression control, backlash compensation, and simplification of controller design are described in detail. In the study on vibration suppression control and simplification of control design, the same performance is realized by only the high-resolution load-side encoder compared with the conventional control methods using both the motor- and load-side encoders. It is an academically innovative research that overturns conventional common sense that both the motor- and load-side information are required for two-inertia system control with high bandwidth. Regarding backlash compensation study, attenuation of the collision caused by backlash is focused. The overshoot of position response becomes larger with the conventional collision mitigation method. There is a trade-off between the control performance and the collision mitigation amount. Based on a detailed discussion on the physical phenomenon, relaxation of the trade-off is successfully achieved by applying a novel switching

controller.

In chapter 4, load-side acceleration control is described. An automobile can be regarded as a two-inertia system in which a vehicle body side (sprung) and a wheel side (unsprung mass) are connected by a flexible transmission part (suspension). In an in-wheel motor vehicle, which has a motor as a driving source in an unsprung mass, the unsprung mass is the motor side and the sprung mass is the load side. In order to improve the ride comfort and the motion performance, a novel acceleration control that suppresses longitudinal vibration of the body is proposed. Longitudinal vibration is difficult to suppress due to its higher frequency than that of vertical vibration unless it is an in-wheel motor vehicle that has a high frequency control bandwidth. Therefore, there are limited studies on longitudinal vibration suppression yet. In this study, based on accurate frequency characteristic measurements of the experimental vehicle, a novel control method considering not only the longitudinal mode but also the rotational mode by the gear in the in-wheel motor unit is proposed. The effectiveness is validated through the experimental in-wheel motor vehicle.

In chapter 5, joint torque control is discussed. With the advent of cooperative robots in the market, attention to force control is rapidly increasing, which requires high performance to force control. This chapter shows that the load-side encoder which is starting to be widely used in industry to improve load-side positioning accuracy can be effectively used also in force control. By using the load-side information, it becomes possible to explicitly compensate for the backlash inherent in the gears, and precise joint torque control is realized.

In chapter 6, torsional angle control is studied. It is possible to improve back drivability by precise control of the torsional angle effectively utilizing the load-side information. Back drivability is an index of how light it feels when applying force from the load side and it is indispensable for interactive operation with human beings in cooperative robots. A proposed control method is a novel technique for improving back drivability by actively using backlash, which is widely known as a cause of performance deterioration in the control of two-inertia systems. Considering the situation where the controlled object contacts with the environment such as human beings, this study quantitatively evaluates how much the performance difference is caused by the presence or absence of the load-side encoder from the viewpoint of human-friendly motion control through simulations and experiments.

In chapter 7, load-side external torque estimation is described. For cooperative robots, machine tools, automobiles, etc., there is a demand to monitor torques externally applied to the systems, and their performance can be improved by monitoring. By effectively utilizing the load-side information, it is possible to estimate robustly against modeling and measurement errors of two-inertia system plant parameters, as compared with the conventional estimation methods. Furthermore, when assuming the distribution of parameters and sensor noise as a normal distribution, a optimal design method in

which the variance of the estimated external torque theoretically becomes the minimum is proposed with the validations through simulations and experiments.

Finally, the conclusion is stated in chapter 8.

In the near future, the two industrial trends (higher required accuracy and lower cost of high-resolution encoders) are expected to accelerate. The spread use of load-side encoder strongly requires new control methods using load-side information effectively. All the control methods proposed in this dissertation respond to the requests from industry, and their importance will increase in the future.

邦文概要

本論文で扱う制御対象は，工作機械のボールねじ駆動ステージや精密位置決めステージ，産業用ロボット，福祉ロボット，電気自動車，HDD，圧延機等，多岐に亘る。これらの制御対象では，制御系の応答速度の高帯域化への需要が高まってきているため，機械系の共振を励起しないような制御器設計が求められている。工作機械のステージにおいてはボールねじ部やナットの変形，ロボットや自動車においてはベルトやギアといった駆動伝達機構の変形，HDD においてはヘッド部の変形，圧延機においてはモータとロール間の軸のねじれが，共振の主要因となる。従来，これらの制御対象は，駆動側，伝達部，負荷側の 3 要素から構成される 2 慣性系にモデリングされ，30 年以上に亘り研究が盛んになされてきた。

2 慣性系が 30 年以上に亘り盛んに研究されてきた理由は，その汎用性によるところが大きい。また，複数の共振モードを持つシステムにおいても主に 1 次共振モードが制御帯域を制限するため，2 慣性系にモデリングして扱うことが多い。本論文で提案される全ての制御手法は，1 次の共振特性を表現できる 2 慣性系モデルを対象としたものであるため，産業界で使用されている様々な制御対象に適用可能である。

また，ロボティクスの発展に伴い，人間と同じ生産ラインで協調して働ける産業用ロボット（協働ロボット）が要求され始め，福祉の分野では高齢者や障害者の方々を介護することのできる介護ロボットが求められ始めている。このような人間と同じ環境の動作を求められるロボットには，人に危害を加えないような人間親和型モーションコントロールが求められる。したがって現在産業界では，人間親和型モーションコントロールを可能にする力の制御が求められている。

従来，工作機械や産業用ロボット，福祉ロボット等の分野では，駆動側エンコーダを用いて駆動側情報をフィードバックするセミクローズド制御が一般に行なわれていた。しかしセミクローズド制御では，低剛性な伝達機構部の軸ねじれにより，最終位置決めをする負荷側における制御精度が劣化してしまう。更にギアやボールねじ等の伝達機構は低剛性であるだけでなく，バックラッシ等の非線形要素を含むため，負荷側の制御精度が劣化してしまう。そこで，精度向上のため，駆動側だけでなく負荷側にもエンコーダを用いてフィードバックするフルクローズド制御の採用が増加してきている。

産業界における急速なエンコーダの高分解能化及び低コスト化が，フルクローズド制御の採用を増加させている。産業用ロボットのロータリーエンコーダとして，20 bit といった高分解能エンコーダが用いられるようになっており，コストに関しても，100 万パルスエンコーダが 10 年前の 100 分の 1 程度の価格になっている。そのため，精密位置決めの分野だけでなく，様々な分野で高分解能エンコーダが用いられるようになってきた。更にエンコーダの耐環境性が向上しているため，自動車分野等の現在レゾルバが用いられ

ている分野でも，今後エンコーダの適用が進むと考えられる。高分解能エンコーダの普及に伴い，今後加速度やジャークといった高次状態量を有効に活用する制御則が求められていくと考えられる。

要求精度の向上及び高分解能エンコーダの低コスト化という 2 つの産業界の流れから，負荷側に高分解能エンコーダを持つ装置が増加している。しかし，このような産業界の流れがあるにも関わらず，負荷側高分解能エンコーダ情報を有効に用いた制御則の研究が十分にされているとは言い難い。そこで本論文では，負荷側高分解能エンコーダ情報を有効に用いた制御法を提案する。主たる 2 慣性系の被制御量である負荷側位置，加速度だけでなく，近年の力制御への要求も鑑みて，軸トルクや負荷側外力の制御・推定に関して，負荷側情報を有効に使用した制御法を提案し，その有効性をシミュレーションや実験によって示している。

第 1 章，第 2 章においては，それぞれ研究背景や実験機に関して述べられる。実験機として，精密位置決めステージ，モータベンチ，産業用ロボットモジュール，インホイールモータ駆動式電気自動車の 4 つが用いられるが，すべて 2 慣性系としてモデリングし，2 慣性系の制御手法を適用する。

第 3 章においては，負荷側位置制御に関して，制振制御，バックラッシ補償，制御器設計の簡単化という 3 つの観点から行われた研究が詳細に述べられる。制振制御と制御設計の簡単化に関する研究においては，駆動側エンコーダと負荷側エンコーダを双方用いる制御法と比べて同等の性能を高分解能負荷側エンコーダのみで実現するという，2 慣性系の制御の従来の常識を覆す学術的に画期的な研究である。バックラッシ補償に関しては，バックラッシに起因する衝突緩和に取り組み，従来の衝突緩和法では位置応答のオーバーシュートが大きくなり，制御性能と衝突緩和量に関してトレードオフがあったが，物理現象への詳細な考察から生まれた適切な切替え条件を持つ制御器の適用により，トレードオフの緩和を実現する。

第 4 章では，負荷側加速度制御に関して述べられる。自動車は，車体側（ばね上）と車輪側（ばね下）がサスペンションという柔軟な伝達部によって繋がれた 2 慣性系と捉えることができる。駆動源であるモータがばね下に収められるインホイールモータ車両では，ばね下が駆動側，ばね上が負荷側となる。乗り心地及び運動性能の改善のため，負荷側である車体の前後振動を抑制する前後加速度制御を提案する。前後振動は，広く研究されている上下方向の振動に対して周波数帯が高く，高帯域制御が可能なインホイールモータ車両でないとその抑制は難しく，まだ研究は多くない。本研究では，正確な周波数特性測定によって可能になった，更に高域に存在するインホイールモータユニット内の減速機に起因する回転方向のモードまでも考慮した制御法を提案し，実際のインホイールモータ車両において，その有効性が示される。

第 5 章では，軸トルク制御に関して述べられる。市場への協働ロボットの登場により，力制御への注目が急速に高まっており，力制御への高性能化が求められる。負荷側位置決め精度向上のために産業界で用いられ始めている負荷側エンコーダが，力制御においても有効に利用できることを示す。負荷側情報の利用により，ギア等に内在するバックラッシを陽に補償することが可能になり，精密な軸トルク制御が実現される。

第 6 章では，軸ねじれ角制御に関して述べられる。負荷側情報を有効に活用した軸ねじれ角の精密な制御によって，バックドライバビリティの改善が可能になる。バックドライバビリティとは，負荷側から力を加えたときにどれくらい軽く感じるかという指標であり，協働ロボット等における人間とのインタラクティブな動作に不可欠なものである。提案制御法は，従来 2 慣性系の制御において性能劣化の原因として広く

知られているバックラッシをあえて積極的に用いることで，バックドライバビリティの改善を図る斬新な手法である。また，制御対象が人間等の環境と接触するシチュエーションを考慮し，負荷側エンコーダの有無が人間親和型モーションコントロールという観点で，どれくらいの性能差をもたらすのかをシミュレーション及び実験によって定量的に評価している。

第 7 章では，負荷側外力推定に関して述べられる。人間と同じ環境で働くことを要求される協働ロボットや，工作機械，自動車等は，系に外部から加わる力をモニタリングする必要性や，モニタリングにより性能が向上する可能性がある。負荷側情報を有効に活用することで，従来の推定手法に比べて，2 慣性系のプラントパラメータのモデル化誤差及び測定誤差に対してロバストな推定が可能になる。更に，パラメータやセンサノイズの分布を正規分布と仮定したときには，推定された外力の分散が理論的に最小となる設計法を提案し，その有効性をシミュレーションと実験によって示す。

最後に，結論が第 8 章で述べられる。

今後，要求精度の向上及び高分解能エンコーダの低コスト化というこの 2 つの産業界の流れは加速し，負荷側におけるエンコーダの利用はますます広がっていくと予想され，負荷側のエンコーダ情報が得られる系における新たな制御法が強く求められている。本論文で提案される全ての制御法は，この産業界からの要請に応えるものであり，今後その重要性が高まるものである。

Acknowledgements（謝辞）

本研究を進めるにあたり，毎週の報告会等において熱心なご指導と的確なご助言を頂いた藤本博志准教授に心から感謝しております。学部生の頃から 6 年間，大変お世話になりました。この研究室で過ごした 6 年間で，研究者としてだけでなく，人として大きく成長することができたと思います。この研究室に入るまでは，自分が博士課程に進学して将来は研究者に，ということは想像もしていませんでしたが，藤本先生と過ごした時間の中で私は大きな影響を受けて，私の人生は大きく変わったように思えます。6 年間大変お世話になりました。そして，これからも宜しくお願い申し上げます。

研究発表会等の場において丁寧なご指導，ご鞭撻を頂いた堀洋一教授に御礼申し上げます。初めに制御工学という学問の面白さを教えて頂いたのは堀先生でした。堀先生のお話はいつも示唆に富んでおり，多くのことを学ぶことができました。ありがとうございました。

また，お忙しい中，私の博士審査に携わって頂いた，古関先生，坂井先生，馬場先生に御礼申し上げます。先生方からの貴重な建設的なご意見により，博士論文の質が大きく向上しました。

私は，藤本先生の計らいで多くの企業との共同研究に携わることができました。共同研究先の方々のおかげで，貴重な経験を多くさせてもらい，大変感謝しております。その中でも特に密接に共同研究をさせて頂いた，DMG 森精機の石井様，熊谷様，山本様，寺田様，伊佐岡様及び，トヨタ自動車株式会社の門崎様，津田様，勝山様，狩野様，姫野様，下屋様に感謝しております。皆様の御陰で，産業応用を見据えた本格的な研究を行うことができました。

博士課程の 3 年間は，日本学術振興会の経済的援助により成立しました。本研究の一部は科研費（16J02698）の助成を受けたものであることを付記します。

藤本研の秘書の皆様には，様々な事務手続きや私の研究費の管理まで，大変お世話になりました。松嶋様，植野様，今泉様，ありがとうございました。

また，研究をするにあたって，たくさんの研究室の先輩方にお世話になりました。研究相談だけでなく，進路のことでもアドバイスを頂きました。同期や後輩とは，日々の研究室生活を共に楽しく送ることができました。楽しい時間をありがとう。6 年間で私が一緒に研究室生活を送ったメンバーは 86 名もいました。多くの友人に支えられた生活であったと感じています。これからも末永く宜しくお願いします。

最後に，私の意思を尊重し，進学に理解を示し，そして深い愛情をもって今まで支え続けてくれた両親に，心から感謝致します。

Contents

Abstract i

Acknowledgments viii

Chapter 1 Introduction 1

1.1 Control systems handled in this dissertation and their problems 1

1.1.1 Needs for position and force control 1

1.1.2 Control systems handled in this dissertation 2

1.1.3 Two-inertia System 2

1.2 Industrial trends and demands 4

1.2.1 Higher resolution and lower cost of encoders 4

1.2.2 From semi-closed control to full-closed control 7

1.2.3 Improvements in bandwidth of joint torque sensors 8

1.2.4 Motivation of this study based on industrial trends and demands 8

1.3 Structure of this dissertation 8

Chapter 2 Experimental setup 10

2.1 High precision positioning stage 10

2.1.1 Linear stage with two linear encoders 10

2.1.2 Derivation of motion equations and modeling by frequency response analyses 13

2.2 Double Encoders Motion Control Module (DEMCM) 14

2.2.1 Proposal of novel structure for industrial robot module 14

2.2.2 Modeling by frequency response analyses 15

2.3 Geared in-wheel motor vehicle 17

2.3.1 In-wheel motor unit and electric vehicle 17

2.3.2 Modeling by frequency response analyses 17

2.4 Two-inertia system motor bench 19

2.4.1 Motor bench with variable physical parameters 19
2.4.2 Modeling by frequency response analyses 19
2.4.3 Backlash width identification using both motor- and load-side encoders . 19

Chapter 3 Load-side position control 23
3.1 Abstract 23
3.2 Vibration Suppression Control 23
3.2.1 Abstract of vibration suppression control 23
3.2.2 Conventional vibration suppression methods 24
Conventional methods using only motor-side information 24
Conventional methods using both motor- and load-side information . . . 26
3.2.3 Proposed method (State FB control using only load-side information) . 26
Reason why motor-side information is unnecessary 27
Design of proposed method 27
Advantages of proposed method 28
3.2.4 Simulations and experiments of vibration suppression control 29
Simulation in ideal resolution (Simulation 1) 30
Simulation in experimental condition (Simulation 2) 32
Experiments of vibration suppression control 33
3.2.5 Conclusion of vibration suppression control 35
3.3 Position control for two-inertia system with backlash 38
3.3.1 Abstract of backlash compensation 38
3.3.2 Conventional backlash compensation methods 38
Problems caused by backlash 38
Piecewise affine model of two-inertia system with backlash 38
Conventional backlash compensation methods 40
3.3.3 Proposed method (Switched damping control) 41
Problems of damping control 41
Switching condition 44
3.3.4 Simulations and experiments of backlash compensation 47
Simulation comparison with conventional method 47
Stability analyses 48
Additional simulation analyses 50
Experimental comparison with conventional method 53

3.3.5 Conclusion of backlash compensation . . . 54
3.4 Self Resonance Cancellation control . . . 55
3.4.1 Abstract of Self Resonance Cancellation control . . . 55
3.4.2 Conventional position control methods . . . 55
P-PI control . . . 55
Self Resonance Cancellation Control (SRC) . . . 56
3.4.3 Proposed method（Load-side SRC (L-SRC)） . . . 57
Design of L-SRC . . . 57
Analyses of SRC and L-SRC in time domain . . . 59
SRC in time domain . . . 59
3.4.4 Simulations and experiments of SRC . . . 60
Simulation comparison with conventional method . . . 61
Experimental comparison with conventional method . . . 65
3.4.5 Conclusion of SRC . . . 68
3.5 Conclusion . . . 72

Chapter 4 Load-side acceleration control 73
4.1 Abstract . . . 73
4.2 Conventional control methods . . . 73
4.2.1 Advantages of electric vehicles . . . 73
4.2.2 Conventional vibration suppression control by in-wheel motor . . . 74
4.2.3 Longitudinal relative velocity FB control . . . 75
4.3 Proposed method (Model-based longitudinal acceleration control) . . . 77
4.3.1 Two degrees of freedom control . . . 77
4.3.2 Dead time compensated observer . . . 78
4.4 Simulations and experiments . . . 80
4.4.1 Simulation comparison with conventional method . . . 80
4.4.2 Experimental comparison with conventional method . . . 82
4.5 Conclusion . . . 84

Chapter 5 Joint Torque Control 85
5.1 Abstract . . . 85
5.2 Conventional force/torque control methods . . . 85
5.3 Joint torque control with backlash compensation based on dead zone model . . . 86
5.3.1 Overview of proposed method . . . 86

Motor-side velocity control . . . 87
Joint torque FF control . . . 87
Joint torque FB control . . . 88
5.3.2 Controller design procedure . . . 88
5.3.3 Simulations . . . 89
Effects of the FF controllers . . . 90
High backdrivability . . . 92
Backlash compensation . . . 93
5.3.4 Experiments . . . 93
5.4 Joint torque control with backlash compensation based on sigmoid function . . . 95
5.4.1 Sigmoid function for backlash compensation . . . 95
5.4.2 Simulations and experiments . . . 97
5.5 Conclusion . . . 98

Chapter 6 Torsional angle control 100
6.1 Abstract . . . 100
6.2 Conventional high backdrivable control methods . . . 101
6.2.1 Backdrivability . . . 101
6.2.2 Conventional backdrivability improvement methods . . . 101
6.3 High backdrivable control . . . 102
6.3.1 Proposal of backdrivable control using backlash . . . 102
6.3.2 Impedance control . . . 106
6.3.3 Simulations and experiments . . . 107
Conditions . . . 107
Validations . . . 108
6.4 Human–machine interactive control . . . 110
6.4.1 Procedure of human–machine interactive motion . . . 110
6.4.2 Double encoder interactive control system . . . 110
Tracking control . . . 110
Recognition of external inputs . . . 110
Impact attenuation . . . 111
High backdrivable control using a load-side encoder and backlash . . . 111
6.4.3 Single encoder interactive control system . . . 111
Tracking control . . . 111

Recognition of external inputs . . . 112
Impact attenuation . . . 112
Turning off . . . 112
6.4.4 Numerical comparisons of interactive control . . . 116
Conditions . . . 116
Simulations and experiments . . . 116
6.5 Conclusion . . . 117

Chapter 7 External torque estimation 119
7.1 Abstract . . . 119
7.2 Conventional estimation methods . . . 119
7.2.1 Estimation using only motor-side encoder . . . 119
7.2.2 Estimation using both motor- and load-side encoders . . . 120
Motor-side estimation . . . 120
Transmission-part estimation . . . 120
Motor-side estimation and Transmission-part estimation . . . 120
7.2.3 Measurement by joint torque sensor . . . 121
7.3 Proposed method (Robust estimation by using load-side information effectively) 122
7.3.1 Proposed method . . . 122
Proposed estimation without joint torque sensor . . . 122
Proposed estimation with joint torque sensor . . . 123
7.3.2 Gain evaluation through simulations and experiments . . . 124
7.4 Proposed minimum variance estimation . . . 127
7.4.1 Gain design for minimum variance estimation . . . 127
7.4.2 Minimum variance evaluation through simulations . . . 130
7.4.3 Minimum variance evaluation through experiments . . . 131
7.5 Conclusion . . . 133

Chapter 8 Conclusion 134

References 137

Publications 148

List of Figures

1.1 Two-inertia system. . . . 2
1.2 Block diagram of two-inertia system. . . . 2
1.3 Frequency response of two-inertia system from motor torque input to motor-side angle and load-side angle. . . . 3
1.4 (Rotational) Velocity resolution and (rotational) acceleration resolution obtained by backward differences versus backward sampling time. . . . 5
1.5 Phase delay caused by the backward differences. . . . 6
1.6 Structure of this dissertation. . . . 9

2.1 Overall structure of high precision positioning stage . . . 11
2.2 High precision positioning stage and its model . . . 11
2.3 Frequency responses of the high precision positioning stage. . . . 12
2.4 Outlook of DEMCM. . . . 14
2.5 Structure of DEMCM. . . . 15
2.6 Frequency responses of DEMCM. . . . 16
2.7 Geared in-wheel motor (IWM) vehicle. . . . 17
2.8 Frequency response of the transfer function from driving force to unsprung longitudinal acceleration of the experimental vehicle. . . . 18
2.9 Longitudinal and rotational quarter-car model. . . . 18
2.10 Two-inertia system motor bench setup. . . . 20
2.11 Frequency characteristics of the two-inertia system motor bench. . . . 21
2.12 Backlash width identification . . . 22

3.1 Block diagram of SFLAC [44]. . . . 24
3.2 Structure of Conventional method 1. . . . 25
3.3 Block diagram of Conventional method 2 (state FB control using both motor- and load-side encoders). . . . 25
3.4 Block diagram of semi-dual loop control [45]. . . . 25
3.5 Block diagram of state feedback control using load-side information (Proposed method). 27
3.6 Block diagram of I-type servo. . . . 28
3.7 Comparison of open-loop characteristics in ideal condition. . . . 30
3.8 Comparison of closed-loop characteristics in ideal condition. . . . 30
3.9 Comparison of the step responses in ideal condition. . . . 31

3.10 Comparison of Nyquist plots with modeling error in Simulation 1. 32
3.11 Comparison of open-loop characteristics. 33
3.12 Comparison of closed-loop characteristics. 34
3.13 Step responses in realistic simulations. 34
3.14 Step responses in the experiment. 35
3.15 Input disturbance responses in the experiment. 36
3.16 Comparison of the state variable obtained by the third order difference in the realistic simulations and the experiment. 37
3.17 Block diagram of the conventional method (Linear damping addition). 42
3.18 Step responses of the load-side angle. 43
3.19 The impact torque comparison when step reference of the load-side angle is input. . . 44
3.20 Motor torque responses when step reference of the load-side angle is input. 45
3.21 The load-side angle responses comparison when step load-side disturbances are input -0.50 Nm at 0.010 s and 1.0 Nm at 0.15 s. 46
3.22 The impact torque comparison when step load-side disturbances are input -0.50 Nm at 0.010 s and 1.0 Nm at 0.15 s. 46
3.23 Typical trajectories for stablity analyses. 47
3.24 Block diagram of the observer-based conventional method. 48
3.25 Step responses of the load-side angle with PID controller. 49
3.26 The impact torque comparison when step reference of the load-side angle is input and the controller is changed to PID. 50
3.27 Step responses of the load-side angle with PID controller when the load-side viscosity is 1.25 times of its nominal value. 51
3.28 The impact torque comparison when step reference of the load-side angle is input and the controller is changed to PID and the load-side viscosity is 1.25 times of its nominal value. 52
3.29 Step responses of the load-side angle in the experiments. 53
3.30 The impact torque comparison when step reference of the load-side angle is input in the experiments. 54
3.31 Block diagram of P-PI control (Conventional method 1). 55
3.32 Block diagram of SRC without viscosity. 57
3.33 Block diagram of L-SRC without viscosity. 57
3.34 Block diagram of L-SRC with PID control. 58
3.35 Block diagram of P-PI control. 59
3.36 Comparison of bode plots of rigid body by L-SRC and one-inertia system. 61
3.37 Comparison of nyquist diagrams. 61
3.38 Comparison of closed loop frequency characteristics. 62
3.39 Comparison of step responses. 62
3.40 Comparison of load-side disturbance responses. 63
3.41 Comparison of Nyquist plots with motor-side inertia change. 64
3.42 Comparison of Nyquist plots with load-side inertia change. 65

3.43 Comparison of Nyquist plots with K80% 66
3.44 Comparison of Nyquist plots with K80% 67
3.45 Comparison of step responses with torsional rigidity change. 69
3.46 Comparison of virtual angle step responses between L-SRC and SRC with K200%. . 70
3.47 Comparison of step response in experiment. 70
3.48 Response of virtual angle in Fig. 3.47. 71
3.49 Response of load-side acceleration in Fig. 3.47. 71

4.1 Block diagram of relative velocity FB control (Conventional method). 75
4.2 Nyquist plot of the transfer function from driving force to relative velocity for open-loop characteristic analysis of conventional method. 76
4.3 Block diagram of the proposed method. 77
4.4 Time chart of the dead-time compensated state observer. 77
4.5 Comparison of a Nyquist plot between the plant with the normal state observer and that with the dead-time compensated state observer. 79
4.6 Comparison of the step responses between the conventional method and the proposed method. 80
4.7 Comparison of the frequency characteristics of the closed-loop characteristics between the conventional method and the proposed method. 80
4.8 Frequency response of the experimental vehicle and the designed FF controller. . . . 81
4.9 Experimental comparison of the PSD of the step responses between the conventional method and the proposed method. 82
4.10 Experimental comparison of FRF from a_b^* to a_b. 83
4.11 Experimental comparison of PSD of a_b driving over the road with disturbance at 50 km/h. 83

5.1 Overview block diagram of the proposed joint torque control. 86
5.2 Detailed block diagram of the proposed joint torque control. 86
5.3 Open loop characteristics of P controller, DOB, and the plant. 89
5.4 Frequency responses from the reference to the joint torque with and without two FF controllers (T_sFF and ω_MFF). 90
5.5 Step responses of joint torque with and without ω_MFF. 90
5.6 Realization of backdrivability. Comparison between the proposed control system and a system without any control when the load-side step disturbance is input. 91
5.7 Comparison between the sinusoidal responses of the joint torque with and without backlash compensation. 92
5.8 Joint torque response of the sinusoidal inputs without backlash compensation in the experiment. 94
5.9 Joint torque response of the sinusoidal inputs without the inverse model based backlash compensation in the experiment. 95
5.10 Comparison of the current responses with backlash compensation in two cases. 96

5.11 Backlash compensation models. 97
5.12 Experimental comparison of the sinusoidal responses of the joint torque with and without the proposed model based backlash compensation. 98

6.1 Human-machine interaction in collaborative robots: rotational movement by worker's push. 100
6.2 Backdrivability. 101
6.3 Schematic of the proposed high backdrivable control motion. 102
6.4 The block diagram of the high backdrivable control methods. 103
6.5 Comparison of velocity responses in impedance control with different FB. 103
6.6 Comparison of backdrivability performance. 104
6.7 Comparison of the load-side velocity and load-side external torque responses with modelling error of the load-side inertia moment and viscosity: $J_L = 0.8J_{Ln}$, $D_L = 1.2D_{Ln}$. 105
6.8 Experimental comparison for backdrivability performance. 105
6.9 Overall procedure of human-machine interactive motion and the comparison between double encoder system and single encoder system. 109
6.10 The block diagrams of double encoder control system and single encoder control system. 109
6.11 The block diagrams and frequency characteristics of SERFOB and DERFOB. 113
6.12 Simulation and experimental comparison of the load-side velocity responses. 114
6.13 Simulation and experimental comparison of the load-side external torque responses. . 114
6.14 Simulation and experimental comparison of the estimated external torque responses. 115
6.15 Simulation and experimental comparison of the motor torque responses. 115

7.1 Block diagrams of the proposed load-side external torque observers with/without a joint torque sensor. 121
7.2 Comparison of the errors when $JM = 1.5J_{Mn}$ and $D_M = 1.5D_{Mn}$, or $K = 1.5K_n$, with various α_M. 125
7.3 Simulation comparison of load-side external torque responses in two cases, and -1.0 N·m step d_M is input at 0.20 s with various α_M. 126
7.4 Experimental comparison of load-side external torque responses in two cases, and -1.0 N·m step d_M is input at 0.20 s with various α_M. 126
7.5 Probability distribution of quantization error with quantization step of q. 128
7.6 Comparison of estimation performance in experiments. 132

Chapter 1

Introduction

1.1 Control systems handled in this dissertation and their problems

1.1.1 Needs for position and force control

Precise and fast position control is highly required in industry. Precise and fast motion can produce high quality products with high throughput. Controlling mechatronic systems such as machine tools, robots, and HDDs with high precision and fastness is difficult to realize due to vibration caused by mechanical resonances. Although it is possible not to excite vibrations by reducing the response speed of the control system, it leads lower productivity in machine tools, industrial robots, and rolling mills, and longer access time in HDDs. Therefore, in industry, there is a strong demand for a high-bandwidth position control method that suppresses vibration without compromising the response speed.

Also, accurate force/torque detection is gathering notable research interest [1–3]. For example, Yamada *et al.* [4] estimated the cutting force for monitoring a machining process, whereas Ohba *et al.* [5] estimated the force to control an injection molding machine, and Katsura *et al.* [6, 7] and Mitsantisuk *et al.* [8] estimated contact forces for control considering external environments. Likewise, force estimation is required to enable haptic applications [9–11]. Also in industry, there is an increasing demand for constructing automated manufacturing systems with the flexibility to handle various types of low quantity production. There are two requirements for industrial robots to construct the aforementioned automated flexible product lines. The first requirement is the capability to complete tasks that are difficult for conventional position-controlled robots to perform such as assembling parts and polishing processing. The application of force/torque-control to industrial robots enlarges the field of automation. The second requirement is the capability to concurrently work with human workers in the same environment safely. Position-controlled industrial robots require large spaces surrounded by fences for safety purposes [12]. However, force-controlled robots do not require fences, and this allows collaboration with human workers to complete complex and various tasks. Additionally, there is an

increasing demand for human-support robots (especially in welfare fields) to deal with the issues of an aging society.

1.1.2 Control systems handled in this dissertation

The control systems dealt with in this dissertation range from ball-screw stages and precision positioning stages, machine tool stages, industrial robots, welfare robots, HDDs, rolling mills and so on. In these plants, since the industrial demand for the responsiveness is increasing, the resonances of the mechanical systems have to be carefully considered not to be excited for higher control performance. For example, deformation of the ball-screw nuts in the machine tool stages, deformation of the transmission mechanism such as belts and gears in robots are the main factors of resonance. Conventionally, these controlled objects have been modeled into two-inertia systems, and researches have been actively conducted [13–15].

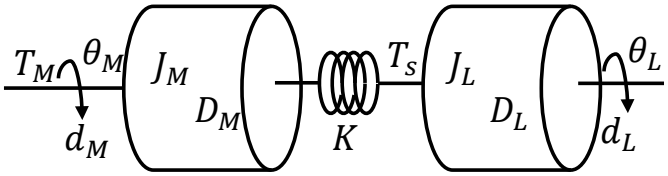

Figure 1.1 Two-inertia system.

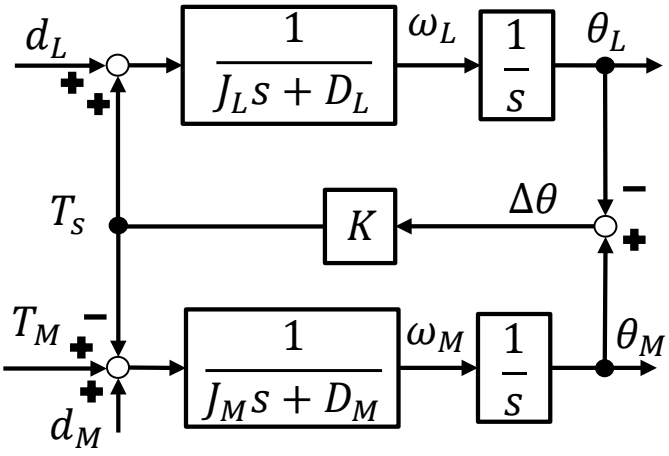

Figure 1.2 Block diagram of two-inertia system.

1.1.3 Two-inertia System

The two-inertia system shown in Fig. 1.1 is an extremely versatile model consisting of three elements: a driving side consisting of a motor, a low rigid transmission mechanism part such as a gear and a ball screw, and a load side. The two-inertia system can express one resonant mode. In this dissertation,

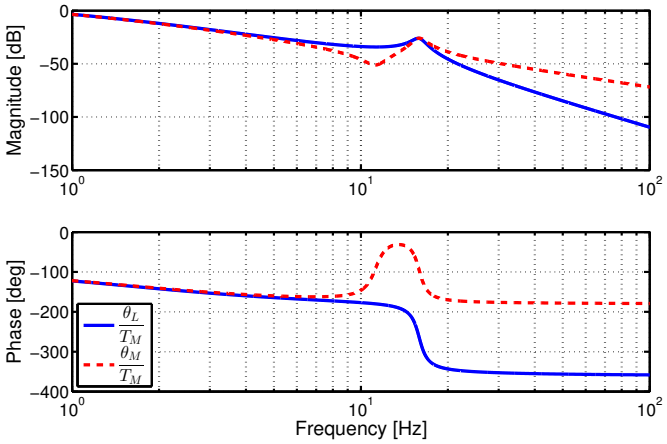

Figure 1.3 Frequency response of two-inertia system from motor torque input to motor-side angle and load-side angle.

a driving side, a transmission mechanism part, and a load side are referred to as a motor side, a transmission part, and a load side, respectively.

Figure 1.2 shows the block diagram of a two-inertia system. Let angle, angular velocity, torque input, torsional rigidity, inertia moment, viscous coefficient, input torque be θ, ω, T, K, J, D, T, respectively. Suffix $_M$ denotes the motor side (or drive side), while suffix $_L$ means the load side. For the sake of simple theoretical studies, the terms D_M and D_L are neglected and the transfer functions (t.f.) from T_M to θ_M, T_M to θ_L are given as below;

$$\frac{\theta_M}{T_M} = \frac{1}{J_M s^2}\frac{s^2+\omega_z^2}{s^2+\omega_p^2}, \tag{1.1}$$

$$\frac{\theta_L}{T_M} = \frac{1}{J_M s^2}\frac{\omega_z^2}{s^2+\omega_p^2}, \tag{1.2}$$

$$\omega_p = \sqrt{K\left(\frac{1}{J_M}+\frac{1}{J_L}\right)}, \tag{1.3}$$

$$\omega_z = \sqrt{\frac{K}{J_L}}, \tag{1.4}$$

where ω_p is the resonance angular frequency and ω_z is the anti-resonance angular frequency.

The equations (1.1), (1.2) indicate that both t.f. $\frac{\theta_M}{T_M}$ and t.f. $\frac{\theta_L}{T_M}$ have one resonant mode. Also, the equations (1.1), (1.2) indicate that t.f. $\frac{\theta_M}{T_M}$ has anti-resonance, while t.f. $\frac{\theta_L}{T_M}$ does not have it.

Load-side feed back (FB) control bandwidth is limited by a resonance due to phase delay. Figure 1.3 shows the bode diagram of t.f. $\frac{\theta_M}{T_M}$ and t.f. $\frac{\theta_L}{T_M}$. As seen in Fig. 1.3, the phase of t.f. $\frac{\theta_M}{T_M}$ is not delayed more than 180 degree due to the existence of anti-resonance, while the phase of t.f. $\frac{\theta_L}{T_M}$ is

Table 1.1 Parameters of two-inertia system used in bode plot Fig. 1.3.

Motor-side moment of inertia J_M	0.010	kgm^2
Motor-side viscosity friction coefficient D_M	0.10	Nms/rad
Torsional rigidity coefficient K	50	Nm/rad
Load-side moment of inertia J_L	0.010	kgm^2
Load-side viscosity friction coefficient D_L	0.10	Nms/rad

delayed more than 180 degree in a frequency band higher than the resonance frequency because there is no anti-resonance.

The problem that instability is caused when load-side FB control bandwidth is higher than the resonance frequency can be considered in the perspective of collocation [16]. A collocated system is a system which has an encoder and an actuator in the same position while a non-collocated system is one which has in different positions. For example, a two-inertia system having an encoder at the load side is a non-collocated system. In a non-collocated system, it is difficult to retain stability under high gain feedback because information with large delay is fed back.

The reason why the two-inertia system has been extensively studied for over 30 years depends largely on its versatility [17]. Also, even in a system having multiple resonance modes such as a rolling mill and a automobile, since the primary resonance mode mainly limits the control bandwidth, it is often modeled and handled as a two-inertia system [18]. All the control methods proposed in this dissertation are targeted for two-inertia systems. Therefore, they can be applied to various controlled objects used in industry.

1.2 Industrial trends and demands

1.2.1 Higher resolution and lower cost of encoders

In industry, the number of encoders with high resolution rapidly increasing. As a rotary encoder for industrial robots, a high resolution encoder such as 24 bit is being used, and research and development of an ultrahigh resolution encoder such as 33 bit is advanced also aiming at further higher resolution [19, 20]. Regarding their cost, the 1 million pulse encoder has become a price of about one hundredth of a decade ago. For this reason, high resolution encoders have been used not only in the field of precision positioning but also in various fields.

Detection of accurate information is required for precise control. An encoder is a device that quantizes and detects position information, which results in unavoidable quantization error depending on its resolution. Assuming that the quantization step of the encoder is Δ, a quantization error of

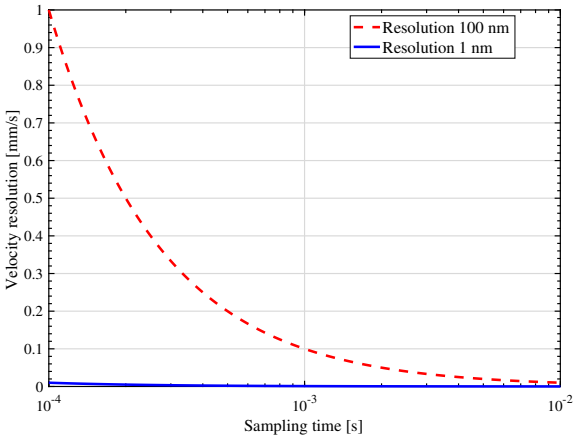

(a) Velocity resolution in translational direction.

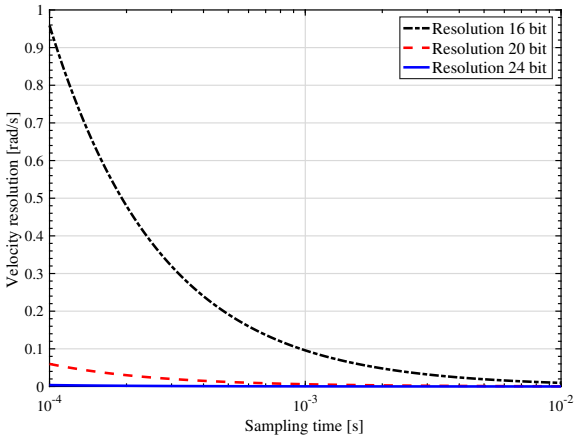

(b) Velocity resolution in rotational direction.

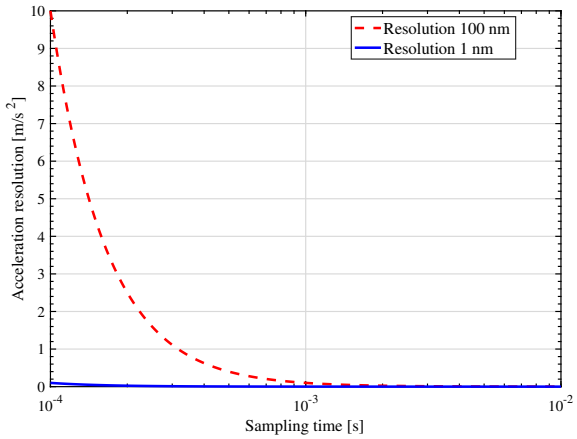

(c) Acceleration resolution in translational direction.

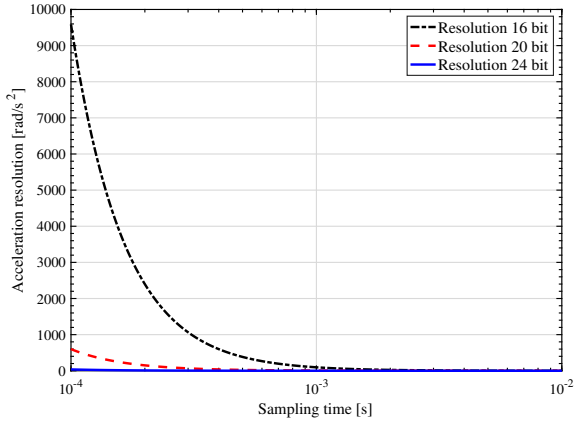

(d) Acceleration resolution in rotational direction.

Figure 1.4 (Rotational) Velocity resolution and (rotational) acceleration resolution obtained by backward differences versus backward sampling time.

the size of $\frac{\Delta}{2}$ is generated at the maximum. Although the resolution enhancement of the encoder is indispensable for accurate position detection, it has a greater influence on accurate detection of higher order state quantities such as velocity and acceleration information than position information detection.

For the detection of velocity and acceleration, the backward difference of the position is often used. The velocity and acceleration obtained by the backward difference are given as below;

$$v[k] = \frac{x[k] - x[k-1]}{T_s}, \tag{1.5}$$

$$a[k] = \frac{v[k] - v[k-1]}{T_s}, \tag{1.6}$$

where $x[k]$, $v[k]$, $a[k]$, T_s are the position, velocity, acceleration at the time k, and backward sampling period, respectively.

When using the encoder with the quantization width Δ, the velocity resolution v_{res} obtained by the first-order backward difference is given by $v_{res} = \Delta/T_s$. Here, Fig. 1.4(a) compares the velocity

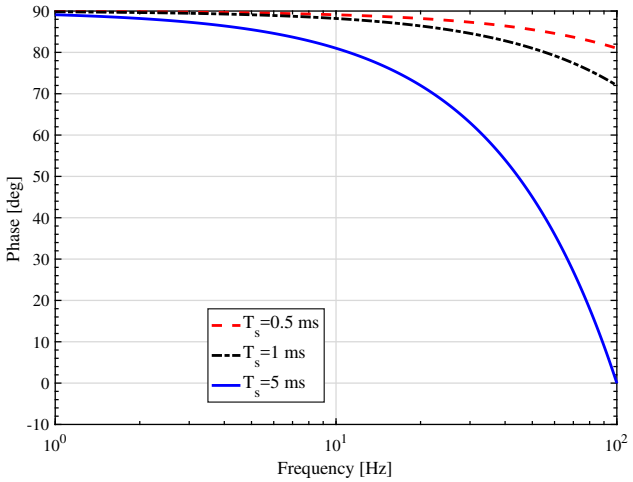

(a) Comparison of phase delay caused by the fist-order backward difference.

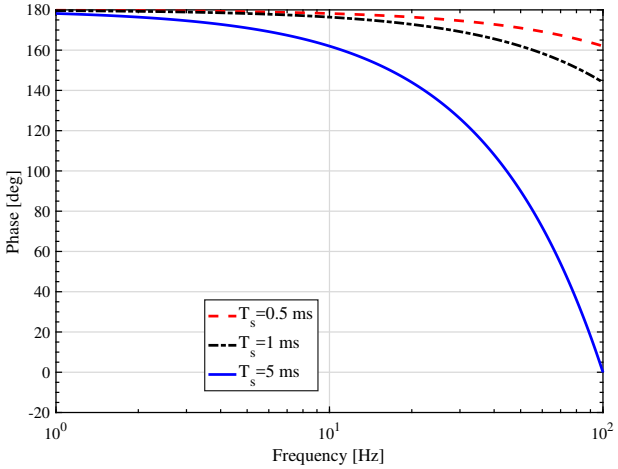

(b) Comparison of phase delay caused by the second-order backward difference.

Figure 1.5 Phase delay caused by the backward differences.

resolution detected by the first-order backward difference when the encoder quantization width is 1 nm and 100 nm. Also for the reference, Fig. 1.4(b) shows the angular velocity resolution detected by the first-order backward difference when the rotary encoder is 16 bit, 20 bit, and 24 bit. As the sampling period becomes smaller, the velocity resolution is degraded, and the velocity resolution is dramatically improved by using the high-resolution encoder. Though longer sampling time can improve the resolution obtained by backward differences, it induces more phase delay.

On the other hand, Fig. 1.5(a) shows the phase delay in different sampling periods. By increasing the sampling period, it is possible to improve the resolution. However, when the sampling period is large, the phase delay increases in the high frequency range as shown in Fig. 1.5(a). For example, in robot control, velocity FB is often applied. When its control sampling frequency and the velocity control bandwidth is assumed to be around 1 kHz and around 10 Hz, respectively, the phase delay caused by backward difference is about 2 degrees. When its sampling frequency is 200 Hz, the delay

is about 10 degrees. This phase delay reduces the phase margin and can induce stability. When in acceleration detction, the phase delay becomes larger as shown in Fig. 1.5(b). Therefore, it is not preferable to increase the sampling period to aim at obtaining high control bandwidth. It is required to increase the resolution of an encoder to reduce the quantization step.

The acceleration resolution a_{res} obtained by the second-order backward difference is given by $a_{res} = \Delta/T_s^2$. The sampling period varies depending on the application, but in the field of motion control, it is about 1 ms. Therefore, every time the backward difference is repeated, the resolution becomes about 1000 times worse. Figures 1.4(c) and 1.4(d) show the acceleration resolution in translational direction and in rotational direction, respectively. As described above, detection of higher order state variables such as acceleration is more difficult because higher order differentials are required, but higher order state quantities can be detected by increasing the resolution of encoders that rapidly advanced in recent years.

Velocity and acceleration information are indispensable for motion control [21]. High resolution encoders are now widely used in the field of robotics, and are promoting cost reduction and a lot of studies on achieving higher resolution have been done [22, 23]. Furthermore, since the environment resistance of the optical encoder has been improved, it is considered that encoders will be applied even in the field of automobiles in the near future. With the popularization of high-resolution encoders, control methods that effectively utilize higher order state quantities are highly required.

1.2.2 From semi-closed control to full-closed control

Conventionally, in the fields of machine tools, industrial robots, welfare robots, etc., semi-closed control feed backing motor-side information using a motor-side encoder is generally performed [24]. However, with semi-closed control, positioning precision on the load side where final positioning precision is required is deteriorated due to the deformation of the transmission mechanism with low rigidity. Furthermore, since the transmission mechanisms such as gears and ball screws are not only flexible but also include nonlinear elements such as backlash, the control accuracy on the load side is deteriorated [25–30].

To enhance the final positioning accuracy even with nonlinearities, full-closed control feed backing both the motor- and load-side information is often applied. To apply full-closed control, the linear encoders are now mounted in standard machine tool stages [31]. Conventionally, industrial robots have been considered difficult to attach encoders to the load side due to the lack of mounting space. In this dissertation, a novel industrial robot module with encoder on the load side is proposed. This device aims at improving the final positioning accuracy by attaching an encoder to the load side, and solves the problem of mounting space etc. by a novel mechanism.

1.2.3 Improvements in bandwidth of joint torque sensors

As described, force control has attracted considerable attentions recently. To realize human-machine interactive motion in cooperative robots, it is required to have sensing capability of external torque input by human [32]. The bandwidth of joint torque sensors about 15 years ago was around several 10 Hz, but now it has been improved to be around 1 kHz. This improvement has enabled us to use the sensor information in real time [33–35]. Most of the cooperative robots in industry have torque sensors in their joints to recognize the contacts with human workers. Therefore, in chapter 7 in this dissertation, the advantages of applying a joint torque sensor for the human-input recognition are evaluated.

1.2.4 Motivation of this study based on industrial trends and demands

Due to the spread of high-resolution encoders and full-closed control, the number of the devices with high-resolution encoders on the load side are increasing. However, despite the trend in industry, it is difficult to say that the study of the control methods using the load-side high-resolution encoder information has been sufficiently done. In this dissertation, control methods using load-side high-resolution encoder information effectively are proposed. Since the trend in industry will accelerate the use of encoders on the load side, there is a strong demand for a new control method in the system with load-side encoder. All control methods proposed in this dissertation respond to the request from industry and their importance will increase in the future.

1.3 Structure of this dissertation

Figure 1.6 shows the structure of this dissertation. This dissertation deals with the control system for two-inertia system. Therefore, the proposed control methods can be applied to various devices. In chapter 2, four experimental devices are introduced and modeled to two-inertia system. From chapters 3 to 7, novel control methods are proposed for each physical values of a two-inertia system as shown in Fig. 1.6. These chapters cover all physical values which should be controlled in a two-inertia system. Backlash nonlinearity is considered in chapters 3, 5, and 6. Thus, this dissertation provides general framework of two-inertia system control using load-side information. Finally, conclusion is given in chapter 8.

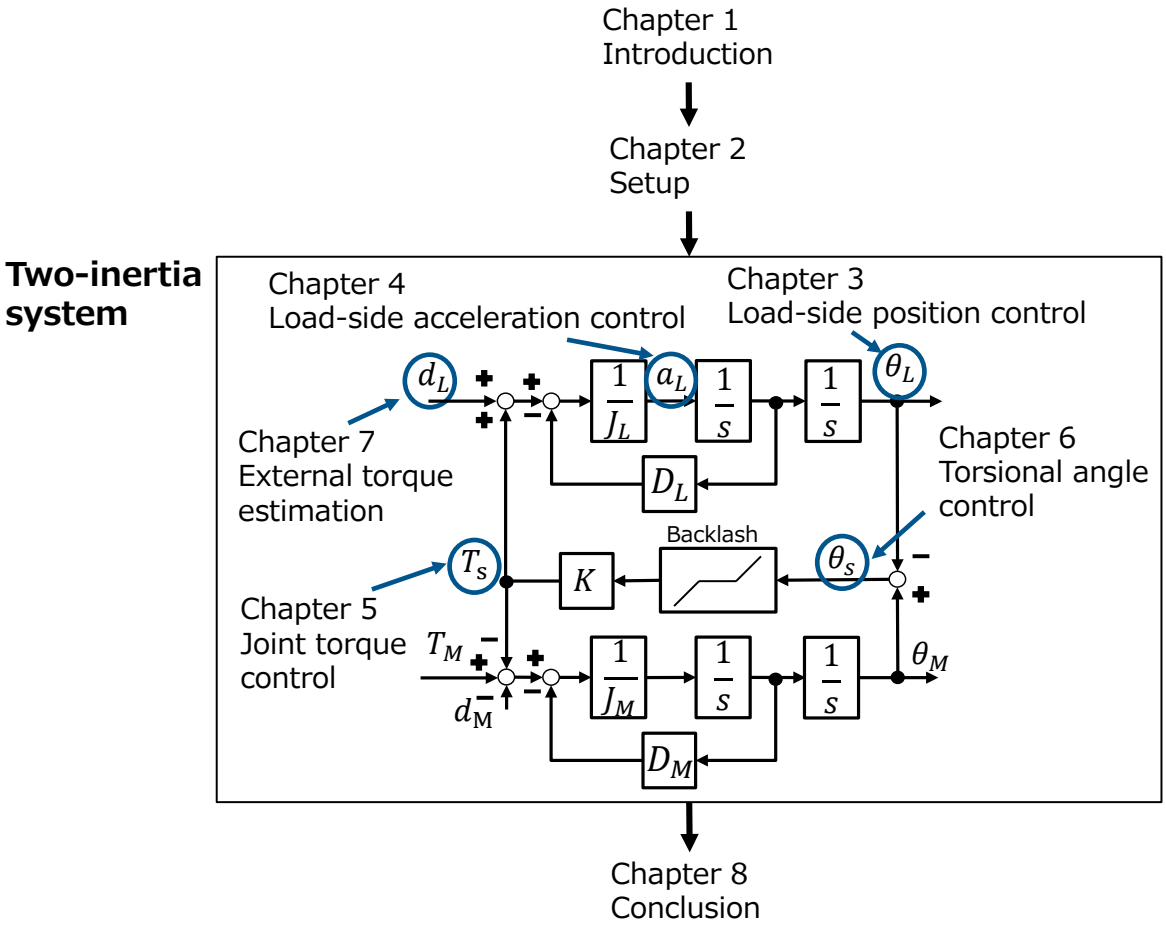

Figure 1.6 Structure of this dissertation.

Chapter 2

Experimental setup

This chapter introduces four experimental setups used in this dissertation. Table 2.1 indicates where the setups are used.

Table 2.1 Chapters and used setups.

Chapter 3.1	High precision positioning stage
Chapter 3.2	Two-inertia system motor bench
Chapter 3.3	Double encoders motion control module
Chapter 4	Geared in-wheel motor vehicle
Chapter 5	Two-inertia system motor bench
Chapter 6	Two-inertia system motor bench
Chapter 7	Two-inertia system motor bench

2.1 High precision positioning stage

2.1.1 Linear stage with two linear encoders

Aiming at industrial application, a precise positioning stage shown in Fig. 2.1 is used as one of the experimental setups. This plant can be modeled as a two-inertia system which consists of the carriage at the motor side and the table at the load side as shown in Figs. 2.2(a) and 2.2(b). It has two linear encoders whose resolution is 1 nm at both motor and load sides. The two linear encoder information are obtained by FPGA implemented in digital signal processor (DSP) via the interpolators. The stage is driven by linear motors and equipped with air guide to avoid nonlinear friction for high precise positioning.

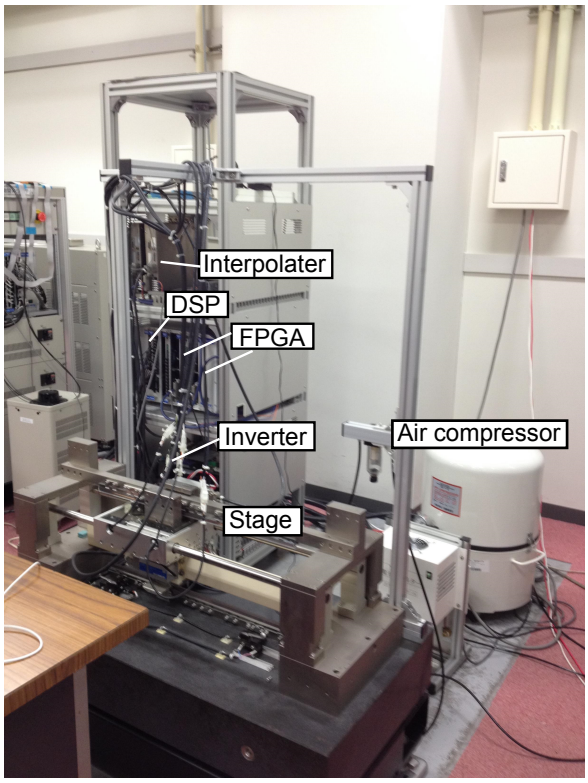

(a) Overview of high precision positioning stage

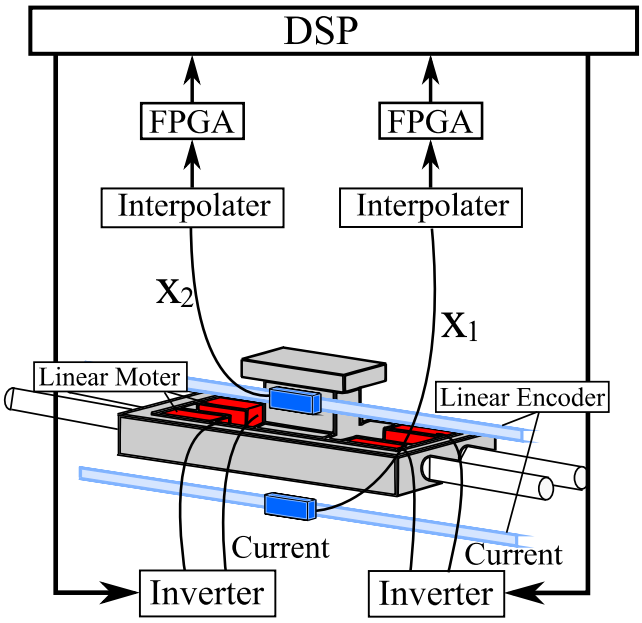

(b) System of high precision positioning stage

Figure 2.1 Overall structure of high precision positioning stage

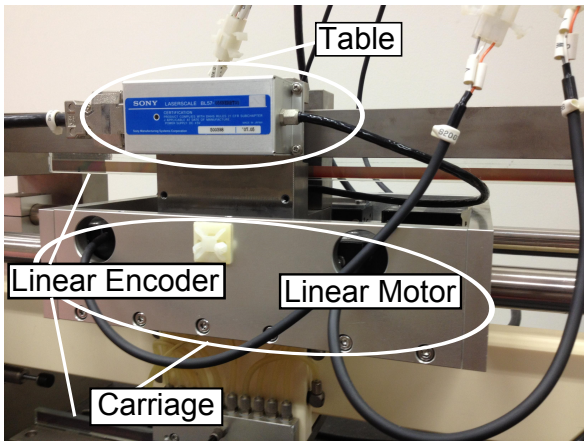

(a) Outlook of high precision positioning stage

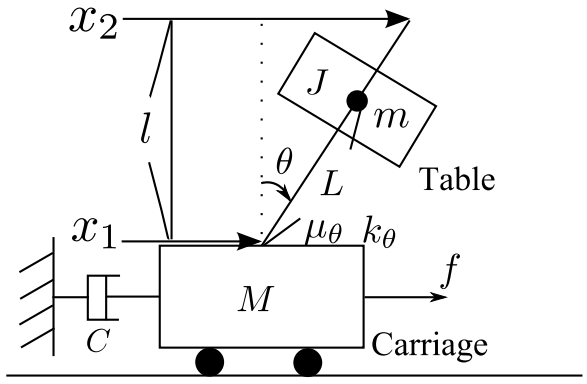

(b) Model of high precision positioning stage

Figure 2.2 High precision positioning stage and its model

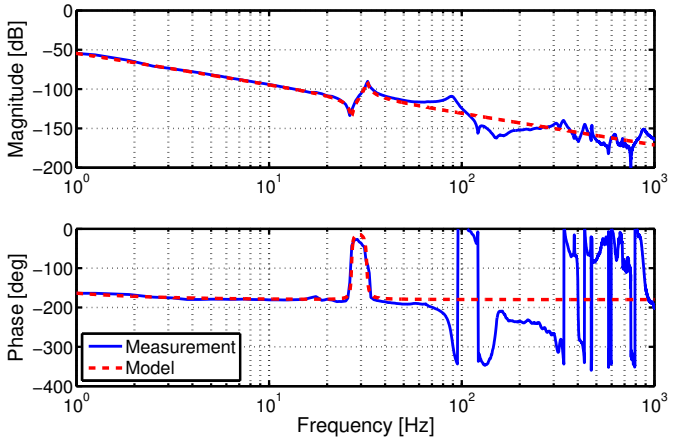

(a) From input to motor-side position.

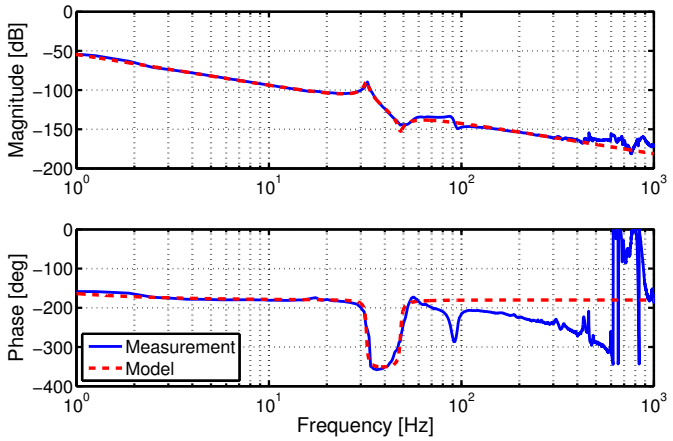

(b) From input to load-side position.

Figure 2.3 Frequency responses of the high precision positioning stage.

2.1.2 Derivation of motion equations and modeling by frequency response analyses

The equation of motion of Fig. 2.2(b) is derived as following;

$$\begin{cases} (J+mL^2)\dfrac{d^2\theta}{dt^2} = -k_\theta\theta - \mu_\theta\dot{\theta} + mgL\sin\theta - mL\cos\theta\dfrac{d^2x_1}{dt^2}, & (2.1)\\ m\dfrac{d^2}{dt^2}(x_1 + L\sin\theta) = N\sin\theta, & (2.2)\\ m\dfrac{d^2}{dt^2}(L - L\cos\theta) = mg - N\cos\theta, & (2.3)\\ M\dfrac{d^2x_1}{dt^2} = f - N\sin\theta - C\dfrac{dx_1}{dt}, & (2.4)\\ x_2 = x_1 + l\tan\theta. & (2.5) \end{cases}$$

Here note that, M, m, C, f are mass of Carriage part, mass of Table part, viscosity coefficient, input force, and J, μ_θ, k_θ are inertia moment, viscosity coefficient, rigidity of pitch direction. Also, N indicates the force between Table and Carriage, and L, l indicate the distance between motor-side encoder and the center of mass of Table and the distance between motor-side encoder and load-side encoder, respectively.

By linear approximation assuming $\theta \simeq 0$, the t.f. $\frac{X_1}{F}$ from input force f to the motor-side position x_1 and the t.f. $\frac{X_2}{F}$ from input force f to the load-side position x_2 are given as following (2.6)–(2.8);

$$\frac{X_1}{F} = \frac{b_{12}s^2 + b_{11}s + b_{10}}{a_4s^4 + a_3s^3 + a_2s^2 + a_1s}, \tag{2.6}$$

$$\frac{X_2}{F} = \frac{b_{22}s^2 + b_{21}s + b_{20}}{a_4s^4 + a_3s^3 + a_2s^2 + a_1s}, \tag{2.7}$$

$$\begin{cases} a_4 = MmL^2 + MJ + mJ,\\ a_3 = M\mu_\theta + m\mu_\theta + (mL^2 + J)C,\\ a_2 = Mk_\theta + mk_\theta - MmgL - m^2gL + \mu_\theta C,\\ a_1 = (k_\theta - mgL)C,\\ b_{22} = mL^2 + J - mLl,\\ b_{12} = mL^2 + J,\\ b_{21} = b_{11} = \mu_\theta,\\ b_{20} = b_{10} = k_\theta - mgL. \end{cases} \tag{2.8}$$

Figures 2.3(a) and 2.3(b) show the frequency responses of t.f. $\frac{X_1}{F}$ and t.f. $\frac{X_2}{F}$. Solid lines indicate the measurement results and dashed lines indicate the fitted models based on (2.6)–(2.8). Identified parameters obtained by fitting are shown in Tab. 2.2. T.f. $\frac{X_1}{F}$ does not delay in phase more than 180 degree because the anti-resonance frequency is lower than the resonance frequency. However, t.f. $\frac{X_2}{F}$

Table 2.2 Parameters of the high precision positioning stage.

Carriage mass M	7.7	kg
Table mass m	5.3	kg
Table Inertia J	1.5×10^{-2}	kgm^2
Viscosity C	24	N/(m/s)
Spring constant k_θ	1.7×10^3	Nm/rad
Decay constant μ_θ	0.20	Nm/(rad/s)
Length L	9.2×10^{-2}	m
Length l	8.5×10^{-2}	m
Thrust coefficient K_t	27	N/A

delays in phase more than 180 degree because the resonance frequency is lower than the anti-resonance frequency. This plant has the same problem as the two-inertia system discussed in chapter 1, where the control bandwidth of the load-side FB is limited by the non-collocation problem.

2.2 Double Encoders Motion Control Module (DEMCM)

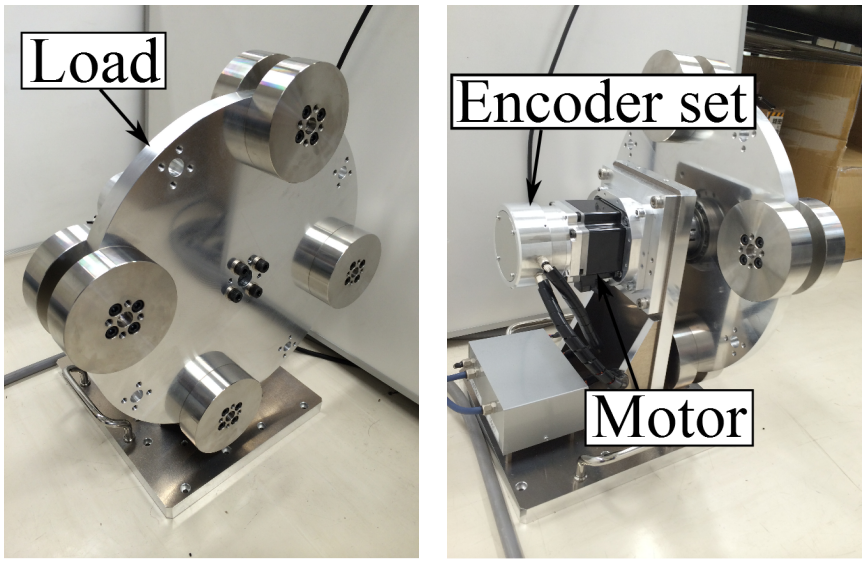

(a) DEMCM (Load-side). (b) DEMCM (Motor-side).

Figure 2.4 Outlook of DEMCM.

2.2.1 Proposal of novel structure for industrial robot module

The setup, named as Double Encoders Motion Control Module (DEMCM), is developed aiming at the application to industrial robots. The overviews of DEMCM are shown in Figs. 2.4(a) and 2.4(b). Industrial robots are difficult to be equipped with an encoder at the load side due to the lack of space

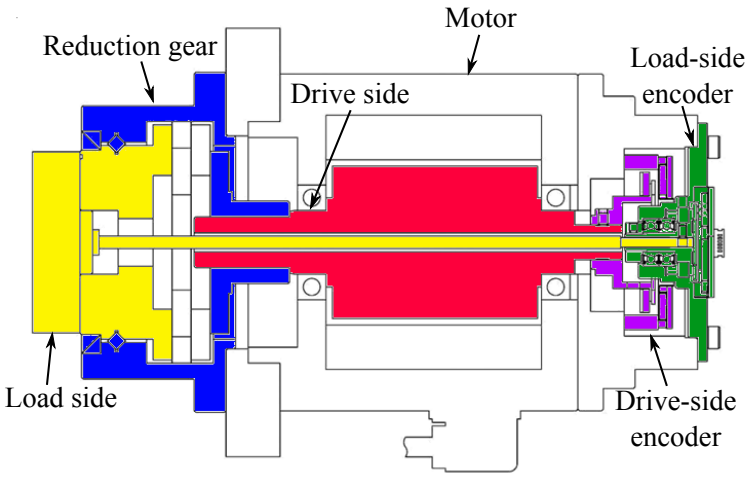

Figure 2.5 Structure of DEMCM.

and the scattering of lubricant, our research group has proposed the novel structure [36]. As shown in Fig. 2.5, there is an output shaft between the load and the load-side encoder through the hollow motor, and the motor-side encoder and the load-side encoder are equipped side by side. The load-side encoder enables to achieve more precise positioning compared with semi-closed control by considering the influence of shaft torsion.

Although the shaft is connected between the gear reducer output and the load side encoder, the shaft has sufficiently high rigidity and the moment of inertia of the load-side encoder is negligibly small. Therefore, the resonance of the shaft exists in a enough high frequency range. The transfer characteristic of the shaft does not affect the characteristics of the system much, and thus it can be modeled as a two-inertia system consisting of a motor, a gear reducer, and a load.

The implemented gear is a harmonic drive gear. The harmonic drive gear is non-backlash. Therefore, backlash compensation studies in this dissertation are conducted in different setup, two-inertia system motor bench. The resolution of two encoders are both 20 bits.

2.2.2 Modeling by frequency response analyses

The measured frequency characteristic of the t.f. from the input torque to the motor-side angle is indicated in Fig. 2.6(a), and that from the input torque to the load-side angle is indicated in Fig. 2.6(b) with the dashed line. The setup has mechanical resonance at 67 Hz.

The frequency characteristics shown in Fig. 2.6(a), 2.6(b) are fitted by a two-inertia model. Solid lines indicate the characteristics of the fitted models. The identified parameters by fitting are shown in Tab. 2.3.

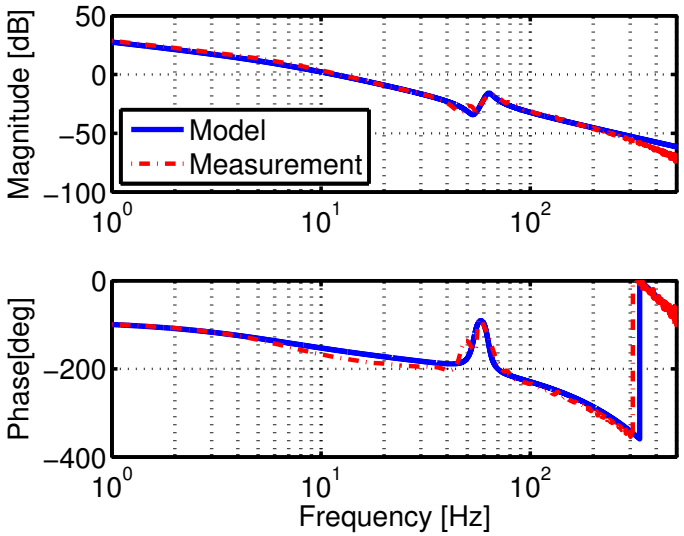

(a) From input torque to motor-side angle.

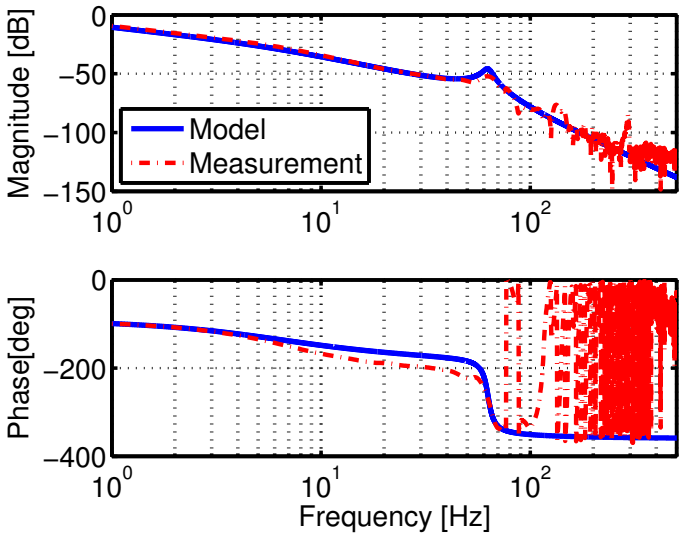

(b) From input torque to load-side angle.

Figure 2.6 Frequency responses of DEMCM.

Table 2.3 Parameters of DEMCM.

Motor-side moment of inertia J_M	1.2e-4	kgm^2
Motor-side viscosity friction coefficient D_M	5.0e-3	Nms/rad
Torsional rigidity coefficient K	3.2e+4	Nm/rad
Load-side moment of inertia J_L	2.8e-1	kgm^2
Load-side viscosity friction coefficient D_L	1.0e+1	Nms/rad
Reduction ratio R	80	

2.3 Geared in-wheel motor vehicle

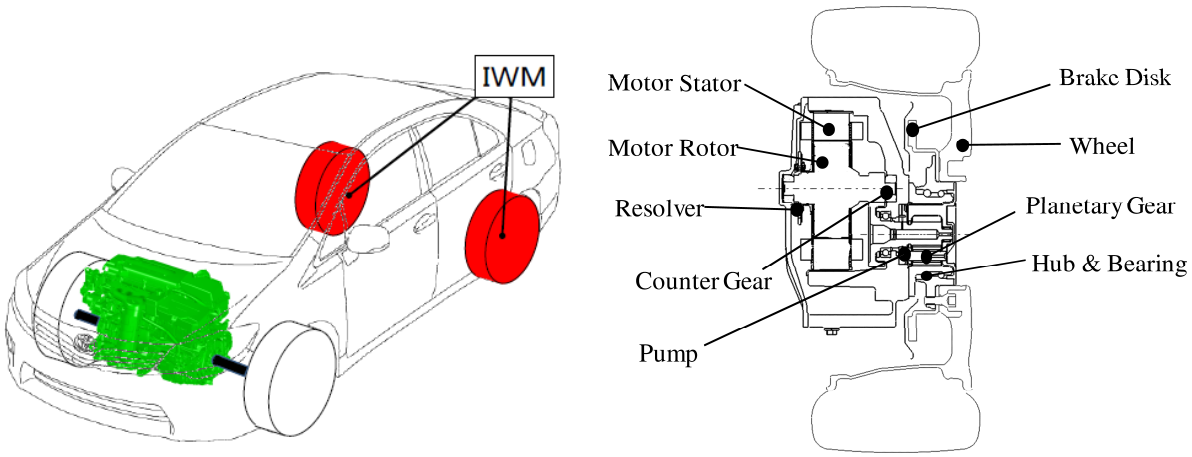

(a) Experimental vehicle with the IWM units. (b) IWM unit in the experimental vehicle.

Figure 2.7 Geared in-wheel motor (IWM) vehicle.

2.3.1 In-wheel motor unit and electric vehicle

The vehicle shown in Fig. 2.7(a) with the in-wheel motor (IWM) units of Fig. 2.7(b) in the two rear wheels is used as the experimental vehicle. The IWM vehicle is developed by Toyota motor corporation. The unit has a counter gear to install the motor into the limited space and a planetary gear to have enough output torque. For details, please see [37].

In this dissertation, only the rear wheels are driven for a proposed control method, and the same controllers are implemented for both left and right rear wheels. The vehicle is equipped with acceleration sensors in the longitudinal direction on the sprung (body) and unsprung mass (hub).

2.3.2 Modeling by frequency response analyses

Frequency characteristics from the driving force to the unsprung longitudinal acceleration of the experimental vehicle is shown in Fig. 2.8. Although the driving force is given by a function of the slip ratio, in this dissertation, the driving force is assumed to be equal to the motor torque divided by the tire radius. The red solid line is a model obtained by fitting and used for simulation purposes and FF control design. Here, a Gauss-Newton formulation approach is applied for fitting [38]. As revealed in the reference by our research group [39], the mode around 10 Hz is caused by the bushing connecting the unsprung part and the body part, and the mode around 27 Hz is a torsional mode in the drive train. The rotational mode appears in the longitudinal direction when the tires are in contact with

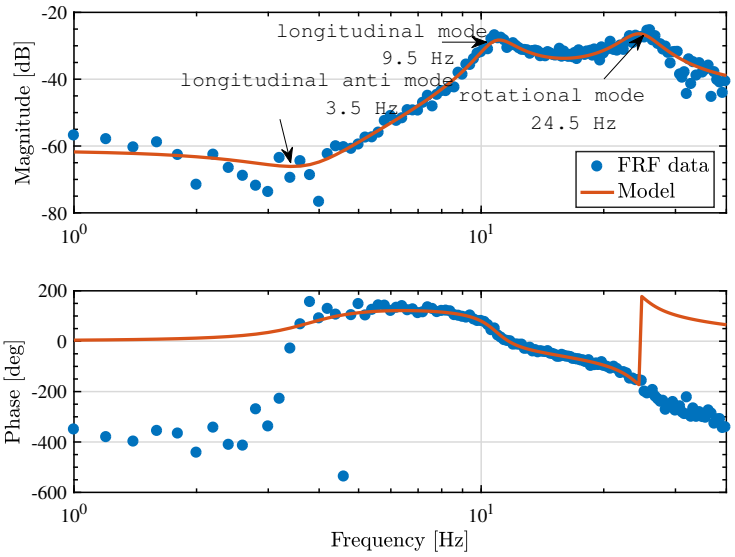

Figure 2.8 Frequency response of the transfer function from driving force to unsprung longitudinal acceleration of the experimental vehicle.

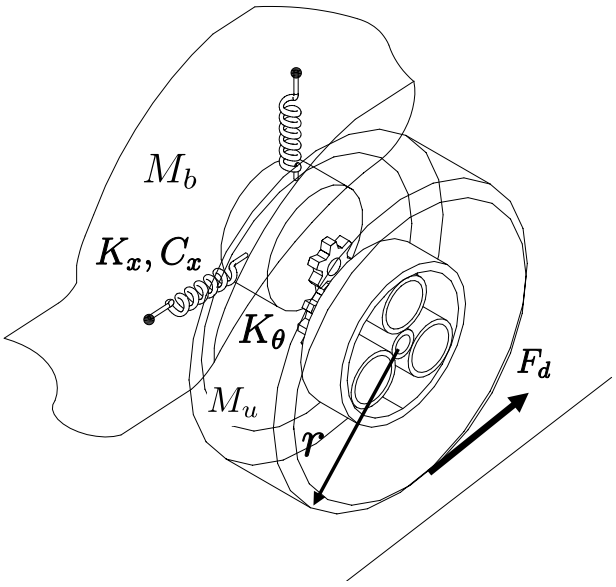

Figure 2.9 Longitudinal and rotational quarter-car model.

the ground. Moreover, since the frequency characteristic to the unsprung acceleration is a collocated system, anti-resonance of the longitudinal mode exists at 3.5 Hz.

The quarter model considering longitudinal and rotational modes is built as Fig. 2.9 based on the frequency response measurement results. The definition of each variable is indicated in Tab. 2.4. In this dissertation, the dynamics in vertical direction are not considered.

Table 2.4 Plant parameters definition of the IWM vehicle model.

M_u	Unsp. mass	a_u	Unsp. longi. acceleration
M_b	Body mass	a_b	Body longi. acceleration
C_x	Longi. viscosity	Δv	Relative velocity
K_x	Longi. stiffness	x_b	Body longi. position
K_θ	Torsional rigidity	x_u	Unsp. longi. position
r	Tire radius	F_d	Driving force

2.4 Two-inertia system motor bench

2.4.1 Motor bench with variable physical parameters

A motor bench with a low stiff joint between two motors is used as the two-inertia system setup. A photograph and a schematic of the setup are shown in Figs. 2.10(a) and 2.10(b), respectively. A high-bandwidth (1 kHz) torque sensor allows the comparison of the measured torque and estimated torque. A flexible joint between the motor side and torque sensor is inserted to exhibit low resonance that is usually introduced by transmission gears.

Controllers are implemented in DSP. The control sampling of current control loop is 10 kHz, and thus, the PI current controller is implemented. The current control bandwidth is experimentally confirmed as 1.2 kHz.

2.4.2 Modeling by frequency response analyses

Frequency characteristics measurements are performed by inputting chirp signals to the current reference. Frequency characteristics of the setup from the motor current to the motor-side angle and from the motor current to the load-side angle are shown in Figs. 2.11(a) and 2.11(b), respectively. As shown in the figures, the setup is modeled as a two-inertia system with an antiresonance frequency of 57 Hz and resonance frequency of 71 Hz. The fitted model is denoted by blue solid lines while the measurement results are denoted by the red dashed lines. The definition of the parameters and the identified value by the fitting are shown in Tab. 2.5 and Tab. 2.6, respectively.

2.4.3 Backlash width identification using both motor- and load-side encoders

Additionally, backlash can be introduced by using a gear coupling. For backlash identification, motor-side velocity control is implemented. As shown in (2.9), backlash can be calculated by inte-

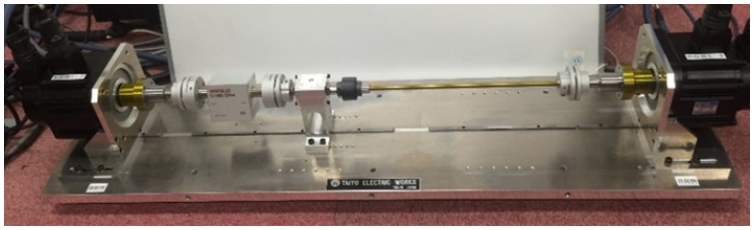

(a) Outlook of the motor bench.

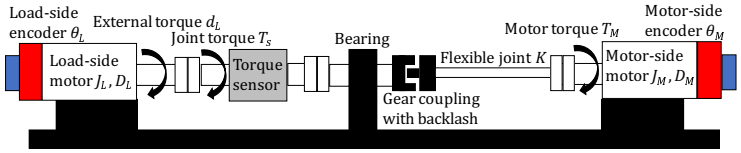

(b) Schematic of the motor bench.

Figure 2.10 Two-inertia system motor bench setup.

Table 2.5 Definition of motor-bench parameters.

Inertia moment	J	Torque constant	K_t
Viscosity coefficient	D	Current	i
Torsional rigidity	K	Angular velocity	ω
Motor torque	T_M	Torsional angular velocity	$\Delta\omega$
Joint torque	T_s	Motor-side disturbance	d_M
External torque	d_L		

Table 2.6 Parameters of the two-inertia system motor bench.

J_M	1.03e-3 kgm^2	J_L	0.870e-3 kgm^2
D_M	8.00e-3 Nms/rad	D_L	1.71e-3 Nms/rad
K	99.0 Nm/rad	K_t	0.173 Nm/A
Backlash width	$\pm$6 mrad		

grating the torsional angular velocity between t_1, when the load separates from the motor side and t_2, when the load contacts the motor side again [40, 41]. Let backlash width be $\pm\epsilon$.

$$2\epsilon = \left| \int_{t_1}^{t_2} (\omega_M - \omega_L) dt \right|. \tag{2.9}$$

In the experiments, backlash width is calculated by not integrating the torsional angular velocity but using the angles at t_1, t_2 obtained by the encoders on drive and load sides. Figure 2.12 shows a part of the identification experiments. Averaging the results leads to $\epsilon = 6.0$ mrad.

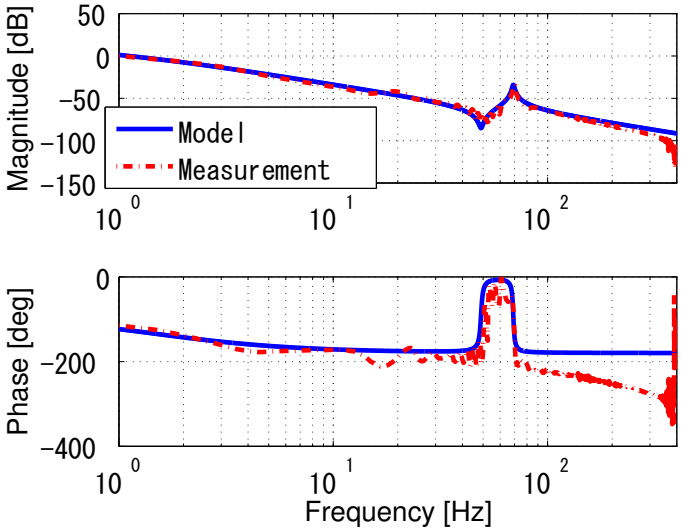

(a) Motor current to motor-side angle.

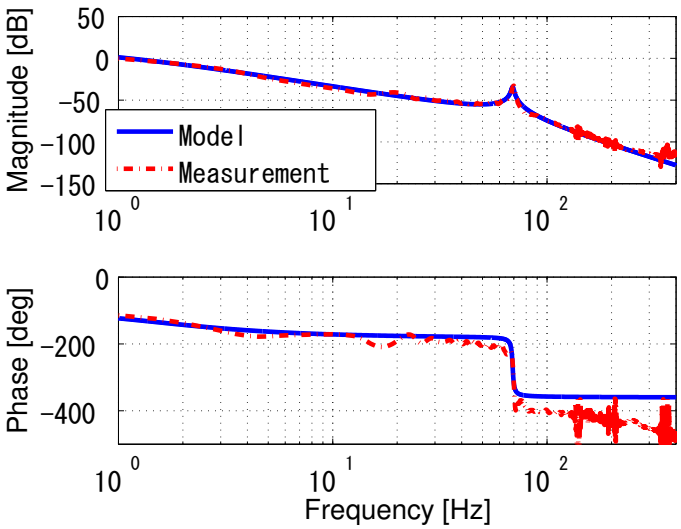

(b) Motor current to load-side angle.

Figure 2.11 Frequency characteristics of the two-inertia system motor bench.

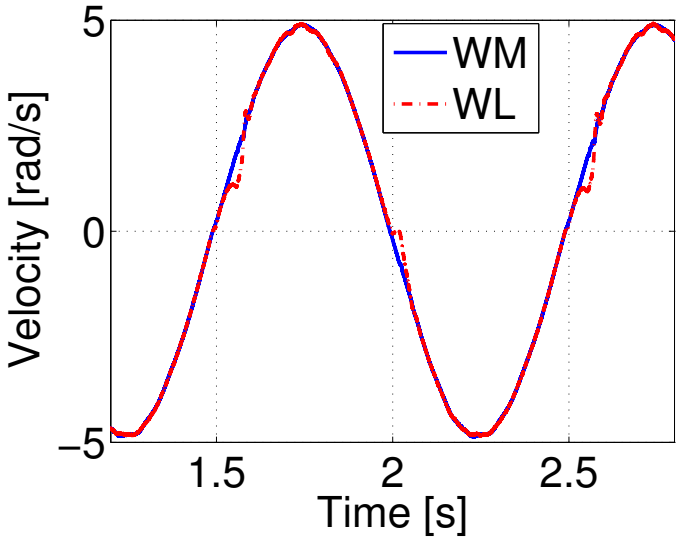

Figure 2.12 Backlash width identification

Chapter 3

Load-side position control

3.1 Abstract

In chapter 3, studies on load-side position control conducted from the three viewpoints, vibration suppression control, backlash compensation, and simplification of controller design are described in detail. In the study on vibration suppression control and simplification of control design, the same performance is realized by only the high-resolution load-side encoder compared with the conventional control methods using both the motor- and load-side encoders. It is an academically innovative research that overturns conventional common sense that both the motor- and load-side information are required for two-inertia system control with high bandwidth. Regarding backlash compensation study, attenuation of the collision caused by backlash is focused. The overshoot of position response becomes larger with the conventional collision mitigation method. There is a trade-off between the control performance and the collision mitigation amount. Based on a detailed discussion on the physical phenomenon, relaxation of the trade-off is successfully achieved by applying a novel switching controller.

3.2 Vibration Suppression Control

3.2.1 Abstract of vibration suppression control

The developments in position control methods have enabled us to obtain a rapid response or high control bandwidth for improving control performance. However, there is an emerging problem in which a control system with a high control bandwidth may excite mechanical vibration, which deteriorates control performance. This is the case especially in a mechanism that has a flexible joint between the motor and the load, such as the feeding tables of machine tools, the arms of industrial robots, and rolling mills. Therefore, there is a strong demand for vibration suppression control with a high control

bandwidth while maintaining productivity. For high-precision control of a two-inertia system, the position information of both the motor side and load side is usually required to obtain a high control bandwidth. In order to reduce the implementation cost and space, a novel control method, which employs the load-side information only, is proposed using a high-resolution encoder. Simulation and experimental results demonstrate that the proposed method exhibits comparable control performance.

3.2.2 Conventional vibration suppression methods

In the control of two-inertia systems, since shaft torsional vibration becomes a problem and deteriorates the control performance, many proposals such as resonance ratio control and state FB control have been presented [13, 42].

Conventional studies on position control of two-inertia systems can be divided into three types depending on whether the encoder is mounted only on the motor side, mounted on both the motor and load sides, or only on the load side. From the viewpoint of cost and maintenance burden, it is better to have fewer encoders, but in order to improve the final positioning accuracy, it is necessary to attach an encoder to the load side. In the past, control method using only the motor-side encoder was widely used to avoid cost increase. However, in recent years, due to the lower cost of the encoder and the higher demand for final positioning accuracy on the load side, the load-side encoder has come to be widely used.

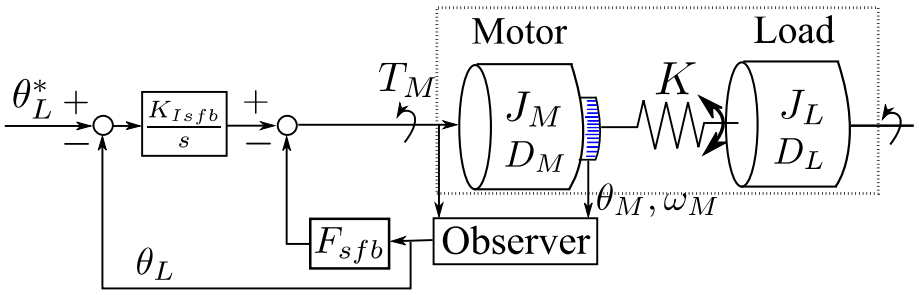

Figure 3.1 Block diagram of SFLAC [44].

Conventional methods using only motor-side information

The resonance ratio control estimates the shaft torsional reaction force, multiply it by a certain gain, and fed back. The shaft torsional reaction force is estimated using reaction force observer from the motor-side velocity detected by the motor-side encoder. Since the apparent inertia of the motor can be changed, the resonance frequency can be changed [14]. It has been shown that good vibration suppression can be obtained when the resonance ratio, which is the ratio of the resonance frequency to the antiresonance frequency, is about $\sqrt{5}$. The relation between Manabe polynomial and the resonance

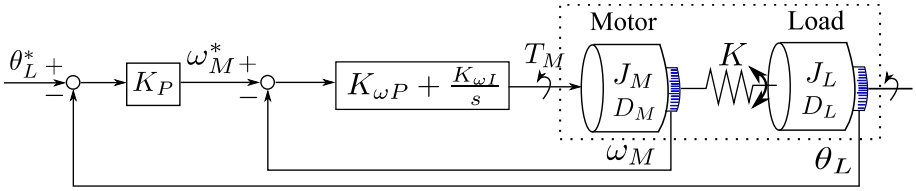

Figure 3.2 Structure of Conventional method 1.

ratio control is also considered in [15]. Resonance ratio control is effective for a two-inertia system plant, but it may adversely affect higher order resonance ignored in modeling into two-inertia systems. Therefore, Katsura proposed a method of controlling vibration suppression of a multi-inertia system by using resonance ratio control for first order resonance and phase lead compensation for higher order resonance in [43].

Vibration can be suppressed by stabilizing the poles of the system by state FB control. Using the input and motor-side velocity, the remaining state variables are estimated by an observer and can be fed back. The SFLAC proposed by Hori shown in Fig. 3.1 is a method to simultaneously suppress disturbance by suppressing vibration with state FB and performing acceleration control on the vibration-suppressed system [44].

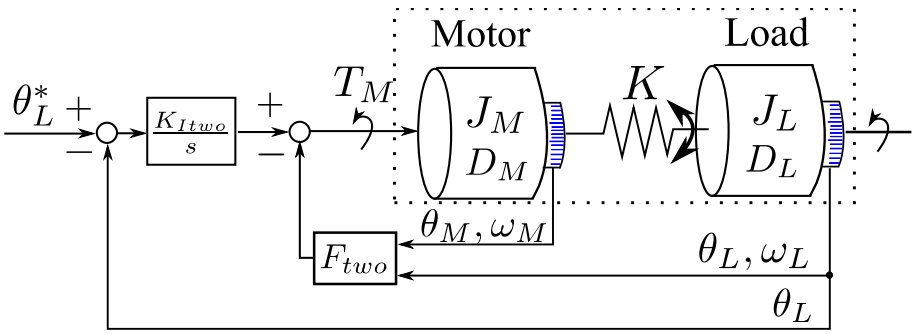

Figure 3.3 Block diagram of Conventional method 2 (state FB control using both motor- and load-side encoders).

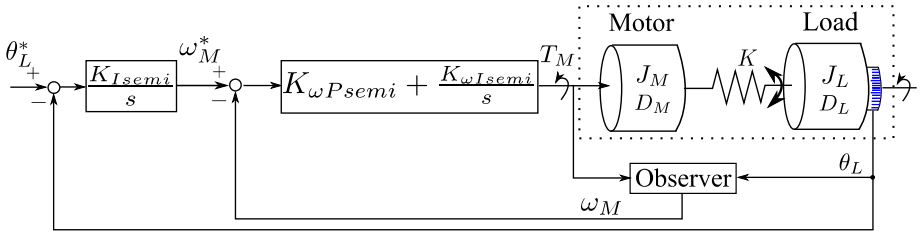

Figure 3.4 Block diagram of semi-dual loop control [45].

Conventional methods using both motor- and load-side information

Today in the industrial society, it is common to synthesize a cascade control system, which has a motor-side velocity FB inner loop with high control bandwidth and a load-side position FB outer loop. Here, this P-PI control method shown in Fig. 3.2 is denoted as Conventional Method 1. In order to make load-side FB control bandwidth higher, collocated motor-side velocity control is required. Conventional Method 1 is easy to apply because the relationship between gain parameters K_P, $K_{\omega P}$, $K_{\omega I}$ and control performances are clear. However, because closed-loop poles cannot be assigned arbitrarily, vibration caused by the plant resonance may appear.

Vibration suppression control becomes possible by state FB as described. It is common to use state observer because state FB control needs all state variables. Observer enables to reduce an encoder but induces deterioration of control performance due to estimation delay and modeling error.

On the other hand, there is a control method, which does state FB control with four state variables (i.e. motor-side position, velocity and load-side position, velocity) obtained by two encoders at the motor side and the load side. The structure of this method is shown in Fig. 3.3. This method has good control performance because it can place closed-loop poles arbitrarily and in addition it is free of estimation delay. Let this method be Conventional Method 2 as a good comparison target to a proposed method.

The control method which feeds back both motor-side position and load-side position like Conventional Method 2 is used on the assumption that both-side home positions have no displacement, but in fact there is a displacement in micro or nano-scale caused by the mounting error of encoders. This displacement leads to deterioration or instability. Conventional Method 1, which is widely used in the industrial society is free from this problem because it uses load-side position and motor-side velocity, not motor-side position. Therefore, it is important in terms of industrial application that control methods do not need both motor-side position and load-side position.

Semi-dual loop control method, proposed in [45], aims at cost and space saving by eliminating a motor-side encoder. Motor-side velocity is estimated by Luenberger state observer and disturbance observer. A proposed method in this section also aims at eliminating the motor-side encoder for the same purpose. In semi-dual loop control, it is difficult to have good control performance because it introduces estimation delay caused by observer and in addition it can not do pole placement.

3.2.3 Proposed method (State FB control using only load-side information)

In the previous study of the position control method described above, the observer is used to estimate the motor- or load-side information, or two encoders are used on the motor and load side.

It is common sense that both motor- and load-side information are required in order to enable high-bandwidth control of two-inertia systems [24]. This proposal is an academically innovative research that reverses the conventional common sense of enabling high-bandwidth control without using motor-side information by applying high-resolution encoder to the load side. Furthermore, since it is possible to reduce the motor-side encoder, it is a practical method which can obtain the merits of cost reduction, maintenance burden reduction, and wiring saving.

Reason why motor-side information is unnecessary

Figure 3.5 shows a block diagram of state FB control using only the load-side information. State FB of four load-side information such as load-side angle, angular velocity, angular acceleration, and jerk to form an I-type servo system as shown in Fig. 3.6. Since state FB is performed only with load-side information, motor-side information is not required.

The reason why we do not need motor-side information is described below. Relative order of t.f. $\frac{\theta_M}{T_M}$ indicated in (1.1) is the second order, and therefore, relative order of t.f. $\frac{\omega_M}{T_M}$ is the first order. On the assumption that integral control is applied, relative order should be the first order in order not to delay in phase more than 180 degree. Meanwhile t.f. $\frac{\theta_L}{T_M}$ shown in (1.2) delays in phase more than 180 degree, because relative order of the t.f. is the forth order. Consequently, it is difficult to obtain high control bandwidth at the load side. However, in case that load-side jerk can be obtained, relative order of the t.f. at the load side becomes the first order, which realizes the control system including integral control with only load-side state variables.

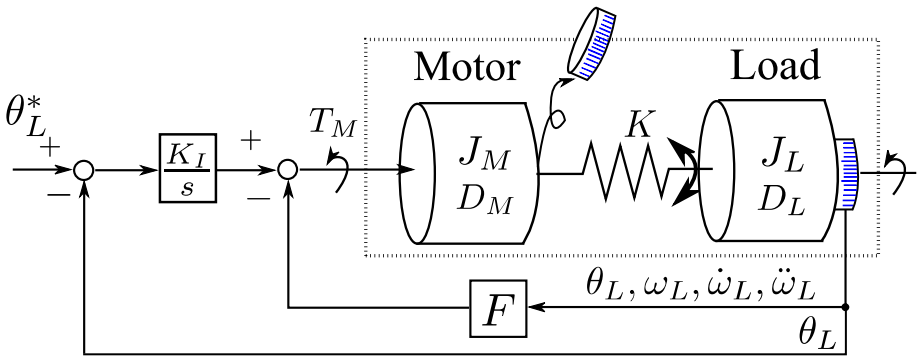

Figure 3.5 Block diagram of state feedback control using load-side information (Proposed method).

Design of proposed method

The order of t.f. $\frac{\theta_L}{T_M}$ shown in (1.2) is the forth order, and therefore the state space realization of t.f. $\frac{\theta_L}{T_M}$ can be given by (3.1)–(3.6) with four state variables $\boldsymbol{x} = [\theta_L\ \omega_L\ \dot{\omega}_L\ \ddot{\omega}_L]^{\mathrm{T}}$.

$$\dot{\boldsymbol{x}} = \boldsymbol{A}\boldsymbol{x} + \boldsymbol{b}T_M, y = \boldsymbol{c}\boldsymbol{x}, \tag{3.1}$$

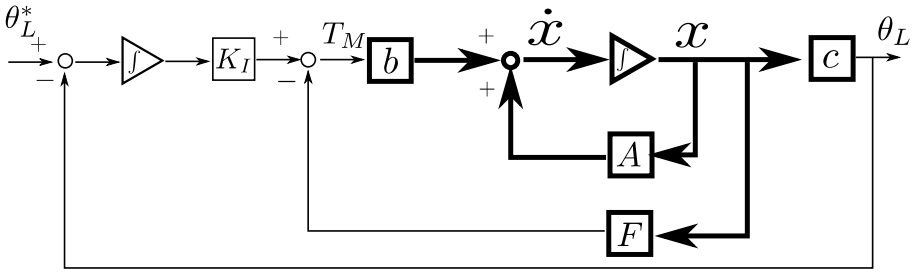

Figure 3.6 Block diagram of I-type servo.

$$\boldsymbol{A} = \begin{bmatrix} 0 & 1 & 0 & 0 \\ 0 & 0 & 1 & 0 \\ 0 & 0 & 0 & 1 \\ 0 & A_{42} & A_{43} & A_{44} \end{bmatrix}, \tag{3.2}$$

$$A_{42} = -\frac{K}{J_M J_L}(D_M + D_L), \tag{3.3}$$

$$A_{43} = -\left(\frac{K}{J_L} + \frac{D_M D_L}{J_M J_L} + \frac{K}{J_M}\right), \tag{3.4}$$

$$A_{44} = -\left(\frac{D_L}{J_L} + \frac{D_M}{J_M}\right), \tag{3.5}$$

$$\boldsymbol{b} = \begin{bmatrix} 0 & 0 & 0 & \frac{K}{J_M J_L} \end{bmatrix}^{\mathrm{T}}, \boldsymbol{c} = \begin{bmatrix} 1 & 0 & 0 & 0 \end{bmatrix}. \tag{3.6}$$

Then state feedback control and integral control for the load-side angle θ_L with a new state variable x_I are applied;

$$T_M = -\boldsymbol{F}\boldsymbol{x} + x_I, \tag{3.7}$$

$$x_I = \frac{K_I}{s}(\theta_L^* - \theta_L), \tag{3.8}$$

$$\frac{d}{dt}\begin{bmatrix} \boldsymbol{x} \\ x_I \end{bmatrix} = \begin{bmatrix} \boldsymbol{A} - \boldsymbol{b}\boldsymbol{F} & \boldsymbol{b} \\ -K_I\boldsymbol{c} & 0 \end{bmatrix}\begin{bmatrix} \boldsymbol{x} \\ x_I \end{bmatrix} + \begin{bmatrix} \boldsymbol{0} \\ K_I \end{bmatrix}\theta_L^*, \tag{3.9}$$

where K_I is a gain of integral control and θ_L^* is a reference of the load-side angle. Vibration suppression control is achieved by placing the poles of the new augmented matrix shown in (3.9) such that vibration can be attenuated.

Advantages of proposed method

Table 3.1 shows the comparison of vibration suppression control methods of a two-inertia system. If pole placement is possible, “Possible” is written down in “Pole assignment”. Pole assignment enables us to increase the degree of freedom in designing control system, and therefore, it becomes easy to

obtain good control performance. If the control system has no state error, '✓' is marked in "Servo". The state error can be suppressed by applying integral control to the load-side position measured by a load-side encoder as far as the system does not lose its stability.

Table 3.1 Comparison of vibration suppression control methods of a two-inertia system.

	Motor-side encoder	Load-side encoder	Pole assignment	Servo
P-PI	Required	Required	Impossible	×
Semi-dual loop control	Unrequired	Required	Impossible	✓
State FB by observer	Required	Unrequired	Possible	×
State FB by encoders	Required	Required	Possible	✓
Proposed method	Unrequired	Required	Possible	✓

Table 3.1 indicates four advantages of the proposed method; unnecessity of a motor-side encoder, no state error, capability of pole placement, being free of the problem that the displacement of the home position between the motor side and the load side. When AC motor is implemented as an actuator, though an encoder is required at the motor side for vector control, a lower-resolution encoder can be implemented to reduce cost compared with an encoder used in the conventional control methods. When encoder-less motor control is implemented, motor-side encoder can be removed without performance deterioration.

3.2.4 Simulations and experiments of vibration suppression control

As a simulation plant and experimental setup, the high precision positioning stage described in chapter 2 is used. The model of the plant can be realized in state space canonical form with state variables $\boldsymbol{z} = [z_1\ z_2\ z_3\ z_4]^{\mathrm{T}}$. The t.f. $\frac{X_2}{F}$ of the plant shown in (2.7) has zeros differing from the t.f. $\frac{\theta_L}{T_M}$ shown in (1.2) of the two-inertia system discussed in section II. Therefore the vector of the output equation of the plant is $\boldsymbol{c'} = [\frac{b_{20}}{a_4}\ \frac{b_{21}}{a_4}\ \frac{b_{22}}{a_4}\ 0] = [c_1\ c_2\ c_3\ 0]$, which means that the plant output (or load-side position) differs from z_1.

With the model shown in Fig. 2.2(b), three methods, Conventional Method 1, 2 and the proposed method are compared in simulations in two different conditions. It should be noted that the proposed method needs only one encoder while the conventional methods need two encoders.

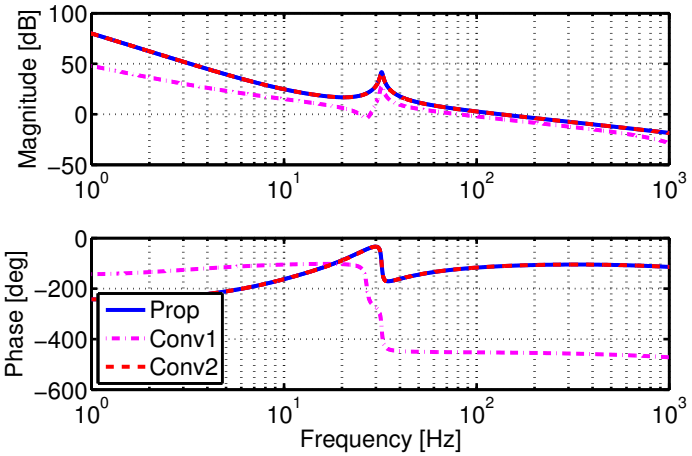

Figure 3.7 Comparison of open-loop characteristics in ideal condition.

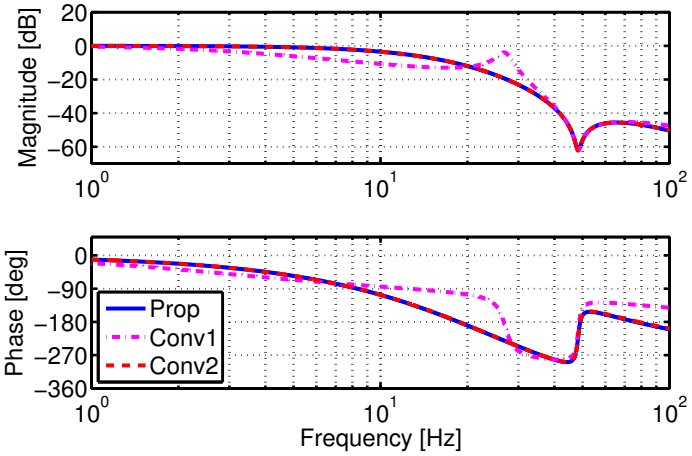

Figure 3.8 Comparison of closed-loop characteristics in ideal condition.

Simulation in ideal resolution (Simulation 1)

Here, simulation is conducted in continuous time. In order to apply the proposed method to the plant, x_2 is converted to z_1, z_2, z_3 with (3.10).

$$\begin{cases} \dfrac{Z_1}{X_2} = \dfrac{1}{c_3 s^2 + c_2 s + c_1}, \\ \dfrac{Z_2}{X_2} = \dfrac{s}{c_3 s^2 + c_2 s + c_1}, \\ \dfrac{Z_3}{X_2} = \dfrac{s^2}{c_3 s^2 + c_2 s + c_1} \end{cases} \tag{3.10}$$

Then z_4 is obtained by pseudo differential whose cut off frequency is 2 kHz. These state variables z_1, z_2, z_3, z_4 are fed back in the proposed method. Also in the conventional methods, pseudo differential whose cut off frequency is 2 kHz is applied to obtain velocity.

Considering the implementation, controllers in ideal condition simulations are synthesized such that

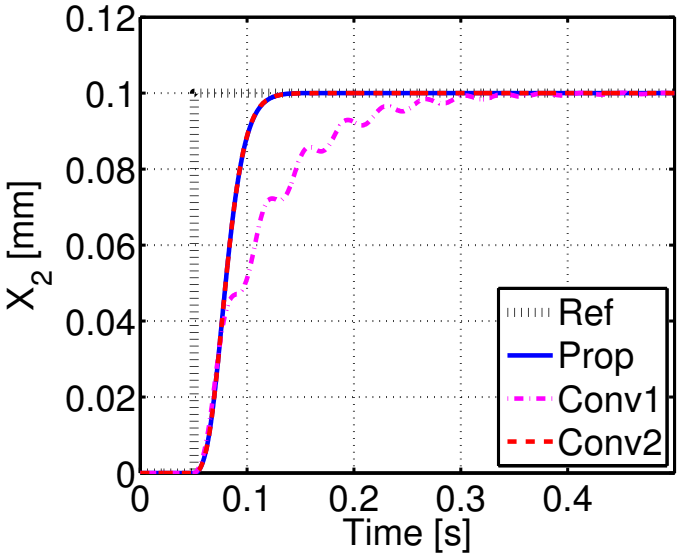

Figure 3.9 Comparison of the step responses in ideal condition.

Table 3.2 Comparison of phase margin and bandwidth in Simulation 1.

	Phase margin [deg]	Bandwidth [Hz]	2% settling time of reference the response [ms]
Conv1	69	2.8	240
Conv2	69	9.2	67
Prop	69	9.2	67

they have enough stability margin. Firstly, Conventional Method 1 is synthesized such that the control bandwidth of velocity control loop is 80 Hz and that of position control loop is 2.8 Hz. In this case the phase margin is 69 degree. Then though Conventional Method 2 and the proposed method can place poles arbitrarily, the poles of the closed loop are placed in quintuple roots way such that the phase margins are 69 degree. These two methods have the same poles because they have the same control structure: state feedback and integral control for the load-side position.

Simulation results are shown in Figs. 3.7–3.9. Figures 3.7 and 3.8 indicate that three methods' phase margins are 69 degree and the control bandwidth is 2.8 Hz in Conventional Method 1, 9.2 Hz in Conventional Method 2 and the proposed method. Table 3.2 shows that the comparison of phase margin and bandwidth in ideal condition. Figure 3.9 demonstrates that the proposed method can suppress the vibration and the fast response can be obtained by the proposed method.

Robustness against modeling error is compared between the conventional method 2 and the proposed method. Two modeling errors of $M = 1.5M_n$, $M = 0.5M_n$ are given as the load-side mass (mass of table) of the plant in the simulation. Here, M_n is the nominal value of the load-side mass.

The open loop characteristics are shown in Fig. 3.10. In addition, since the open loop character-

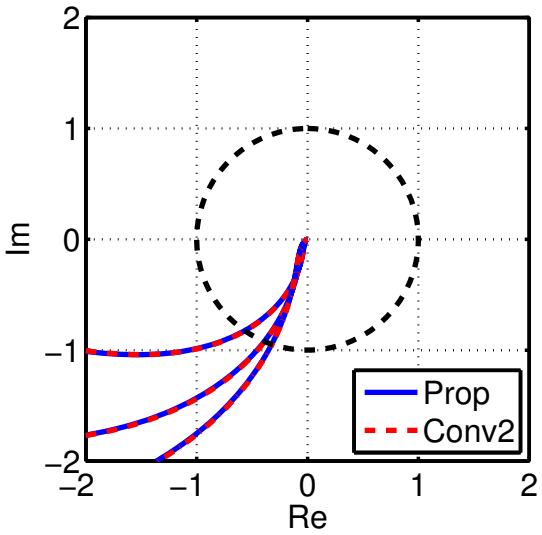

Figure 3.10 Comparison of Nyquist plots with modeling error in Simulation 1.

istics of the case without modeling error ($M = 1.0M_n$) are also plotted for reference. Simulations are performed in three ways, and in total 6 open loop characteristics are plotted. The open loop characteristic when there is no modeling error is the center line, and the open loop characteristic when the two lines shown above and below it have modeling error of ± 50 %. Even when modeling error is given, the characteristics are similarly changed in the conventional method 2 and the proposed method. Therefore, it is considered that there is no deterioration of the robustness to the modeling error by reducing the motor-side encoder.

Simulation in experimental condition (Simulation 2)

In simulation 2, considering applying not only to this precise positioning stage plant but also to a general two-inertia system, x_2 is converted to z_1 by (3.11) not by (3.10) and then z_2, z_3, z_4 are obtained by multiple backward differences.

$$\frac{Z_1}{X_2} = \frac{1}{c_3 s^2 + c_2 s + c_1} \tag{3.11}$$

Velocity, acceleration and jerk are obtained by multiple 5 kHz backward differences with the high-resolution encoder whose resolution is 1nm. Controllers are discretized by sampling frequency 5 kHz. The Butterworth low pass filter (LPF: $F(n, f_c)$) is designed, where n denotes the order of the LPF and f_c denotes the cut off frequency. One LPF ($F(2, 2k)$) is applied to velocity, two LPFs ($F^2(2, 2k)$) to acceleration, and three LPFs ($F^3(2, 2k)$) to jerk.

Conventional Method 2 and the proposed method are synthesized such that their poles are placed in the same places as those of the two methods. Then the phase margins of Conventional Method

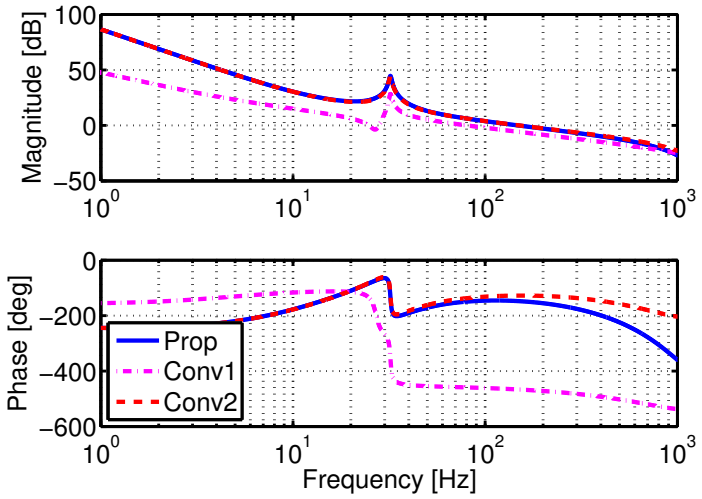

Figure 3.11 Comparison of open-loop characteristics.

Table 3.3 Comparison of phase margin and bandwidth in realistic simulations.

	Phase margin [deg]	Bandwidth [Hz]	2% settling time of the reference response [ms]
Conv1	45	5.2	390
Conv2	56	9.2	68
Prop	45	9.2	67

2 and the proposed method become 56 degree and 45 degree respectively. This difference is due to the influence of LPFs. In order to obtain high-order state variables, the proposed method needs more LPFs than the conventional methods. Conventional Method 1 is synthesized such that its phase margin becomes 45 degree as same as that of the proposed method. Then the control bandwidth of velocity control loop becomes 80 Hz and that of position control loop becomes 5.2 Hz.

Simulation results are shown in Figs. 3.11–3.13. Figures 3.11 and 3.12 indicate three methods' phase margins and that the control bandwidth is 5.2 Hz in Conventional Method 1, 9.2 Hz in Conventional Method 2 and the proposed method.

The step responses are compared in Fig. 3.13. Table 3.3 shows that the comparison of phase margin and bandwidth in realistic simulations. The proposed method can suppress the vibration and the fast response is obtained thanks to the high control bandwidth compared with Conventional Method 1.

Experiments of vibration suppression control

The conditions of the experiments are the same as those in realistic simulations. Experimental results of the step response are shown in Fig. 3.14. Experimental results are close to the simulation results shown in Fig. 4.6. It is presumed that the disappearance of the vibration of Conventional

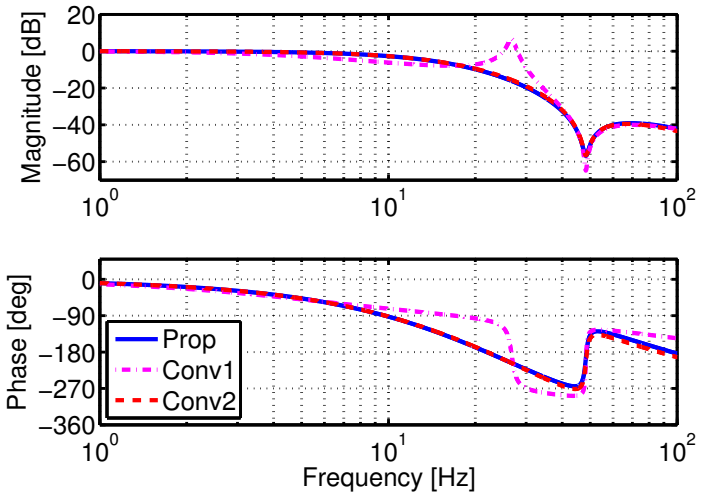

Figure 3.12 Comparison of closed-loop characteristics.

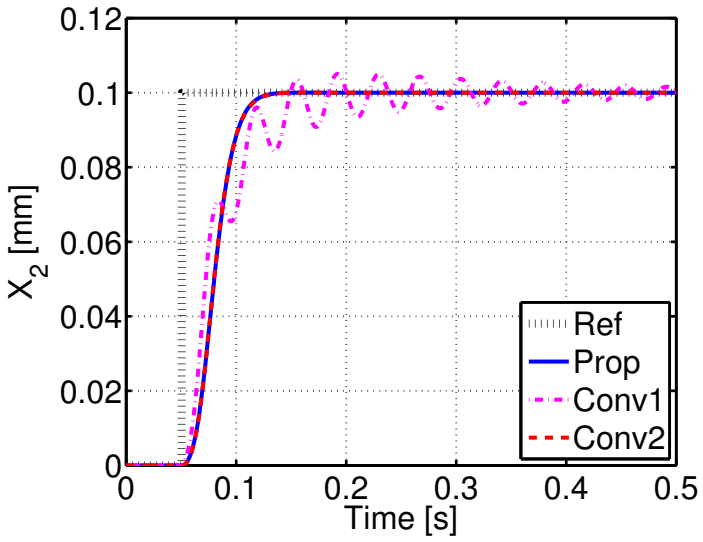

Figure 3.13 Step responses in realistic simulations.

Method 1 seen in the simulation is due to non-linear friction.

The input-disturbance responses are compared in Fig. 3.15. Impulse-like input disturbance which is constant at -10 N from 0.020 s to 0.030 s was applied. The response of Conventional Method 1 has larger maximum amplitude and slow settling. Conventional Method 2 and the proposed method have the comparable performance. Table 3.4 shows that the comparison of the settling time and the maximum amplitude of the disturbance response.

A difficulty of the proposed method lies in obtaining high-order state variables. Figure 3.16 shows the simulation and experimental results of z_4 with LPFs in the step response of the proposed method shown in Figs. 3.13 and 3.14. Because z_4 is obtained by the third order difference, it is considered to

Table 3.4 Comparison of the 2% settling time and the maximum amplitude of the disturbance response in experiments.

	2% settling time of the reference response [ms]	Max amplitude of the disturbance response [um]
Conv1	130	20
Conv2	74	6.1
Prop	66	5.1

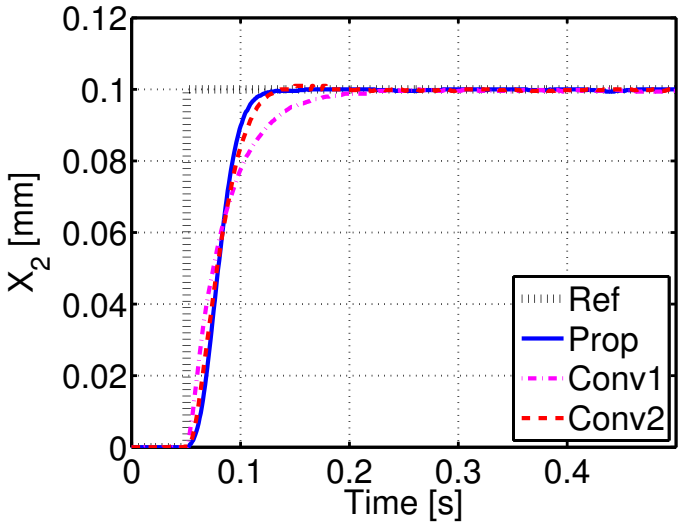

Figure 3.14 Step responses in the experiment.

be equivalent to jerk if plant is the two-inertia system shown in Fig. 1.2. Figure 3.16 shows that z_4, which is equivalent to jerk is badly subject to the influence of noise.

In the simulations and experiments, LPFs are applied to improve the resolution of high-order state variables. As a result, the phase margin of the proposed method has become smaller than that of Conventional Method 2. In order to obtain better control performance, novel methods to obtain high order state variables precisely with less delay by applying the novel encoder system [46] and utilizing the efficient polynomial approximation [47, 48] etc. will be studied in the future.

3.2.5 Conclusion of vibration suppression control

Though it was considered that both the motor-side and the load-side information were required for vibration suppression control with high control bandwidth, this study proposed a novel vibration suppression control method only using load-side state variables by utilizing a high-resolution encoder, which is now widely used in various industrial fields.

The proposed method can remove the motor-side encoder and therefore it is advantageous in terms

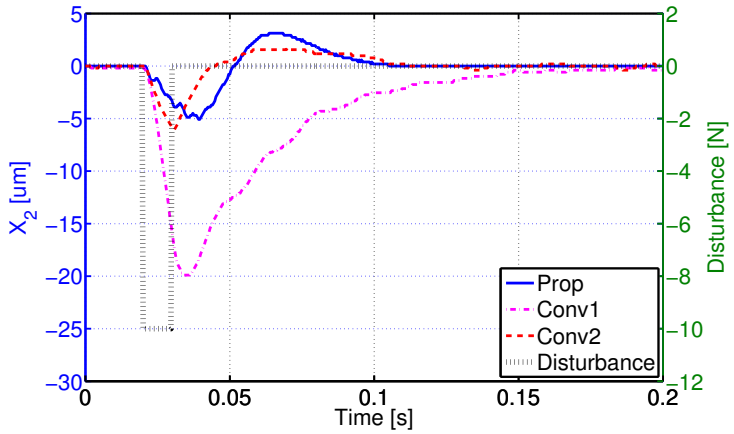

Figure 3.15 Input disturbance responses in the experiment.

of cost reduction of an encoder and space saving. The proposed method has several merits: unnecessity of a motor-side encoder, no estimation delay, no steady error, capability of pole placement, being free of the problem that the displacement of the home positions between the motor side and the load side. Since the proposed method's target is a two-inertia system, it has various applications such as industrial robots and machine tools etc.

The comparable performance of the proposed method is demonstrated by the simulations in ideal condition. It should be noted that the proposed method needs only one encoder while the conventional methods need two encoders.

The control performance of the proposed method is limited by LPFs, which are applied to obtain high-order state variables. Therefore, novel methods to obtain high order state variables precisely with less delay by applying the novel encoder system [46] and utilizing the efficient polynomial approximation [47, 48] etc. will be studied in the future.

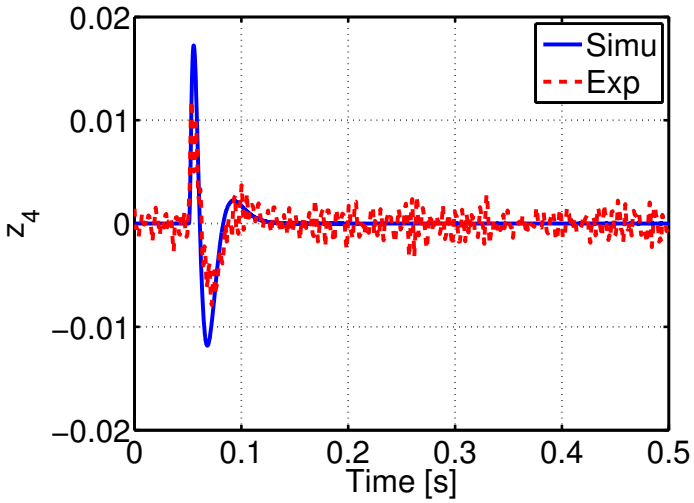

Figure 3.16 Comparison of the state variable obtained by the third order difference in the realistic simulations and the experiment.

3.3 Position control for two-inertia system with backlash

3.3.1 Abstract of backlash compensation

Backlash degrades positioning accuracy and can induce mechanical wear and breakage by collisions. Therefore, a lot of studies have been conducted on backlash compensation. The simplest control method for the impact attenuation is torsional damping addition by FB of torsional velocity. This study reveals the advantages and disadvantages of the torsional damping addition. Based on the analyses, a novel switched damping control is proposed to realize the responses with smaller overshoot while attenuating the impact. The mechanical system and the proposed controller are described as piecewise affine (PWA) systems for analyses. The performance of the proposed method is compared with a linear damping control method in simulations and experiments.

3.3.2 Conventional backlash compensation methods

Problems caused by backlash

In controlling geared mechanical systems, backlash is one of the most important nonlinearities that degrade control performance. Backlash can degrade the accuracy of the load-side positioning, generate limit cycles, and induce mechanical wear and breakage by large impacts caused by collisions between the driving (motor) and driven (load) sides. Since backlash has nondifferentiable property denoted "hard" nonlinearity, it is not easy to compensate effectively.

Piecewise affine model of two-inertia system with backlash

Several models of two-inertia systems with backlash have already been proposed [49]. The physically reasoned model denoted as "exact model" by introducing a state of the angle between backlash has been proposed in [50]. Though several studies (e.g. [51] and [52]) have used the exact model, in [53] it is stated that the dynamics of the introduced state can be neglected in the practical applications. Since our simulation studies also confirmed that the effect can be neglected, this study also uses an alternative approach of the deadzone and linear damping model for the modeling of a two-inertia system with backlash. The PWA model of the plant will be used in simulations plants and the stability analyses later.

Equation of motion of a two-inertia system with deadzone and linear damping are expressed as

Table 3.5 Definition of plant parameters.

Inertia moment	J	Motor torque	T_M
Viscosity coefficient	D	Joint torque	T_s
Torsional rigidity	K	Torsional damping	D_B
Angle	θ	Angular velocity	ω
Torsional angle	θ_B	Torsional angular velocity	ω_B
Deadzone width	β	Load-side disturbance	d_L

follows;

$$\begin{cases} J_M\dot{\omega}_M + D_M\omega_M = T_M - T_s, & (3.12)\\ J_L\dot{\omega}_L + D_L\omega_L = T_s + d_L, & (3.13)\\ \theta_B = \theta_M - \theta_L, & (3.14)\\ \omega_B = \omega_M - \omega_L, & (3.15) \end{cases}$$

$$T_s = \begin{cases} 0, & \text{if } |\theta_B| < \beta,\ \ i = 0,\\ D_B\omega_B + K(\theta_B - \beta), & \text{if } \theta_B \geq \beta,\ \ i = 1,\\ D_B\omega_B + K(\theta_B + \beta), & \text{if } \theta_B \leq -\beta,\ \ i = 2. \end{cases} \quad (3.16)$$

The definition of the variables is given in Tab. 3.5. Subscripts M, L, and B indicate the motor-side, load-side, and backlash related quantities, respectively. It is called that the cases $i = 0$ as Backlash mode, $i = 1$ as Positive contact mode, $i = 2$ as Negative contact mode, respectively. By modeling the system as a PWA system, the well-established theories can be employed (see e.g. in [54, 55]). In this study, PWA system of the below form are considered;

$$\dot{x} = A_i x + a_i + Bu, \qquad \forall x \in X_i, \quad (3.17)$$

$$G_i x + g_i \geq 0, \qquad x \in X_i \ \ i \in I, \quad (3.18)$$

$$F_i x + f_i = F_j x + f_j, \qquad x \in X_i \cap X_j \ \ i, j \in I. \quad (3.19)$$

Here, (3.17) indicates differential equations holding in the separated state space $\forall x \in X_i$. u indicates input and a_i is affine term. $\{X_i\}_{i\in I} \subseteq \boldsymbol{R}^4$ is a partition of the state space into closed polyhedral cells with pairwise disjoint interior. The index set of the cells is denoted I. The inequalities (3.18) indicate the partitions of the state space. The equations (3.19) indicate the boundaries of the jointed two cells of the state space.

Then, the system expressed in (3.12)–(3.16) is rewritten in a PWA notation as follows;

$$A_0 = \begin{bmatrix} -\frac{D_L}{J_L} & 0 & 0 & 0 \\ -\frac{D_M}{J_M} + \frac{D_L}{J_L} & -\frac{D_M}{J_M} & 0 & 0 \\ 1 & 0 & 0 & 0 \\ 0 & 1 & 0 & 0 \end{bmatrix}, \tag{3.20}$$

$$a_0 = \begin{bmatrix} 0 & 0 & 0 & 0 \end{bmatrix}^{\mathrm{T}}, \tag{3.21}$$

$$G_0 = \begin{bmatrix} 0 & 0 & 0 & 1 \\ 0 & 0 & 0 & -1 \end{bmatrix}, \quad g_0 = \begin{bmatrix} \beta \\ \beta \end{bmatrix}, \tag{3.22}$$

$$F_0 = \begin{bmatrix} 0 & 0 & 0 & 1 \end{bmatrix}, \quad f_0 = 0, \tag{3.23}$$

$$A_1 = \begin{bmatrix} -\frac{D_L}{J_L} & \frac{D_B}{J_L} & 0 & \frac{K}{J_L} \\ -\frac{D_M}{J_M} + \frac{D_L}{J_L} & -\frac{D_M}{J_M} - \frac{D_B}{J_M} - \frac{D_B}{J_L} & 0 & -\frac{K}{J_M} - \frac{K}{J_L} \\ 1 & 0 & 0 & 0 \\ 0 & 1 & 0 & 0 \end{bmatrix}, \tag{3.24}$$

$$a_1 = \begin{bmatrix} -\frac{K\beta}{J_L} & \frac{K\beta}{J_M} + \frac{K\beta}{J_L} & 0 & 0 \end{bmatrix}^{\mathrm{T}}, \tag{3.25}$$

$$G_1 = \begin{bmatrix} 0 & 0 & 0 & 1 \end{bmatrix}, \quad g_1 = -\beta, \tag{3.26}$$

$$F_1 = \begin{bmatrix} 0 & 0 & 0 & 0 \end{bmatrix}, \quad f_1 = \beta, \tag{3.27}$$

$$A_2 = A_1, \quad a_2 = -a_1, \tag{3.28}$$

$$G_2 = -G_1, \quad g_2 = g_1, \tag{3.29}$$

$$F_2 = F_1, \quad f_2 = -f_1, \tag{3.30}$$

$$x = \begin{bmatrix} \omega_L \\ \omega_B \\ \theta_L \\ \theta_B \end{bmatrix}, \quad B = \begin{bmatrix} 0 & \frac{1}{J_L} \\ \frac{1}{J_M} & -\frac{1}{J_L} \\ 0 & 0 \\ 0 & 0 \end{bmatrix}, \quad u = \begin{bmatrix} T_M \\ d_L \end{bmatrix}. \tag{3.31}$$

Conventional backlash compensation methods

A lot of studies have been conducted on backlash compensation [49,56]. Geared mechanical systems are often simplified and modeled as two-mass/inertia systems with backlash. In [49] the compensation methods are divided into two groups. The first one is "strong" action group which moves the motor side quickly [57, 58]. One of the strong compensation methods is an inverse model compensation of the backlash model, but it requires large peak in the motor torque and induces mechanical wear by large impacts caused by collisions. The second one is "weak" action group, which includes gear torque compensation [59, 60], switching control [53], fractional order control [61–63], and model predictive

control (MPC) [51, 52], etc.

Among the backlash compensation methods, MPC is studied intensively these days due to the several reasons. The first reason is that MPC can deal with the plant model with backlash directly by hybrid system modeling. Two-inertia systems with backlash can be modeled as PWA systems. Though it is not easy to apply MPC to the motion control of mechanical systems due to low sampling times of control systems, MPC for PWA systems can be calculated offline for a given set of states, which is called Explicit MPC [51]. The second reason is that MPC can reduce the impact torque by collisions by constraining and penalizing the torsional velocity (the difference of the motor- and load- sides velocities) within backlash [51, 52]. However, Explicit MPC for PWA systems still need large computation sources. Therefore, this study develops a simple and industrial-oriented control algorithm, which is intuitive and easy to tune, for motion control applications.

3.3.3 Proposed method (Switched damping control)

The simplest control method for the impact attenuation of the collisions is torsional damping addition by FB of torsional velocity. This study reveals the advantages and disadvantages of the torsional damping addition. By the detailed analyses of how the added torsional damping works, a novel switched damping control is proposed to overcome the disadvantage while holding the advantage. The proposed method shows the responses with smaller overshoot while attenuating the impact. The plant model of the two-inertia system with backlash and the switched damping controller are described as PWA systems, and the stability analyses are conducted in PWA framework.

Problems of damping control

Torsional damping addition control is widely known as one of the effective control methods for a two-inertia system without backlash. Hung in [64] has revealed that the mechanical systems with transmission elasticities behave similarly to the rigid body by torsional damping addition. The vibration caused by the transmission elasticity can be effectively damped. As for a two-inertia system with backlash, the studies on MPC often add damping to the torsional part by constraining or penalizing the torsional velocity term (see e.g. [51] and [52]). This is for avoiding the mechanical wear and breakage by reducing the impact torque and the number of rebounds. However, MPC needs large computation and MPC is challenging to be implemented in standard motion control applications. Though the studies in [51] and [52] try to reduce the computation costs by partially calculating in offline, they still need large computation sources. Therefore, our approach is to develop a simple control algorithm, which is intuitive and easy to tune in applications. Damping addition controller is implemented in inner loop with a load-side position controller in outer loop. In this study, PD controller is applied for

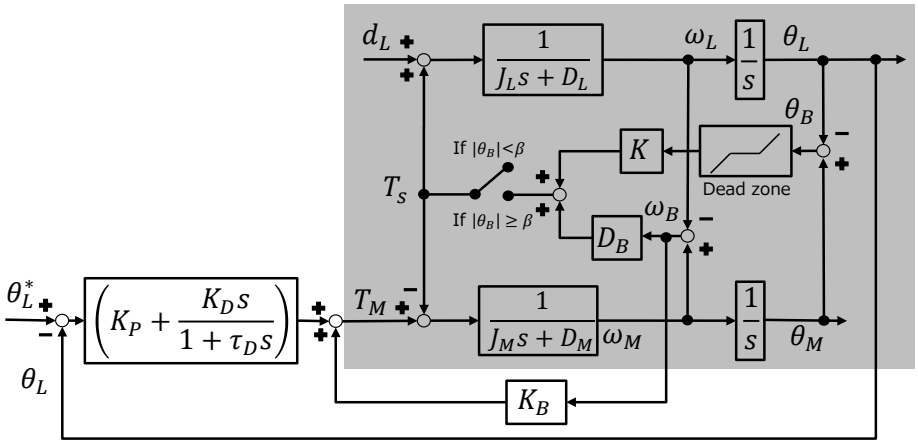

Figure 3.17 Block diagram of the conventional method (Linear damping addition).

positioning as a widely used technique. The block diagram is shown in Fig. 3.17. The motor torque T_M is calculated as follows;

$$T_M = T_{PD} + T_B, \tag{3.32}$$

$$T_{PD} = \left(K_P + \frac{K_D s}{1 + \tau_D s}\right)(\theta_{Lref} - \theta_L), \tag{3.33}$$

$$T_B = K_B \omega_B. \tag{3.34}$$

The control efforts by PD controller T_{PD} and damping controller T_B are expressed in (3.33) and (3.34), respectively. Here, θ_{Lref} is a reference value of the load-side angle.

The simplest control method for torsional damping addition is a FB of torsional velocity with gain K_B as already shown in (3.34). The negative gain K_B attenuates the impact torque by adding the linear damping, but the added damping delays the rising time simultaneously. There is a trade-off between the impact attenuation and the fast responses when designing. The gain should be designed by considering the allowable impact torque of the mechanical system.

To confirm the impact attenuation effect, simulation is conducted using the two-inertia system motor bench introduced in chapter 2. The gains of PD controller are designed by the pole placement method to achieve sufficient fast response, and then the gain K_B is designed to reduce the impact torque. The gains of PD controllers are designed such that their closed poles are placed to be $(s+\omega_1)(s^2+2\zeta\omega_2 s+\omega_2^2)$, $\omega_1 = 2\pi \cdot 18$, $\omega_2 = 2\pi \cdot 15$, and $\zeta = 0.70$ assuming the plant model is rigid body. K_B is designed to be -0.80. The value of the controller parameters in the all control methods are the same for the sake of a fair comparison.

Figures 3.18 and 3.19 show the responses of the load-side angle and the joint torque when the 0.30 rad step reference is given for the load-side angle at 0.010 s. Step reference indicated by the green dotted line is filtered with the first order low-pass filter whose cutoff frequency is 20 Hz. Initial position

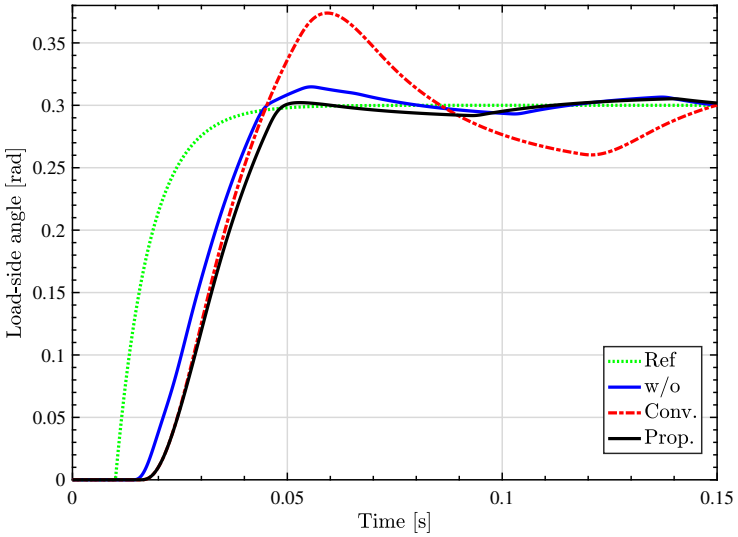

(a) The responses around the rising phase.

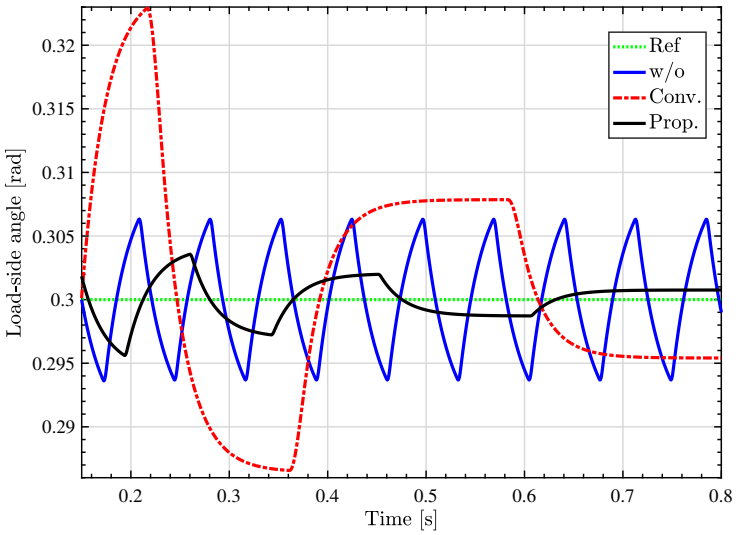

(b) The responses around the settling phase.

Figure 3.18 Step responses of the load-side angle.

of the motor side is at the middle of the deadzone. The blue solid line indicates the response without inner damping controller, that is, $K_B = 0$, while the red dashed line indicates the response with linear damping controller. Figure 3.18(a) shows that the load-side angle responses around rising phase. As expected, with damping control, the transient responses are delayed a little compared to the responses without damping control. On the other hand, the impact torque is attenuated by damping addition as shown in Fig. 6.6(d). In this case, 44% of the first impact torque is reduced. Also, Fig. 3.18(b) shows that stable limit cycle is induced in the response without damping while not seen in Conventional method thanks to the damping addition.

However, Fig. 3.18(a) shows that the response with damping controller has larger overshoot, and thus results in larger vibration also in settling phase as shown in Fig. 3.18(b). The reason why the

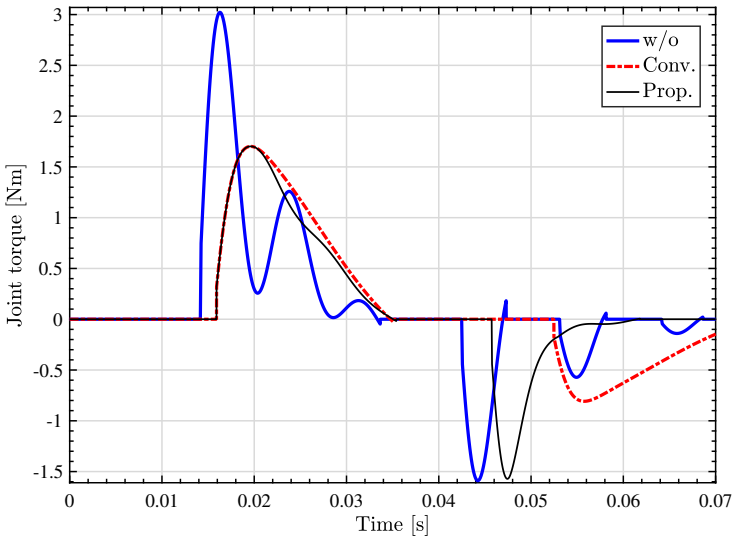

Figure 3.19 The impact torque comparison when step reference of the load-side angle is input.

larger overshoot is caused by damping addition is revealed by analyzing the behavior of the motor- and load-sides. Firstly, the motor side in backlash is accelerated and has the collision with the load side. In this acceleration phase, the linear damping should be added for the impact attenuation. After small rebounds, the load side is required to decelerate for settling. In this deceleration phase, the motor side moves from the positive contact state to the negative contact state. With the added damping, this motor-side traversal motion is delayed, and the load side has more time to move. Thus, larger overshoot is caused by damping addition.

The above consideration is confirmed by analyzing the motor torque responses. Figure 3.20(a) shows that the comparison of the motor torque responses, and Fig. 3.20(b) shows the respective control efforts (T_{PD} and T_B) in Conventional method. Figure 3.20 indicates that the linear damping controller decreases the motor torque at the rising phase, and increases the motor torque at the braking phase starting from about 0.035 s. The increase of the motor torque at the braking phase leads the slow traversal motion of the motor side. In this way, linear damping addition generates large overshoot, though it can reduce the impact torque. Switched damping control method is proposed to solve this trade-off.

Switching condition

The above analyses indicate that linear damping is required in acceleration phase for impact attenuation, but not required in deceleration phase for avoiding large overshoot. When the direction of the motion is negative, linear damping is required in deceleration phase, but not required in acceleration phase. To realize these two demands, switched damping control is proposed.

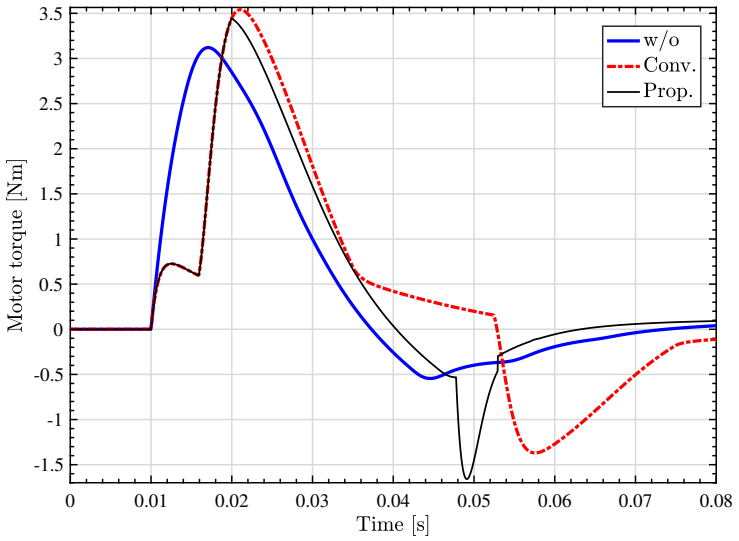

(a) Motor torque responses comparison.

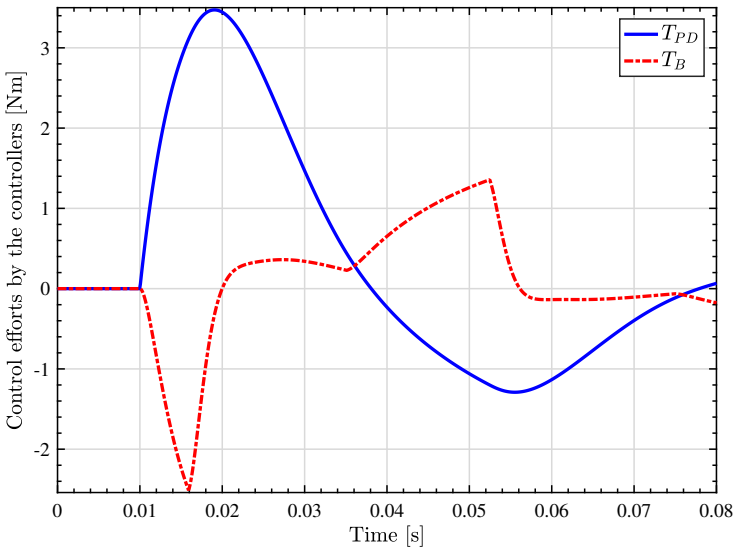

(b) Detalis of the control efforts in Conventional method.

Figure 3.20 Motor torque responses when step reference of the load-side angle is input.

Proposed method switches the gain K_B according to the state variables as follows;

$$K_B = \begin{cases} \text{const} < 0, & \text{if }, \omega_B * \omega_L \geq 0, \\ 0, & \text{else.} \end{cases} \tag{3.35}$$

The switching condition can be equally converted to $(0 \leq \omega_L \leq \omega_M) \vee (\omega_M \leq \omega_L \leq 0)$ for additional interpretation. The switching is done based on the plant's state variables to include the closed-loop system into PWA frame. The switching condition indicates that when the directions of the motor- and load-sides velocities are same and the motor-side velocity is faster than the load-side velocity, the damping is added, and otherwise not. In this way, the acceleration phase is approximately expressed by the condition only using the plant's state variables.

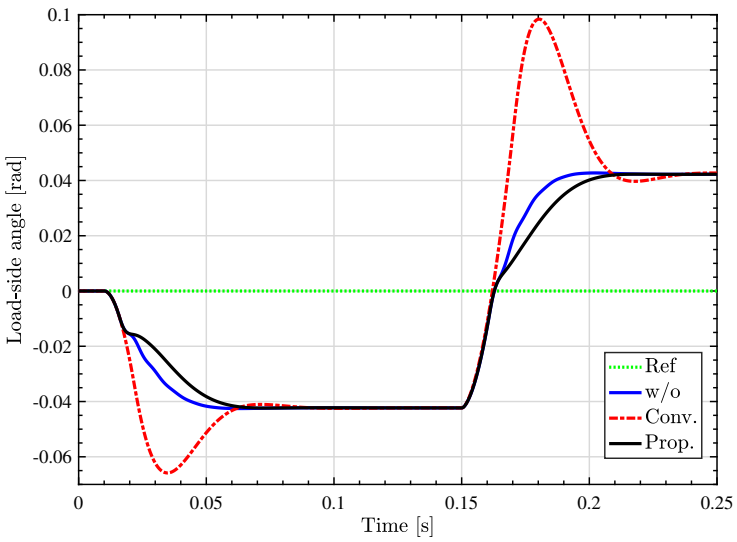

Figure 3.21 The load-side angle responses comparison when step load-side disturbances are input -0.50 Nm at 0.010 s and 1.0 Nm at 0.15 s.

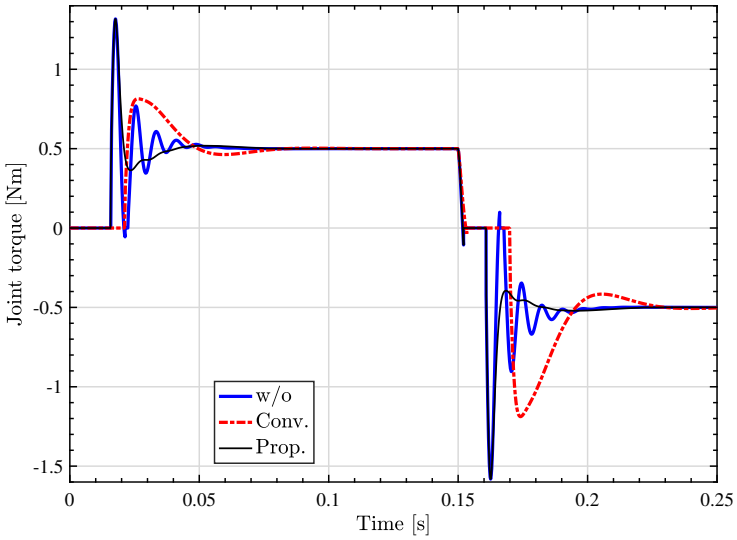

Figure 3.22 The impact torque comparison when step load-side disturbances are input -0.50 Nm at 0.010 s and 1.0 Nm at 0.15 s.

It is confirmed by numerous simulations that the switching condition works correctly both in target value responses and load-side disturbance responses. For example, the disturbance responses are considered. When the load-side disturbance is input, the two-inertia system is either in backlash mode or in contact mode. When the system is in backlash mode, the load-side disturbance makes the load side faster than the motor side. In this case, there should not be damping because the motor side should have the contact with the load side as soon as possible for disturbance suppression. Therefore, Proposed method has better performance than Conventional method. When the system is in positive contact mode, the positive disturbance makes the load side faster than the motor side. In this case,

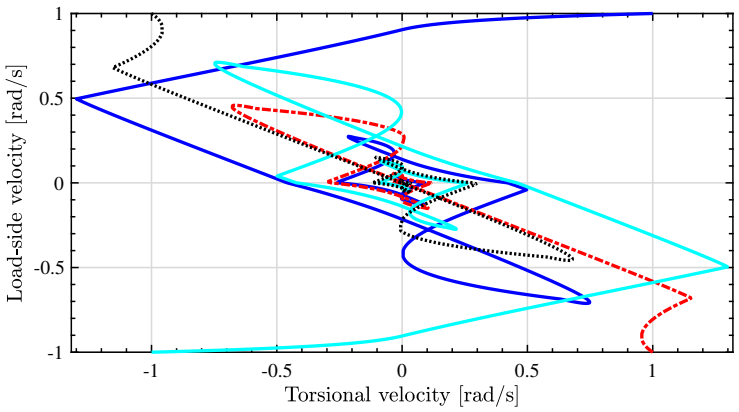

(a) Free responses in backlash mode.

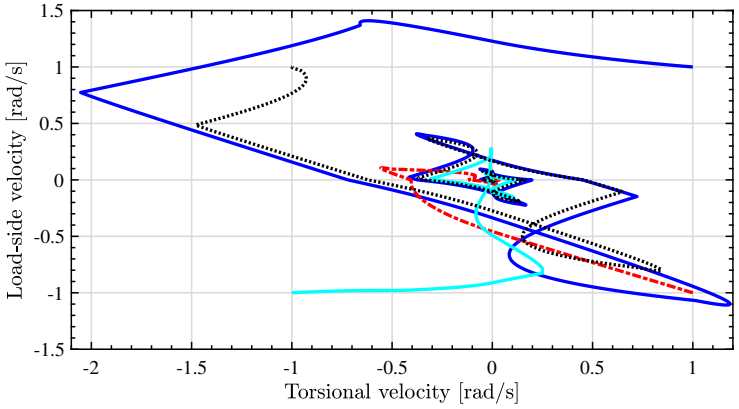

(b) Free responses in contact mode.

Figure 3.23 Typical trajectories for stablity analyses.

there should not be damping, and the condition works correctly. When the negative disturbance is input, the velocities become to $\omega_M \leq \omega_L \leq 0$. In this case, there should be damping because the motor side should not move away to have the contact with the load side as soon as possible for disturbance suppression. Thus, Proposed method shows better performance than the method without damping.

The switching condition does not perform efficiently in some cases, e.g. in the rebounding and releasing phase after the impacts, the motor-side velocity becomes smaller than the load-side velocity, that is, the damping controller does not work. In the phase, there should be damping because the motor side should not move away to have a contact as soon as possible to accelerate/decelerate the load side in positive/negative direction motion. However, in most cases the switching condition performs appropriately.

3.3.4 Simulations and experiments of backlash compensation

Simulation comparison with conventional method

The advantages of Proposed control method are shown in Figs. 3.18 and 3.19. In Fig. 3.18, Proposed method shows almost same size of the overshoot as the method without damping while the impact

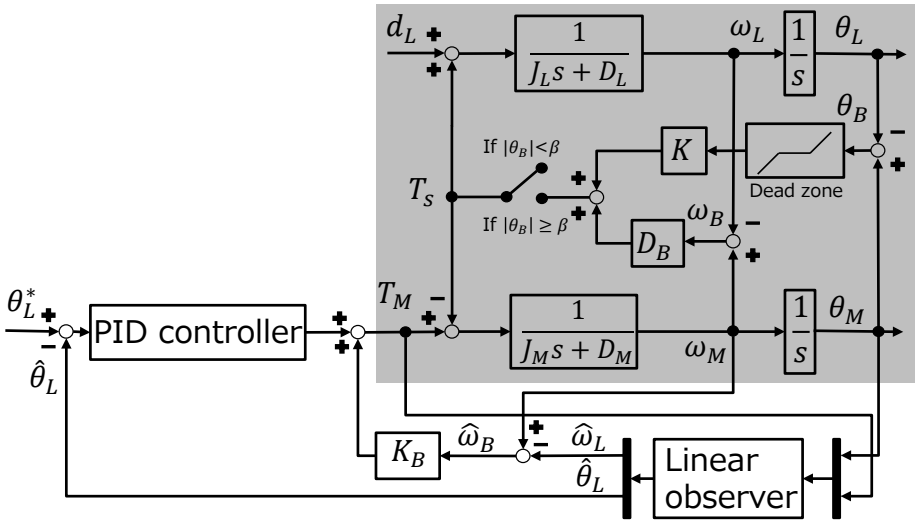

Figure 3.24 Block diagram of the observer-based conventional method.

torque is much smaller. Fig. 3.20(a) shows that Proposed method attenuates the impact by reducing the motor torque as Conventional method in acceleration phase. The simulation results validate the advantages of switching damping controller by relaxing the tradeoff between overshoot and impact attenuation.

Figures 3.21 and 3.22 show the load-side angle responses and the joint torque responses when step load-side disturbances are input -0.50 Nm at 0.010 s and 1.0 Nm at 0.15 s. Initial condition is that both motor- and load- sides are not moving and the motor-side is at the middle of the deadzone. The angle response in Conventional method in red dashed line shows less disturbance suppression performance since the damping makes the motor side move away from the load side. The joint torque responses shown in Fig. 3.22 indicate that the impact torque is reduced in Conventional method but not reduced in Proposed method. For disturbance suppression, damping should not be added to have the contacts between the motor and load sides as soon as possible in terms of controllability of the load side. Therefore, Proposed method shows better performance than Conventional method. Moreover, Proposed method shows better performance than the method without damping, since after the impact, the motor-side velocity becomes larger than the load-side velocity and the damping controller works not to move the motor side away from the load side.

Stability analyses

Stability is analyzed by using the PWA systems notation. The closed-loop system with Proposed method consists of the state space divided into 12 cells since the plant has 3 cells about θ_B and the switched damping controller has 4 cells about ω_L and ω_B. Since the positive contact mode and the negative contact mode in (3.16) have the symmetrical dynamics, it is enough to consider

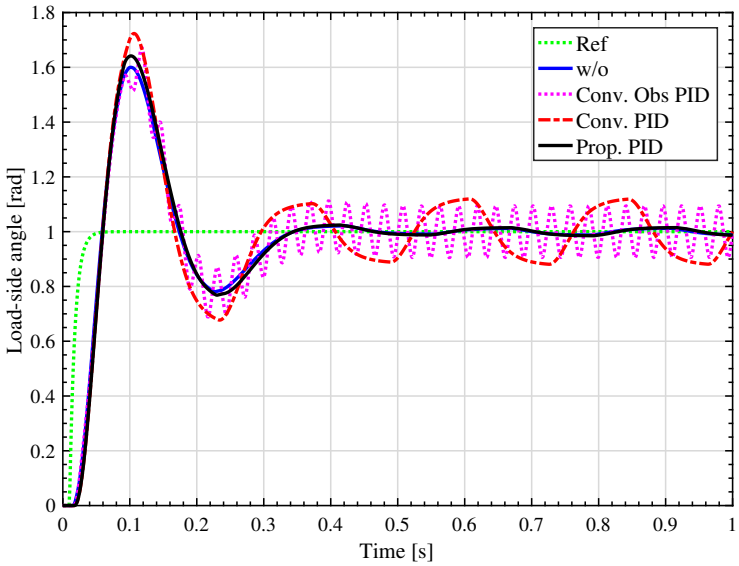

(a) The responses around the rising phase.

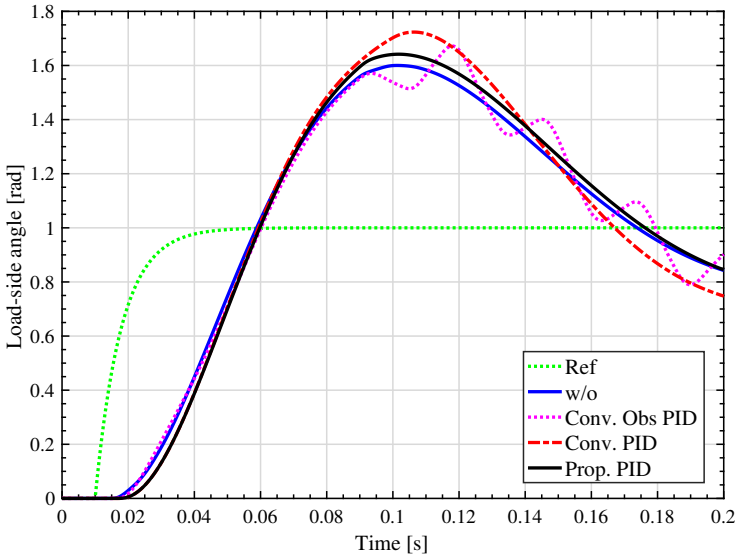

(b) The responses around the settling phase.

Figure 3.25 Step responses of the load-side angle with PID controller.

two cases: backlash mode and contact mode, which results in considering 8 cells in total. Though there are toolboxes for finding Lyapunov function for stability analyses (e.g. [65]), it was not possible to find a suitable Lyapunov function candidate for our closed-loop systems with internal deadzone nonlinearity and switching control, both in PWA notation. Therefore, the stability is analyzed by seeing the convergence of the typical trajectories starting from different 8 cells. Figure 3.23(a) shows the free responses in backlash mode (θ_B=0 rad) with four cases of initial conditions: (ω_B [rad/s], ω_L [rad/s])=(1.0, 1.0), (1.0, -1.0), (-1.0, -1.0), (-1.0, 1.0). Figure 3.23(b) shows the free responses in contact mode (θ_B=0.010 rad) with the four cases. Figure 3.23 indicate the convergence of the typical trajectories starting from different 8 cells.

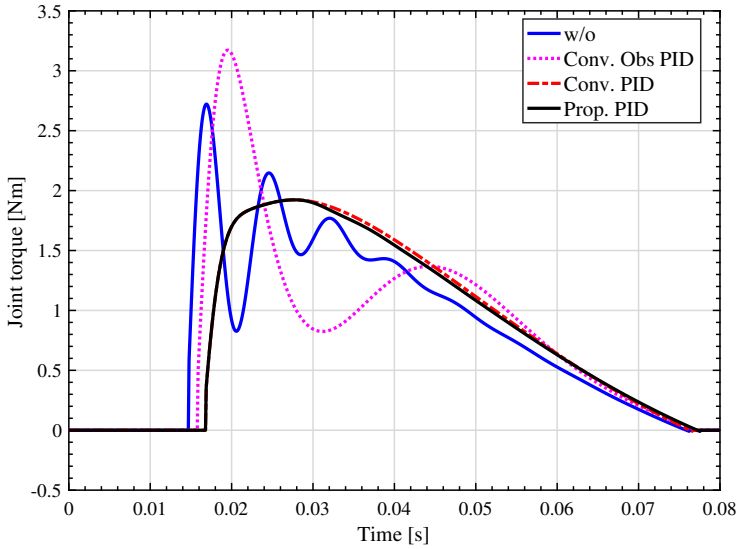

(a) The responses around the rising phase.

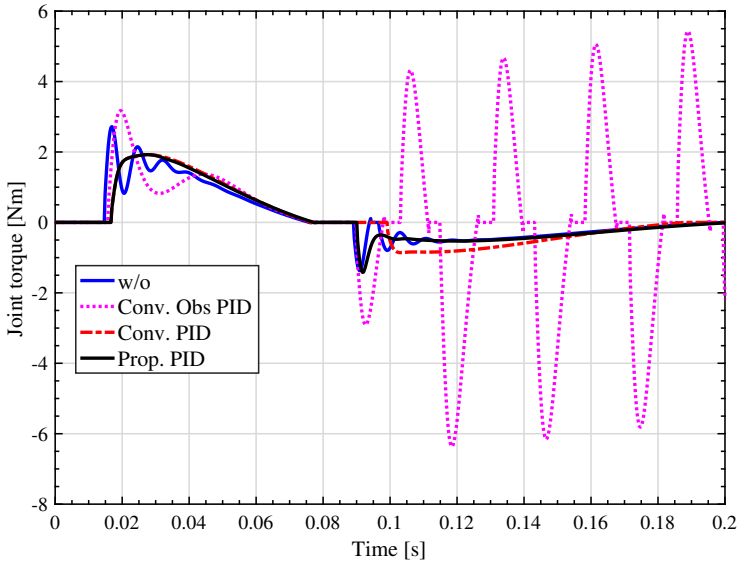

(b) The responses around the settling phase.

Figure 3.26 The impact torque comparison when step reference of the load-side angle is input and the controller is changed to PID.

Additional simulation analyses

In order to eliminate steady state error, I controller is required in precise position control. Therefore, additional simulations are conducted to investigate the effects of introducing the I controller into outer position control (i.e. PD position controller is changed to PID controller). Moreover, to analyze modeling error effects, another conventional method is introduced. It is a linear damping addition control, but load-side velocity is estimated with a state observer. The block diagram is shown in Fig. 3.24. The difference is whether the observer is used or not, which results in whether the load-side encoder is necessary or not. Since the state observer uses the plant model, it is vulnerable to the plant

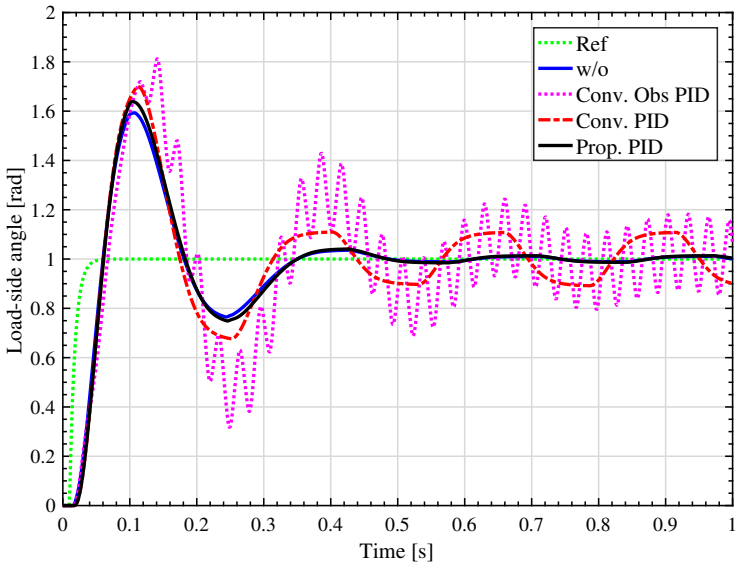

(a) The responses around the rising phase.

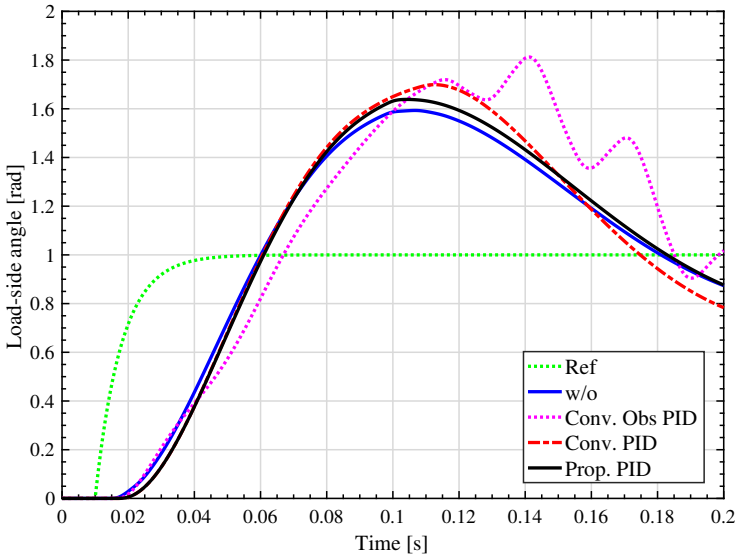

(b) The responses around the settling phase.

Figure 3.27 Step responses of the load-side angle with PID controller when the load-side viscosity is 1.25 times of its nominal value.

parameter variations. Furthermore, as the backlash nonlinearity is not included in the state observer model, the modeling error effect is nonnegligible.

Figures 3.25 and 3.26 show the responses of the load-side angle and the joint torque when the 0.30 rad step reference is given for the load-side angle at 0.010 s. The PID controller is designed by pole placement at 4 Hz. The cutoff frequency of the observer is 40 Hz. The other conditions are the same as Figs. 3.18 and 3.19. The blue solid line indicates the response without inner damping controller, that is, $K_B = 0$, while the magenda dotted line indicates the response with linear damping controller and the observer for load-side velocity estimation and the red dashed line indicates the response with linear damping controller. Figure 3.25(a) shows that the load-side angle responses around rising

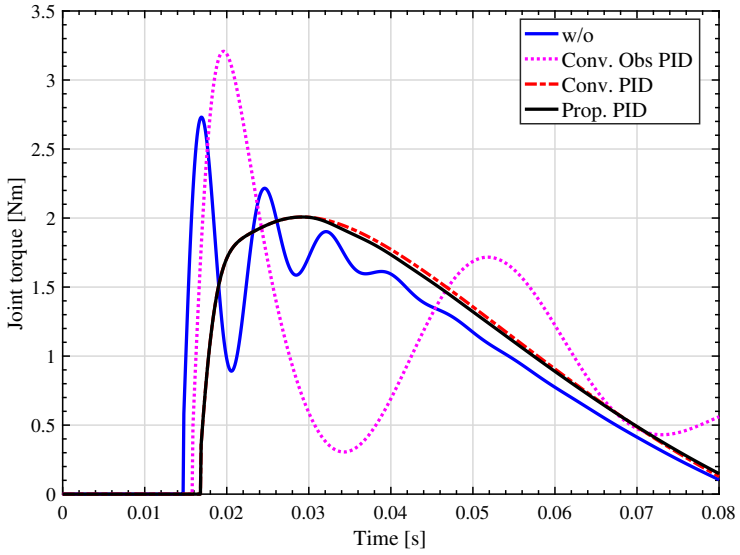

(a) The responses around the rising phase.

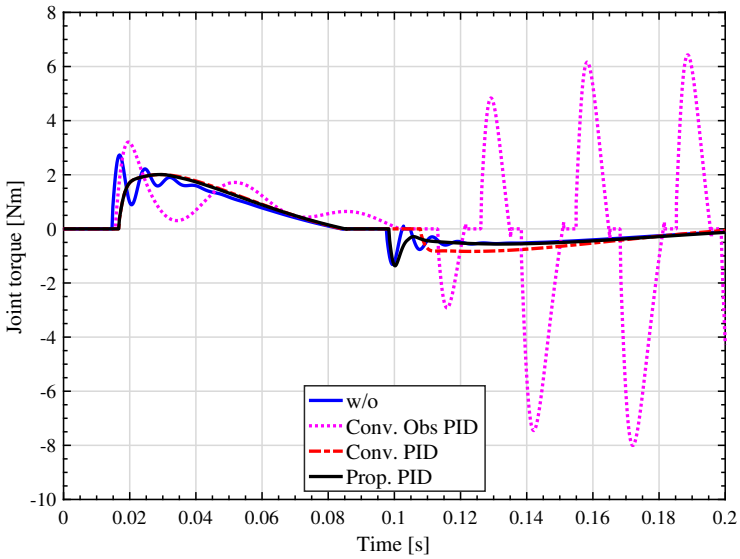

(b) The responses around the settling phase.

Figure 3.28 The impact torque comparison when step reference of the load-side angle is input and the controller is changed to PID and the load-side viscosity is 1.25 times of its nominal value.

phase. Likewise to the PD controller case, with damping control, the transient responses are delayed a little compared to the responses without damping control. On the other hand, the impact torque is attenuated by damping addition as shown in Fig. 3.26. Even if the I controller is introduced, the same tendency can be observed. Also, it is observed that the observer deteriorates the control performance due to the backlash modeling error. It cannot attenuate the impact joint torque and can increase the impact. When the load-side parameter is changed from nominal value, the performance can be worsened. Figure 3.27 and 3.28 show the responses of the load-side angle and the joint torque when the load-side velocity is changed to 1.25 times as its nominal value. The response with the observer is deteriorated more than the other methods, showing its lack of robustness. The usage of load-side

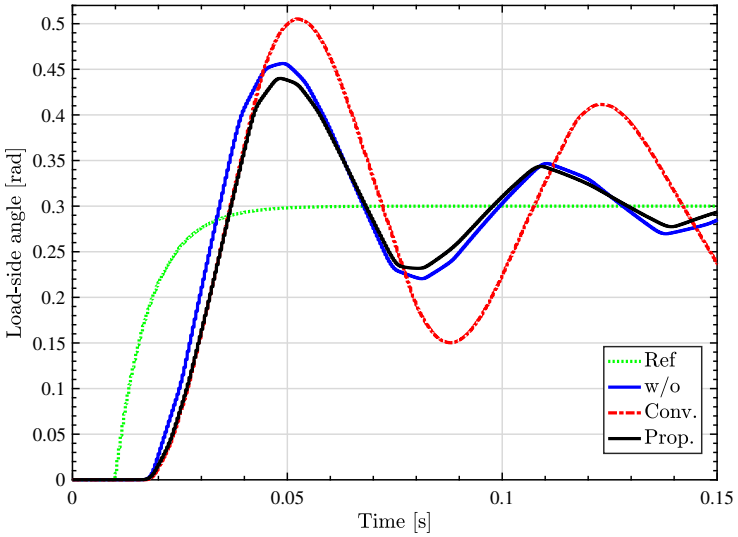

(a) The responses around the rising phase.

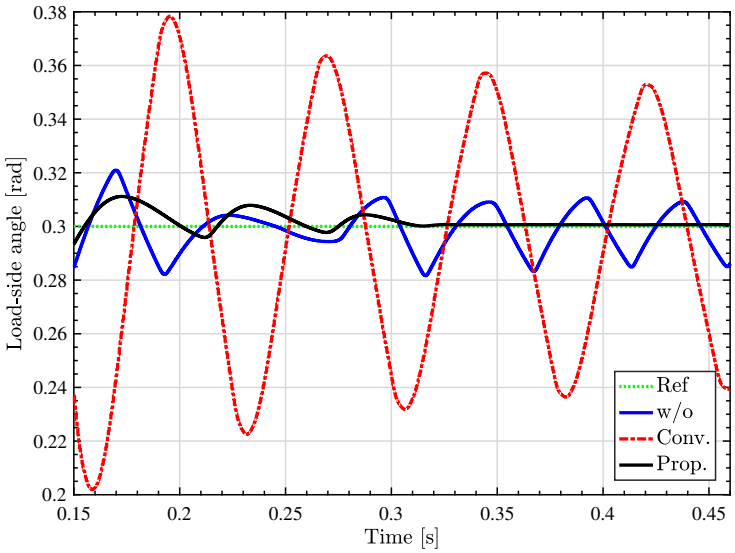

(b) The responses around the settling phase.

Figure 3.29 Step responses of the load-side angle in the experiments.

encoder is highly required for backlash compensation in two-inertia systems.

Experimental comparison with conventional method

The controller parameters are set to be the same as those in the simulations, and PD controller is discretized by Tustin conversion and implemented with the sampling frequency of 2.5 kHz. Initial position is set at the middle point of the backlash by the motor-side position controller.

Figures 3.29 and 3.30 show the load-side angle responses and the joint torque responses in the experiments, respectively. They show the similar tendency to the simulation ones shown in Figs. 3.18 and 3.19. The amplitude of overshoot is different between Fig. 3.18 and Fig. 3.29(a) due to the modeling errors such as parameter identification error and unmodeled nonlinear friction. Figure 3.29(a)

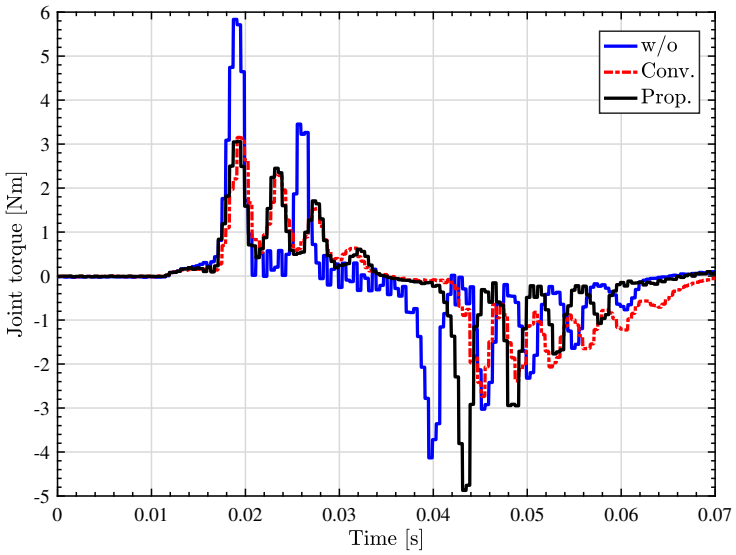

Figure 3.30 The impact torque comparison when step reference of the load-side angle is input in the experiments.

indicates that the Conventional method shows the delayed transient responses with larger overshoot compared to the method without damping. The Proposed method shows better settling response as shown in Fig. 3.29(b). The first impact torque is reduced by damping addition as shown in Fig. 3.30. As for the second impact in braking phase, Conventional method reduces the impact torque with added damping, but this generates large overshoot. Proposed method does not attenuate the second impact, which indicates that the switching condition works correctly.

3.3.5 Conclusion of backlash compensation

Torsional damping addition can attenuate impacts by backlash, but it simultaneously deteriorates the transient responses of the load-side position. To solve this trade-off, the effect of the torsional damping addition is analyzed, and the switched damping control method is proposed. Proposed method shows the responses without large overshoot while attenuating the impact torque in the simulations and the experiments. The local stability is analyzed in the phase-plane while the whole system description is provided by using the PWA formalism.

3.4 Self Resonance Cancellation control

3.4.1 Abstract of Self Resonance Cancellation control

In the past 20 years, control methods for two-inertia systems have changed from semi-closed control to full-closed control in order to achieve higher precision positioning. Though there is a trend toward the expansion of the use of load-side encoders in the industry, it is hardly to say that control methods using load-side information are sufficiently studied. Therefore, our research group has proposed control methods using a load-side encoder such as Self Resonance Cancellation Control (SRC) in [66]. We have demonstrated the advantages of SRC [67, 68], but it needs two encoders. In order to reduce the implementation cost and space, a novel form of SRC, which employs the load-side information only, is proposed using a high-resolution encoder at the load side. The proposed method inherits the main advantages of SRC even though it can remove a motor-side encoder. Simulation and experimental results demonstrate that the comparable performance can be obtained by the proposed method without using motor-side information.

3.4.2 Conventional position control methods

P-PI control

Today in the industrial society, it is common to synthesize a cascade control system, which has a motor-side velocity feedback inner loop with high control bandwidth and a load-side position feedback outer loop. In this study, this P-PI control method shown in Fig. 3.31 is denoted as Conventional Method 1. In order to make load-side feedback control bandwidth higher, collocated motor-side velocity control is required. Conventional Method 1 is easy to apply because the relationship between gain parameters K_P, $K_{\omega P}$, $K_{\omega I}$ and control performances are clear. However, because closed-loop poles cannot be assigned arbitrarily, vibration caused by the plant resonance may appear.

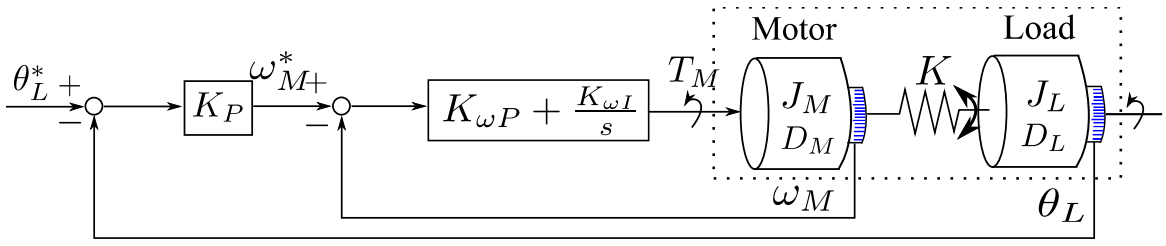

Figure 3.31 Block diagram of P-PI control (Conventional method 1).

Self Resonance Cancellation Control (SRC)

To simplify the theoretical study, the reduction ratio and viscosity friction are regarded as 1 and 0 respectively, and the plant model is expressed like the plant part of Fig. 3.32. In this model, the t.f. from the input torque to the motor-side angle and that to the load-side angle are shown in following equations, where ω_p and ω_z indicate resonance frequency and antiresonance frequency, respectively.

$$\frac{\theta_M}{T_M} = \frac{1}{J_M s^2}\frac{s^2+\omega_z^2}{s^2+\omega_p^2}, \tag{3.36}$$

$$\frac{\theta_L}{T_M} = \frac{1}{J_M s^2}\frac{\omega_z^2}{s^2+\omega_p^2}, \tag{3.37}$$

$$\omega_p = \sqrt{\frac{K}{J_M}+\frac{K}{J_L}}, \tag{3.38}$$

$$\omega_z = \sqrt{\frac{K}{J_L}}. \tag{3.39}$$

SRC is the control method characterized by using both motor- and load-side information [66]. It has two main advantages; 1) improving the control bandwidth, 2) simplifying the controller design. As shown in Fig. 3.32, the transfer function from input to motor-side angle and that to the load-side angle are multiplied by α, β and then combined.

$$\frac{\theta_{SRC}}{T_M} = \alpha\frac{\theta_M}{T_M} + \beta\frac{\theta_L}{T_M} \tag{3.40}$$

α and β are designed such that the resonance poles of the transfer functions from input to a virtual angle θ_{SRC} are cancelled by zeroes. When α and β are designed as inertia ratio $\alpha = \frac{J_M}{J_M+J_L}$, $\beta = \frac{J_L}{J_M+J_L}$, (3.41) is obtained.

$$\begin{aligned}\frac{\theta_{SRC}}{T_M} &= \frac{J_M}{J_M+J_L}\frac{1}{J_M s^2}\frac{s^2+\omega_z^2}{s^2+\omega_p^2} + \frac{J_L}{J_M+J_L}\frac{1}{J_M s^2}\frac{\omega_z^2}{s^2+\omega_p^2} \\ &= \frac{1}{(J_M+J_L)s^2}\end{aligned} \tag{3.41}$$

The characteristic from input to the virtual angle becomes rigid body because the resonance poles are canceled. Open loop characteristic has no resonance when θ_{SRC} is fed back. This enables to improve control bandwidth. Controller design is simplified because the plant model is reduced to the one-inertia model from the two-inertia model. Though there is an infinite number of α and β that cause pole zero cancellation, it is better to design them such that they do not include the torsional rigidity K. SRC has robustness to the variance of the torsional rigidity by not using the torsional rigidity in the controller. Note that SRC considering viscosity friction has been already proposed in [69].

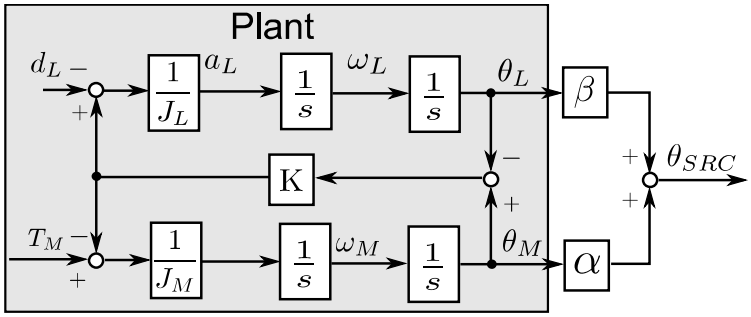

Figure 3.32 Block diagram of SRC without viscosity.

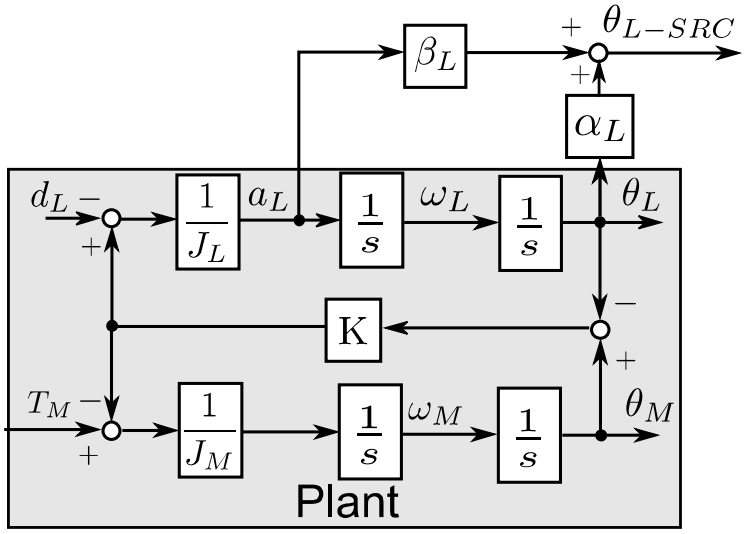

Figure 3.33 Block diagram of L-SRC without viscosity.

3.4.3 Proposed method（Load-side SRC (L-SRC)）

Design of L-SRC

As shown in Fig. 3.33, SRC can be implemented with only load-side information as following;

$$\frac{\theta_{L-SRC}}{T_M} = \alpha_L \frac{\theta_L}{T_M} + \beta_L \frac{s^2\theta_L}{T_M}. \tag{3.42}$$

This novel method is named Load-side SRC (L-SRC). In (3.42), designing $\alpha_L = 1, \beta_L = \frac{1}{\omega_p^2}$ leads to (3.43).

$$\frac{\theta_{L-SRC}}{T_M} = \frac{\theta_L}{T_M} + \frac{1}{\omega_p^2}\frac{s^2\theta_L}{T_M} = \frac{1}{(J_M + J_L)s^2} \tag{3.43}$$

The characteristic from input to θ_{L-SRC} becomes rigid body. L-SRC uses resonance frequency in β_L. Therefore, it loses one of the SRC advantage of robustness to the variance of torsional rigidity. However, it has the big advantage of removing the motor-side encoder.

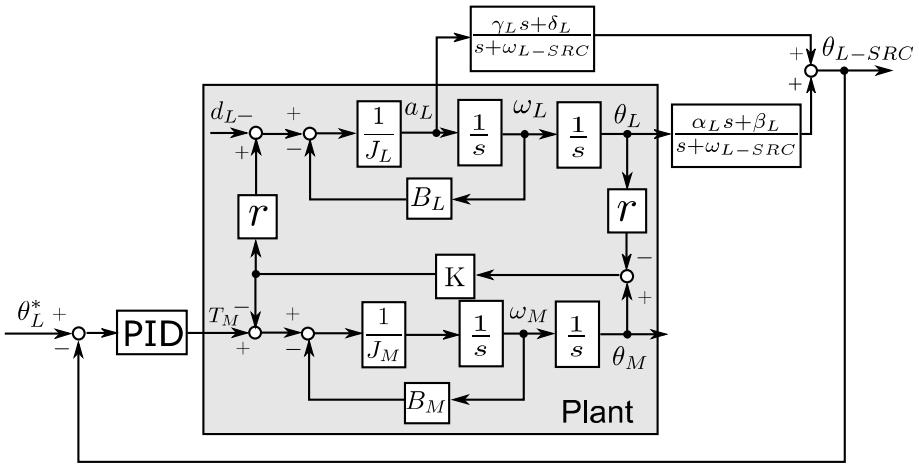

Figure 3.34 Block diagram of L-SRC with PID control.

As shown in Fig. 3.34, to consider the viscosity friction effect, design parameters are expanded as (3.44).

$$\frac{\theta_{L-SRC}}{T_M} = \frac{\alpha'_L s + \beta'_L}{s + \omega_{L-SRC}} \frac{\theta_L}{T_M} + \frac{\gamma'_L s + \delta'_L}{s + \omega_{L-SRC}} \frac{s^2 \theta_L}{T_M} \tag{3.44}$$

By designing the parameters as following, the characteristic from input to θ_{L-SRC} becomes $1/(J_{all}s^2 + B_{all}s)$.

$$\omega'_p = \sqrt{K\left(\frac{1}{J_M} + \frac{r^2}{J_L}\right)}, \tag{3.45}$$

$$J_{all} = J_M + \frac{J_L}{r^2}, \quad B_{all} = B_M + \frac{B_L}{r^2}, \tag{3.46}$$

$$\alpha'_L = r + r\frac{B_M B_L}{\omega'^2_p J_M J_L}, \quad \beta'_L = r\frac{B_M + \frac{B_L}{r^2}}{J_M + \frac{J_L}{r^2}}, \tag{3.47}$$

$$\gamma'_L = \frac{r}{\omega'^2_p}, \quad \delta'_L = \frac{r}{\omega'^2_p}\left(\frac{B_M}{J_M} + \frac{B_L}{J_L}\right), \tag{3.48}$$

$$\omega_{L-SRC} = \frac{J_{all}}{B_{all}}. \tag{3.49}$$

Note that the resonance frequency changes dependently on reduction ratio from ω_p to ω'_p.

As shown in Fig. 3.34, the load-side angle can be controlled when θ_{L-SRC} is fed back and the reference value of load-side angle θ_L^* is input. This is because the angle has more integrals than the acceleration. Conventional SRC using the motor-side angle and the load-side angle has steady-state error. Though the solutions of this problem have been proposed in [69, 70], L-SRC is straightforward and easy to understand.

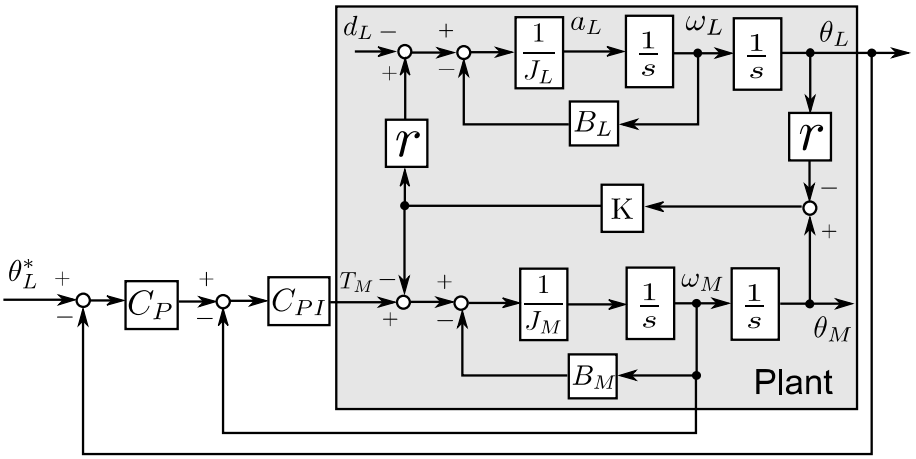

Figure 3.35 Block diagram of P-PI control.

Analyses of SRC and L-SRC in time domain

SRC has been analyzed in frequency domain because it is designed based on transfer functions. By analysis in time domain, the reason why L-SRC needs resonance frequency becomes clear.

For simplification, assume the input is an impulse. Transfer functions (3.36) become (3.50) and (3.51).

$$\theta_M(s) = \frac{1}{J_M s^2}\left(1 - \omega_p \frac{\omega_p}{s^2+\omega_p^2} + \frac{\omega_z^2}{s^2+\omega_p^2}\right), \tag{3.50}$$

$$\theta_L(s) = \frac{\omega_z^2}{J_M}\frac{1}{\omega_p}\frac{1}{s^2}\frac{\omega_p}{s^2+\omega_p^2}. \tag{3.51}$$

Inverse Laplace transform leads to the following equations (3.52) and (3.53).

$$\theta_M(t) = \frac{1}{J_M}\frac{\omega_z^2}{\omega_p^2}t + \frac{1}{J_M}\left(\frac{1}{\omega_p} - \frac{\omega_z^2}{\omega_p^3}\right)\sin(\omega_p t), \tag{3.52}$$

$$\theta_L(t) = \frac{1}{J_M}\left(\frac{\omega_z^2}{\omega_p^2}t - \frac{\omega_z^2}{\omega_p^3}\sin(\omega_p t)\right). \tag{3.53}$$

SRC in time domain

Conventional SRC plant in time domain is defined as (3.54).

$$\begin{aligned}\theta_{SRC}(t) &= \alpha\theta_M(t) + \beta\theta_L(t) \\ &= \frac{1}{J_M}\frac{\omega_z^2}{\omega_p^2}(\alpha+\beta)t + \frac{1}{J_M}\left(\left(\frac{\alpha}{\omega_p} - (\alpha+\beta)\frac{\omega_z^2}{\omega_p^3}\right)\sin(\omega_p t)\right)\end{aligned} \tag{3.54}$$

To make SRC plant rigid, α and β are designed such that the coefficient of the vibration term becomes 0.

$$\frac{\alpha}{\omega_p} - (\alpha+\beta)\frac{\omega_z^2}{\omega_p^3} = 0 \tag{3.55}$$

$$\frac{\alpha}{J_M} = \frac{\beta}{J_L} \tag{3.56}$$

(3.56) indicates how to design α and β such that SRC plant becomes rigid body. Though there is an infinite number of α and β that satisfy (3.56), when α and β are designed as inertia ratio $\alpha = \frac{J_M}{J_M+J_L}$, $\beta = \frac{J_L}{J_M+J_L}$, SRC plant becomes the one-inertia model $\frac{\theta_{SRC}}{T_M} = \frac{1}{(J_M+J_L)s^2}$.

Impulse response of the transfer function from the input to the load-side acceleration is (3.57).

$$a_L(t) = \frac{1}{J_M}\frac{\omega_z^2}{\omega_p}\sin(\omega_p t). \tag{3.57}$$

L-SRC plant in time domain is defined like (3.58).

$$\begin{aligned}\theta_{L-SRC}(t) &= \alpha_L\theta_L(t) + \beta_L a_L(t) \\ &= \frac{1}{J_M}\left(\frac{\omega_z^2}{\omega_p^2}\alpha_L t + \left(\beta_L\frac{\omega_z^2}{\omega_p} - \alpha_L\frac{\omega_z^2}{\omega_p^3}\right)\sin(\omega_p t)\right)\end{aligned} \tag{3.58}$$

To make it rigid, α_L and β_L should be designed as (3.59).

$$\alpha_L = \beta_L\omega_p^2. \tag{3.59}$$

The above-mentioned time domain analysis leads to the following conclusions.

1. The second derivatives in time domain change the vibration term to sin, cos, -sin. With the second derivatives the phase becomes inverse compared to the angle phase. Therefore, combining the angle and the acceleration can cancel the vibration.
2. Resonance frequency comes out by derivative. Therefore, designing parameters without torsional rigidity is impossible unless both motor and load angle are utilized.

L-SRC loses the advantage of SRC that is robust against the variance of torsional rigidity. However, in motion control of industrial robots, not only the variance of torsional rigidity, but also the variance of inertia should be considered. The evaluation of the robustness and adaptation to the variance of resonance frequency will be studied in the future.

3.4.4 Simulations and experiments of SRC

The plant model used in simulations is the identified DEMCM model in chapter 2. In simulations, the true values of angle, angular velocity, and angular acceleration are obtained.

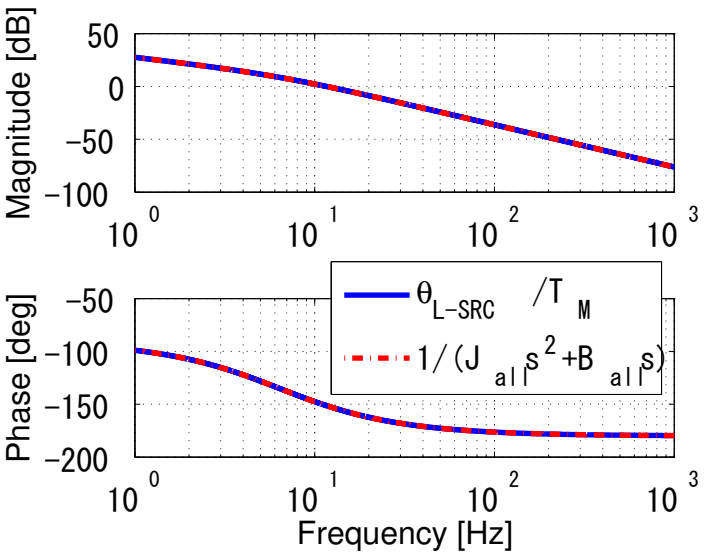

Figure 3.36 Comparison of bode plots of rigid body by L-SRC and one-inertia system.

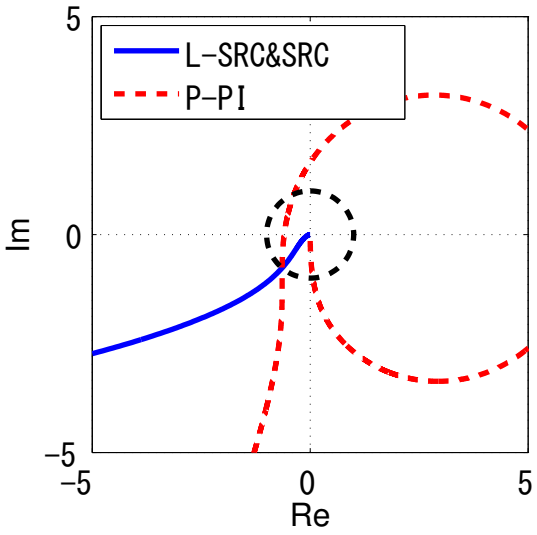

Figure 3.37 Comparison of nyquist diagrams.

L-SRC indicated in Fig. 3.34 is compared with SRC and P-PI control indicated in Fig. 3.35. Note that while SRC and P-PI control need two encoders, L-SRC needs only one encoder. The objective of L-SRC is to obtain same performance without motor-side encoder.

Simulation comparison with conventional method

Figure 3.36 shows the comparison of the rigid body model by L-SRC and one-inertia model $1/(J_{all}s^2 + B_{all}s)$ in bode plots. The transfer characteristic from input to θ_{L-SRC} completely matches that of one-inertia model.

For fair comparison, three methods are designed such that the phase margins of them are same.

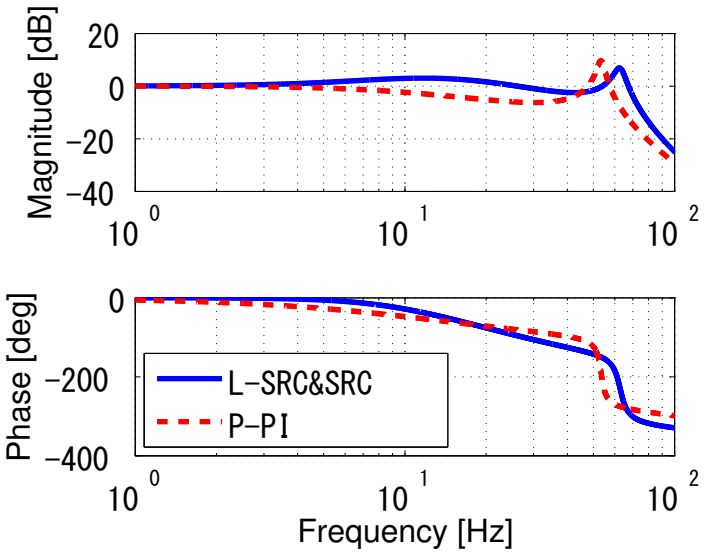

Figure 3.38 Comparison of closed loop frequency characteristics.

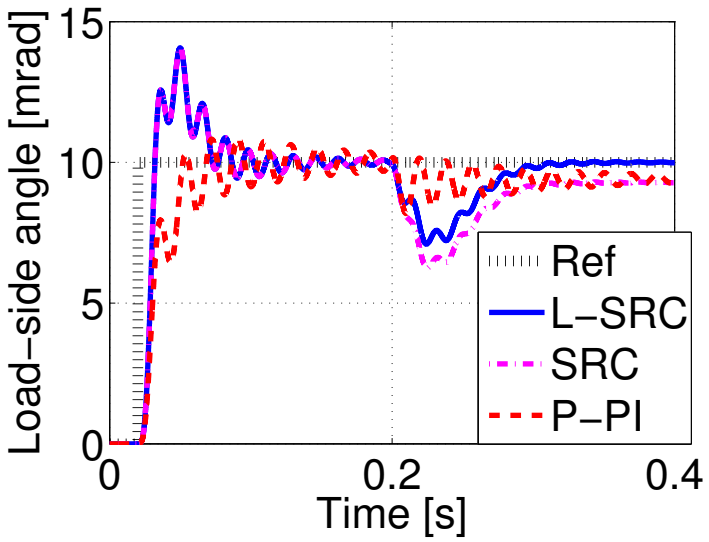

Figure 3.39 Comparison of step responses.

Note that the closed loop characteristics of L-SRC and SRC match completely. For fair comparison in terms of phase margin, the number of integral in open loop should be the same. Since P-PI control has an integral in the minor velocity loop, the position controller for L-SRC and SRC is chosen as PID controller. The virtual plant, which is $1/(J_{all}s^2 + B_{all}s)$ by L-SRC and SRC has an integral. Therefore, applying integral control to this plant leads to large overshoot, but the angle can be controlled without steady-state error even under the step disturbance. On the other hand, since P-PI control does not have an integral in position loop, it does not have large overshoot, but the angle cannot be controlled without steady-state error under the step disturbance. Though there is a difference in controller structure, it is important to compare the proposed method and the method

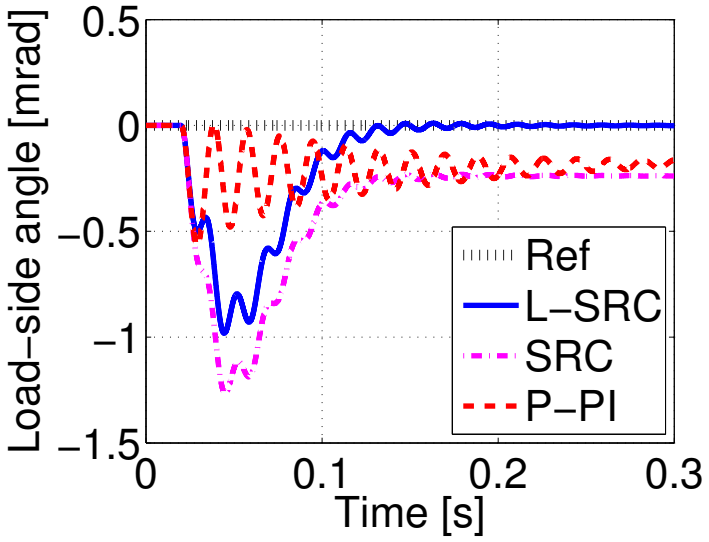

Figure 3.40 Comparison of load-side disturbance responses.

widely used in the industry, and therefore P-PI control is adopted as a competitor.

Firstly, the motor-side angular velocity PI compensator in P-PI control is designed such that the control bandwidth is 120 Hz.

Secondary, PID position compensator in L-SRC and SRC, and P position compensator in P-PI control are designed such that the phase margins of the three methods become 50 deg equally. PID compensator is designed based on pole placement method with the rigid body model.

Figure 3.37 shows the comparison of open loop characteristics. SRC and L-SRC can remove the resonance characteristic from open loop, while P-PI control is badly influenced by the resonance.

With the above-mentioned controllers, closed loop characteristics of the load-side angle are evaluated for the three methods. Figure 3.38 shows the comparison of closed loop frequency characteristics. The control bandwidth of L-SRC is higher than that of P-PI control and the same as that of SRC even though it does not use motor-side information.

Figure 3.39 shows the step response. As a reference value of load-side angle, 10 mrad step signal filtered by the low pass filter with cut off frequency 100 Hz is input at 0.020 s. L-SRC and SRC have larger overshoot, but they show rapid response and better damping characteristics.

Figure 3.40 shows the load-side disturbance responses. 10 Nm step disturbance is input at the load side at 0.020 s. While L-SRC has no steady-state error, SRC and P-PI have steady-state error under the load-side step disturbance. L-SRC is superior to SRC and P-PI control in terms of load-side disturbance suppression performance.

In order to analyze the stability when the modeling error is large, Figs. 3.41(a) and 3.41(b) show the comparison of Nyquist plots when motor-side inertia fluctuates, and Figs. 3.42(a) and 3.42(b) when

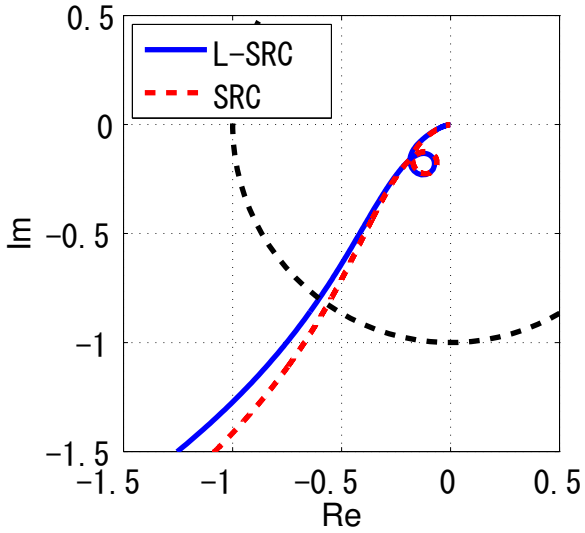

(a) JM80%

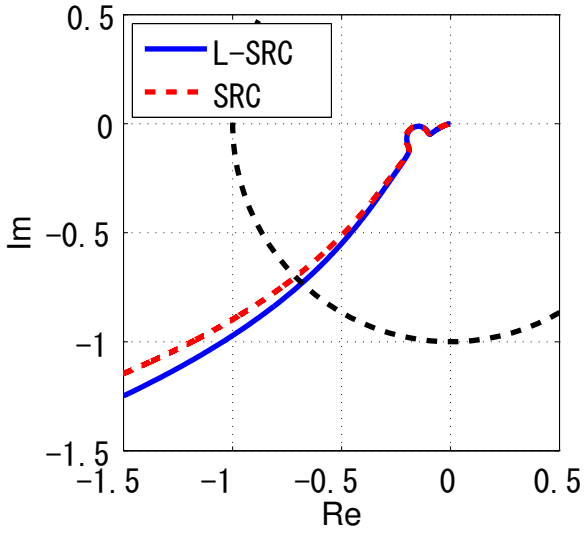

(b) JM120%

Figure 3.41 Comparison of Nyquist plots with motor-side inertia change.

load-side inertia fluctuates. It can be said that the robustness of SRC and L-SRC has both advantages and disadvantages when the motor-side inertia fluctuates. On the other hand, when the load-side inertia fluctuates, the L-SRC has a large resonance characteristic in the open loop characteristic. This is considered to be due to the fact that the L-SRC uses only the load-side information.

Figures 3.43(a) and 3.43(b) show the comparison of Nyquist plots when torsional rigidity fluctuates 80% of the nominal value, and Figs. 3.44(a) and 3.44(b) when torsional rigidity fluctuates 120% of the nominal value. Although the virtual angle cannot be rigid characteristic by the parameter fluctuation of the torsional rigidity in the L-SRC, SRC is robust because it does not require shaft torsional rigidity to generate virtual angle. Also, since the P-PI control cannot eliminate the resonance characteristic, the gain margin is small.

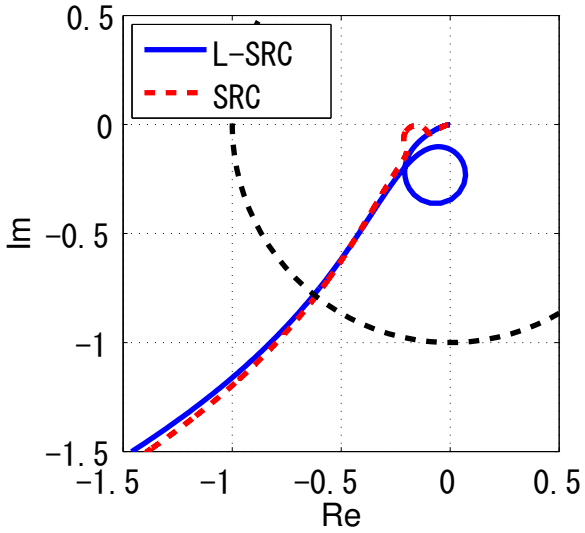

(a) JL80%

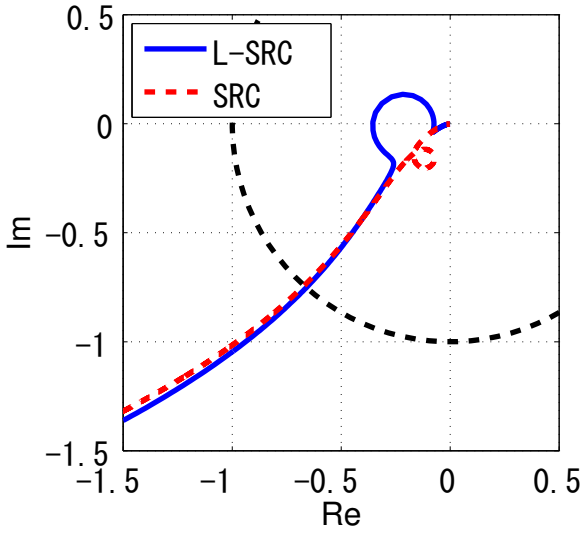

(b) JL120%

Figure 3.42 Comparison of Nyquist plots with load-side inertia change.

Then, Figs. 3.45(a), 3.45(b), and 3.45(c) show the comparison of step response of the load-side angle when torsional rigidity is changed to 50%, 80%, and 200%, respectively. The performance does not deteriorate greatly with increase of the torsional rigidity, but in the case of decrease, the degree of performance deterioration differs. When the torsional rigidity is 50% of the nominal value, although the L-SRC and P-PI control is unstable, the SRC maintains stability. As described above, the L-SRC is inferior to SRC in terms of robustness, but this is a trade-off with not using a motor-side encoder.

Experimental comparison with conventional method

The controllers in experiments are the same as those in simulations and discretized by Tustin conversion with sampling period 0.20 ms. Acceleration used in L-SRC is obtained by the second

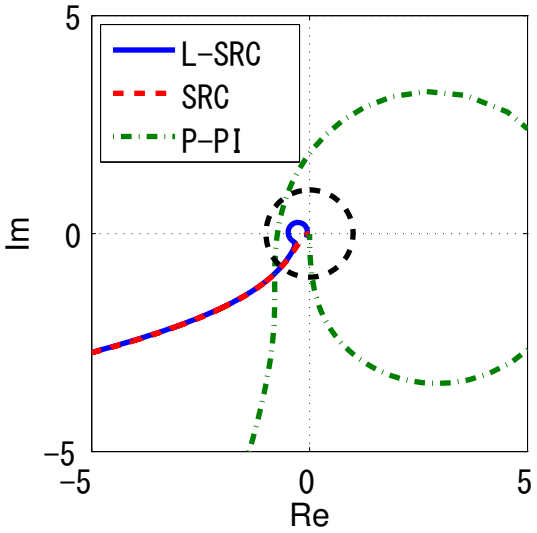

(a) K80%

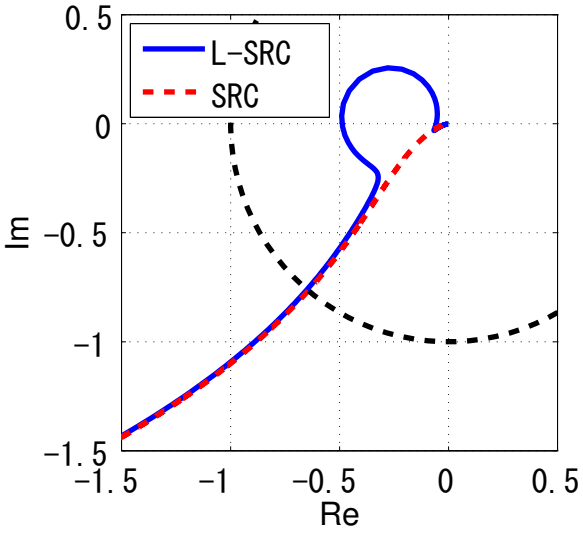

(b) Zoom of Fig. 3.43(a)

Figure 3.43 Comparison of Nyquist plots with K80%

order backward difference with sampling frequency 5 kHz. Then to improve the resolution of obtained acceleration, the first order low pass filter with cut off frequency 1 kHz is applied.

Figure 3.47 shows the comparison of the step responses in the experiments. As a reference value of load-side angle, 10 mrad step signal filtered by the low pass filter with cut off frequency 100 Hz is input at 0.020 s. Compared to the simulation result shown in Fig. 3.39, the responses are well similar except that the vibration is damped. It is considered that there are two causes of the damping. One is nonlinear friction effect, which cannot be identified in frequency characteristics measurement. The other one is the harmonic gear characteristic that torsional rigidity increases nonlinearly as the torsional angle becomes larger [71].

Figure 3.48 shows the step response of the virtual angle. Since the transfer characteristic becomes

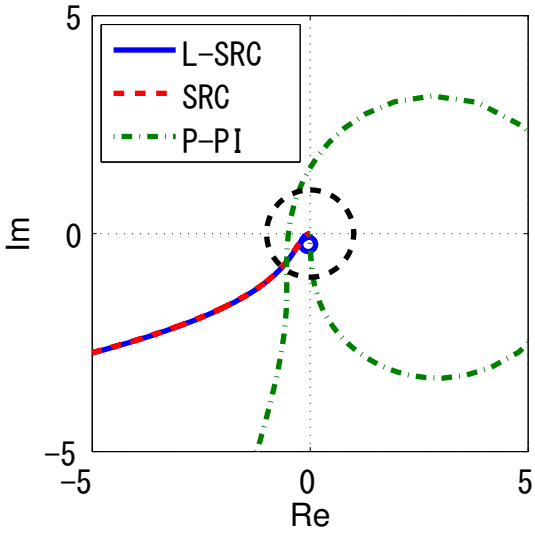

(a) K120%

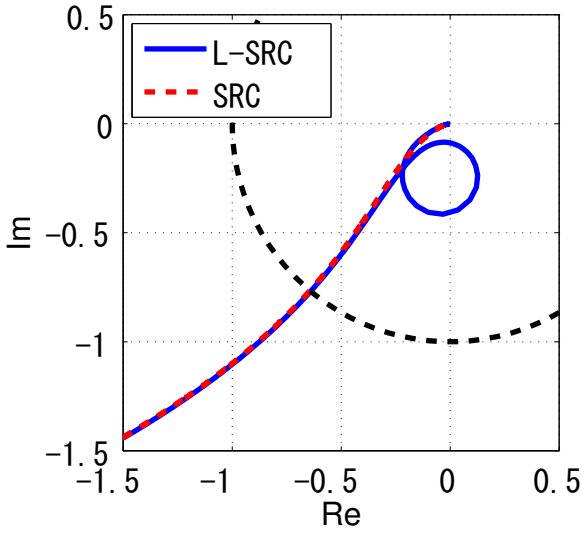

(b) Zoom of Fig. 3.44(a)

Figure 3.44 Comparison of Nyquist plots with K80%

rigid, no vibration is observed. θ_{L-SRC} indicated in solid line is a little noisy because of acceleration noise. However, Fig. 3.47 indicates that the noise has little effect on the position response. Figure 3.49 shows the angular acceleration response. Solid line indicates the acceleration obtained by the second order backward difference, while dashed line indicates the low pass filtered acceleration. Without low pass filter, the limit of resolution is observed. Even if the acceleration signal without the filter is fed back in an experiment, it is confirmed that load-side angle can be controlled without much deterioration in performance. Therefore, though the setup has the 20 bits high-resolution encoder, L-SRC can be implemented to the device with a little lower resolution encoder if the properly designed low pass filter is applied to obtain acceleration.

3.4.5 Conclusion of SRC

Considering the industrial trend toward the increase of high-resolution encoders at the load side, a novel form of SRC (L-SRC), which does not need motor-side information is proposed. The proposed method inherits the main two advantages of SRC, and moreover can remove the motor-side encoder. Sensorless control methods give several advantages such as the reduction of cost, maintenance, and complex wiring. The advantage of the proposed method is verified quantitatively in simulations and experiments by comparison with conventional SRC and P-PI control. Since L-SRC uses the resonance frequency, the performance deteriorates dependently on the variance of inertia and torsional rigidity. To avoid the deterioration in control performance, online adaptation to the variance of resonance frequency will be studied in the future.

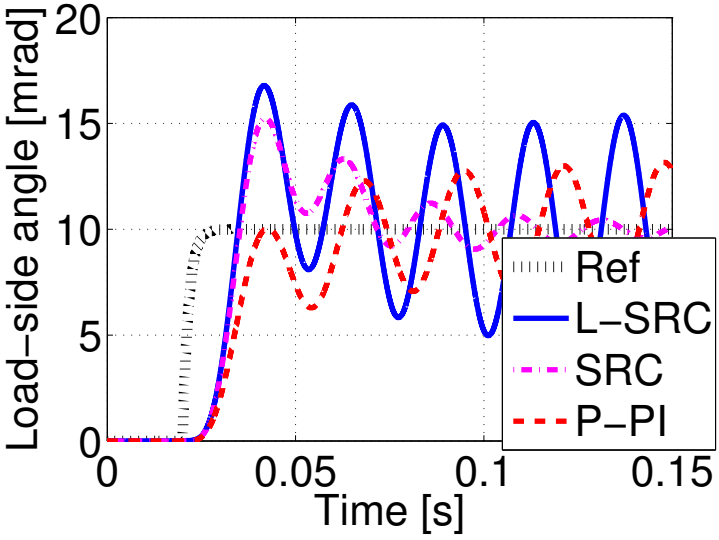

(a) K50%

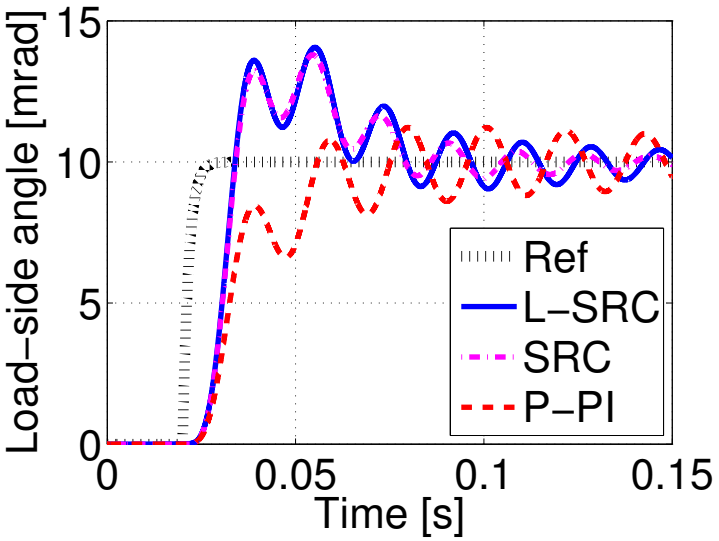

(b) K80%

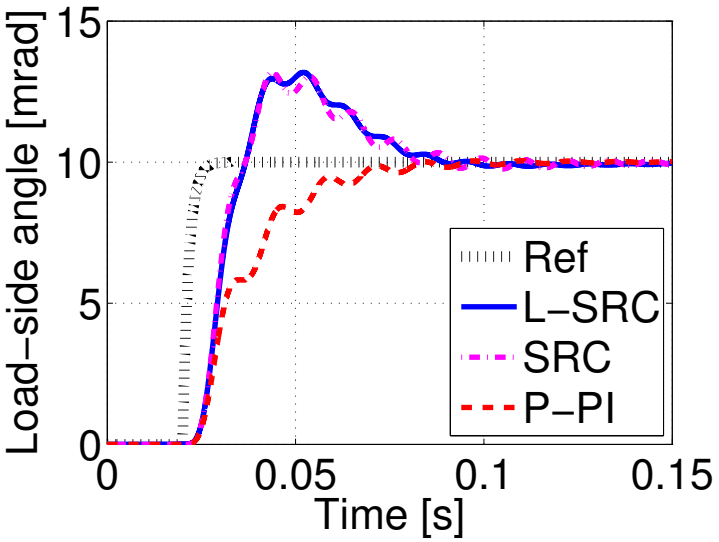

(c) K200%

Figure 3.45 Comparison of step responses with torsional rigidity change.

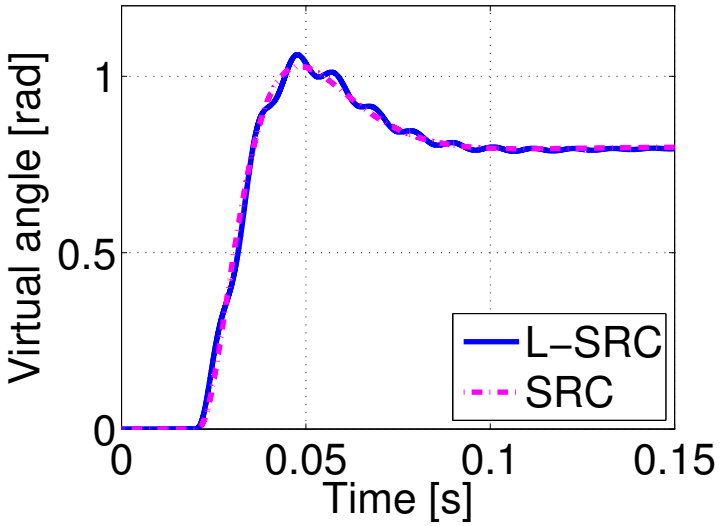

Figure 3.46 Comparison of virtual angle step responses between L-SRC and SRC with K200%.

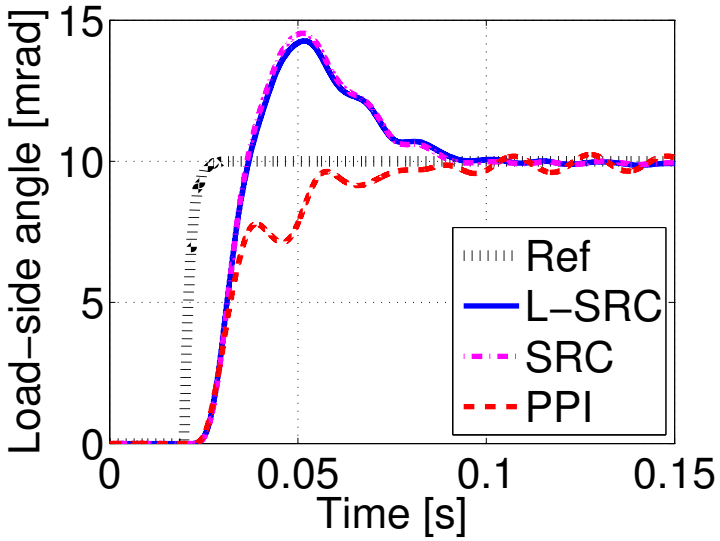

Figure 3.47 Comparison of step response in experiment.

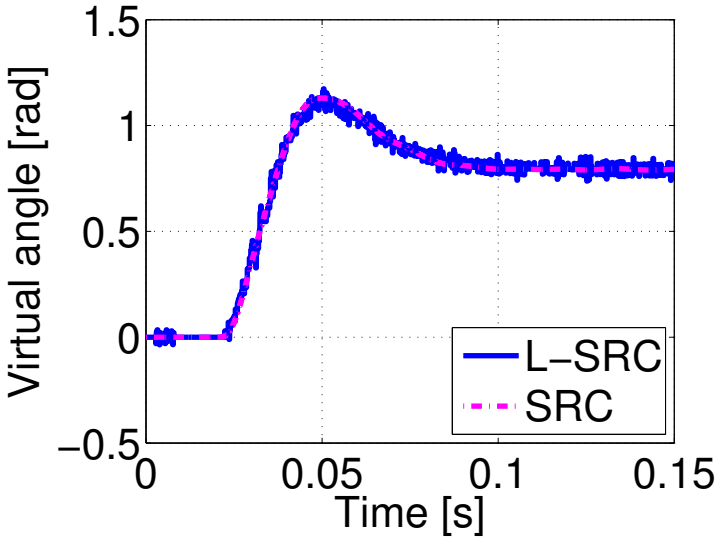

Figure 3.48 Response of virtual angle in Fig. 3.47.

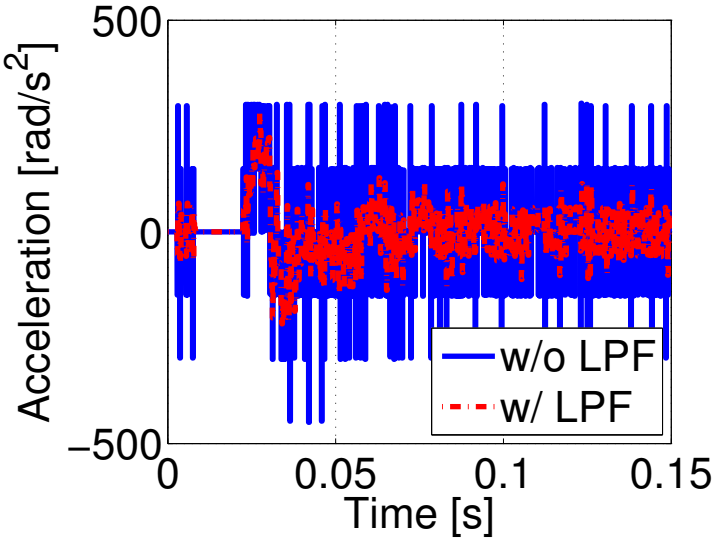

Figure 3.49 Response of load-side acceleration in Fig. 3.47.

3.5 Conclusion

Three studies on load-side position control conducted from the viewpoints, vibration suppression control, backlash compensation, and simplification of controller design are conducted. In the study on vibration suppression control and simplification of control design, the same performance is realized by only the high-resolution load-side encoder compared with the conventional control methods using both the motor- and load-side encoders. The control performance of the proposed vibration suppression method is limited by LPFs. Therefore, novel methods to obtain high order state variables precisely with less delay will be studied in the future. As to the simplification of controller design study, since L-SRC uses the resonance frequency, the performance deteriorates dependently on the variance of inertia and torsional rigidity. To avoid the deterioration in control performance, online adaptation to the variance of resonance frequency will be studied in the future. Regarding backlash compensation study, attenuation of the collision caused by backlash is focused. There is a trade-off between the control performance and the collision mitigation amount in conventional methods. Relaxation of the trade-off is successfully achieved by applying a novel switching controller.

Chapter 4

Load-side acceleration control

4.1 Abstract

In vehicle motion control, it is important to improve both dynamic performance and ride comfort by vibration suppression. Vehicles with combustion engines or on-board motors can only suppress resonant modes in the low frequency band such as the heave, pitch, and roll modes due to the limitation in torque responsiveness. However, in the case of vehicles with in-wheel motors, it is possible to suppress vibration in the higher frequency range. In order to improve motion performance and ride comfort, this study proposes a two degrees of freedom control using an experimentally identified plant model of a geared in-wheel motor vehicle. Application of the proposed method improves the vehicle body longitudinal response characteristics while suppressing the vibration. In order to further improve the performance, a state observer that takes the delay of CAN communication into consideration is applied while securing stability margin. The effectiveness of the proposed method is evaluated by simulations and experiments.

4.2 Conventional control methods

4.2.1 Advantages of electric vehicles

Electric vehicles (EVs) are attracting a lot of attentions due to the recent increase of public eco-awareness. Besides, EVs have higher motion performance than internal combustion engine vehicles thanks to their motor characteristics. Electric motors have three major advantages over internal combustion engines: the faster response to torque variations, the direct measurement of the applied output torque from the electric current value, and the distributed arrangement of the traction force. By utilizing these advantages effectively, advanced vehicle motion control can be realized [72–74]. Due to the flexible motor arrangement, various drive train configurations are possible in EVs. Currently,

the on-board motor system, which adopts an arrangement similar to a conventional combustion engine vehicles is often adopted in industry [75] . However, our research group is expecting that an in-wheel motor (IWM) system, which has motors inside each wheel is going to gain attentions in the future. From a design perspective, IWM systems have the advantage of increasing the degree of freedom in the interior layout of vehicles and reducing the total weight of the drive train [37]. From a control perspective, torque vectoring enables higher motion performance and the shorter drive shaft removes low frequent resonances, a strong limitation in current control structures [76–78].

4.2.2 Conventional vibration suppression control by in-wheel motor

One disadvantage of IWMs is the increase in unsprung mass. This increases vibrations in 4-25 Hz, a frequency range reported to be unpleasant to vehicle passengers [79, 80]. In order to improve motion performance and ride comfort, a few vibration suppression control methods for heave, pitch, and roll modes, which lie in the several Hz bands have been proposed utilizing torque vectoring control schemes [81,82]. Some studies introduce additional structure with spring and annular bushing into the wheel to improve ride comfort [83,84], while other studies take advantage of the higher torque response of IWM systems without additional hardware. The studies have proposed advanced control methods to compensate resonances around 10 Hz in both vertical [85] and longitudinal directions [86–88]. Katsuyama *et al*. have proposed a simple industrial oriented feedback control utilizing unsprung vertical velocity in [85]. The advantage of the proposed method has been shown by the experiments on the geared IWM vehicle. Ohno *et al*. in [86] have proposed a backlash compensation method to attenuate the impact of gear backlash. By attenuating the impact, excitation of longitudinal vibration can be avoided. Takesaki *et al*. in [87] have proposed the pitch rate FB control for pitch vibration suppression, and the specified step settling FF control for longitudinal vibration suppression. They considered that the longitudinal vibration is caused by the bushings, but the proposed model is evaluated only by the stepwise braking in time domain. Also, the performance evaluation is limited in the simulations. About the longitudinal vibration suppression method proposed by Fukudome in [88], this paper describes the method in detail and compares the performance of the method with our proposed method.

Despite the recent surge in IWM research, most studies focus on conventional motion control approaches with limited consideration of the vehicle dynamics. This is because experimental identification of the frequency characteristics of EVs are very limited. One of the limited number of the studies with experimental identification of EVs is conducted by Montonen *et al*. In [89], experimental identification of series electric hybrid bus is conducted. They have introduced the identification method from two-mass control field, and exploited PRBS, chirp, and stepped sine signals for excitation. Especially,

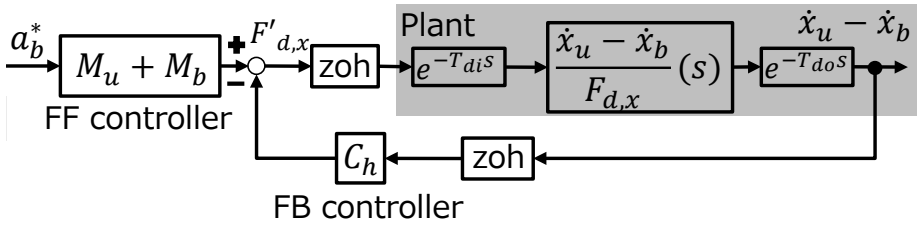

Figure 4.1 Block diagram of relative velocity FB control (Conventional method).

experimental identification of the dynamics of IWM vehicles are scarce and limited to time domain identification [87, 88]. A few theoretical approaches simulate the deterioration of dynamic behavior with IWMs [90, 91]. Tuononen *et al*. have compared the frequency characteristics of the vehicles with different drivetrain configuration such as OBMs and IWMs. However, the studies do not provide accurate experimental validation.

In the IWM system, deterioration of ride comfort due to an increase in the unsprung mass is of concern as described. However, by utilizing the fast torque responses of the IWM system, vibration suppression for the unsprung vertical axis mode and the longitudinal axis mode that lay in a higher frequency band (10 Hz and above) are studied. The control of the vibration mode in these high frequency bands is possible only with the IWM system, which has a high-bandwidth torque response characteristic.

4.2.3 Longitudinal relative velocity FB control

The longitudinal vibration of the vehicle around 10 Hz is caused by the bushings connecting the unsprung and the body. In order to improve ride comfort, the reference [88] proposed a virtual damping method by relative velocity feedback between the unsprung and body of the vehicle.

The block diagram of the method is indicated in Fig. 4.1. Where C_h is the relative velocity feedback gain, and F'_d is the new control input. The definition of the parameters of the plant (geared in-wheel motor vehicle) are given in chapter 2. In addition, T_{di} and T_{do} indicate input and output delay mainly due to CAN communication. The dead time reduces the phase margin of the plant. Also, on the assumption that the total mass is known, we define the relative velocity feedback method including FF control with only DC gain compensation as the conventional method. A comparison between the conventional method and the proposed method designed based on the precise plant model is conducted.

In the case of the conventional method, the transfer function from the driving force to the body acceleration is expressed as the following equation;

$$\frac{a_b}{F'_d} = \frac{C_x s + K_x}{M_u M_b s^2 + ((M_u + M_b)C_x + M_b C_h)s + (M_b + M_u)K_x}. \tag{4.1}$$

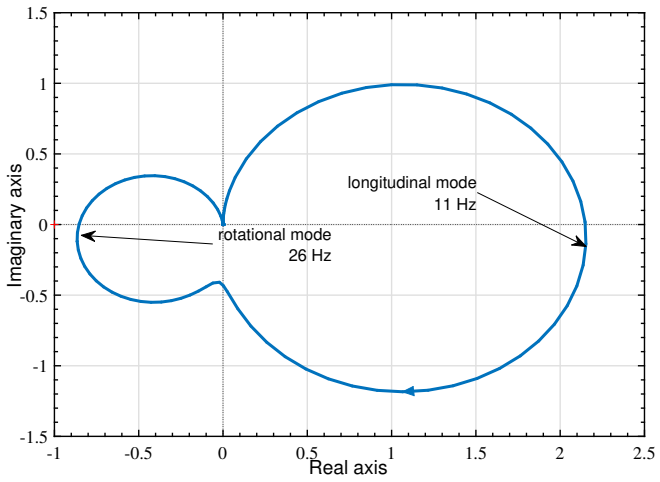

Figure 4.2 Nyquist plot of the transfer function from driving force to relative velocity for open-loop characteristic analysis of conventional method.

For the sake of simplicity, the influence of dead time is not considered here. As is clear from (4.1), there is just a single gain element to add damping. Even if the plant parameters are unknown, it has the advantage that gain tuning is easy by trial and error. However, since the conventional method can do only damping addition, it is not possible to improve the target value response characteristic of the vehicle body longitudinal acceleration.

As shown by the fact that research on precise experimental modelling of IWM vehicles is limited [91], conventional control methods for IWM vehicles do not use the plant parameters much. In order to realize high-bandwidth control that brings out the potential of IWM systems, it is necessary to accurately model IWM drives by actual measurements. Therefore, in the reference [39], our research group has conducted precise frequency characteristic measurements of the IWM vehicle and obtained accurate plant parameters.

The obtained accurate plant model enables precise frequency analyses. Figure 4.2 shows the open loop characteristic from the driving force to the relative velocity, which is used in a conventional longitudinal vibration suppression method. Resonance draws a circle in the Nyquist plot. The right circle is by the longitudinal mode, and the left circle is by the torsional mode. Although the rotational mode lies in a relatively high frequency range, the mode should be included in the model since it greatly affects stability. It is obvious from Fig. 4.2 that the gain of the relative velocity feedback is limited by the rotational mode.

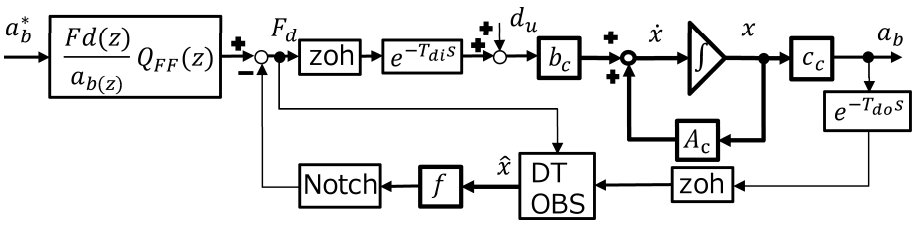

Figure 4.3 Block diagram of the proposed method.

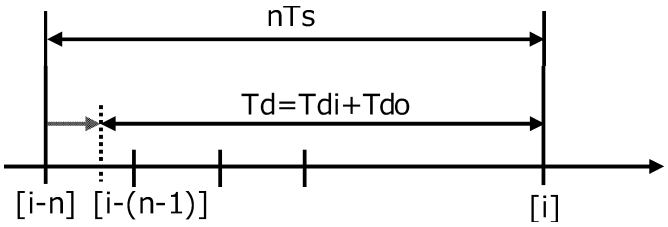

Figure 4.4 Time chart of the dead-time compensated state observer.

4.3 Proposed method (Model-based longitudinal acceleration control)

This study proposes a longitudinal acceleration control method with a high bandwidth based on an accurate model identified by [39]. It aims at improving both motion performance and riding comfort by vibration suppression. From the reference [39], the experimental IWM vehicle not only has a longitudinal mode around 10 Hz caused by the bushings, but also a second longitudinal mode around 27 Hz caused by a rotational resonance. The rotational vibration couples in the longitudinal axis when the tires are contacted to the ground, and these two modes degrade the control performance severely. In the proposed method, a feedforward (FF) controller based on an accurate inverse model of the plant suppresses vibration and realizes a high-bandwidth target value response characteristic. Furthermore, a state FB controller and notch filter compensate for modeling errors. Also, dead time caused by CAN communication prohibits further improvements of performance by reducing phase margin. In order to cope with this problem, a state observer considering dead time is applied to ensure stable margin and realize high-bandwidth control.

4.3.1 Two degrees of freedom control

Since the precise plant parameters have been obtained by frequency characteristic measurement performed in the reference [39], it has become possible to design model-based controllers. By applying two degrees of freedom control including a state FB control, this study proposes a longitudinal vibration suppression control method aiming at simultaneous improvements of motion performance

and ride comfort.

The block diagram of the proposed method is shown in Fig. 4.3. Here, $\boldsymbol{f}$ indicates the state feedback gain, zoh represents the zero-order hold, DTOBS represents the state observer considering the dead time, which is described later, and Notch represents the notch filter. With the state variable vector $\boldsymbol{x} = [x_1, \dot{x_1}]^{\mathrm{T}}$, which is obtained from (4.1) with $C_h = 0$, the plant model is expressed in state space in the continuous time as;

$$\dot{\boldsymbol{x}} = \boldsymbol{A_c}\boldsymbol{x} + \boldsymbol{b_c}F_d, \quad a_b = \boldsymbol{c_c}\boldsymbol{x}, \tag{4.2}$$

$$\boldsymbol{A_c} = \begin{bmatrix} 0 & 1 \\ -\frac{M_u+M_b}{M_u M_b}K_x & -\frac{M_u+M_b}{M_u M_b}C_x \end{bmatrix}, \tag{4.3}$$

$$\boldsymbol{b_c} = \begin{bmatrix} 0 & \frac{1}{M_u M_b} \end{bmatrix}^{\mathrm{T}}, \quad \boldsymbol{c_c} = \begin{bmatrix} K_x & C_x \end{bmatrix}. \tag{4.4}$$

The proposed method consists of a FF controller $\frac{F_d(z)}{a_b(z)}Q_{FF}(z)$ based on a precise inverse model of the plant model, and as a state FB controller considering the longitudinal mode and a notch filter suppressing the rotational mode. $Q_{FF}(z)$ is a low-pass filter to make the FF controller proper. The FF controller is discretized by Tustin conversion and its sampling time is 4.096 ms.

The state observer for estimating the state variable vector $\boldsymbol{x}$ is designed in the discrete-time system for implementation as follows;

$$\hat{\boldsymbol{x}}[i] = \boldsymbol{A_d}\hat{\boldsymbol{x}}[i-1] + \boldsymbol{b_d}u[i-1] + \boldsymbol{K}(y[i-1] - \boldsymbol{c_d}\hat{\boldsymbol{x}}[i-1]), \tag{4.5}$$

$$\boldsymbol{e}[i] = \boldsymbol{x}[i] - \hat{\boldsymbol{x}}[i] = (\boldsymbol{A_d} - \boldsymbol{K}\boldsymbol{c_d})\boldsymbol{e}[i-1]. \tag{4.6}$$

Note that $\boldsymbol{A_d}$, $\boldsymbol{b_d}$ and $\boldsymbol{c_d}$ are obtained with zero-order holds of $\boldsymbol{A_c}$, $\boldsymbol{b_c}$, and $\boldsymbol{c_c}$ at sampling period T_s, u is input, y is output, and $\boldsymbol{K}$ represents the observer gain.

4.3.2 Dead time compensated observer

Non-unique to the experimental vehicle considering in this paper, a CAN bus, generally used for communication in automotive has a significant delay and reduces the phase margin of the control system. In order to further increase the bandwidth to improve motion performance, it is necessary to consider the influence of dead time. To avoid a reduction of the stability margin, a state observer considering dead time is thus applied [92].

A state observer considering dead time is formulated as follows. When the sum of the input and output delay by CAN is defined as $T_d = T_{di} + T_{do}$, n that satisfies $(n-1)T_s < T_d < nT_s$ is determined. The output signal $y(iT_s)$ available at the time iT_s is represented as follows with reference to the time

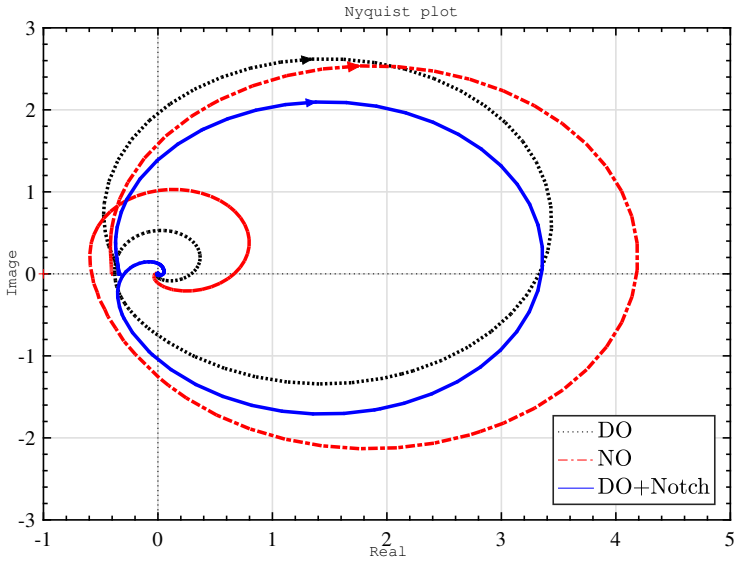

Figure 4.5 Comparison of a Nyquist plot between the plant with the normal state observer and that with the dead-time compensated state observer.

chart shown in Fig. 4.4.

$$y[i] = \boldsymbol{c_{dead}}\boldsymbol{x}[i-n] + \boldsymbol{d_{dead}}u[i-n], \tag{4.7}$$

$$\boldsymbol{c_{dead}} = \boldsymbol{c_c}e^{\boldsymbol{A_c}(nT_s - T_d)}, \tag{4.8}$$

$$\boldsymbol{d_{dead}} = \int_0^{nT_s - T_d} \boldsymbol{c_c}e^{\boldsymbol{A_c}\tau}\boldsymbol{b_c}d\tau. \tag{4.9}$$

Then, the state observer considering the dead time can be configured as follows;

$$\hat{\boldsymbol{x}}[i] = \boldsymbol{A_d}^n\hat{\boldsymbol{x}}[i-n] + \left[\boldsymbol{A_d}^{n-1}\boldsymbol{b_d}, \cdots, \boldsymbol{b_d}\right]\begin{bmatrix} u[i-n] \\ \vdots \\ u[i-1] \end{bmatrix} + \boldsymbol{A_d}^{n-1}\boldsymbol{K}(y[i] - \boldsymbol{c_{dead}}\hat{\boldsymbol{x}}[i-n] - \boldsymbol{d_{dead}}u[i-n]),$$

$$\boldsymbol{e}[i] = (\boldsymbol{A_d}^n - \boldsymbol{A_d}^{n-1}\boldsymbol{K'}\boldsymbol{c_{dead}})\boldsymbol{e}[i-n]. \tag{4.10}$$

The value of $(\boldsymbol{c_{dead}}\hat{\boldsymbol{x}}[i-n] - \boldsymbol{d_{dead}}u[i-n])$ is calculated by the state variables at the time $(i-n)T_s$ with the advancement of the time $(nT_s - T_d)$ by using the analytic solution of the state equation. This calculated value should be output at the time iT_s with a delay of T_d, which is expressed as $\hat{y}[i] = \boldsymbol{c_{dead}}\hat{\boldsymbol{x}}[i-n] - \boldsymbol{d_{dead}}u[i-n]$. By comparing $\hat{y}[i]$ and the plant output signal $y(iT_s)$ at the time iT_s in the observer's correction term and feeding back the difference, the dead time compensated state observer is composed. By designing the eigenvalues of $(\boldsymbol{A_d}^n - \boldsymbol{A_d}^{n-1}\boldsymbol{K'}\boldsymbol{c_{dead}})$ in the unit circle with the observer gain $\boldsymbol{K'}$, accurate state estimation is achieved even with a large delay.

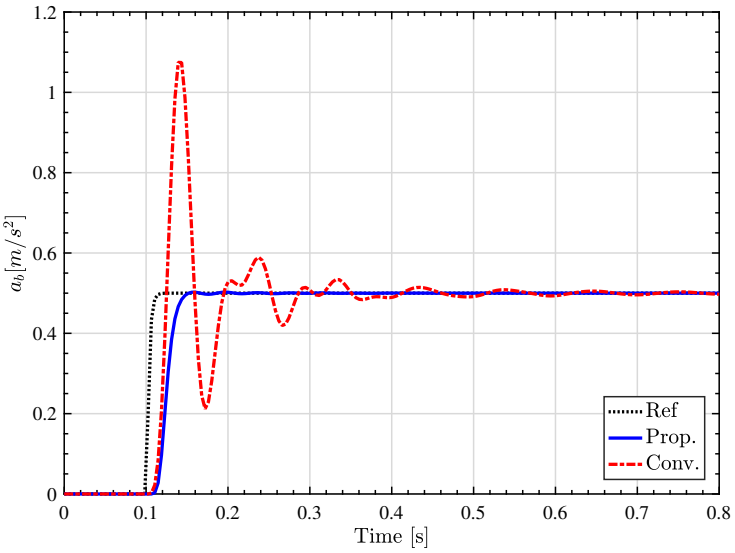

Figure 4.6 Comparison of the step responses between the conventional method and the proposed method.

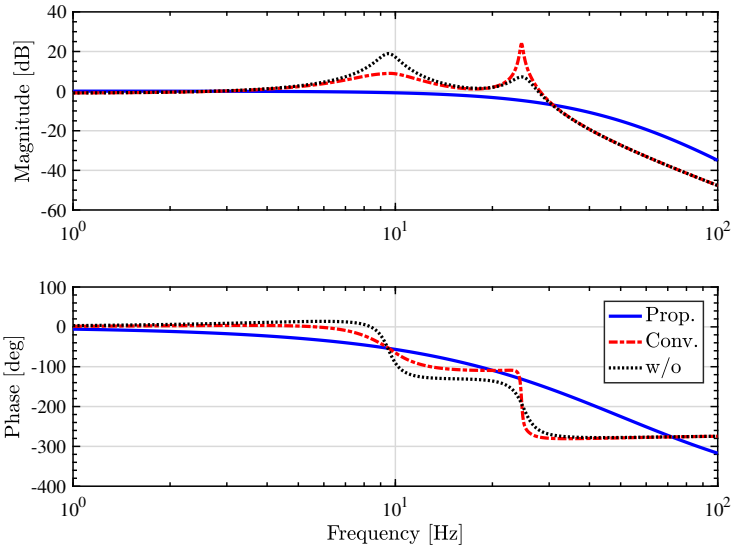

Figure 4.7 Comparison of the frequency characteristics of the closed-loop characteristics between the conventional method and the proposed method.

4.4 Simulations and experiments

4.4.1 Simulation comparison with conventional method

A comparison of Nyquist plots is shown in Fig. 4.5 with both the normal and dead-time compensated state observers. The later uses the identified dead-time $T_{di} = T_{do} = 5.70$ ms obtained in the reference [39] and is integrated into the vehicle with the state FB controller. The poles of the state FB and observer are designed to be 20 Hz in the two methods. The state observer considering the dead time

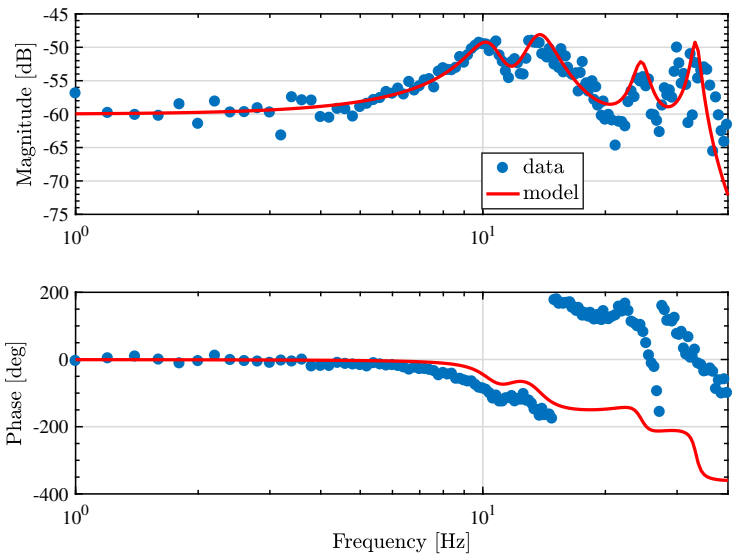

(a) FRF from driving force to body longitudinal acceleration.

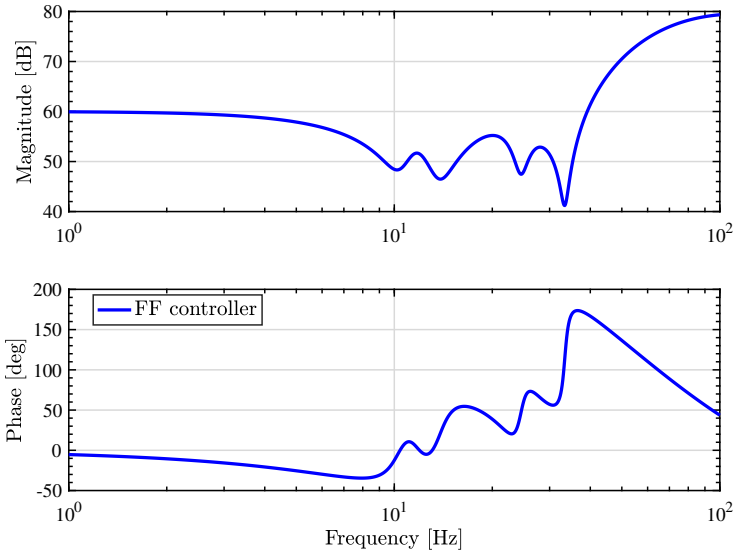

(b) FF controller designed based on the precise model.

Figure 4.8 Frequency response of the experimental vehicle and the designed FF controller.

(Deadtime compensated Observer) indicated by the black and dashed line shows that the phase is recovered compared to the conventional state observer (Normal Observer) indicated by the red and dotted line. Also, the gain of the rotational mode is suppressed. Furthermore, the blue and solid line shows the characteristics when a notch filter is applied to the rotational mode, in addition to the state observer considering the dead time, which shows that gain stabilization is achieved.

To compare the target response characteristics, the step responses of the body longitudinal acceleration using the conventional and proposed method are compared in Fig. 4.6. Here, in order to make the FF controller proper, at least a third-order low-pass filter is necessary, but to sufficiently lower the gain in the high frequency range, five first-order low-pass filters with a cutoff frequency of 50 Hz are applied. As a body longitudinal acceleration reference, a step command with a value of 0.50 m/s^2 is

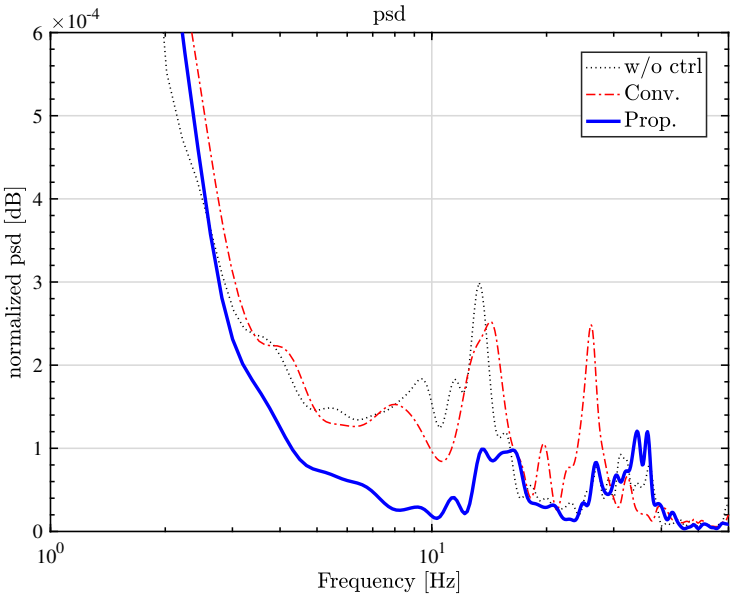

Figure 4.9 Experimental comparison of the PSD of the step responses between the conventional method and the proposed method.

passed through a first-order low-pass filter with a cutoff frequency of 50 Hz at 0.10 s. The conventional method indicated by the red and dashed line has a large vibration caused by the rotational mode, and it becomes unstable as the gain of the relative velocity feedback is further increased (see Fig. 4.2). As a result, also the longitudinal mode cannot be damped sufficiently, and significant vibrations remains in the response. On the other hand, the proposed method indicated by the blue and solid line shows a good response with less vibration.

Next, both the frequency responses in body longitudinal acceleration of the conventional and proposed control methods are shown in Fig. 4.7. In the conventional method case, indicated by the red and dashed line, the peak of the longitudinal mode is lowered by the relative velocity FB control, but the rotational mode is still excited. In the case of the proposed method, indicated by the solid and blue line, high control bandwidth is realized with significant vibration suppression.

4.4.2 Experimental comparison with conventional method

In the experimental vehicle, the relative velocity is calculated by integrating the difference between the body and unsprung accelerations obtained from the longitudinal acceleration sensor attached to the body and unsprung mass. Since the acceleration sensor has an offset component and noise, bandpass filters are applied. Also, since the proposed method uses only the body acceleration, the proposed method is superior to the conventional method in terms of the number of required acceleration sensors.

In the experiments, a higher-order model obtained by the frequency measurement shown in

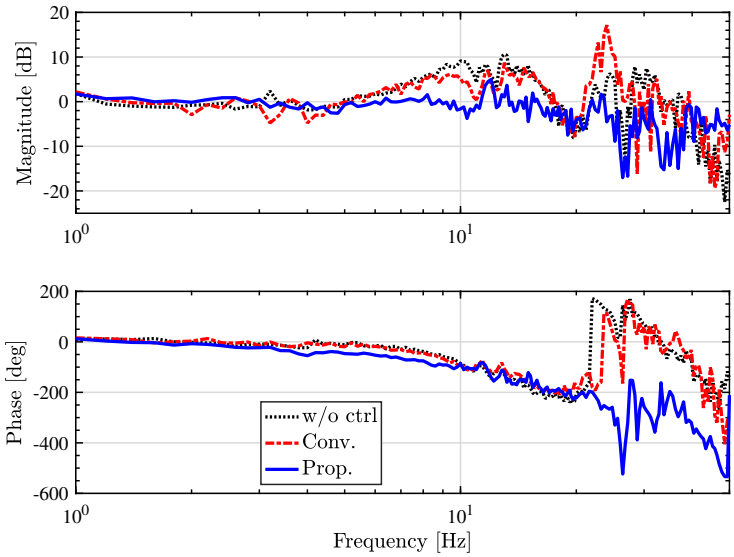

Figure 4.10 Experimental comparison of FRF from a_b^* to a_b.

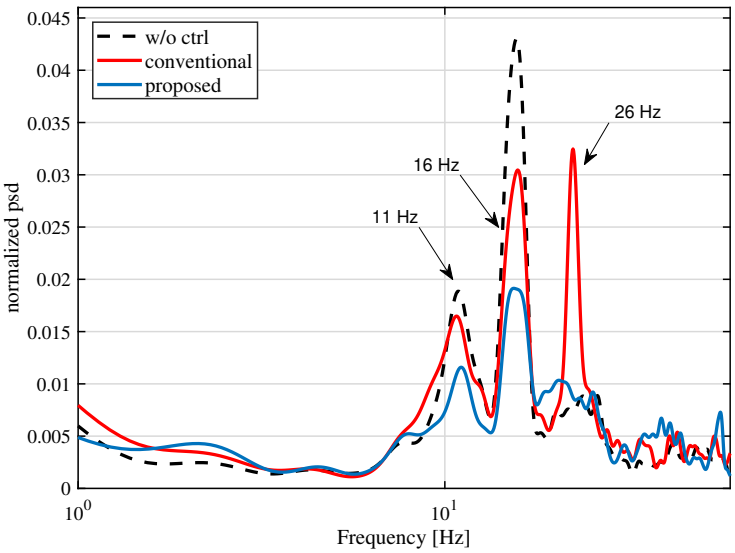

Figure 4.11 Experimental comparison of PSD of a_b driving over the road with disturbance at 50 km/h.

Figs. 4.8(a) and (b) is used for the inverse model of FF controller aiming at even better performance. The five first-order low-pass filters with a cutoff frequency of 50 Hz are applied to make the FF controller proper.

Figure 4.9 shows the comparison of the power spectral density (PSD) of the longitudinal acceleration obtained from the body acceleration sensor when the longitudinal acceleration step command is applied to the experimental vehicle. Since the signal of the acceleration sensors are too noisy to show the responses in time domain, a PSD comparison is shown in Fig. 4.9. Though both the conventional and proposed method suppress the longitudinal mode, the proposed method suppresses the longitudinal mode more. Also, the conventional method increases the gain of the rotational mode while the

proposed method suppresses the rotational mode.

Figure 4.10 shows the target value frequency characteristics of the body longitudinal acceleration. The tendency of the experimental results is similar to that of the simulation results shown in Fig. 4.7. The conventional method suppresses the longitudinal mode around 10 Hz, but it amplifies the rotational mode around 25 Hz. The proposed method shows high control bandwidth while suppressing the multiple resonant modes.

Figure 4.11 shows the PSD of the body longitudinal acceleration when the vehicle runs over the road with disturbances with constant vehicle velocity control at 50 km/h. The disturbance suppression performance comparison is conducted to evaluate the FB controller performance. Both of the peaks at 11 Hz and 16 Hz appear because in this experimental condition both the motor torque and the road disturbances are input to the vehicle. The conventional method suppresses the two modes, but amplifies the rotational mode as expected. On the other hand, the proposed method suppresses all the modes sufficiently.

4.5 Conclusion

In order to achieve a high control bandwidth in the targeted systems of EVs, the high torque response characteristics in the IWM system are effectively utilized. We have proposed a longitudinal vibration suppression control method with two degrees of freedom control based on a precise model of the IWM vehicle. With the proposed method, simulations and experiments show the fast body acceleration responses with the suppression of the vibration in the longitudinal direction. These are caused by the longitudinal mode around 10 Hz and the rotational mode around 27 Hz. In addition, aiming at further higher control bandwidths and modelling error correction, a state observer that takes the dead time into consideration is applied to deal with the CAN communication delays reducing the stability margin. By applying the dead time compensated state observer, higher performance is achieved with ample stable margin.

The driving force which is determined by the function of the slip ratio is approximated by the value calculated by dividing the motor torque by the tire radius in this study. For further improvements, driving force control is required in order to consider slip effects in the near future.

Chapter 5

Joint Torque Control

5.1 Abstract

Force/torque control is attracting considerable attention as a method for constructing flexible product lines and developing human-support robots. Industrial robots and human-support robots are modeled as two-inertia systems to consider their transmission characteristics such as low rigidity and nonlinearity. In industries, the reduced cost of high-resolution encoders has increased the number of devices with load-side encoders, used to achieve more precise positioning at the load side of the two-inertia system. However, studies on control methods that use load-side encoder information are limited. Therefore, the present study proposes a precise joint torque control method to consider nonlinearities in transmission mechanisms by using load-side encoder information. The effective use of the load-side encoder information enables the proposed method to exhibit high control bandwidth characteristics and to compensate for backlash. Simulation and experimental results demonstrate the advantages of the proposed method.

5.2 Conventional force/torque control methods

Several studies on joint torque control methods were conducted [93, 94]. Oh *et al.* in [95] proposed a disturbance observer (DOB) using torsional angle instead of motor-side angle to enhance zero impedance characteristics, which indicates the backdrivability of the mechanical system. Backdrivability is important for human-support application [96, 97]. Therefore, the backdrivability performance of our proposed method will be discussed and evaluated later. Several studies consider the backlash effect for more precise joint torque control [49,98]. Most studies consider backlash effect as joint torque disturbance. Kaneko *et al.* in [99] deal with the nonlinear torsional rigidity in harmonic drive gears by compensating joint torque disturbance calculated by torque sensor information and both motor- and load-side encoders information. Odai *et al.* in [100] compensate joint torque disturbance by DOB. This

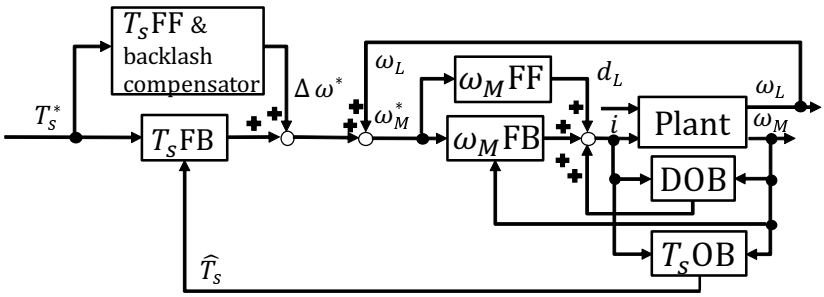

Figure 5.1 Overview block diagram of the proposed joint torque control.

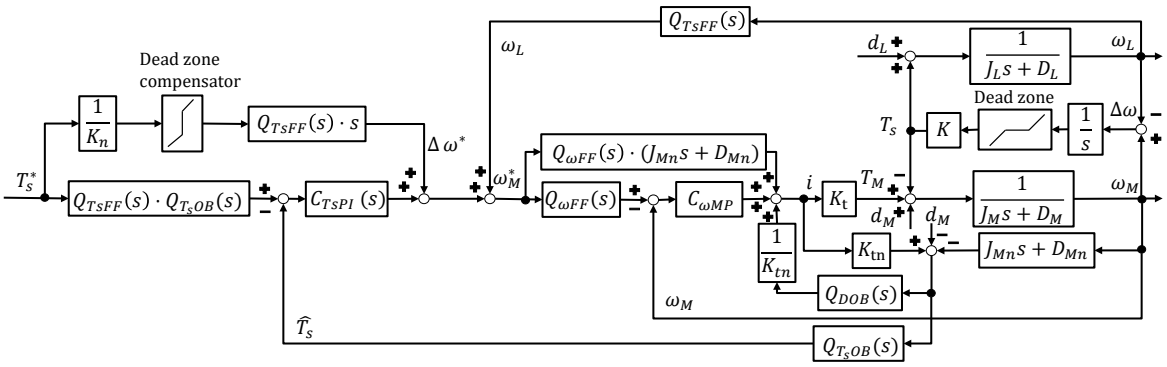

Figure 5.2 Detailed block diagram of the proposed joint torque control.

framework is further examined in [101] and [102]. However, it is necessary to compensate backlash not by FB controllers (such as DOB) but by FF controllers, since the backlash effect is fast. It is necessary to move the motor side very quickly during the reversal motion.

5.3 Joint torque control with backlash compensation based on dead zone model

5.3.1 Overview of proposed method

Conventional studies compensate the backlash effect by only using a FB controller such as DOB [100,102]. However, it is necessary to also compensate the backlash effect in the FF controller since its effect is fast and it always appears at the reversal points of motion (i.e., The joint torque reference value indicates when the backlash effect appears. With respect to the disturbance responses, it is necessary to compensate for the backlash effect by using FB controllers). Therefore, a proposed method includes the FF backlash compensator. Backlash is extracted when torsional angular velocity is controlled in the inner loop, and it is compensated with an inverse model of the deadzone in the FF controller.

Figures 5.1 and 5.2 show an overview and a detailed block diagram of the proposed method, respectively. The proposed method mainly consists of the following three parts: motor-side velocity control

(ω_M FF, ω_M FB, and DOB), joint torque FF control (T_s FF), and joint torque FB control (T_s FB and T_s OB). Specifically, T_s OB indicates a joint torque observer.

Motor-side velocity control

In order to control torsional velocity, the motor-side velocity P control with a DOB is implemented. In Fig. 5.2, $C_{\omega MP}$ indicates a P controller with gain $K_{\omega MP}$, and $Q_{DOB}(s)$ indicates a first-order low pass filter (LPF) whose cutoff frequency determines the bandwidth of DOB. The motor-side velocity exhibits less phase delay when compared with the load-side velocity since it corresponds to the collocated side. Therefore, motor-side velocity is first controlled and subsequently load-side velocity obtained by the load-side encoder Δ is used to control ω based on (5.1):

$$\Delta\omega = \omega_M - \omega_L. \tag{5.1}$$

The reference value of the motor-side angular velocity is generated by using the reference value of the torsional angular velocity and the obtained load-side angular velocity as follows:

$$\omega_M^* = \Delta\omega^* + \omega_L. \tag{5.2}$$

where subscript * indicates the reference value.

A motor-side angular velocity FF controller is also applied to achieve a high control bandwidth. High control bandwidth of the inner loop is required to quickly compensate the backlash, and it improves the performance of the outer loop. Thus, the FF controller is implemented as $(J_{Mn}s + D_{Mn})$ based on the assumption that the reaction joint torque to the motor side is decoupled by DOB. The subscript $_n$ indicates the reference value. The DOB decouples the motor side and load side under its bandwidth, and thus, the plant is considered as $\frac{1}{J_{Mn}s+D_{Mn}}$ within the DOB bandwidth. Furthermore, $Q_{\omega FF}(s)$ is a first-order LPF to realize the FF controller.

Joint torque FF control

The joint torque FF control compensates for the backlash and improves the reference-tracking performance. It is possible to deal with the fast backlash effect by using the FF controller for precise control. The joint torque FF controller generates the torsional angular velocity reference value from the joint torque reference value. We consider an inverse model of the transfer function from $\Delta\omega$ to T_s, and thus, the reference value of the torsional angular velocity is generated by using the reciprocal of the torsional rigidity, the inverse model of backlash, and the derivative. The derivative is implemented as a pseudo differential with the first-order LPF $Q_{TsFF}(s)$. The backlash is modeled as a deadzone, and thus, the inverse model of the deadzone is applied.

In Fig. 5.2, the load-side angular velocity is filtered with $Q_{TsFF}(s)$. The load-side angular velocity

is delayed with the filter to synchronize the torsional angular velocity generated by the joint torque FF controller that exhibits delay due to $Q_{TsFF}(s)$.

Joint torque FB control

The joint torque FB control suppresses modeling errors and disturbance by using the joint torque estimated by a joint torque observer with a PI controller. The joint torque observer estimates the joint torque even with nonlinearities in transmission mechanisms since it estimates the reaction torque. Therefore, it is not possible to compensate the backlash effect caused by modeling errors and disturbance by using the FF controller. However, it is suppressed by the FB controller. Specifically, $Q_{T_sOB}(s)$ is a first-order LPF that determines the estimation bandwidth. The PI controller $C_{T_sPI}(s)$ is designed by the pole placement to the plant, namely $T_s = \frac{k}{s}\Delta\omega$.

5.3.2 Controller design procedure

As a setup, two-inertia system motor bench introduced in chapter 2 is used.

First, DOB is designed. The nominal parameters of the torque constant K_{tn} and the inverse model of motor-side plant $(J_{Mn}s + D_{Mn})$ are designed based on the identified parameters. Subsequently, the cutoff frequency of $Q_{DOB}(s)$ is experimentally tuned as 80 Hz in our setup. The cutoff frequency is influenced by the precision of parameter identification and quantization noise by encoder signals.

Second, motor-side velocity P controller is tuned by considering the stable margin. Open loop characteristics of P controller, DOB, and the plant are shown in Fig. 5.3. In the analysis, backlash nonlinearity is removed from the plant. P gain $K_{\omega MP}$ is increased till phase margin reaches 60.

Third, the motor-side velocity FF controller is designed based on the identified values of the motor-side parameters (J_{Mn} and D_{Mn}). As discussed, the FF controller design is based on the decoupling by DOB. Therefore, the bandwidth of the FF controller is designed based on the DOB bandwidth. The bandwidth of the FF controller is determined by the cutoff frequency of the first-order LPF $Q_{\omega FF}(s)$, and thus, the cutoff frequency of $Q_{\omega FF}(s)$ is designed as identical to that of $Q_{DOB}(s)$.

Fourth, the joint torque FF controller is designed. The deadzone model is uniquely determined by the deadzone width that is identified by using both motor- and load-side encoders. The filter of $Q_{T_sFF}(s)$ is designed based on $Q_{\omega FF}(s)$. The joint torque FF controller generates the reference value of the torsional angular velocity that generates the reference value of the motor-side velocity based on (5.2). Therefore, the bandwidth of the joint torque FF controller should not exceed the bandwidth of the motor-side velocity FF controller. Subsequently, the cutoff frequency of $Q_{T_sFF}(s)$ is designed as identical to that of $Q_{\omega FF}(s)$ and $Q_{DOB}(s)$.

Finally, the joint torque FB controller is designed. PI controller $C_{T_sPI}(s) = K_{T_sP} + \frac{K_{T_sI}}{s}$ is designed

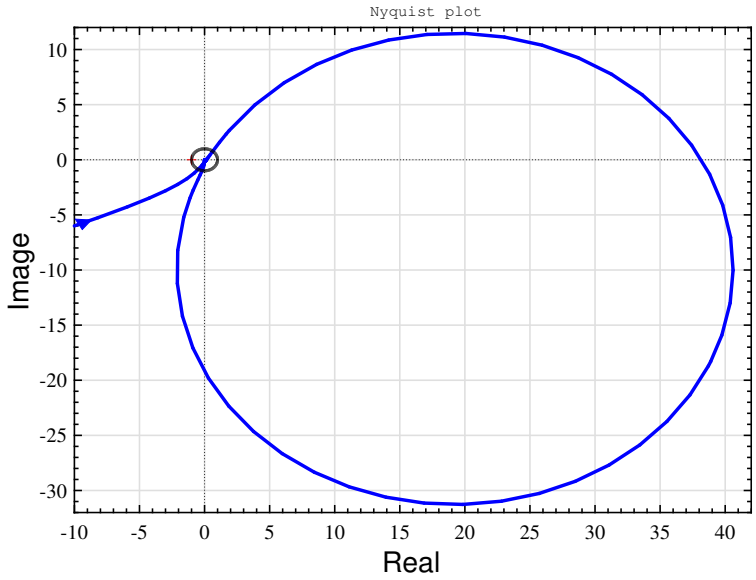

(a) Open loop charcteristics with the designed controller.

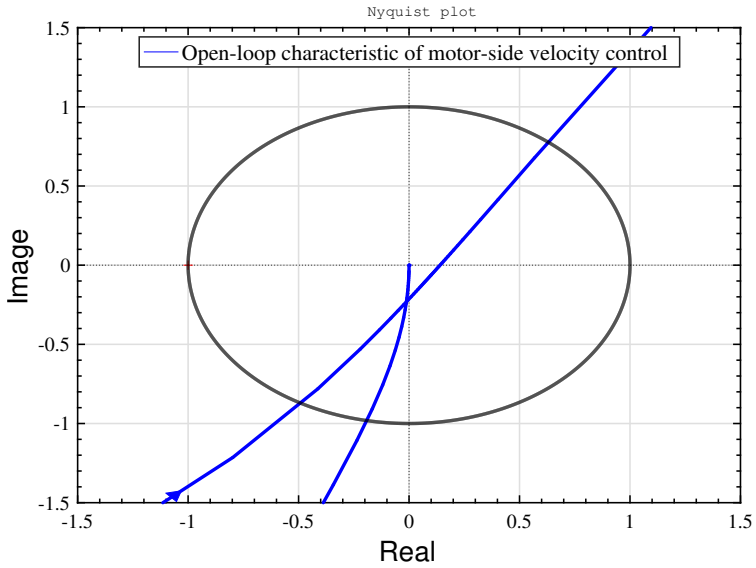

(b) Magnified view of Fig. 5.3(a).

Figure 5.3 Open loop characteristics of P controller, DOB, and the plant.

by the pole placement to the plant, $T_s = \frac{k}{s}\Delta\omega$. The poles are placed on the real axis and tuned experimentally. In this study, the poles are placed at 35 Hz. The cutoff frequency of the first-order LPF $Q_{T_sOB}(s)$ is designed to significantly exceed the bandwidth of the PI control. The cutoff frequency is designed as 80 Hz.

5.3.3 Simulations

The model used in simulations is the two-inertia system model whose parameters are shown in Table 1. It should be noted that the deadzone model is not included in the plant unless clearly stated. The effect of deadzone is analyzed later.

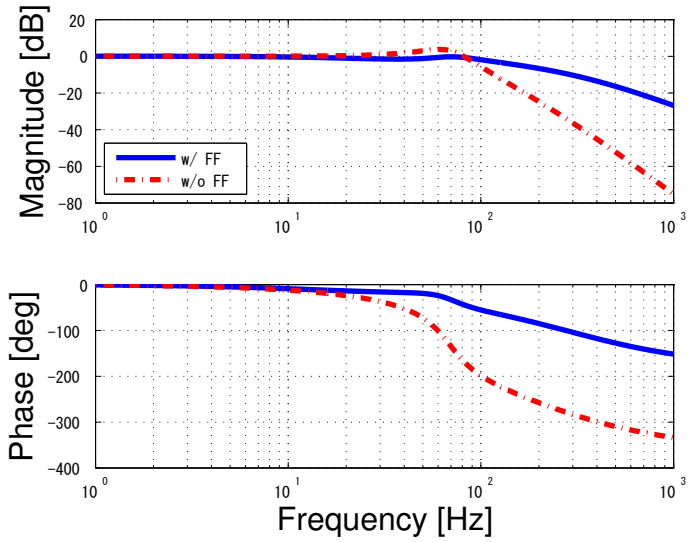

Figure 5.4 Frequency responses from the reference to the joint torque with and without two FF controllers (T_sFF and ω_MFF).

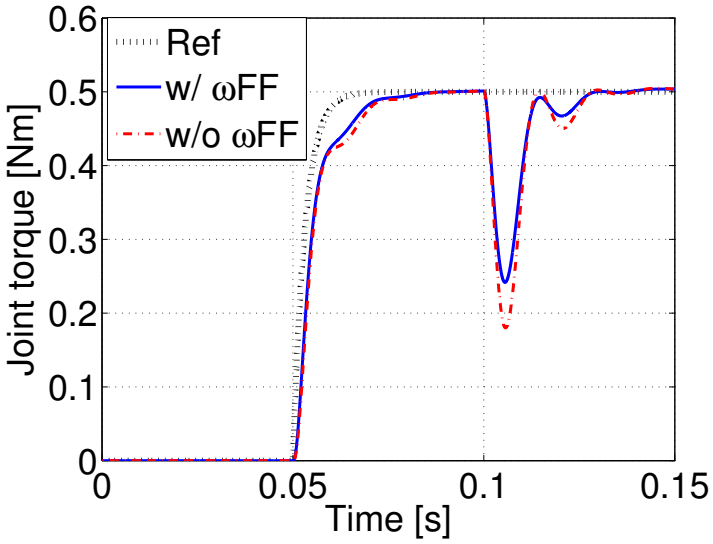

Figure 5.5 Step responses of joint torque with and without ω_MFF.

Effects of the FF controllers

First, the effectiveness of applying FF controllers is evaluated. Figure 5.4 compares the frequency characteristics of the transfer function from the reference to the joint torque between with and without two FF controllers, the joint torque FF controller, and motor-side angular velocity FF controller. The response with FF in the blue solid line exhibits higher control bandwidth characteristics. Two FF controllers improve the reference tracking performance.

Figure 5.5 evaluates the effect of the motor-side angular velocity FF controller. In Fig. 5.5, a 0.50 Nm

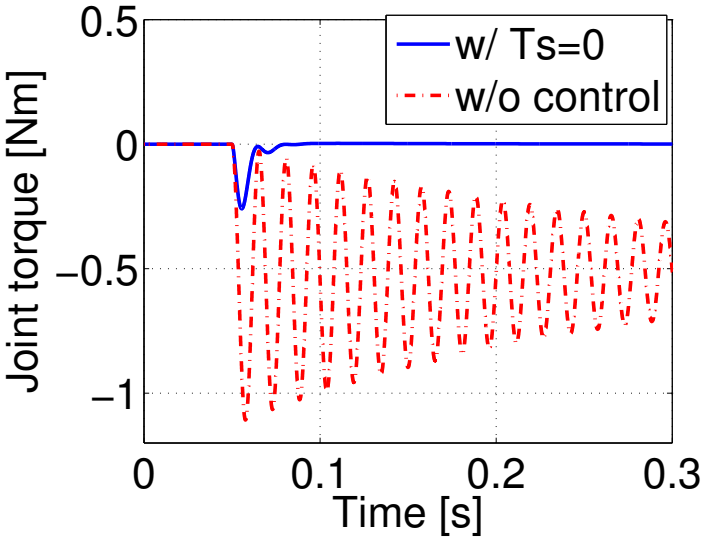

(a) Joint torque responses.

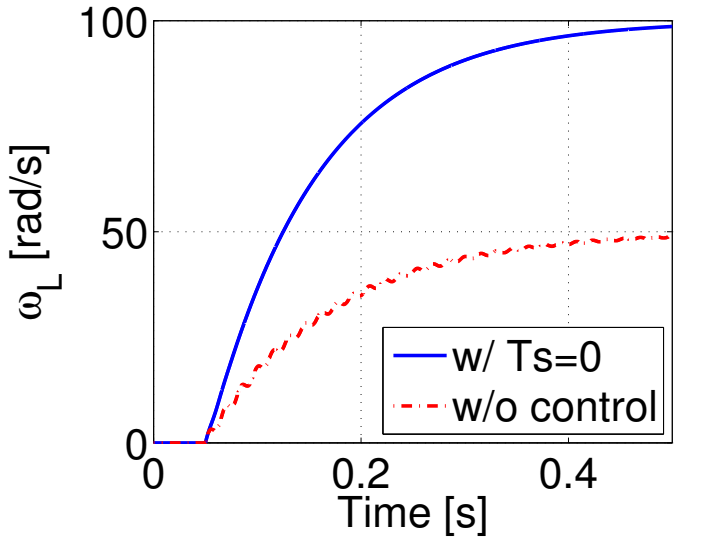

(b) Load-side angular velocity responses.

Figure 5.6 Realization of backdrivability. Comparison between the proposed control system and a system without any control when the load-side step disturbance is input.

step reference is input at 0.050 s and a -1.0 Nm step load-side disturbance is input at 0.10 s. The black dotted line denotes the reference value of the joint torque, the blue solid line denotes the response with the motor-side angular velocity FF controller, and the red dashed line denotes the response without the motor-side angular velocity FF controller. The joint torque responses are precisely controlled in both cases. However, the motor-side angular velocity FF control slightly improves the initial responsiveness. Disturbance suppression is also improved by applying the motor-side angular velocity FF controller that increases the inner loop control bandwidth.

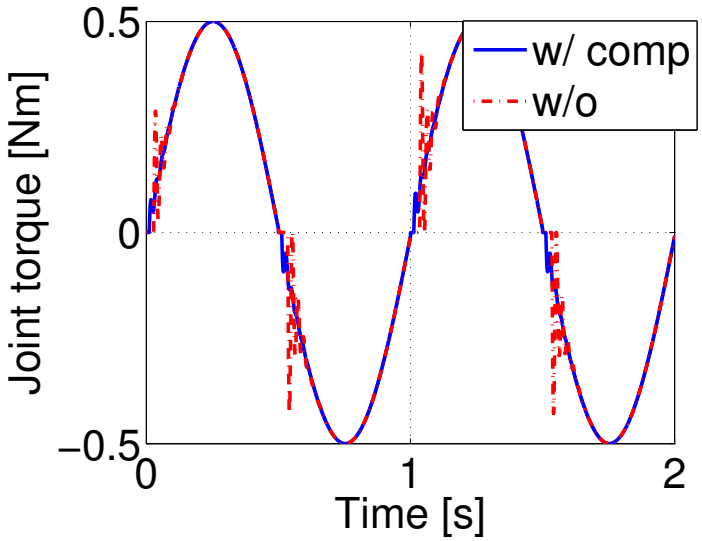

(a) Sinusoidal responses of the joint torque.

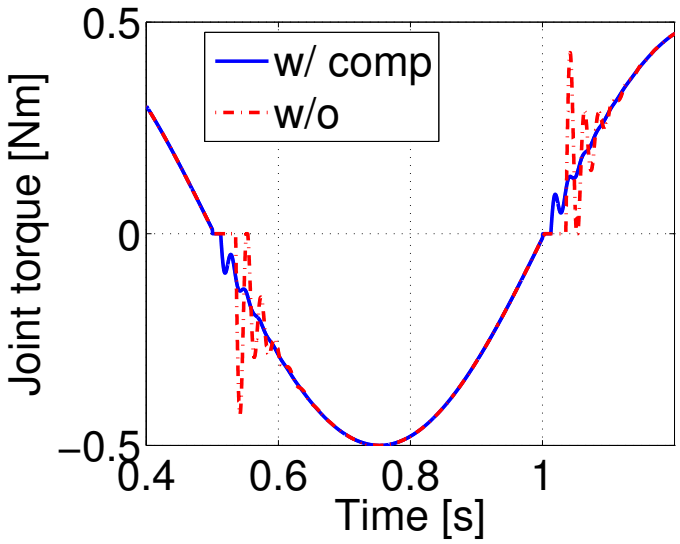

(b) Zoom of Fig. 5.7(a).

Figure 5.7 Comparison between the sinusoidal responses of the joint torque with and without backlash compensation.

High backdrivability

The joint torque control method also improves backdrivability. Backdrivability is important for realizing human–machine interactive motion [103, 104] because it indicates the ease of moving the devices from the load side. Specifically, backdrivability is essential in wearable robots since it determines the ease for the users to move [105]. The main factors that deteriorate the backdrivability include motor-side impedance and friction amplified by the gear. An enhancement in the backdrivability in industrial robots and human-support robots allows workers to easily move the robots and prevent injury to humans or hardware destruction when robots collide with humans [94].

Backdrivability is enhanced by controlling the joint torque at 0 Nm because the joint torque works as a disturbance when a human inputs external torque on the load side. Backdrivability is evaluated by the load-side velocity with an input to the load side. The joint torque reference is set as 0.0 Nm, and a -1.0 Nm step load-side disturbance is input at 0.050 s in Fig. 5.6. The blue solid line indicates the response with the proposed control while the red dashed line indicates the response without any control. As shown in Figure 5.6(a), the proposed method enables the joint torque to reach 0.0 Nm within 0.050 s. As shown in Figure 5.6(b), the load-side angular velocity response with the proposed method is faster with the same amount of load-side disturbance input, thereby suggesting that the proposed method enhances backdrivability by removing the motor-side impedance. Additionally, the vibration in the velocity response is reduced because $T_s = 0$ control decouples the load and motor sides. Our simulation model does not include friction and the reduction ratio is 1. However, the improvement of backdrivability by the proposed method is clear.

Backlash compensation

Backlash affects the response at motion reversal points, and thus, sinusoidal responses are shown in Fig. 5.7. The blue solid line denotes the joint torque response with an inverse model of deadzone in the FF controller while the red dashed line denotes the response without the inverse model in the FF controller. The initial position corresponds to the middle point of the deadzone. Without backlash compensation, the response remains at 0 Nm at the reversal points. After the deadzone width, the response exhibits large vibration due to a collision between the motor and load side. The results clearly show that the proposed backlash compensation method improves the response.

5.3.4 Experiments

In the experiments, backlash compensation performance is evaluated in our setup. The conditions in the experiments are the same as those in the simulations. Controllers are discretized by using a Tustin conversion with a sampling frequency of 2 kHz. Figure 5.8 shows the joint torque responses with a sinusoidal input. The black dotted line denotes the reference of the joint torque, the blue solid line denotes the estimated joint torque by the joint torque observer, and the red dashed line denotes the measured joint torque by the joint torque sensor equipped for the performance evaluation of the joint torque observer. Deterioration in the joint torque response due to backlash is clearly observed at the reversal points. Additionally, the results show that the joint torque is precisely estimated by the joint torque observer even with backlash nonlinearity.

The responses with backlash compensation based on the inverse deadzone model are shown in Fig. 5.9. In the experiments, the cut-off frequency of the pseudo-differential in the joint torque FF

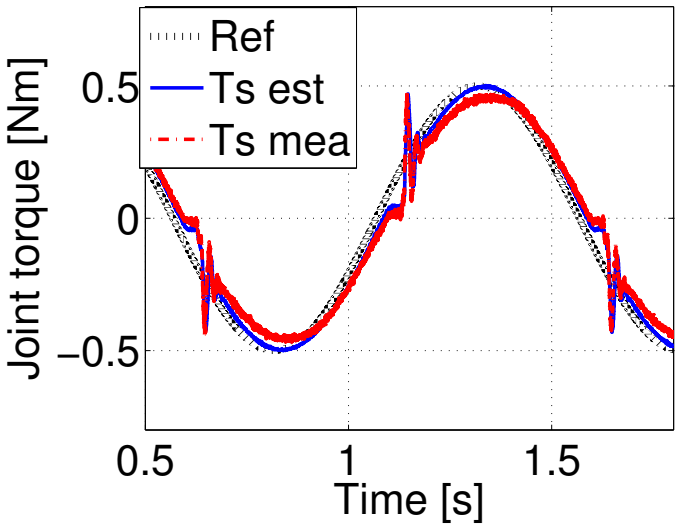

(a) Sinusoidal response of the joint torque.

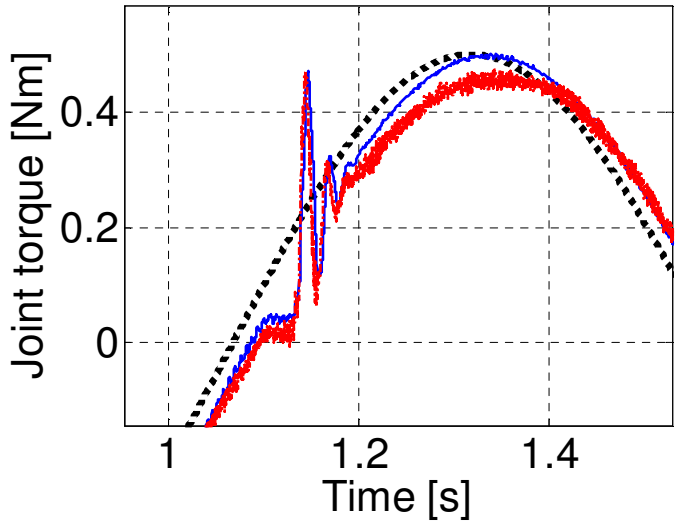

(b) Zoom of Fig. 5.8(a).

Figure 5.8 Joint torque response of the sinusoidal inputs without backlash compensation in the experiment.

controller is decreased to 10 Hz to avoid exceeding the maximum motor current. Figure 5.9 shows the maximum amplitude of the response after the reversal points are suppressed when compared to Fig. 5.8. However, a spike in the joint torque and current is produced in the compensation timing as shown in Figs. 5.9 and 5.10(a). This spike is caused by the differential of the inverse deadzone model in the FF controller. Therefore, it is also necessary to improve the compensation model such that the differential of the model is smooth. A novel compensation model is proposed based on this requirement in the next section.

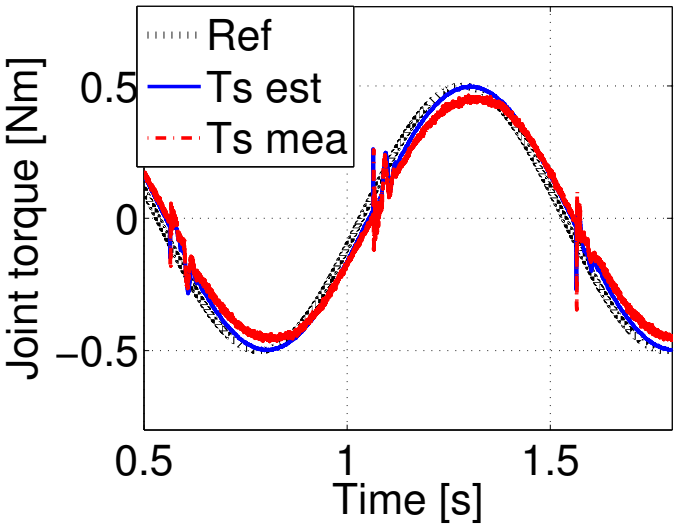

(a) Sinusoidal response of the joint torque.

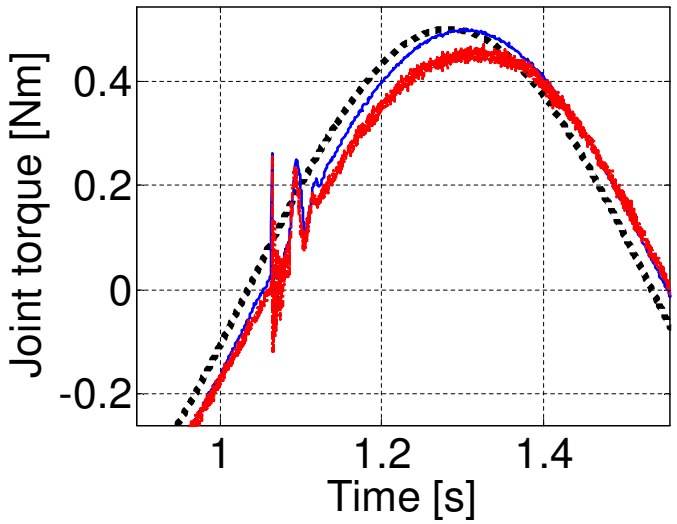

(b) Zoom of Fig. 5.9(a).

Figure 5.9 Joint torque response of the sinusoidal inputs without the inverse model based backlash compensation in the experiment.

5.4 Joint torque control with backlash compensation based on sigmoid function

5.4.1 Sigmoid function for backlash compensation

In order to improve the response and reduce the maximum motor current, a novel backlash compensation model is proposed by using the following sigmoid function;

$$\zeta(x) = K_{sig}\left(\frac{1}{1+e^{-ax}} - \frac{1}{2}\right). \tag{5.3}$$

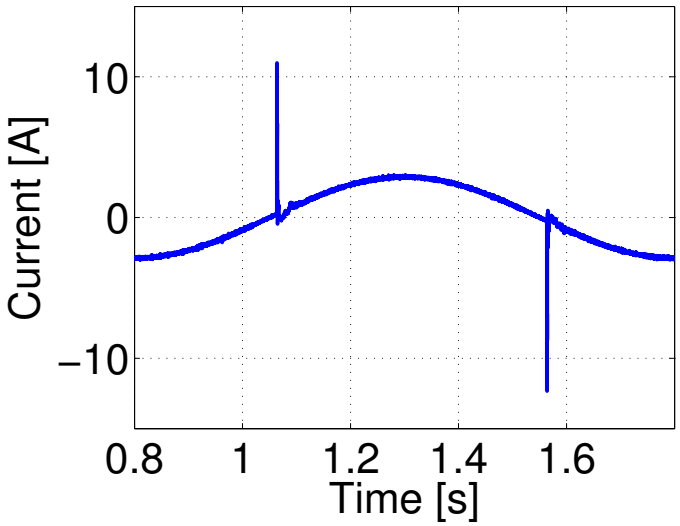

(a) Inverse deadzone model case.

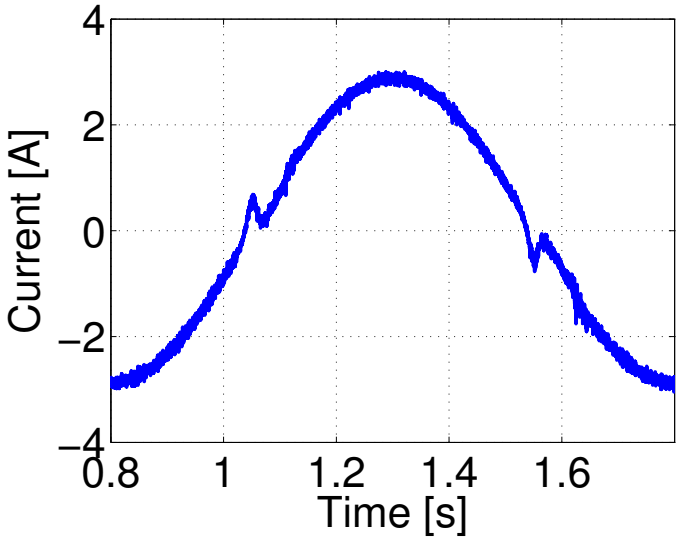

(b) Proposed sigmoid-based model case.

Figure 5.10 Comparison of the current responses with backlash compensation in two cases.

Specifically, K_{sig} is the total gain, and a is the gain that determines the similarity to the inverse deadzone model as shown in Fig. 5.11(a). As shown in Fig. 5.11(b), tangential lines are drawn at the points $-x_1$ and x_1 where the slope of sigmoid function is 1. By defining the new model as (5.4), a smoothed inverse deadzone model is developed as follows;

$$\zeta_p(x) = \begin{cases} x + x_1 + \zeta(-x_1), & (x < -x_1) \\ \zeta(x), & (-x_1 \leq x \leq x_1) \\ x - x_1 + \zeta(x_1). & (x > x_1) \end{cases} \tag{5.4}$$

The pseudo differential of this smoothed model is the output of the FF controller, and thus, a lower maximum motor current is required. After a is tuned experimentally, K_{sig} is tuned by comparing the intercepts of the tangential lines and the identified deadzone width.

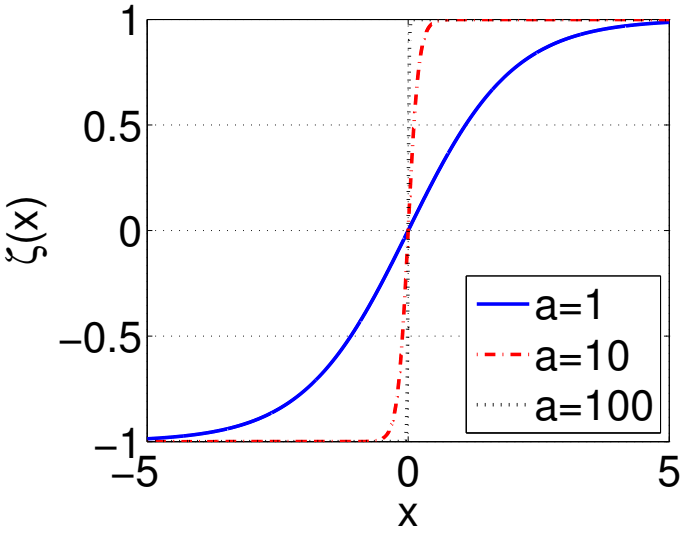

(a) Sigmoid function with variable a.

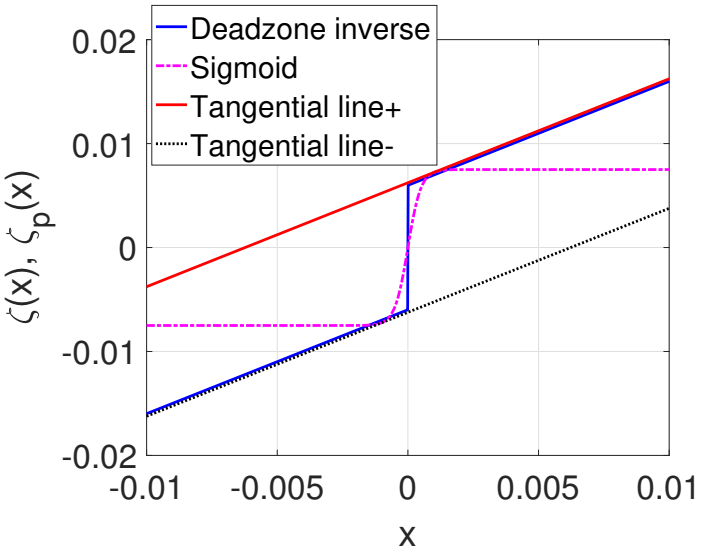

(b) Inverse model of deadzone and the proposed model.

Figure 5.11 Backlash compensation models.

5.4.2 Simulations and experiments

A comparison of the joint torque response between systems with and without the proposed model based backlash compensation is shown in Fig. 5.12. Specifically, K_{sig} and a are tuned to 0.050 and 5000, respectively. The black dotted line denotes the reference of the joint torque, the blue solid line denotes the joint torque response with the proposed backlash compensation, and the red dashed line denotes the response without backlash compensation in the FF controller. The results indicate a clear improvement with no spike in the joint torque response in the proposed method. The current response is shown in Fig. 5.10(b). The proposed compensation method significantly decreases the required maximum motor current.

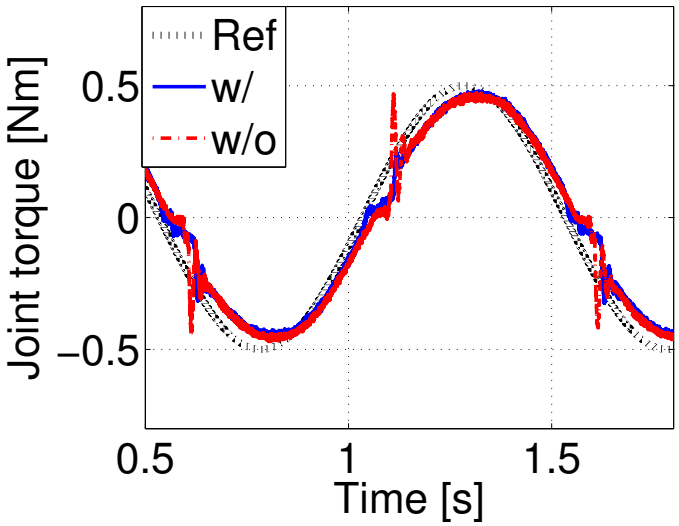

(a) The sinusoidal responses of the joint torque.

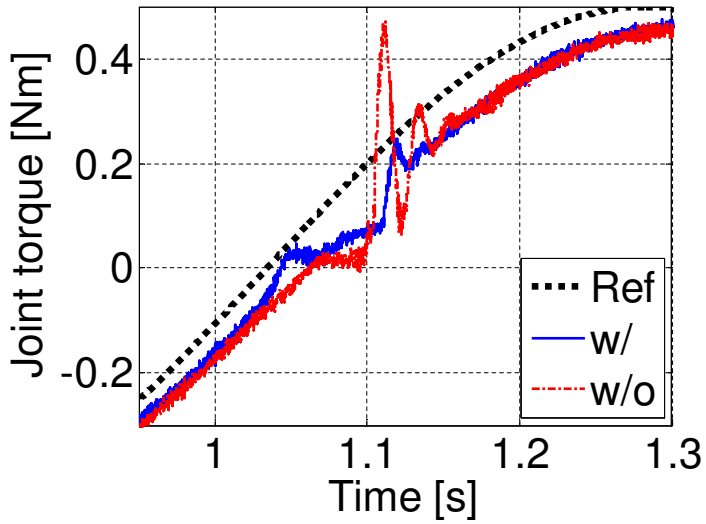

(b) Zoom of Fig. 5.12(a).

Figure 5.12 Experimental comparison of the sinusoidal responses of the joint torque with and without the proposed model based backlash compensation.

5.5 Conclusion

In this study, a novel control method is proposed by using load-side encoder information to improve the performance of joint torque control. The effective use of the load-side encoder information enables the proposed method to exhibit high control bandwidth characteristics and compensate for the backlash in the FF controller. The performance of the proposed method is evaluated through simulations and experiments. Moreover, the experimental results indicated that the inverse deadzone model based backlash compensation produced a spike in the compensation timing, and thus, a novel backlash compensation model is proposed. The experimental results verify that the proposed model

exhibits better performance when compared to that of the inverse deadzone model and reduces the required maximum current. A future study will consider a backlash compensation method that more effectively utilizes the load-side encoder information to further improve the performance.

Chapter 6

Torsional angle control

6.1 Abstract

The demand for robots working with humans, known as collaborative robots, has increased recently. Collaborative robots must be human-friendly; they must ensure safety and flexibly follow human's instructions. In industry, as the cost of high-resolution encoders has decreased, the number of devices with load-side encoders has significantly increased. However, studies on control methods using load-side encoder information are limited. Therefore, in this study, a high backdrivable control method for geared mechatronic systems is proposed using the load-side encoder information and backlash. The proposed high backdrivable control method utilizes the idling characteristics of backlash, by precise position control using both the motor- side and load-side encoders. The performance of the proposed method is verified and compared to impedance control. Moreover, the advantages of employing a load-side encoder to collaborative robots are demonstrated by simulations and experiments.

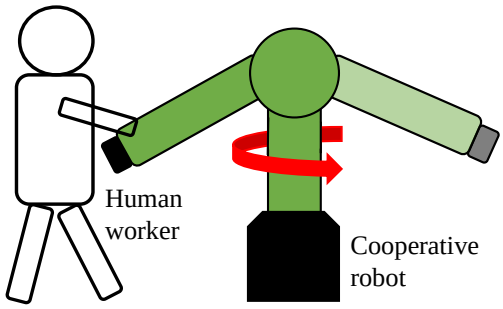

Figure 6.1 Human-machine interaction in collaborative robots: rotational movement by worker's push.

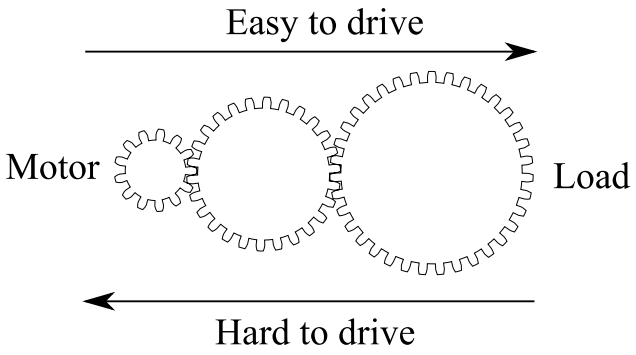

Figure 6.2 Backdrivability.

6.2 Conventional high backdrivable control methods

6.2.1 Backdrivability

The demands for robots working with humans have increased recently [106, 107]. Collaborative robots possess the capability of advancing factory automation and reducing welfare work burdens. Collaborative robots must be human-friendly; they need to ensure safety [12], and must flexibly follow human's instructions, as shown in Fig. 6.1.

Backdrivability is an important characteristic for realizing human-machine interactive motion in collaborative robots, because it indicates the ease of moving mechatronic systems externally. Figure 6.2 indicates the idea of backdrivability. The main factors that cause backdrivability deterioration are the motor-side impedance and friction, which are amplified by the gear reducer. By enhancing the backdrivability in collaborative robots, workers can move the robots easily and safely, which improves working productivity and enables safe human-machine interaction [94]. Especially, backdrivability is essential in wearable robots, since users cannot move arbitrarily in low backdrivable systems.

6.2.2 Conventional backdrivability improvement methods

The existing studies for backdrivability enhancement can be categorized into two groups based on their approach: hardware change and software change. Backdrivability enhancement by hardware change is effective and widely studied [98, 108, 109], but involves high cost and the application is

limited. For example, series elastic actuators (SEAs), which are intensively studied for wearable robot application, consist of a flexible spring to improve backdrivability [103,105,110]. Further, because the gear ratio amplifies the motor-side impedance and friction, direct drive actuators have been developed to enhance backdrivability and applied to flexible robots [111].

On the other hand, changing software or control methods does not restrict the system configuration. One of the most widely studied backdrivable control methods is impedance control [112]. The impedance control requires external force/torque detection by force/torque sensors or sensorless estimation. Though force/torque sensors are currently used in collaborative robots, the sensors with high cost deteriorate the control performance by reducing the rigidity of robot systems. To avoid these disadvantages, the sensorless approach is widely studied, however, it is subject to modeling errors of the plant parameters and delay for estimation. The proposed high backdrivable control method addresses this problem as it does not require the external force/torque detection by its position-based control structure. This study compares the performance of a proposed control with a impedance control as a conventional method.

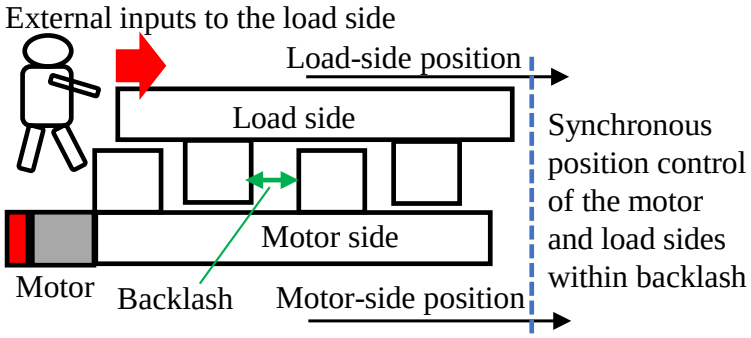

Figure 6.3 Schematic of the proposed high backdrivable control motion.

6.3 High backdrivable control

6.3.1 Proposal of backdrivable control using backlash

For a successful human-machine interaction, high backdrivability is required for collaborative robots to follow human instructions. A novel high backdrivable control method is proposed using a load-side encoder and backlash. When a human exerts an external torque from the load side, the load side becomes difficult to move because the friction and impedance of the motor are amplified by the gear ratio. Within the backlash width, the human only feels the load-side impedance since the load side is not connected to the motor side. To utilize this idling characteristic, when an external torque is input, the proposed high backdrivable control method controls the motor-side position such that the motor

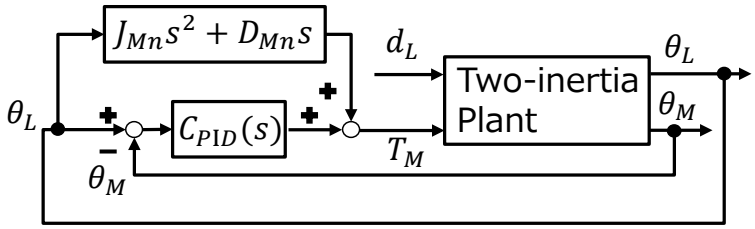

(a) Proposed high backdrivable control method using a load-side encoder and backlash.

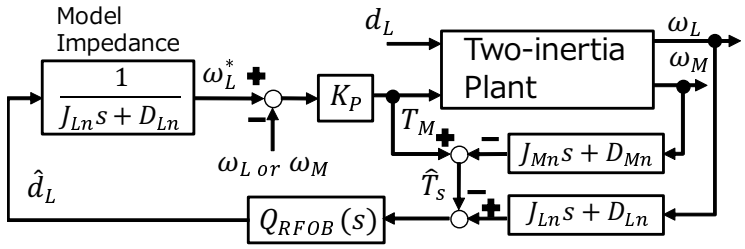

(b) Conventional method: Impedance control method using a load-side encoder.

Figure 6.4 The block diagram of the high backdrivable control methods.

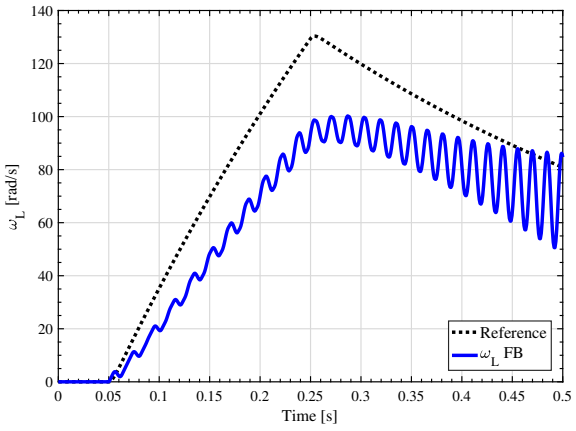

(a) ω_L response in ω_L FB impedance control.

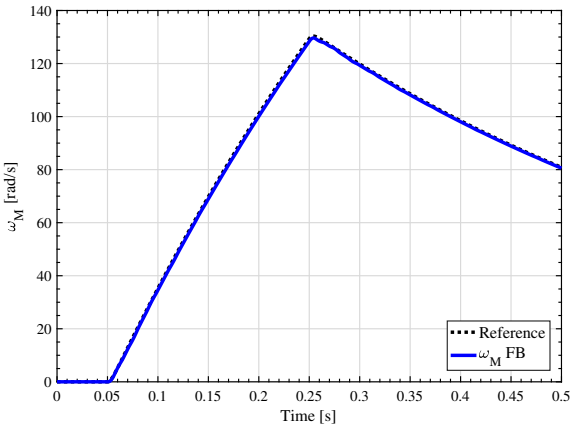

(b) ω_M response in ω_M FB impedance control.

Figure 6.5 Comparison of velocity responses in impedance control with different FB.

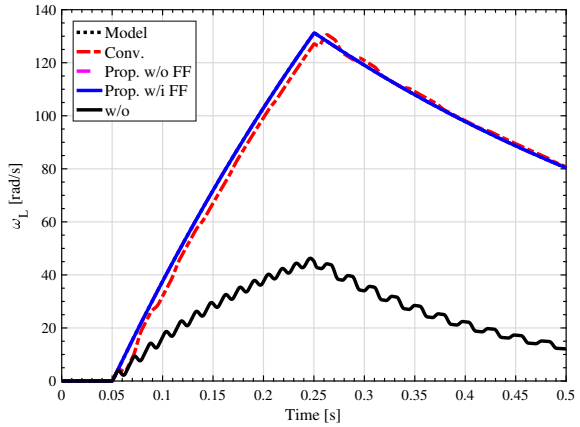

(a) Load-side velocity responses.

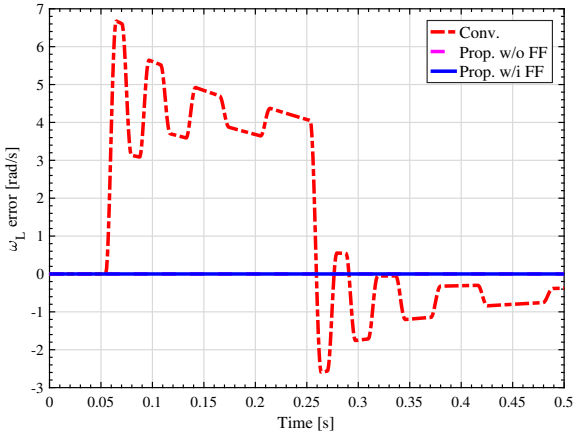

(b) Error of the load-side velocity responses.

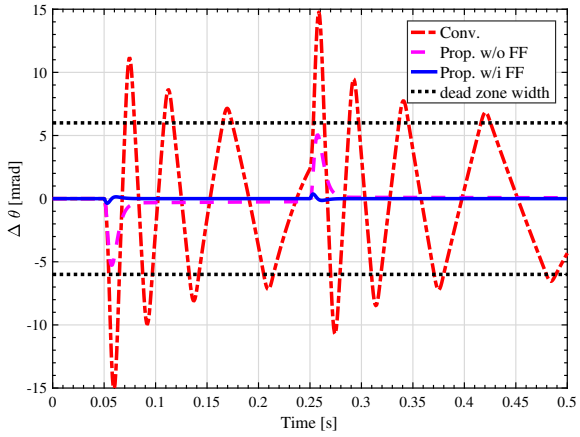

(c) Torsional angle responses.

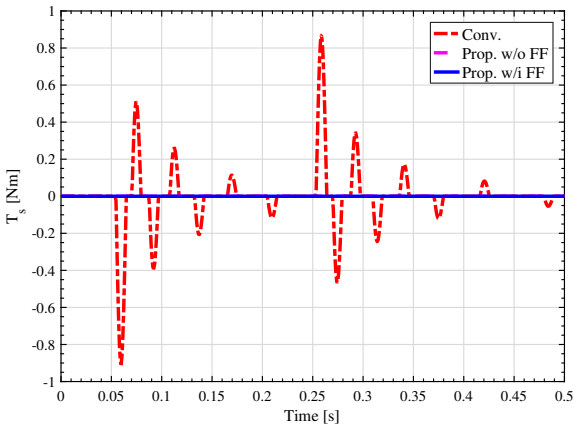

(d) Joint torque responses.

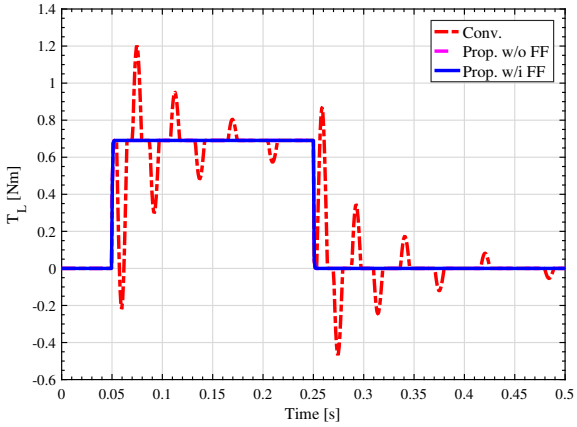

(e) Load-side torque responses.

Figure 6.6 Comparison of backdrivability performance.

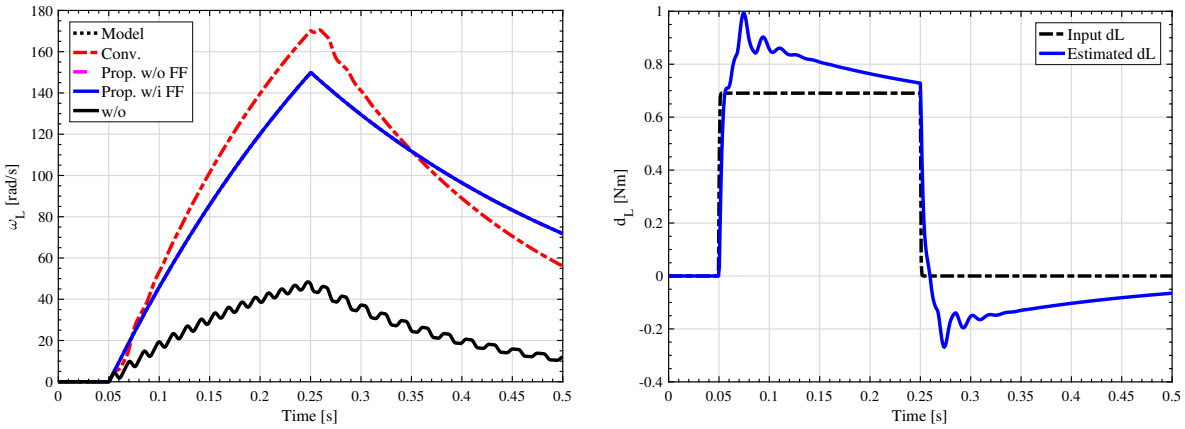

(a) Load-side velocity responses. Conventional method has much error from Model response. Note that Model, Prop. w/o FF, and Prop. w/i FF responses are perfectly matched.

(b) Load-side external torque responses and estimated responses. Estimation shown in solid blue line has error to the input in dashed black line due to load-side modeling errors.

Figure 6.7 Comparison of the load-side velocity and load-side external torque responses with modelling error of the load-side inertia moment and viscosity: $J_L = 0.8J_{Ln}$, $D_L = 1.2D_{Ln}$.

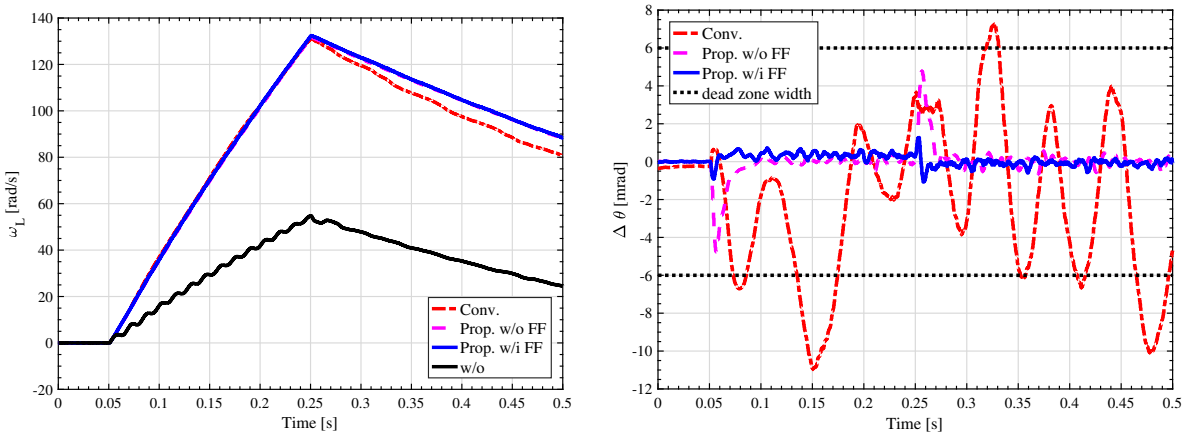

(a) Load-side velocity responses.

(b) Torsional angle responses.

Figure 6.8 Experimental comparison for backdrivability performance.

side follows the load side within the backlash width. A schematic of the proposed high backdrivable control motion is given in Fig. 6.3. The motor-side position is synchronously controlled with the load-side position within backlash width.

The block diagram of the proposed high backdrivable control method is shown in Fig. 6.4(a). Here, $C_{PID}(s)$ indicates a PID controller and subscript $_n$ denotes nominal values. The high backdrivable control method is a motor-side position control whose command value is the load-side position obtained by the load-side encoder. In the operating range of the method, the plant model becomes the only motor-side model, because the motor and load sides are separated by the backlash. Therefore, the FF controller and PID controller are designed only based on the motor-side plant parameters and do not require the load-side plant parameters, which makes the proposed method robust against load-side plant parameter variation. This is a strong advantage since the load-side inertia varies in robots depending on the posture.

The proposed method enhances backdrivability by making the load side be in idling condition. Therefore, the total impedance is controlled to be the load-side impedance in ideal condition. When it is required to lower the total impedance more, assist by the joint torque is necessary. In that case, precise external input torque estimation and joint torque estimation are essential for realizing assistance. Precise external input torque and joint torque estimation method is proposed in chapter 7. Backdrivability enhancement by assist can be realized the impedance control and the method proposed in chapter 7. This chapter focuses on the simple industrial-oriented backdrivable enhancement, which does not require any estimation.

6.3.2 Impedance control

For the improvement of backdrivability, impedance control is the most widely employed technique [113–117]. Impedance control realizes the desired impedance by velocity FB control, with respect to a velocity command value generated through model impedance expressing the desired impedance. In this study, a P controller with gain K_p is implemented as the velocity controller. The block diagram of the implemented impedance control is given in Fig. 6.4(b). Here, $Q_{RFOB}(s)$ is the first-order LPF used for realization.

To realize impedance control, it is necessary to detect the external torque input to the model impedance. Though force/torque sensors could be applied to detect external force/torque by human inputs, these sensors present disadvantages such as high cost, low stiffness, and nonlinearities [118]. Therefore, sensorless estimation is preferred.

In this study, a reaction force observer (RFOB) which was proposed in [119] is applied to estimate the external torque. Unless the two-inertia system dynamics is considered, the estimation is vulnerable

to resonant vibration. For a fair comparison between the proposed high backdrivable control and impedance control in terms of sensor configuration, the RFOB using both the motor-side and load-side encoders considering resonant dynamics is applied for the external torque estimation in impedance control as shown in Fig. 6.4(b). Here, $Q_{RFOB}(s)$ is the first-order LPF for realization.

Then, load-side impedance control is realized by load-side velocity control with the load-side velocity command value generated through the model impedance, which is designed to be equal to the load-side impedance. The simulation result of the impedance control performance evaluation is shown in Fig. 6.5(a). Because the load-side velocity, which is a non-collocated information with a large phase delay, is used in the FB control, the gain K_p cannot be increased. Therefore, the velocity does not follow the command value. Because the load-side information FB with a large phase delay hinders the increase in velocity controller gain, the motor-side velocity FB control is implemented. The velocity command value and motor-side velocity response are shown in Fig. 6.5(b). Using information of the collocated system enables high gain, and the response is clearly improved. We define this impedance control method with the FB of the motor-side velocity as the conventional method and compare it with the proposed method.

6.3.3 Simulations and experiments

Conditions

The advantages of the proposed high backdrivable control method are evaluated by comparison with a conventional method: impedance control. The backdrivability is evaluated by the load-side velocity response when a step load-side external torque d_L is input between 0.05-0.25 s. A first-order LPF with a cut-off frequency of 500 Hz is implemented to the step command of the external torque. The PID controller of the proposed method is designed using the pole placement method with only the motor-side plant. The triple poles are placed on the real axis, at 60 Hz. The frequency of the pole is determined to the fullest extent experimentally. The second-order LPF $Q(s) = \frac{1}{s^2+2\zeta\omega_n+\omega_n^2}$ for realizing the FF controller in the proposed method is tuned as $\zeta = 0.30$ and $\omega_n = 2\pi \cdot 700$. Here, ζ is designed to be small in order to reduce the phase delay. The value of the model impedance used in the impedance control, is designed to be equal to the impedance of the load side so that only the load-side impedance is felt from the load-side external torque. The velocity controller gain K_p is designed to be $K_p = 1.5$, and is increased till it loses stability experimentally. Unless otherwise stated, no modeling error is given in the simulations. The experimental conditions are the same as those in the simulations.

Validations

Figure 6.6(a) shows the comparison of the load-side velocity response of the impedance control method (Conv.), the proposed method without FF controller (Prop. w/o FF), the proposed method (Prop. w/i FF), and the plant without any controller (w/o). The model represents a reference because it indicates a response when the same external torque is applied to the load-side plant model instead of the two-inertia model. With no control, the backdrivability is low. The velocity does not significantly increase, and vibration occurs at the resonance frequency. Because the response of the proposed method and the conventional method mostly overlaps with the response of the model, the backdrivability is improved, and the impedance from the load side coincides with the load-side impedance. Figure 6.6(b) indicates the errors in the load-side velocity responses from the model response. It must be noted that the errors of the proposed methods are kept 0. The load-side velocity response of the conventional method has an error from the response of the model, because the gain K_p cannot be sufficiently increased due to the delay in external torque estimation.

Torsional angle response shown in Fig. 6.6(c) reveals the reason for the error. In the proposed method, the torsional angle response is within the range of backlash (dead zone width), indicated by the dotted black line, but the torsional angle response in the conventional method exceeds the backlash width. Because the model impedance is designed to be the load-side impedance, the joint torque should be 0 Nm. However, as shown in Fig. 6.6(d), the joint torque is not always 0 Nm in the conventional method due to collisions between the motor and load sides. As a result, the joint torque acts as a disturbance. The load torque T_L shown in Fig. 6.6(e) does not coincide with the input external torque, resulting in an error in the load-side velocity in the conventional method. Furthermore, by including the FF controller, the torsional angle is further suppressed. Thus, the torsional angle can be kept within the backlash width even if a large disturbance is input in a high-frequency range.

Next, the effects of modeling error are analyzed when the load-side inertia and the viscosity, which easily fluctuate in robotics applications, become 0.80 and 1.2 times the nominal value. The load-side velocity response is shown in Fig. 6.7(a), and the external torque estimated in the conventional method is shown in Fig. 6.7(b). It is important to note that the responses in the proposed methods precisely coincide with the input external torque. The estimated external torque has an error due to modeling error. Therefore, a large error occurs in the load-side velocity response. Furthermore, since the proposed method is not required to estimate the external torque and does not require the load-side plant parameters on controller design, the performance does not deteriorate.

Figure 6.8(a) shows an experimental comparison of the velocity responses in the conventional method, proposed method without the FF controller, proposed method, and the plant without

control. The results are similar to the simulation results shown in Fig. 6.6(a). Since a modeling error exists, the velocity responses differ between the conventional method and proposed method, especially in the response during deceleration. Vibration is observed in the load-side velocity in the conventional method, while the proposed methods demonstrate responses without vibration.

Figure 6.8(b) shows an experimental comparison of the torsional angle responses. The experiment is conducted for the verification of the simulation shown in Fig. 6.6(c). While the torsional angle is suppressed in the proposed method, the conventional method does not suppress the torsional angle within the range of the backlash, which deteriorates the load-side velocity response. The torsional angle is suppressed further by application of the FF controller, indicating that the FF controller can withstand a larger disturbance in higher frequency range.

	Tracking control	Recognition of external inputs	Impact attenuation	Backdrivable control or Turning off
Double encoder	Precise at the load side	More precise and faster detection	Maximum braking	Backdrivable control using backlash
Single encoder	Vulnerable to flexibilities and nonlinearities	Estimation suffering from resonance	Maximum braking	Turning off (zero input)

Figure 6.9 Overall procedure of human-machine interactive motion and the comparison between double encoder system and single encoder system.

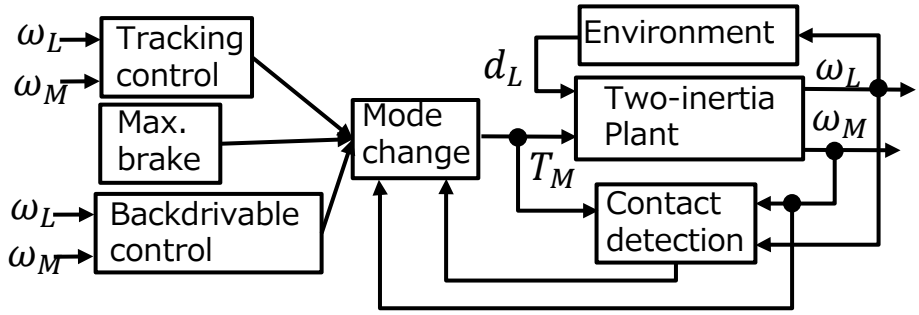

(a) Double encoder control system: DE system.

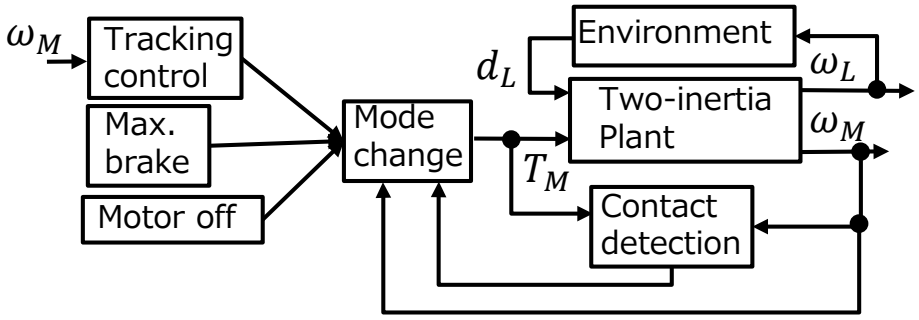

(b) Single encoder control system: SE system.

Figure 6.10 The block diagrams of double encoder control system and single encoder control system.

6.4 Human–machine interactive control

6.4.1 Procedure of human–machine interactive motion

In this study, the scenario in which a human suddenly pushes a collaborative robot during its velocity tracking operation is considered. The human-machine interaction can be divided into four phases: tracking control, recognition of external inputs, impact attenuation, and backdrivable control. In order to realize a safe and flexible operation, a double encoder (DE) control system is applied. The advantages obtained by applying a load-side encoder to a collaborative robot for human-machine interaction are revealed in each phase by comparing with a single encoder (SE) control system.

Figure 6.9 shows the overall procedure of human-machine interaction and the comparison between DE and SE control system. First, the robots are controlled by velocity/position control. When a human pushes a robot, a collaborative robot must recognize the external force input and attenuate the impacts between the human and machine as quickly as possible. In this study, it is assumed that the robots are unaware of the time of external force input by the human; therefore, only the FB control can be applied to attenuate the impact. After contact between the human and robot, the robot is operated by a novel high backdrivable control method to follow the human's pushing action. Finally, the structures of the DE control system and SE control system are shown in Fig. 6.10. The following two subsections describe the procedure of human-machine interaction of DE and SE control systems.

6.4.2 Double encoder interactive control system

Tracking control

Tracking control indicates all the position and velocity controls. In this study, the PI-P controller, which consists of a load-side velocity PI controller and motor-side velocity P controller, is implemented as the tracking controller. Generally, with only a motor-side encoder, achieving a precise and fast tracking performance at the load side is difficult, due to the low-frequency resonant modes and nonlinearities caused by gear reducers. With a load-side encoder, precise tracking control at the load side can be achieved even with unknown nonlinearities in the gear reducers.

Recognition of external inputs

To avoid the drawbacks of using the force/torque sensors, the RFOB is applied to estimate external torque. When the estimated external torque exceeds the threshold value, which is designed beforehand, the robots recognizes contact with a human.

The RFOB using both the motor-side and load-side encoder information, known as double encoders

RFOB (DERFOB) in this paper, is utilized to consider the two-inertia resonant characteristics [8]. The block diagram of the two-inertia-model-based RFOB is shown in Fig. 6.11(a). The transfer function from the external torque to the estimated torque is expressed as;

$$\frac{\hat{d}_L}{d_L} = Q_{RFOB}(s). \tag{6.1}$$

Here, the subscript ˆ indicates the estimated values. The equation (6.1) shows an ideal estimation characteristic. Also, Fig. 6.11(c) shows the frequency characteristic from the external torque to the estimated external torque when the cutoff frequency of $Q_{RFOB}(s)$ is 1 kHz. DERFOB response indicated in the blue solid line shows an ideal low-pass characteristic.

Impact attenuation

The maximum braking is the best FB-based impact attenuation method. Therefore, rapid detection of the contact is important for actuating the maximum negative torque as soon as possible, to attenuate the impact. The usage of load-side encoder enables faster detection of the contact, as shown in the gain and phase characteristics in a high-frequency range of Fig. 6.11(c). When the estimated value exceeds the designed threshold value (-2.0 Nm), the maximum negative torque (-5.0 Nm) is input to attenuate the impact.

High backdrivable control using a load-side encoder and backlash

After maximum braking, when the motor-side velocity becomes zero, the proposed high backdrivable control method is turned on.

6.4.3 Single encoder interactive control system

Tracking control

The SE control system does not contain a load-side encoder. Therefore, achieving a precise and fast tracking performance at the load side is difficult due to the low-frequency resonant modes and nonlinearities caused by gear reducers. For precise tracking control, a precise modeling of the gear dynamics including the nonlinearities are required.

However, for proper comparison, the semi-closed controller is not applied, and the same PI-P controller, which utilizes the load-side encoder information is implemented in order to achieve the same conditions at impact.

Recognition of external inputs

With only a motor-side encoder, a rigid-body model expressed as (6.2) is used as the estimation model in RFOB, which is known as single-encoder RFOB (SERFOB) in this paper.

$$P_{alln}(s)^{-1} = J_{alln}s + D_{alln}, \tag{6.2}$$
$$J_{alln} = J_{Mn} + J_{Ln}, \;\; D_{alln} = D_{Mn} + D_{Ln}.$$

The block diagram of rigid-body-model-based RFOB is shown in Fig. 6.11(b). When it is assumed that a modeling error does not exist, the transfer function from the external torque to the estimated torque is expressed as (6.3). The equation (6.3) confirms that it has resonant characteristics even without any modeling error.

$$\frac{\hat{d}_L}{d_L} = Q_{RFOB}(s) * \frac{J_{all}Ks + D_{all}K}{J_M J_L s^3 + (J_M D_L + J_L D_M)s^2 + (J_M K + D_M D_L + J_L K)s + (D_M K + D_L K)} \tag{6.3}$$

Figure 6.11(c) shows the frequency characteristic from the external torque to the estimated external torque. While the DERFOB response indicated by the solid blue line demonstrates an ideal low-pass characteristic, the SERFOB response indicated by the dashed red line reaches a large peak at resonance, because its estimation model does not consider the two-inertia resonance characteristic. The response in the high-frequency range is important for the rapid and proper detection of contact with human, to achieve maximum attenuation of the impact. Also, the proper threshold value cannot be easily designed with the resonant characteristics in SERFOB due to a large vibration. The load-side encoders enable the robots to quickly detect contacts by humans, by considering resonant characteristics, which enable the robots to further attenuate the impulse.

Impact attenuation

When the estimated value exceeds the designed threshold value, the maximum negative torque is input to attenuate the impact. The impact attenuation phase in SE control system is the same as that in DE control system.

Turning off

After maximum braking, when the motor-side velocity becomes zero, the system is turned off (i.e., the control output becomes zero).

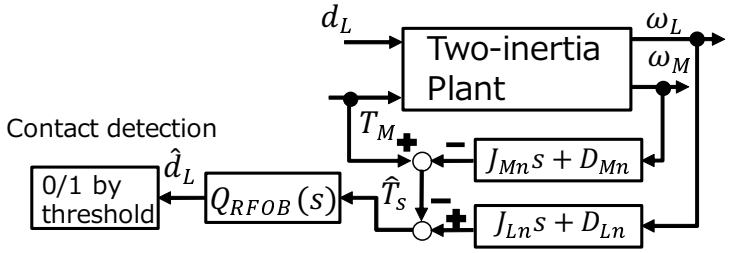

(a) Block diagram of two-inertia model based RFOB using double encoders (DERFOB).

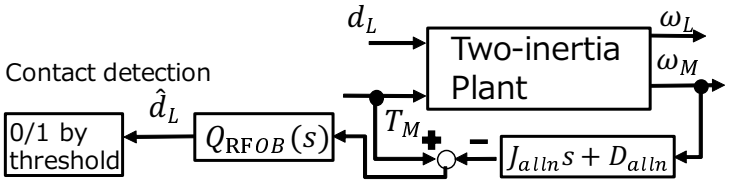

(b) Block diagram of rigid body model based RFOB using single encoder (SERFOB).

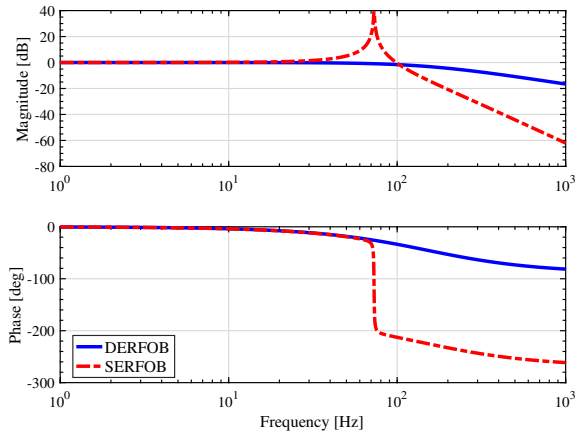

(c) Frequency characteristics comparison between SERFOB and DERFOB. SERFOB suffers from two-inertia system resonant characteristic.

Figure 6.11 The block diagrams and frequency characteristics of SERFOB and DERFOB.

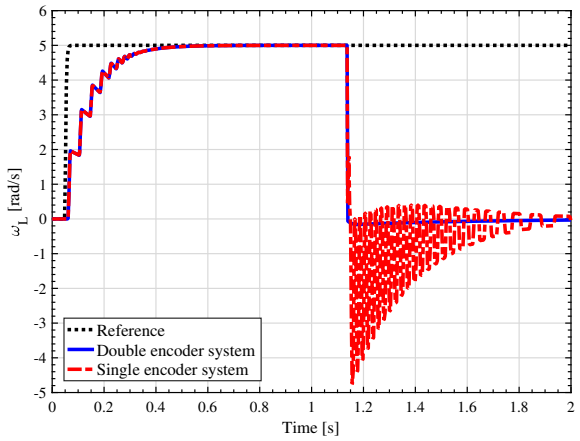

(a) Load-side velocity responses with the contact to the environment.

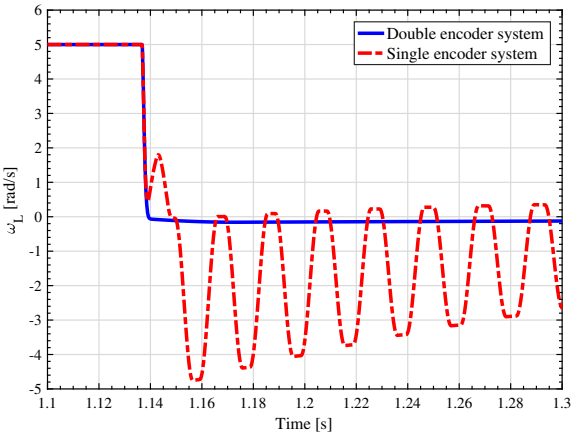

(b) Zoom of Fig. 6.12(a) around the contact timing.

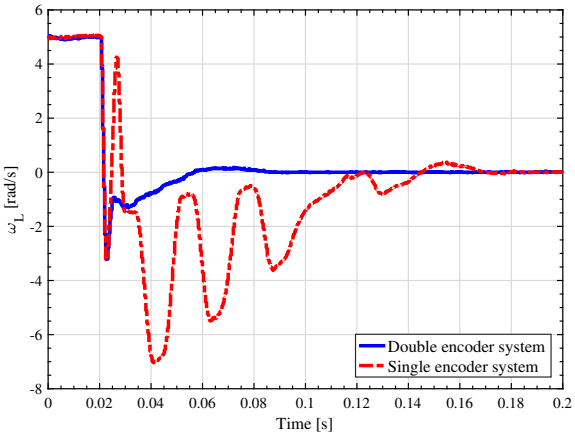

(c) Experimental validation of Fig. 6.12(b).

Figure 6.12 Simulation and experimental comparison of the load-side velocity responses.

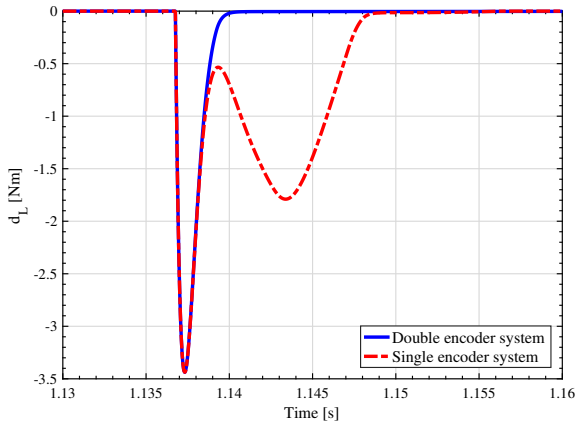

(a) Load-side external torque responses.

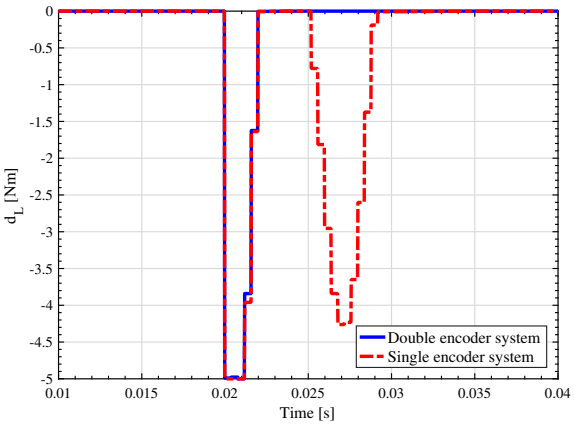

(b) Experimental validation of Fig. 6.13(a).

Figure 6.13 Simulation and experimental comparison of the load-side external torque responses.

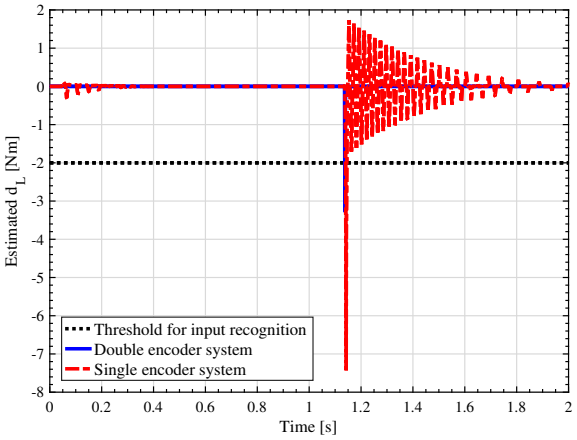

(a) Estimated external torque responses.

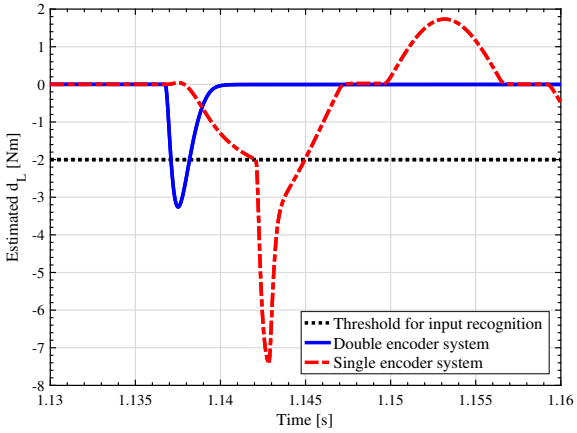

(b) Zoom of Fig. 6.14(a) around the contact timing.

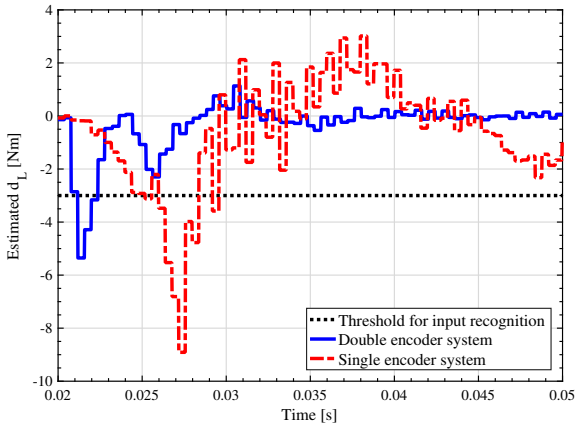

(c) Experimental validation of Fig. 6.14(b).

Figure 6.14 Simulation and experimental comparison of the estimated external torque responses.

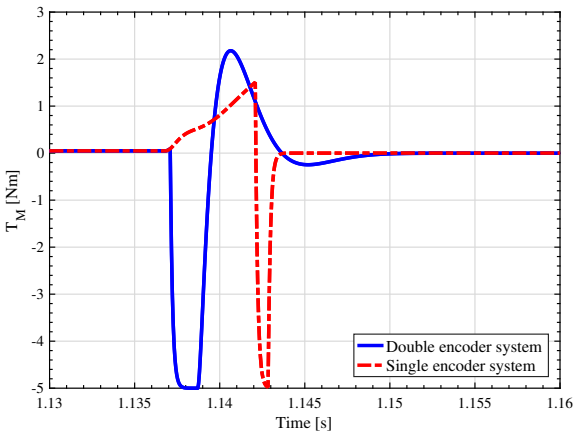

(a) Motor torque responses.

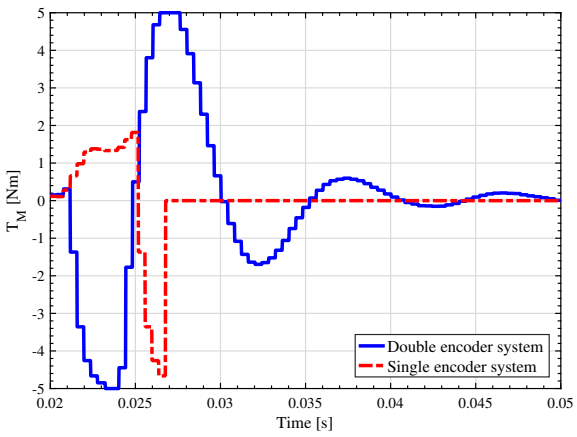

(b) Experimental validation of Fig. 6.15(a).

Figure 6.15 Simulation and experimental comparison of the motor torque responses.

6.4.4 Numerical comparisons of interactive control

Conditions

The scenario where a human suddenly pushes a collaborative robot during its velocity tracking operation is considered. For high reproducibility of external torque inputs, a torque imitating a human's sudden pushing action is input by the load-side motor in the experiments.

Generally, collaborative robots comprise soft covers over their surface to prevent injury to human workers. Therefore, a spring and damper impedance model is used to simulate the impedance between the soft-covered robot and human. The value of torsional rigidity and the damping coefficient of impedance model are set as 1.0 Nm/rad and 1.0 Nms/rad, respectively. The impedance model is placed at a 5.0 rad distance from the initial position.

The experimental conditions are the same as those in the simulations. In the experiments, the spring-damper impedance model is implemented using the load-side motor. The input external torque is measured by the torque reference of the load-side motor. It is noted that the threshold value for contact detection is experimentally changed to -3.0 Nm.

Simulations and experiments

The step velocity reference is filtered with a first-order low-pass filter whose cutoff frequency is 50 Hz. The control performances of the DE control system are indicated by solid blue lines and the SE control system are indicated by dashed red lines. The load-side velocity responses are shown in Fig. 6.12. The contact between plant's load side and the spring-damper impedance model occurred at around 1.137 s. The load-side velocity response in the SE system has a large vibration due to collisions between the motor and load sides after the system is turned off, while the response in DE system has no vibration because the high backdrivable control method controls the motor side to follow the load side.

Figure 6.13(a) shows the external torque caused by the contact between plant and spring-damper impedance model. The DE control system decreases the impulse, which is calculated by the product of torque and time. In other words, the DE system can reduce the thickness of the soft covering material on collaborative robots. The DE system can reduce the impulse owing to faster detection of external inputs. Figure 6.13(b) shows the experimental verification of the simulation shown in Fig. 6.13(a). The DERFOB decreases the impulse by faster contact detection than SERFOB as shown and described later.

The estimated external torque is shown in Fig. 6.14. By considering the resonant characteristics, DERFOB can detect the contact faster than SERFOB by about 5 ms. Moreover, SERFOB has a large

vibration due to the resonance. Figure 6.14(c) shows the experimental verification of the simulation shown in Fig. 6.14. As in the simulation, the SE system has a large vibration due to the resonance, and the DE control system can detect the contact faster than the SE system by about 4 ms.

Figure 6.15(a) shows the motor torque response around the timing of the contact to the spring-damper impedance model. The motor torque in the DE system quickly reaches to the maximum negative torque (-5.0 Nm), and then, when the motor-side velocity reaches zero, the proposed high backdrivable control method is turned on. To make the motor-side angle follow the load-side angle, a positive torque is input. On the other hand, the motor torque in SE system increases gradually even after the contact because SERFOB cannot quickly detect the contact. The motor torque quickly increases to the maximum negative torque, and then, the motor torque is turned off. The motor torque response indicates that the DE control system works correctly. Finally, Fig. 6.15(b) shows the experimental verification of Fig. 6.15(a). The experimental results are similar to the simulation results. Though the motor torque in the experiment is larger than that in the simulation due to the friction and the modeling error, we can confirm that the mode-switching algorithm for human–machine interactive motion properly works also in the experiments.

6.5 Conclusion

Owing to the increasing use of load-side encoders in industry, a novel high backdrivable control method was proposed using the load-side encoder information and backlash. Although the system with backlash is known to be difficult to control, the backlash has an ideal characteristic for backdrivability. The proposed method utilized the characteristic that the load side idles in the backlash width. The proposed high backdrivable control method is compared to impedance control, and the following features are observed:

- The external force need not be estimated (neither a force sensor nor a RFOB are required)
- Robust against load-side parameters
- Easy to design (the controllers are based only on motor-side parameters)
- Impossible to change the load-side impedance

Second, on comparison with robots without a load-side encoder, the advantages of applying a load-side encoder to collaborative robots were presented in human-machine interactive motion. The advantages of applying the load-side encoder to collaborative robots are as follows:

- Precise tracking control even with transmission nonlinearities,
- Precise and fast detection of the contact for impact attenuation,

- High backdrivable control by active use of backlash.

These advantages were validated through simulations and experiments.

Chapter 7

External torque estimation

7.1 Abstract

Sensorless external torque estimation is becoming important for a myriad of industrial applications. The load-side torque in a two-inertia system with encoder on the load can be estimated by using either of two observers that present different robustness against modeling and measurement errors on the motor and transmission. By combining these observers, this study proposes a load-side external torque observer with high estimation accuracy even under modeling and measurement errors. Also, analyses of the observer with and without a joint torque sensor unveil the advantages and limitations of applying a joint torque sensor for external torque estimation. Moreover, a systematic approach is derived to select the gains of the proposed observers, whose proper instantiation can minimize the estimation variance by considering the variance of the plant parameters and sensor measurements. It is also validated that the high performance of the proposed method through simulations and experiments.

7.2 Conventional estimation methods

One of the most widely used force/torque estimation methods is reaction force observer (RFOB) proposed in [119]. However, it is well known that estimation accuracy is deteriorated when RFOB is applied to the two-inertia plants [4, 120]. Therefore, the dynamics of a two-inertia system have to be considered. In this study, six estimation methods are compared.

7.2.1 Estimation using only motor-side encoder

The load-side external torque can be estimated with only motor-side encoder by implementing state observer. Assuming a stepwise load-side external torque $\dot{d}_L = 0$, the load-side external torque can be estimated by estimating the augmented state vector. Since the state observer using only motor-side

encoder requires all plant parameters, it suffers from modeling error effect severely.

7.2.2 Estimation using both motor- and load-side encoders

Motor-side estimation

When the two-inertia system has both motor- and load-side encoders, there are mainly two conventional methods for load-side external torque estimation proposed in [121] and [122]. In both methods, the load-side external torque d_L is estimated from the joint torque T_s and the torque obtained by an inverse model of the load-side model and load-side velocity as follows;

$$\hat{d}_L = (J_{Ln}s + D_{Ln})\omega_L - T_s. \tag{7.1}$$

Here, subscripts $_n$ and $\hat{}$ indicates that the variables are nominal parameters and estimated values, respectively.

Two methods differ in terms of how to estimate joint torque. The method proposed in [121] estimates the joint torque from the motor-side dynamics as follows;

$$\hat{T}_{sM} = T_M - (J_{Mn}s + D_{Mn})\omega_M - d_M. \tag{7.2}$$

The motor torque T_M is measurable by a current sensor and the motor-side disturbance d_M, which mainly consists of the motor-side friction, can be measured beforehand. In this study, this estimation method is called as Motor-side estimation since it uses motor-side dynamics.

Transmission-part estimation

In [122], the joint torque is estimated from the transmission-part information as follows;

$$\hat{T}_{sK} = \theta_s K_n. \tag{7.3}$$

Here, the torsional angle θ_s can be measured by using both motor- and load-side encoders. This approach avoids the friction modeling error of $D_{Mn} \cdot \omega_M$ and d_M in (7.2). However, the value of $\hat{T}_{sK}$ can be deteriorated by the modeling error of torsional rigidity and nonlinearities in transmission mechanisms [123]. In series elastic actuators equipped with well-identified linear springs, transmission-part estimation is preferred [95, 124]. In this study, the estimation is called as transmission-part estimation.

Motor-side estimation and Transmission-part estimation

This study proposes accurate load-side external torque estimation that is robust against modeling and measurement errors by combining the estimation methods proposed in [121] and [122], specifically the estimated $\hat{T}_{sM}$, $\hat{T}_{sK}$. The combination of is not novel, as Mitsantisuk *et al.* [125] used both

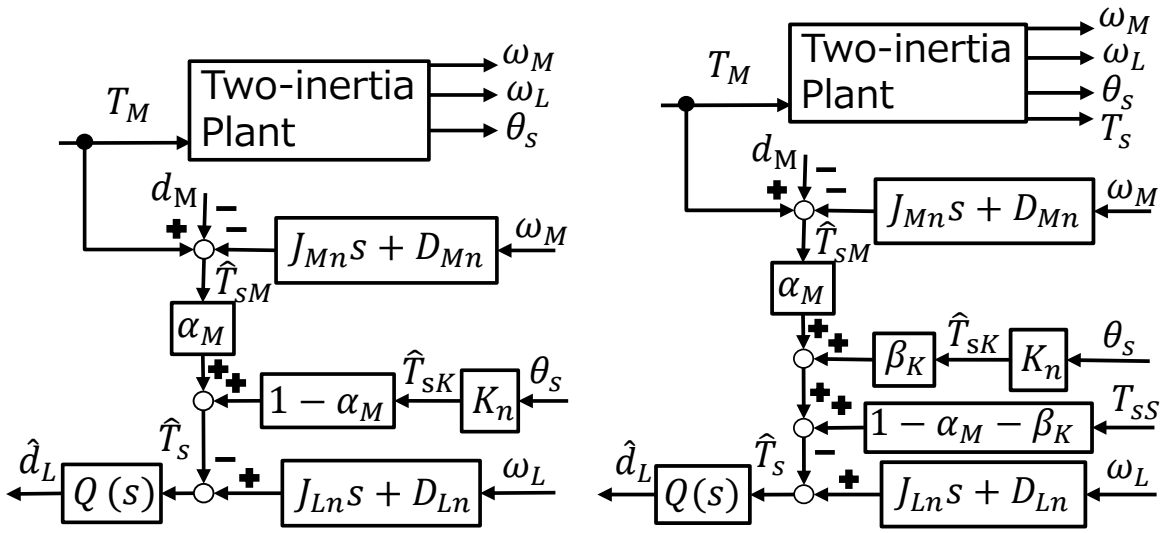

(a) The proposed load-side external torque observer without a joint torque sensor.

(b) The proposd load-side external torque observer with a joint torque sensor.

Figure 7.1 Block diagrams of the proposed load-side external torque observers with/without a joint torque sensor.

methods for estimation, by calling the expression in (7.2) multi-encoder disturbance observer and that in (7.3) load-side disturbance observer. However, they define these observers for identification of the torsional rigidity by comparing their estimated values and assuming that the multi-encoder disturbance observer returns the true value. Likewise, both methods have been combined in other approach by employing different frequency ranges to enhance the estimation bandwidth [126]. This chapter introduces gains determining the ratio between the motor-side and transmission-part estimation in the same frequency range to improve the robustness against modeling and measurement errors. For the details on parameter variation effects from the disturbance observer, refer to [127]. This chapter focuses on accurate estimation rather than disturbance suppression.

7.2.3 Measurement by joint torque sensor

Most of the cooperative robots in industry have joint torque sensors. Therefore, the joint torque can be directly obtained by the joint torque sensor. The joint torque obtained by the torque sensor is robust against modeling errors, but it suffers from measurement noise. In this study, the joint torque obtained by the torque sensor is denoted as T_{sS}.

7.3 Proposed method (Robust estimation by using load-side information effectively)

7.3.1 Proposed method

Analyses of load-side external force observer are conducted. Proposed methods introduce the gains determining the ratio between the motor-side and transmission-part estimation to improve the robustness against modeling and measurement errors. About the load-side parameter variation, it can be calculated from the posture obtained by the joint encoders in robots, and from the CAM data in machine tool stages, for example. Also, the load-side parameter can be identified precisely in real time by applying the proposed method because the proposed method enables precise joint torque estimation. Therefore, this study focuses on the motor-side and transmission-part modeling error effects and the measurement error effects.

Based on the fact that the use of the high-bandwidth joint torque sensors is rapidly increasing in industry, the case with and without a joint torque sensor are considered.

Proposed estimation without joint torque sensor

The motor and load angular velocities and the torsional angle can be measured using the corresponding encoders. First, it is considered that no joint torque sensor available. Assuming a stepwise load-side external torque $\dot{d}_L = 0$, the augmented state equation of the plant is expressed as;

$$\begin{bmatrix} \dot{\omega}_M \\ \dot{\omega}_L \\ \dot{\theta}_s \\ \dot{d}_L \end{bmatrix} = \begin{bmatrix} -\frac{D_M}{J_M} & 0 & -\frac{K}{J_M} & 0 \\ 0 & -\frac{D_L}{J_L} & \frac{K}{J_L} & \frac{1}{J_L} \\ 1 & -1 & 0 & 0 \\ 0 & 0 & 0 & 0 \end{bmatrix} \begin{bmatrix} \omega_M \\ \omega_L \\ \theta_s \\ d_L \end{bmatrix} + \begin{bmatrix} \frac{1}{J_M} \\ 0 \\ 0 \\ 0 \end{bmatrix} T_M,$$

$$y = \begin{bmatrix} 1 & 0 & 0 & 0 \\ 0 & 1 & 0 & 0 \\ 0 & 0 & 1 & 0 \end{bmatrix} \begin{bmatrix} \omega_M \\ \omega_L \\ \theta_s \\ d_L \end{bmatrix}. \tag{7.4}$$

Then, a first-order minimal-order observer estimating d_L is introduced as (7.5) and (7.6), where z is a scalar state variable of the observer and $L = [l_1,\ l_2,\ l_3]$ is the observer gain vector.

$$\dot{z} = A_r z + B_r T_M + F_r y, \quad \hat{d}_L = z + Ly,$$
$$A_r = -\frac{l_2}{J_{Ln}}, \quad B_r = -\frac{l_1}{J_{Mn}}, \tag{7.5}$$

$$F_r = \begin{bmatrix} -\frac{1}{J_{Ln}} l_1 l_2 + \frac{D_{Mn}}{J_{Mn}} l_1 - l_3 & -\frac{1}{J_{Ln}} l_2^2 + \frac{D_{Ln}}{J_{Ln}} l_2 + l_3 & -\frac{1}{J_{Ln}} l_2 l_3 + K_n \left(\frac{1}{J_{Mn}} l_1 - \frac{1}{J_{Ln}} l_2 \right) \end{bmatrix}. \tag{7.6}$$

To analyze the physical meaning of the observer given by (7.5) and (7.6), it is convenient to represent it as a block diagram. Then, the equivalent conversion of the block diagram results in that shown in Fig. 7.1(a), whose variables are defined as follows;

$$Q(s) = \frac{\frac{l_2}{J_{Ln}}}{s + \frac{l_2}{J_{Ln}}}, \tag{7.7}$$

$$\alpha_M = \frac{J_{Ln}}{J_{Mn}} \frac{l_1}{l_2}. \tag{7.8}$$

The first-order low pass filter, $Q(s)$, determines the estimation bandwidth, i.e., the bandwidth is defined by observer gain l_2, and α_M determines the ratio between $\hat{T}_{sM}$ and $\hat{T}_{sK}$ as follows;

$$\hat{T}_s = \alpha_M \hat{T}_{sM} + (1 - \alpha_M)\hat{T}_{sK}. \tag{7.9}$$

Equation (7.9) indicates that α_M can be designed considering the accuracy of $\hat{T}_{sM}$ and $\hat{T}_{sK}$, where the former depends on the accuracy of motor parameters and friction model, whereas the latter depends on the accuracy of torsional rigidity and nonlinear models when nonlinearities in transmission mechanisms such as backlash occur. Given that l_2 is experimentally selected according to the desired bandwidth and stable margin, α_M is designed by observer gain l_1 and indicates the amount of motor-side information that is used. Specifically, when α_M is 1 (i.e., l_1 is $\frac{J_{Mn}}{J_{Ln}} l_2$), the proposed observer is equivalent to the estimation proposed in [121], whereas when α_M is 0 (i.e., l_1 is 0), the proposed observer is equivalent to the estimation proposed in [122]. Therefore, the proposed load-side external torque observer extends these conventional observers by including them as particular cases. If the system has a joint torque sensor, the minimal-order observer can be derived similarly, with the resulting block diagram shown in Fig. 7.1(b).

Proposed estimation with joint torque sensor

Likewise, an estimation with joint torque sensor is analyzed. The augmented state equation is expressed as follows. Please note that state vector is changed compared to (7.4).

$$\begin{bmatrix} \dot{\omega}_M \\ \dot{\omega}_L \\ \dot{T}_s \\ \dot{d}_L \end{bmatrix} = \begin{bmatrix} -\frac{D_M}{J_M} & 0 & -\frac{1}{J_M} & 0 \\ 0 & -\frac{D_L}{J_L} & \frac{1}{J_L} & \frac{1}{J_L} \\ K & -K & 0 & 0 \\ 0 & 0 & 0 & 0 \end{bmatrix} \begin{bmatrix} \omega_M \\ \omega_L \\ T_s \\ d_L \end{bmatrix} + \begin{bmatrix} \frac{1}{J_M} \\ 0 \\ 0 \\ 0 \end{bmatrix} T_M$$

$$y = \begin{bmatrix} 1 & 0 & 0 & 0 \\ 0 & 1 & 0 & 0 \\ 0 & 0 & 1 & 0 \end{bmatrix} \begin{bmatrix} \omega_M \\ \omega_L \\ T_s \\ d_L \end{bmatrix} \tag{7.10}$$

Then, a 1st-order minimal dimension observer is introduced as (7.5), but only F_r changes to (7.11) .

$$F_r = F_{rT_s} = \begin{bmatrix} -\frac{1}{J_L}l_1l_2 + \frac{D_M}{J_M}l_1 - Kl_3 & -\frac{1}{J_L}l_2^2 + \frac{D_L}{J_L}l_2 + Kl_3 & -\frac{1}{J_L}l_2l_3 + \frac{1}{J_M}l_1 - \frac{1}{J_L}l_2 \end{bmatrix} \quad (7.11)$$

In the same way, the block diagram shown in Fig. 7.1(b) is derived through equivalent conversion. The variable β_K in Fig. 7.1(b) is defined as follows;

$$\beta_K = J_{Ln}\frac{l_3}{l_2}s. \quad (7.12)$$

α_M and β_K determine the ratio between $\hat{T}_{sM}$, $\hat{T}_{sK}$, and the measured joint torque T_s by the sensor as follows;

$$\hat{T}_s = \alpha_M\hat{T}_{sM} + \beta_K\hat{T}_{sK} + (1 - \alpha_M - \beta_K)T_s. \quad (7.13)$$

β_K indicates how much the torsional information is used. In designing β_K, the observer gain l_3 can be used.

The relationship between the observer gains and modeling errors are confirmed through the analyses with modeling errors. Here, the dynamics of the observer error are expressed as below;

$$\begin{aligned} \dot{e} = -\frac{1}{J_{Ln}}l_2e - \Delta J_L l_2 d_L - l_1\Delta J_M T_M \\ + \begin{bmatrix} e_1 & e_2 & e_3 \end{bmatrix} \begin{bmatrix} \omega_M \\ \omega_L \\ T_s \end{bmatrix}, \end{aligned} \quad (7.14)$$

$$e_1 = \left(\frac{\Delta D_M}{J_{Mn}} + D_{Mn}\Delta J_M + \Delta J_M\Delta D_M\right)l_1 + \Delta K l_3, \quad (7.15)$$

$$e_2 = \left(\frac{\Delta D_L}{J_{Ln}} + D_{Ln}\Delta J_L + \Delta J_L\Delta D_L\right)l_2 - \Delta K l_3, \quad (7.16)$$

$$e_3 = \Delta J_M l_1 - \Delta J_L l_2. \quad (7.17)$$

The equations indicate that the motor-side parameter error and the transmission parameter error are related only to the two observer gains l_1 and l_3, respectively. However, the load-side parameter error depends only on l_2, which means that l_1 and l_3 cannot have any influences on the robustness to the load-side parameters. In the framework of the state observer for load-side external torque estimation, it has become clear that there is an inevitable trade-off between the load-side parameter error effect and the estimation bandwidth even with a joint torque sensor.

7.3.2 Gain evaluation through simulations and experiments

Simulations and experiments without using a joint torque sensor is conducted. In analyses, there are no motor disturbance during simulations, i.e., $d_M = 0$, and no nonlinearity in the transmission mechanisms. The cutoff frequency of $Q(s)$ was experimentally determined to be 150 Hz.

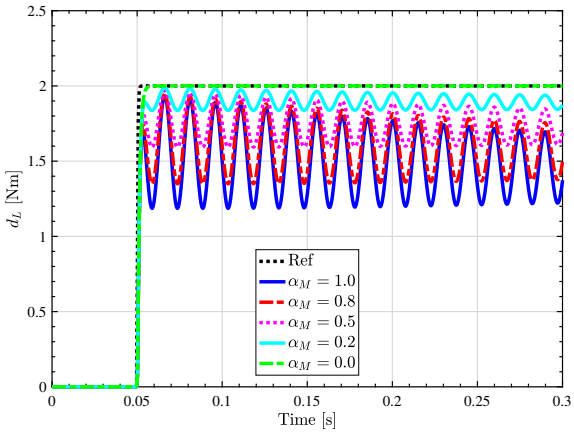

(a) Case1:$J_M = 1.5J_{Mn}$, $D_M = 1.5D_{Mn}$ with various α_M.

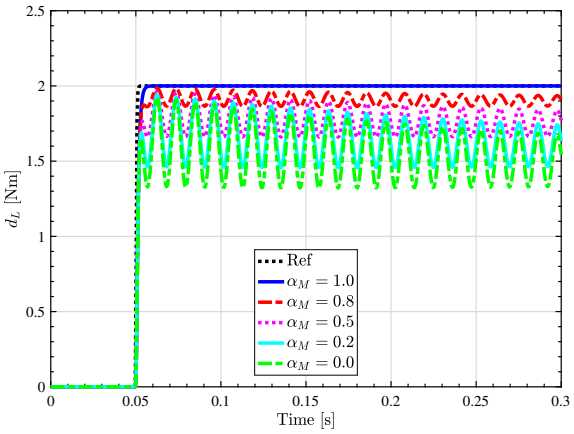

(b) Case2:$K = 1.5K_n$ with various α_M.

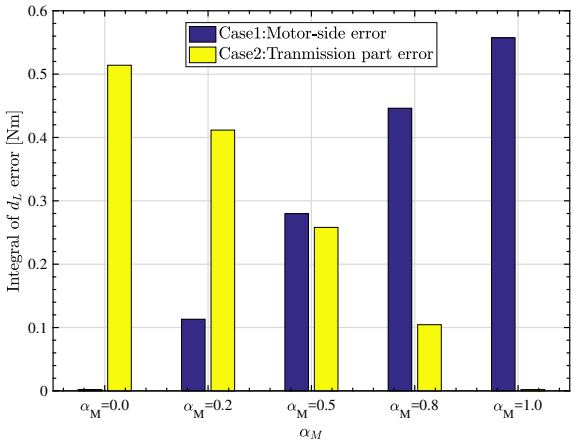

(c) Comparison of the integral of the estimation errors in the left two cases.

Figure 7.2 Comparison of the errors when $JM = 1.5J_{Mn}$ and $D_M = 1.5D_{Mn}$, or $K = 1.5K_n$, with various α_M.

Theoretical analyses indicate a sensitivity tradeoff between motor and transmission modeling errors depending on α_M. Figure 7.2(a) shows the estimated external torque responses when the motor has modeling errors ($J_M = 1.5J_{Mn}$, $D_M = 1.5D_{Mn}$) for a 2.0 N·m torque step applied to d_L at 0.050 s, as indicated in the black dotted line. When $\alpha_M = 0$, the estimated response shows an ideal low pass characteristic without deterioration by modeling errors of motor parameters. Figure 7.2(a) shows that the estimation accuracy increases for smaller values of α_M. Figure 7.2(b) shows the estimated external torque when the transmission has modeling errors ($K = 1.5K_n$). When $\alpha_M = 1$, the estimated response shows an ideal low pass characteristic without deterioration by modeling errors of transmission parameters, and the estimation accuracy increases as α_M approaches 1. Figure 7.2(c) shows the estimation errors in Figs. 7.2(a) and 7.2(b). The vertical axis in Fig. 7.2(c) corresponds to the one-second integral of the estimation error, i.e., $\int_{0.050}^{1.050}(d_{LRef} - \hat{d}_L)dt$, and d_{LRef} is the input load-side external torque denoted as Ref in Figs. 7.2(a) and 7.2(b). Clearly, small α_M values reduce the influence of

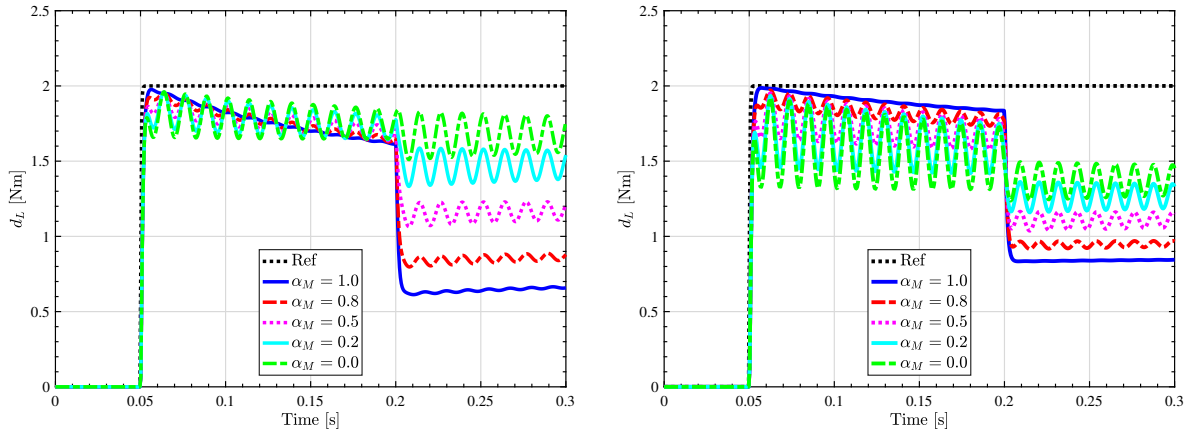

(a) Larger error in motor side than transmission part: $D_M = 1.5D_{Mn}$, $K = 1.2K_n$.

(b) Larger error in transmission part than motor side: $D_M = 1.2D_{Mn}$, $K = 1.5K_n$.

Figure 7.3 Simulation comparison of load-side external torque responses in two cases, and -1.0 N·m step d_M is input at 0.20 s with various α_M.

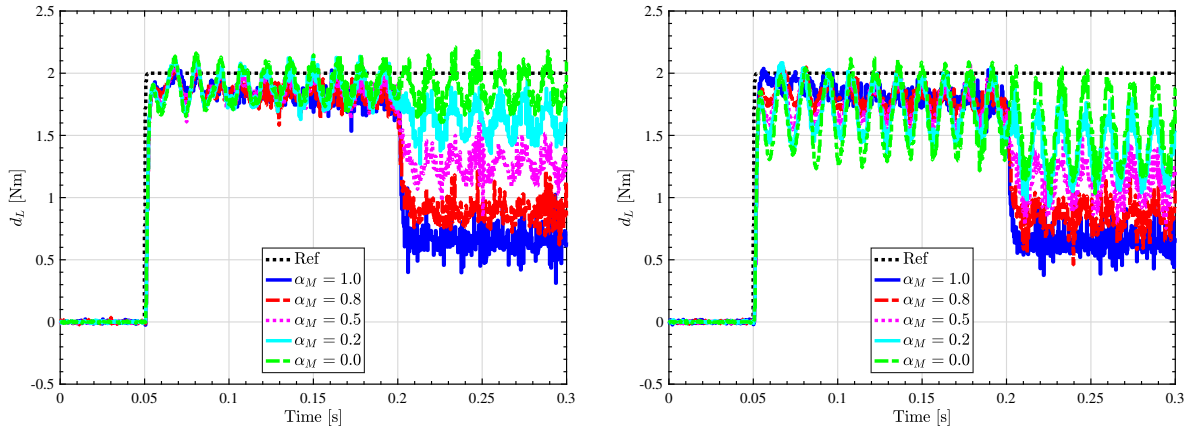

(a) Larger error in motor side than transmission part: $D'_{Mn} = D_{Mn}/1.5$, $K'_n = K_n/1.2$.

(b) Larger error in transmission part than motor side:$D'_{Mn} = D_{Mn}/1.2$, $K'_n = K_n/1.5$.

Figure 7.4 Experimental comparison of load-side external torque responses in two cases, and -1.0 N·m step d_M is input at 0.20 s with various α_M.

motor model errors, and α_M approaching 1 reduces the influence of transmission model errors.

In practice, every plant parameter has errors, and in some cases the transmission model can be assumed to present either smaller or larger errors than the motor model. Then, α_M can be selected for more accurate estimation considering the balance between the model parameter errors between the motor and transmission. Figure 7.3(a) shows the estimated torque when larger modeling error is attributed to the motor than to the transmission model. Specifically, +50% error is set to the motor viscosity and +20% error to the torsional rigidity (i.e., $D_M = 1.5D_{Mn}$, $K = 1.2K_n$). Moreover, a -0.50 N·m step motor torque disturbance is applied at 0.20 s. As a large modeling error is given to the motor parameters, better responses are obtained as α_M approaches 0. In fact, small α_M values retrieve a gradual decrease by D_M error, and the effect of the sudden decrease by d_M is mitigated

for the estimated external torque. In contrast, vibration induced by the torsional rigidity modeling error increases for small α_M values. Figure 7.3(b) shows the torque estimation when larger modeling error is attributed to the transmission than to the motor model. Hence, +20% error is set to the motor viscosity and +50% error to the torsional rigidity (i.e., $D_M = 1.2D_{Mn}$, $K = 1.5K_n$). The graph confirms that the estimation accuracy improves as α_M approaches 1. The simulation results suggest that the proposed load-side external torque observer enables more accurate estimation than conventional observers provided that gain α_M is adequately designed.

The simulation results shown in Figs. 7.3(a) and 7.3(b) are confirmed through experiments. The designed observer was discretized by the Tustin transformation with sampling frequency of 2.5 kHz and load-side external torque d_L input by the load-side motor. Modeling error was introduced by varying the observer parameters (e.g., $D'_{Mn} = D_{Mn}/1.5$) instead of the plant parameters. Therefore, the conditions in the experiments are different from those of the simulations, but similar results were expected.

Figure 7.4(a) shows the estimated response when $D'_{Mn} = D_{Mn}/1.5$ and $K'_n = K_n/1.2$. The large modeling error on the motor-side parameters makes the estimation accuracy improve as α_M approaches 0. When $\alpha_M = 0$, both the decrease in the estimated torque caused by modeling error in D_M and the influence of d_M at 0.20 s are removed. Figure 7.4(b) shows the estimated torque when $D'_{Mn} = D_{Mn}/1.2$ and $K'_n = K_n/1.5$. As expected, the estimation accuracy improves as α_M approaches 1 because a larger error is present in the transmission model. In both cases, the experimental results confirm the simulation outcomes, thus validating the proposed observer.

7.4 Proposed minimum variance estimation

7.4.1 Gain design for minimum variance estimation

In the previous section, it is demonstrated that the estimation accuracy can be changed according to the value of the gain and the accuracy of plant parameters. Instead of manual adjustment, a systematic design for the gain is more suitable in practical settings. In this section, a gain design method is proposed to minimize the variance for estimating d_L assuming that the range of plant parameter variations is known. This is a valid assumption as a variation from the nominal values of plant parameters (e.g., motor inertia moment, viscosity, and torsional rigidity change up to ±5%, ±30%, and ±20%, respectively) can be often assumed. To determine α_M, it is also assumed that the plant parameters follow a Gaussian probability distribution and are independent from each other. Each distribution has mean μ, which is equal to the nominal value of the parameter, and variance σ^2, which depends on the reliability of each parameter. For instance, if the torsional rigidity is assumed to

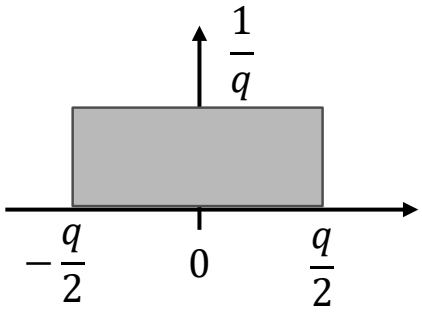

Figure 7.5 Probability distribution of quantization error with quantization step of q.

change from 0.80 to 1.20 of the nominal value within 99.7% probability, variance σ^2 can be obtained as $3\sigma^2$=0.20μ.

In the proposed observer, d_L is estimated as;

$$\hat{d}_L = (J_{Ln}s + D_{Ln})\omega_L - \alpha_M \hat{T}_{sM} - (1-\alpha_M)\hat{T}_{sK}. \tag{7.18}$$

and α_M should be designed to minimize the variance of $\hat{d}_L$. The estimation variance can be calculated as;

$$\begin{aligned}\sigma^2_{\hat{d}_L} &= \sigma^2_L + \alpha_M^2\sigma^2_{\hat{T}_{sM}} + (1-\alpha_M)^2\sigma^2_{\hat{T}_{sK}} \\ &= (\sigma^2_{\hat{T}_{sM}} + \sigma^2_{\hat{T}_{sK}})\left(\alpha_M - \frac{\sigma^2_{\hat{T}_{sK}}}{\sigma^2_{\hat{T}_{sM}} + \sigma^2_{\hat{T}_{sK}}}\right)^2 + \frac{\sigma^2_{\hat{T}_{sM}}\sigma^2_{\hat{T}_{sK}}}{\sigma^2_{\hat{T}_{sM}} + \sigma^2_{\hat{T}_{sK}}} + \sigma^2_L,\end{aligned} \tag{7.19}$$

where $\sigma^2_{\hat{d}_L}$, σ^2_L, $\sigma^2_{\hat{T}_{sM}}$, and $\sigma^2_{\hat{T}_{sK}}$ are the variances of d_L, load-side, motor-side, and transmission-part estimations, respectively. Equation (7.19) indicates that $\sigma^2_{\hat{d}_L}$ can be minimized using the following α_M;

$$\alpha_M = \frac{\sigma^2_{\hat{T}_{sK}}}{\sigma^2_{\hat{T}_{sM}} + \sigma^2_{\hat{T}_{sK}}}. \tag{7.20}$$

Then, $\sigma^2_{\hat{T}_{sM}}$ and $\sigma^2_{\hat{T}_{sK}}$ can be calculated by linear approximation of (7.2) and (7.3);

$$\sigma^2_{\hat{T}_{sM}} = \dot{\omega}_M^2\sigma^2_{J_M} + \omega_M^2\sigma^2_{D_M} + J^2_{Mn}\sigma^2_{\dot{\omega}_M} + D^2_{Mn}\sigma^2_{\omega_M} + \sigma^2_{d_M}, \tag{7.21}$$

$$\sigma^2_{\hat{T}_{sK}} = (\theta_M - \theta_L)^2\sigma^2_K + K_n^2\sigma^2_{\theta_M} + K_n^2\sigma^2_{\theta_L}, \tag{7.22}$$

where $\sigma^2_{J_M}$, $\sigma^2_{D_M}$, σ^2_K, and $\sigma^2_{d_M}$ are the variances of the corresponding parameter, and $\sigma^2_{\theta_M}$, $\sigma^2_{\theta_L}$, $\sigma^2_{\omega_M}$, and $\sigma^2_{\dot{\omega}_M}$ are the measurement variances, which are caused by the quantization error from the encoder.

The probability distribution of quantization error is uniform distribution as shown in Fig. 7.5. In the calculation of the variance of the estimated external torque (7.19), the required assumption is that each probability distribution is independent from each other. Therefore, though the derived

probability distribution of the estimation is not a Gaussian probability distribution, minimum variance estimation can be achieved even if the encoder quantization error does not follow a Gaussian probability distribution.

When the resolution of the encoder is q, the variance of the quantization error is calculated as;

$$\sigma^2(q) = \int_{-\frac{q}{2}}^{\frac{q}{2}} \frac{1}{q} x^2 dx = \frac{q^2}{12}. \tag{7.23}$$

When the angular velocity and angular acceleration are obtained by backward difference, their resolutions are calculated as $\omega_{res}(q) = \frac{q}{T_s}$ and $\dot{\omega}_{res}(q) = \frac{q}{T_s^2}$, respectively, where T_s is the sampling time. Therefore, the variances of the encoder measurements can be calculated by substituting the resolutions into (7.23).

The proposed method can be extended to introduce a joint torque sensor, whose block diagram is shown in Fig. 7.1(b). The sensor is robust against modeling errors but suffers from noise. Therefore, combining the three obtained joint torques, $\hat{T}_{sM}$, $\hat{T}_{sK}$, and T_{sS}, can improve the estimation accuracy. Gains α_M and β_K can be designed to minimize the variance of the estimated d_L.

The noise of the joint torque sensor is also assumed to follow a Gaussian probability distribution. In the proposed observer with the sensor, d_L is estimated as;

$$\hat{d}_L = (J_{Ln}s + D_{Ln})\omega_L - \alpha_M \hat{T}_{sM} - \beta_K \hat{T}_{sK} - (1 - \alpha_M - \beta_K)T_{sS}. \tag{7.24}$$

The estimation variance can be calculated as;

$$\begin{aligned}
\sigma^2_{\hat{d}_{LS}} = {} & (\sigma^2_{\hat{T}_{sM}} + \sigma^2_{\hat{T}_{sS}}) \left(\alpha_M - \frac{\sigma^2_{\hat{T}_{sS}}}{\sigma^2_{\hat{T}_{sM}} + \sigma^2_{\hat{T}_{sS}}} (1 - \beta_K) \right)^2 \\
& + \frac{\sigma^2_{\hat{T}_{sM}} \sigma^2_{\hat{T}_{sK}} + \sigma^2_{\hat{T}_{sK}} \sigma^2_{\hat{T}_{sS}} + \sigma^2_{\hat{T}_{sS}} \sigma^2_{\hat{T}_{sM}}}{\sigma^2_{\hat{T}_{sM}} + \sigma^2_{\hat{T}_{sS}}} \left(\beta_K - \frac{\sigma^2_{\hat{T}_{sS}} \sigma^2_{\hat{T}_{sM}}}{\sigma^2_{\hat{T}_{sM}} \sigma^2_{\hat{T}_{sK}} + \sigma^2_{\hat{T}_{sK}} \sigma^2_{\hat{T}_{sS}} + \sigma^2_{\hat{T}_{sS}} \sigma^2_{\hat{T}_{sM}}} \right)^2 \\
& + \frac{\sigma^2_{\hat{T}_{sM}} \sigma^2_{\hat{T}_{sK}} \sigma^2_{\hat{T}_{sS}}}{\sigma^2_{\hat{T}_{sM}} \sigma^2_{\hat{T}_{sK}} + \sigma^2_{\hat{T}_{sK}} \sigma^2_{\hat{T}_{sS}} + \sigma^2_{\hat{T}_{sS}} \sigma^2_{\hat{T}_{sM}}} + \sigma^2_L,
\end{aligned} \tag{7.25}$$

where $\sigma^2_{\hat{d}_{LS}}$ and $\sigma^2_{T_{sS}}$ are the variance of d_L estimation with joint torque sensor and that of the sensor measurement, respectively. Therefore, $\sigma_{\hat{d}_{LS}}$ can be minimized using the following α_M and β_K;

$$\alpha_M = \frac{\sigma^2_{\hat{T}_{sK}} \sigma^2_{\hat{T}_{sS}}}{\sigma^2_{\hat{T}_{sM}} \sigma^2_{\hat{T}_{sK}} + \sigma^2_{\hat{T}_{sK}} \sigma^2_{\hat{T}_{sS}} + \sigma^2_{\hat{T}_{sS}} \sigma^2_{\hat{T}_{sM}}}, \tag{7.26}$$

$$\beta_K = \frac{\sigma^2_{\hat{T}_{sS}} \sigma^2_{\hat{T}_{sM}}}{\sigma^2_{\hat{T}_{sM}} \sigma^2_{\hat{T}_{sK}} + \sigma^2_{\hat{T}_{sK}} \sigma^2_{\hat{T}_{sS}} + \sigma^2_{\hat{T}_{sS}} \sigma^2_{\hat{T}_{sM}}}. \tag{7.27}$$

Comparing the proposed method with and without joint torque sensor shows that the variance of

Table 7.1 Sensor configurations in six estimation methods.

	motor-side encoder	load-side encoder	joint torque sensor
Only motor-side encoder estimation	✓		
Motor-side estimation	✓	✓	
Transmission-part estimation	✓	✓	
Prop. w/o torque sensor	✓	✓	
Torque-sensor-based estimation		✓	✓
Prop. w/i torque sensor	✓	✓	✓

the estimated d_L always reduces using the joint torque sensor;

$$\begin{aligned}\sigma^2_{\hat{d}_L} - \sigma^2_{\hat{d}_{LS}} &= \frac{\sigma^2_{\hat{T}_{sS}}\sigma^2_{\hat{T}_{sM}}}{(\sigma^2_{\hat{T}_{sM}} + \sigma^2_{\hat{T}_{sK}})(\sigma^2_{\hat{T}_{sM}}\sigma^2_{\hat{T}_{sK}} + \sigma^2_{\hat{T}_{sK}}\sigma^2_{\hat{T}_{sS}} + \sigma^2_{\hat{T}_{sS}}\sigma^2_{\hat{T}_{sM}})} \\ &> 0. \end{aligned} \tag{7.28}$$

Note that besides the variance reduction, the estimation accuracy is not influenced by the error of nominal parameters when using a joint torque sensor, as T_{sS} can be obtained with robustness against modeling errors of the nominal parameters.

7.4.2 Minimum variance evaluation through simulations

The simulations and experiments for minimum variance estimation considered six methods: only motor-side encoder estimation, motor-side estimation, transmission-part estimation, proposed estimation without joint torque sensor, torque-sensor-based estimation, and proposed estimation with joint torque sensor. The load-side external torque can be estimated only using the motor-side encoder by implementing the state observer. Assuming a stepwise load external torque $\dot{d}_L = 0$, it can be estimated from the augmented state vector. Given that the state observer using only the motor-side encoder requires all plant parameters, it is severely affected by modeling errors. The sensor configurations for the six evaluated methods are listed in Tab. 7.1. To compare the performance of each method, we evaluated the variance and L_2 norm error of the load-side external torque through simulations. The L_2 norm error is analyzed to evaluate the robustness against the nominal model error (i.e., μ error in Gaussian probability distribution). A 1.0 N·m step load-side external torque was input to the six estimation methods undergoing plant parameter variations. Simulation is conducted 10000 times, and the variance and L_2 norm error of the load-side external torque are averaged.

The motor and transmission model parameters were randomly chosen from their probability distribu-

tions in each simulation, and the joint torque sensor measurement noise also followed the corresponding Gaussian probability distribution. The $3\sigma^2$ plant parameter variation in the simulated plant is given as follows: J_M:±5%, D_M:±50%, K:±30%, d_M:±0%. The variances of plant parameters, $\sigma^2_{J_M}$, $\sigma^2_{D_M}$, σ^2_K, and $\sigma^2_{d_M}$, in α_M and β_K design were based on these variations, and those of encoder measurements, $\sigma^2_{\theta_M}$, $\sigma^2_{\theta_L}$, $\sigma^2_{\omega_M}$, and $\sigma^2_{\dot{\omega}_M}$, were given for a 20-bit resolution according to (7.23). In addition, the variance of the torque sensor was determined assuming that 99.7% of the torque sensor noise lies within the 1.0% of the rated measurable torque (20 N·m). Therefore, $3\sigma^2_{T_{sS}} = 20 \cdot 0.010$.

Table 7.2 lists the estimation performance of the six evaluated methods. In the estimation based only on the motor-side encoder, the variance and error of the estimated torque are much larger than those from the other methods, thus indicating the clear advantage of applying a load-side encoder for external torque estimation. In the proposed method without joint torque sensor, the variance reduces compared to both the motor-side and transmission-part estimation, despite the sensor configurations of the three methods being the same. The proposed method without torque sensor can reduce the variance and L_2 norm error by using the plant parameter and measurement information (i.e., the variance of the Gaussian probability distribution). Compared with the torque-sensor-based estimation, the variance in the proposed method is larger, because the variance of the torque sensor measurement was small in this simulation.

When the system has a joint torque sensor, the proposed method further reduces the estimation variance to the smallest value among the evaluated methods. Still, regarding the L_2 norm error, our method is inferior to the torque-sensor-based estimation, because the proposed method determines gains α_M and β_K that minimize the variance instead of the L_2 norm error. Moreover, as the model parameters of the motor and transmission (J_M, D_M, and K) varied during simulation, the torque-sensor-based estimation retrieves a smaller L_2 norm error as it is not influenced by the parameter variation. In practice, however, the torque sensor measurements do not follow the Gaussian probability distribution by the presence of offset, drift, and hysteresis, resulting in deterioration of the estimation accuracy. The experimental results presented in the sequel show this deterioration by unmodeled effects of the torque sensor.

7.4.3 Minimum variance evaluation through experiments

During the experiments to evaluate minimum variance estimation, the nominal plant parameters of the two-inertia system motor bench in chapter 2 is used for the observers. To select α_M and β_K, the variances of the plant parameters, $\sigma^2_{J_M}$, $\sigma^2_{D_M}$, σ^2_K, and $\sigma^2_{d_M}$, were set to $3\sigma^2$ of the parameters: J_M:±1%, D_M:±10%, K:±20%, and d_M:±0%. The variance of the joint torque sensor was determined based on the assumption that 99.7% of its noise lies within the 0.050% of the rated measurable torque.

Table 7.2 Statistical analyses in simulations.

	Variance	L_2 norm error
Only motor-side encoder	8.8e-3	1.1e+2
Motor-side	1.2e-3	3.0e+1
Transmission-part	1.5e-3	4.4e+1
Prop. w/o torque sensor	1.0e-3	1.8e+1
Torque-sensor-based	9.8e-4	9.8
Prop. w/i torque sensor	9.4e-4	1.4e+1

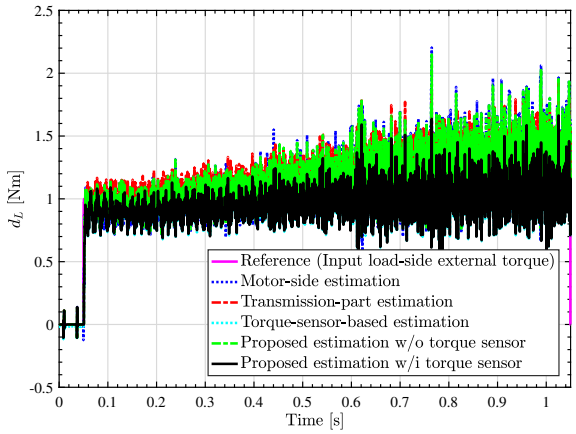

Figure 7.6 Comparison of estimation performance in experiments.

In addition, we removed the offset of the joint torque sensor measurements and applied a 1.0 N·m step load-side external torque for 1.0 s.

Figure 7.6 shows the comparison of the estimation performance. In Fig. 7.6, the response of only motor-side encoder estimation is not shown because the response is too noisy. The variance and L_2 norm error of the proposed estimation method are listed in Tab. 7.3. The tendency of the experimental results is similar to that of the simulation results shown in Tab. 7.2. Using only the motor-side encoder, it is difficult to determine an accurate estimation. Still, the proposed methods show the smallest variance and errors for the same sensor configuration. Unlike simulation, the L_2 norm error of the proposed method with joint torque sensor was smaller than that of the torque-sensor-based estimation in the experiments. This opposite trend is likely to be caused by the nonlinearities of the torque sensor signal. Although the real measurements from the joint torque sensor deteriorate the estimation accuracy, the proposed method improves estimation by combining the information from both encoders.

Table 7.3 Experimental results.

	Variance	L_2 norm error
Only motor-side encoder	0.959	5.96e+3
Motor-side	0.219	4.21e+2
Transmission-part	0.226	4.49e+2
Prop. w/o torque sensor	0.218	4.07e+2
Torque-sensor-based	0.148	1.43e+2
Prop. w/i torque sensor	0.147	1.39e+2

7.5 Conclusion

By analyzing the minimal-order observer for load-side external torque estimation, a novel observer is proposed. The proposed method combines two conventional observers for increased estimation accuracy by considering the modeling and measurement errors in the motor and transmission of a two-inertia system. Furthermore, a load-side external torque observer considering a joint torque sensor, which notably improves the robustness against modeling errors is proposed. Then, for minimum variance estimation of load-side external torque, it is derived that a systematic design for the observer gains based on the variance of the plant parameters and measurements. Simulation and experimental results verify the high performance of the proposed observers compared to similar methods.

Chapter 8

Conclusion

This dissertation proposed the control methods for a two-inertia system using load-side information effectively. Thanks to their versatilities, the proposed control methods can be applied to various industrial devices. The performance of the all control methods are evaluated by the simulations and the experiments, and thus they are validated as the practical solutions.

In chapter 3, studies on load-side position control conducted from the three viewpoints, vibration suppression control, backlash compensation, and simplification of controller design are described in detail. In the study on vibration suppression control and simplification of control design, the same performance is realized by only the high-resolution load-side encoder compared with the conventional control methods using both the motor- and load-side encoders. It is an academically innovative research that overturns conventional common sense that both the motor- and load-side information are required for two-inertia system control with high bandwidth. However, it is still challenging to use jerk for FB, which requires the LPF, though high-resolution encoder is used. The induced delay prohibits from achieving high control bandwidth. Therefore, a novel method to obtain high order state variable with accuracy and less delay is highly required. This future work is very important for motion control field. Regarding backlash compensation study, attenuation of the collision caused by backlash is focused. The overshoot of position response becomes larger with the conventional collision mitigation method. There is a trade-off between the control performance and the collision mitigation amount. Based on a detailed discussion on the physical phenomenon, relaxation of the trade-off is successfully achieved by applying a novel switching controller. The future work is global stability analyses of the switching controller and the plant model with deadzone in a piecewise affine model framework.

In chapter 4, load-side acceleration control is described. An automobile can be regarded as a two-inertia system in which a vehicle body side (sprung) and a wheel side (unsprung mass) are connected by a flexible transmission part (suspension). In an in-wheel motor vehicle, which has a motor as a

driving source in an unsprung mass, the unsprung mass is the motor side and the sprung mass is the load side. In order to improve the ride comfort and the motion performance, a novel acceleration control that suppresses longitudinal vibration of the body is proposed. Longitudinal vibration is difficult to suppress due to its higher frequency than that of vertical vibration unless it is an in-wheel motor vehicle that has a high frequency control bandwidth. Therefore, there are limited studies on longitudinal vibration suppression yet. In this study, based on accurate frequency characteristic measurements of the experimental vehicle, a novel control method considering not only the longitudinal mode but also the rotational mode by the gear in the in-wheel motor unit is proposed. The effectiveness is validated through the experimental in-wheel motor vehicle. In this study, the driving force which is determined by the function of the slip ratio is approximated by the value calculated by dividing the motor torque by the tire radius. In order to further improve the performance, the driving force control is necessary to consider slip effects. Also, though this study focuses on the longitudinal dynamics, the IWM simultaneously generates the longitudinal force and the vertical force. Therefore, the novel model and the control method considering the interference between the longitudinal and the vertical dynamics are required for better motion performance and ride comfort.

In chapter 5, joint torque control is discussed. With the advent of cooperative robots in the market, attention to force control is rapidly increasing, which requires high performance to force control. This chapter shows that the load-side encoder which is starting to be widely used in industry to improve load-side positioning accuracy can be effectively used also in force control. By using the load-side information, it becomes possible to explicitly compensate for the backlash inherent in the gears, and precise joint torque control is realized. The proposed joint torque control can be applied to automobiles. In the geared EVs, the sound caused by backlash collision is a big problem. This backlash compensation control method can reduce the sound and mechanical wear caused by backlash collision in the reversal points of acceleration and deceleration.

In chapter 6, torsional angle control is studied. It is possible to improve back drivability by precise control of the torsional angle effectively utilizing the load-side information. Back drivability is an index of how light it feels when applying force from the load side and it is indispensable for interactive operation with human beings in cooperative robots. A proposed control method is a novel technique for improving back drivability by actively using backlash, which is widely known as a cause of performance deterioration in the control of two-inertia systems. Considering the situation where the controlled object contacts with the environment such as human beings, this study quantitatively evaluates how much the performance difference is caused by the presence or absence of the load-side encoder from the viewpoint of human-friendly motion control through simulations and experiments.

In chapter 7, load-side external torque estimation is described. For cooperative robots, machine

Table 8.1 How to deal with backlash.

Objective	Backlash compensation method	Where to read details
Load-side position control with impact attenuation	Switching damping addition	Chapter 3.3
Precise Joint torque control	Inverse-model-based compensation	Chapter 5
High backdrivable control	Synchronous position control within backlash width	Chapter 6

tools, automobiles, etc., there is a demand to monitor torques externally applied to the systems, and their performance can be improved by monitoring. By effectively utilizing the load-side information, it is possible to estimate robustly against modeling and measurement errors of two-inertia system plant parameters, as compared with the conventional estimation methods. Furthermore, when assuming the distribution of parameters and sensor noise as a normal distribution, a optimal design method in which the variance of the estimated external torque theoretically becomes the minimum is proposed with the validations through simulations and experiments.

The geared industrial devices often suffer from backlash. Therefore, the control methods proposed in this dissertation compensate backlash effectively, but in different ways. The backlash compensation methods are listed in Tab. 8.1 according to the objectives. Load-side position control with backlash impact attenuation is realized by the switching damping addition control as described in chapter 3.3. Precise joint torque control even with backlash is achieved by the inverse model based compensation as described in chapter 5. By using the load-side information effectively, the backlash nonlinearity is extracted to compensate in a FF way. For a high backdrivable control, inherent backlash is actively used in chapter 6. This novel method does not require external input force estimation, which leads high robustness.

This dissertation proposes the control methods for all control variables in a two-inertia system, which use load-side encoder information effectively. The performance of the methods is evaluated through the experiments, validating their practical uses in industrial devices. The series of studies provide a general framework of two-inertia system control using load-side information.

In the near future, the two industrial trends (higher required accuracy and lower cost of high-resolution encoders) are expected to accelerate. The spread use of load-side encoder strongly requires new control methods using load-side information effectively. All the control methods proposed in this dissertation respond to the requests from industry, and their importance will increase in the future.

References

[1] T. T. Phuong, K. Ohishi, C. Mitsantisuk, Y. Yokokura, K. Ohnishi, R. Oboe, and A. Sabanovic: "Disturbance Observer and Kalman Filter Based Motion Control Realization", *IEEJ J. Ind. Appl.*, Vol. 7, No. 1, pp. 1–14 (2018)

[2] T. Yoshioka, A. Yabuki, Y. Yokokura, K. Ohishi, T. Miyazaki, and T. T. Phuong: "Stable Force Control of Industrial Robot Based on Spring Ratio and Instantaneous State Observer", *IEEJ J. Ind. Appl.*, Vol. 5, No. 2, pp. 132–140 (2016)

[3] T. T. Phuong, K. Ohishi, Y. Yokokura, and C. Mitsantisuk: "FPGA-Based High-Performance Force Control System With Friction-Free and Noise-Free Force Observation", *IEEE Trans. Ind. Electron.*, Vol. 61, No. 2, pp. 994–1008 (2014)

[4] Y. Yamada and Y. Kakinuma: "Sensorless cutting force estimation for full-close controlled ball-screw-driven stage", *The Int. J. Advanced Manufacturing Technology*, Vol. 87, No. 9, pp. 3337–3348 (2016)

[5] Y. Ohba, M. Sazawa, K. Ohishi, T. Asai, K. Majima, Y. Yoshizawa, and K. Kageyama: "Sensorless Force Control for Injection Molding Machine Using Reaction Torque Observer Considering Torsion Phenomenon", *IEEE Trans. Ind. Electron.*, Vol. 56, No. 8, pp. 2955–2960 (2009)

[6] S. Katsura and K. Ohnishi: "Force Servoing by Flexible Manipulator Based on Resonance Ratio Control", *IEEE Trans. Ind. Electron.*, Vol. 54, No. 1, pp. 539–547 (2007)

[7] K. Daisuke, Y. Kakinuma, and S. Katsura: "Sensorless Cutting Force Control using Parallel Disturbance Observer", *JSME The 5th International Conference on Leading Edge Manufacturing in 21st Century*, LEM21-OSAKA (2009)

[8] C. Mitsantisuk, M. Nandapaya, K. Ohishi, and S. Katsura: "Design for Sensorless Force Control of Flexible Robot by Using Resonance Ration Control Based on Coefficient Diagram Method", *Automatika*, Vol. 54, No. 1, pp. 62–73 (2013)

[9] Y. Asai, Y. Yokokura, and K. Ohishi: "Fine Force Reproduction of Environmental Haptic Sensations Based on Momentum Control", *IEEE Trans. Ind. Electron.*, Vol. 63, No. 7, pp. 4304–4313 (2016)

[10] T. Tsuji, T. Seki, and S. Sakaino: "Intrinsic Contact Sensing for Touch Interface With Movable

Structure", *IEEE Trans. Ind. Electron.*, Vol. 64, No. 9, pp. 7342–7349 (2017)

[11] S. Fukushima, H. Sekiguchi, Y. Saito, W. Iida, T. Nozaki, and K. Ohnishi: "Artificial Replacement of Human Sensation Using Haptic Transplant Technology", *IEEE Trans. Ind. Electron.*, Vol. 65, No. 5, pp. 3985–3994 (2018)

[12] G. B. Avanzini, N. M. Ceriani, A. M. Zanchettin, P. Rocco, and L. Bascetta: "Safety Control of Industrial Robots Based on a Distributed Distance Sensor", *IEEE Trans. Control Syst. Technol.*, Vol. 22, No. 6, pp. 2127–2140 (2014)

[13] K. Szabat and T. Orlowska-Kowalska: "Vibration Suppression in a Two-Mass Drive System Using PI Speed Controller and Additional Feedbacks—Comparative Study", *IEEE Trans. Ind. Electron*, Vol. 54, No. 2, pp. 1193–1206 (2007)

[14] K. Yuki, T. Murakami, and K. Ohnishi: "Vibration Control of a 2 Mass Resonant System by the Resonance Ratio Control", *Trans. IEE of Japan. IA*, Vol–D. 113, No. 10 (1993) (in Japanese)

[15] Y. Hori: "2-Inertia System Control using Resonance Ratio Control and Manabe Polynomials", *Trans. IEE of Japan. IA*, Vol–D. 114, No. 10 (1994) (in Japanese)

[16] F. Sakai, M. Hikizu, Y. Kamiya, and H. Seki: "Precision Positioning Which Contains Flexible Mechanical System : Fusion of Semi-closed and Full-closed Loop Control", *J. JSPE*, Vol. 66, No. 9 (2000) (in Japanese)

[17] Y. Hori: "Vibration Suppression and Disturbance Rejection Control on Torsional Systems", *Proc. of IFAC Workshop on Motion Control*, pp. 41–50 (1995)

[18] Y. Hori, H. Iseki, and K. Sugiura: "Basic consideration of vibration suppression and disturbance rejection control of multi-inertia system using SFLAC (state feedback and load acceleration control)", *IEEE Trans. Ind. Applications*, Vol. 30, No. 4, pp. 889–896 (1994)

[19] Magnescale: "Laserscale BH20", *http : //www.magnescale.com/mgs/product/BH*20*.html*, Access(20181225) (in Japanese)

[20] National Institute of Advanced industrial Science and Technology: "Ultra high precision, ultra high resolution rotary encoder", *http : //www.aist.go.jp/aist_j/press_release/pr*2014*/pr*20140423*/pr*20140423*.html*, Access(20181225) (in Japanese)

[21] K. Irie, S. Katsura, and K. Ohishi: "Wideband Motion Control by Position and Acceleration Input Based Disturbance Observer", *Trans. IEE of Japan. IA*, Vol–D. 127, No. 6 (2007)

[22] S. Sakagami, T. Kiriyama, and K. Ogiwara: "Length: High resolution technology of linear encoder", SICE, Vol. 44, No. 10, pp. 662–667 (2005) (in Japanese)

[23] S. Fujisawa: "Linear encoders applied high resolution technology which is compatible with high speed response", *Trans. IEE of Japan. IA*, Vol–D. 121, No. 8, pp. 887–893 (2001) (in Japanese)

[24] J. Hu and F. Hu: "Analysis and Design to the Asymptotic Behavior of the Semi/Full/Dual-closed Loop Feedback Position Control System", *Proc. of the SICE Annual Conference 2012*, pp. 1096–1101 (2012)

[25] M. Iwasaki, M. Kainuma, M. Yamamoto, and Y. Okitsu: "Compensation by Exact Linearization Method for Nonlinear Components in Positioning Device with Harmonic Drive Gearings", *Journal of JSPE*, Vol. 78, No. 7, pp. 624–630 (2012)

[26] M. Yamamoto, M. Iwasaki, M. Kainuma, Y. Okitsu, K. Yuki, K. Sasaki, and T. Yajima: "Compensation for Synchronous Component of Angular Transmission Errors in Harmonic Drive Gearings", *Proc. of the 11th IEEE International Workshop on Advanced Motion Control*, pp. 361–365 (2010)

[27] H. Zhang, S. Ahmed, and G. Liu: "Torque Estimation Technique of Robotic Joint with Harmonic Drive Transmission", *IEEE International Conference on Robotics and Automation (ICRA–2013)*, pp. 3034–3039 (2013)

[28] M. Iwasaki, M. Miyaji, and N.Matsui: "High-Precision Contouring Control of Table Drive System in Machine Tools Using Lost Motion Compensation", *Trans. IEE of Japan. IA*, Vol–D. 125, No. 6 (2005)

[29] Z. Jamaludin, H. Van Brussel, and J. Swevers: "Friction Compensation of an XY Feed Table Using Friction-Model-Based Feedforward and an Inverse-Model-Based Disturbance Observer", *IEEE Trans. on Industrial Electronics*, Vol. 56, No. 10, pp. 3848–3853 (2009)

[30] M. Yoshihiro and M. Iwasaki: "Initial friction compensation by disturbance observer based on rolling friction model", *Proc. of the 35th Annual Conference of the IEEE Ind. Electron Society (IECON-2009)*, pp. 3124–3129 (2009)

[31] DMGMORI Annual Report 2017, *https : //www.dmgmori.co.jp/corporate/ir/*, Access(20181225)

[32] S. Oh, K. Kong, and Y. Hori: "Design and Analysis of Force-Sensor-Less Power-Assist Control", *IEEE Trans. Ind. Electron.*, Vol. 61, No. 2, pp. 985–993 (2014)

[33] K. Nakamura, H. Fujimoto, and M. Fujitsuna: "Torque Ripple Suppression Control for PM motor considering the Bandwidth of Torque Meter", *Trans. IEE of Japan. IA*, Vol–D. 130, No. 11 (2010)

[34] T. Kawakami, K. Ayusawa, H. Kaminaga, and Y. Nakamura: "High–Fidelity Joint Drive System by Torque Feedback Control Using High Precision Linear Encoder", *IEEE International Conference on Robotics and Automation (ICRA–2010)*, pp. 3904–3909 (2010)

[35] T. Kawakami, K. Ayusawa, H. Kaminaga, C. Ott, and Y. Nakamura: "Development of Joint Driving Mechanism with Rigid Torque Sensor and its Torque Control Systems", *Proc. of the JSME Conference on Robotics and Mechatronics*, No. 08–4, pp. 1–4 (2008)

[36] S. Yamada, K, Inukai, H. Fujimoto, K. Omata, Y. Takeda, and S. Makinouchi: "Proposal of joint torque control for a two-inertia system using a load-side encoder", *Proc. IEE of Japan Technical Meeting Record*, MEC–14–157, pp. 57–62 (2014) (in Japanese)

[37] S. Murata: "Innovation by in-wheel-motor drive unit", *Vehicle System Dynamics: Int. J. Vehicle Mechanics and Mobility*, Vol. 50, No. 6, pp. 807–830 (2012)

[38] R. Pintelon, P. Guillaume, Y. Rolain, J. Schoukens, and H. Van Hamme: "Parametric identification of transfer functions in the frequency domain-a survey", *IEEE Trans. Automatic control*, Vol. 39, No. 11, pp. 2245–2260 (1994)

[39] T. Beauduin, S. Yamada, H. Fujimoto, T. Kanou, and E. Katsuyama: "Experimental Modal Analysis of Electric Vehicles with Geared In-Wheel Motor", *IEEE Int. Conf. Advanced Intelligent Mechatronics (AIM)*, pp. 541–546 (2017)

[40] S. Villwock and M. Pacas: "Time-Domain Identification Method for Detecting Mechanical Backlash in Electrical Drives", *IEEE Trans. Ind. Electron*, Vol. 56, No. 2, pp. 568–573 (2012)

[41] K. Yuki, T. Murakami, and K. Ohnishi: "Study of on-line backlash identification for PMSM servo system", *Proc. of the 38h annual conference on IEEE Industrial Electronics Society (IECON)*, pp. 2036–2042 (2012)

[42] G. Zhang and J. Furusho: "Speed Control of Two-Inertia System by PI/PID Control", *IEEE Trans. Ind. Electron*, Vol. 47, No. 3, pp. 603–609 (2000)

[43] S. Katsura and K. Ohnishi: "Vibration Control of Multi-Mass Resonant System Based on Phase-Lead Compensator", *Trans. IEE of Japan. IA*, Vol–D. 126, No. 12 (2006)

[44] Y. Hori: "2-Mass System Control based on Load-Side Acceleration Control and State Feedback", *Trans. IEE of Japan. IA*, Vol–D. 125, No. 5 (1992) (in Japanese).

[45] M. Ruderman, W. Maebashi, and M. Iwasaki: "Semi-dual Loop Control of Two-Mass Actuator System using Luenberger State Observer", *Proc. of the 39th Annual Conference of the IEEE Ind. Electron Society (IECON–2013)*, pp. 6561–6556 (2013)

[46] M. Kanematsu, H. Zhu, T. Miyajima, H. Fujimoto, Y. Hori, S. Makinouchi, and R. Kido: "Angular Acceleration Detection Method by Ultra-high Resolution Encoder with Hybrid Sampling Time for Automotive Motor application", *Proc. IEE of Japan Technical Meeting Record*, RM-13-72, LD-13-82, HCA-13-048, 2013 (in Japanese).

[47] R.J.E. Merry, M.J.G. van de Molengraft, and M. Steinbuch: "Velocity and acceleration estimation for optical incremental encoders", *Mechatronics 20*, pp. 20–26 (2010)

[48] H. Zhu and T. Sugie: "Velocity estimation of motion system based on low-resolution encoders", *ASME Trans. Journal of Dynamic System, Measurement and Control*, Vol. 135, No. 011006 (2013)

[49] M. Nordin and P. Gutman: "Controlling mechanical systems with backlash -a survey", *Automat-*

ica, 38, pp. 1633–1649 (2002)

[50] M. Nordin, J. Galic, and P. Gutman: "New models for backlash and gear play", *Int. Jour. Adaptive control and signal processing*, Vol. 11, No. 1, pp. 49–63 (1997)

[51] P. Rostalski, T. Besselmann, M. Baric, F. Van Belzen, and M. Morari: "A hybrid approach to modelling, control and state estimation of mechanical systems with backlash", *Int. Jour. Control*, Vol. 80, No. 11, pp. 1729–1740 (2007)

[52] Y. Li, A. Hansen, J. Karl Hedrick, and J. Zhang: "A receding horizon sliding control approach for electric powertrains with backlash and flexible half-shafts", *Int. Jour. Vehicle System Dynamics*, pp. 1–19 (2017)

[53] A. Formentini, A. Oliveri, M. Marchesoni, and M. Storace: "A Switched Predictive Controller for an Electrical Powertrain System With Backlash", *IEEE Trans. Power Electron.*, Vol. 32, No. 5, pp. 4036–4047 (2017)

[54] M. Johansson and A. Rantzer: "Computation of Piecewise Quadratic Lyapunov Functions for Hybrid Systems", *IEEE Trans. Autom. Control*, Vol. 43, No. 4, pp. 555–559 (1998)

[55] M. Johansson: "Piecewise Linear Control Systems", *Springer* (2003)

[56] I. Ponce, Y. Orlov, L. Aguilar, and J. Alvarez: "Nonsmooth H_∞ synthesis of non-minimum-phase servo-systems with backlash", *Control Engineering Practice*, Vol. 46, pp. 77–84 (2016)

[57] A. Azenha and J. A. T. Machado: "Variable structure control of robots with nonlinear friction and backlash at the joints", *Proc. IEEE Int. Conf. Robotics and Automation*, pp. 366–371 (1996)

[58] M. Itoh: "Suppression of Transient Vibration for Geared Mechanical System with Backlash Using Model-Based Control", *JSME Int. Jour. Series C Mechanical Systems, Machine Elements and Manufacturing*, Vol. 47, No. 1, pp. 327–334 (2004)

[59] M. Odai and Y. Hori: "Speed control of 2-inertia system with gear backlash using gear torque compensator", *IEEE Int. Workshop Adv. Motion Control*, pp. 234–239 (1998)

[60] M. Yang, D. Xu, W. Zheng, and X. Lang: "Shaft Torque Limiting Control Using Shaft Torque Compensator for Two-Inertia Elastic System With Backlash", *IEEE/ASME Trans. Mechatronics*, Vol. 21, No. 6, pp. 2902–2911 (2016)

[61] C. Ma and Y. Hori: "Fraction-Order Control: Theory and Applications in Motion Control", *IEEE Industrial Electronics Magazine*, Vol. 1, No. 4, pp. 6–16 (2007)

[62] M. Odai and Y. Hori: "Controller Design Robust to Nonlinear Elements based on Fractional Order Control System", *Trans. IEE of Japan. IA*, Vol–D. 120, No. 1, pp. 11–18 (2000) (in Japanese)

[63] M. Yang, Y. Fu, X. Lv, and D. Xu: "Mechanical Resonance Suppression in Servo System Based on The Fractional Order Low-Pass Filter", *9th Int. Conf. Power Electronics ECCE Asia*, pp. 594–599 (2015)

[64] J. Y. Hung: "Control of Industrial Robots that Have Transmission Elasticity", *IEEE Trans. Ind. Electron.*, Vol. 38, No. 6, pp. 421–427 (1991)

[65] S. Hedlund and M. Johansson: "A toolbox for computational analysis of piecewise linear systems", *Proc. of European Control Conf. (ECC)*, pp. 4578–4583 (1999)

[66] K. Sakata, H. Fujimoto, and K. Saiki: "Design of Feedback Control for Robustness of Resonance Mode using Multiple Sensors for High-Precision Gantry Stage", *Proc. of IEE of Japan Technical Meeting Record*, IIC–11–065, pp. 43–48 (2011) (in Japanese)

[67] Y. Seki, H. Fujimoto, and K. Saiki: "Optimal Mechanical Parameter Design Using Self Resonance Cancellation Control for Gantry-Type High Precision Stage", *Proc. of the 12th International Workshop on Advanced Motion Control, Sarajevo*, pp. 1–6 (2012)

[68] K. Inukai, H. Fujimoto, K. Omata, Y. Takeda, and S. Makinouchi: "Vibration Suppression Position Control of Robot Servo Motor Using Load Side Encoder", *Proc. of IEEJ Technical Meeting Record*, MEC–14–158, pp. 63–68 (2015) (in Japanese)

[69] M. Aoki, H. Fujimoto, Y. Hori, and T. Takahashi: "Robust Resonance Suppression Control based on Self Resonance Cancellation Disturbance Observer and Application to Humanoid Robot", *Proc. of the IEEE International Conference on Mechatronics (ICM–2013)*, pp. 623–628 (2013)

[70] K. Sakata, H. Asaumi, K. Hirachi, K. Saiki, and H. Fujimoto: "Frequency Separation Self Resonance Cancellation for Vibration Suppression Control of a Large-Scale Stage Using Multiple Position Sensors", *Proc. of the 39th Annual Conference of IEEE Ind. Electron Society (IECON–2013)*, pp. 6478–6483 (2013)

[71] T. D. Tuttle and W. P. Sheering: "A nonlinear model of a harmonic drive gear transmission", *IEEE Trans. on Robotics and Automation*, Vol. 12, No. 3, pp. 368–374 (1996)

[72] Y. Hori: "Future vehicle driven by electricity and Control-research on four-wheel-motored "UOT electric march II"", *IEEE Trans. on Ind. Electron.*, Vol. 51, No. 5, pp. 954–962 (2004)

[73] M. Yoshimura and H. Fujimoto: "Proposal of Slip Ratio Control of Electric Vehicle with Instantaneous Speed Observer and Multirate PWM", *Trans. IEE of Japan. IA*, Vol–D. 131, No. 5, pp. 721–728 (2011) (in Japanese)

[74] H. Zhou, F. Jia, H. Jing, Z. Liu, and L. Guvenc: "Coordinated Longitudinal and Lateral Motion Control for Four Wheel Independent Motor-Drive Electric Vehicle", *IEEE Trans. on Vehicular Technology*, Vol. 67, No. 5, pp. 3782–3790 (2018)

[75] N. Amann, J. Bocker, and F. Prenner: "Active damping of drive train oscillations for an electrically driven vehicle", *IEEE/ASME Trans. on Mechatronics*, Vol. 9, No. 4, pp. 697–700 (2004)

[76] V. Ivanov, D. Savitsuki, J. Orus, J. Manuel Rodriguez, A. Sorniotti, and P. Gruber: "All-Wheel-Drive Electric Vehicle with On-board Motors: Experimental Validation of the Motion Control

Systems", *41st Annu. Conf. the IEEE Ind. Electron. Soc. (IECON)*, pp. 1729–1734 (2015)

[77] J. Manuel Rodriguez, R. Meneses, and J. Orus: "Active vibration control for electric vehicle compliant drivetrains", *39th Annu. Conf. the IEEE Ind. Electron. Soc. (IECON)*, pp. 2590–2595 (2013)

[78] F. Bottiglione, A. Sorniotti, and L. Shead: "The effect of half-shaft torsion dynamics on the performance of a traction control system for electric vehicles", *J. Automobile Engineering*, Vol. 229, No. 9, pp. 1145–1159 (2012)

[79] M. Anderson and D. Harty: "Unsprung Mass with In-Wheel Motors-Myths and Realities", *Int. Symposium on Advanced Vehicle Control (AVEC)*, pp. 261–266 (2010)

[80] V. Roel, B. Igo, and N. Henk: "Influence of In-Wheel Motors on the Ride Comfort of Electric Vehicles", *Int. Symposium on Advanced Vehicle Control (AVEC)*, pp. 835–840 (2010)

[81] N. Ochi, H. Fujimoto, and Y. Hori: "Proposal of Roll Angle Control Method Using Positive and Negative Anti-dive Force for Electric Vehicle with Four In-wheel Motors", *IEEE Int. Conf. Mechatronics (ICM)*, pp. 815–820 (2013)

[82] D. Akaho, M. Nakatsu, E. Katsuyama, K. Takakuwa, and K. Yoshizue: "Development of Vehicle Dynamics Control System for In-Wheel-Motor Vehicle", *JSAE Annu. Congress (Autumn)*, No. 120, pp. 1–6 (2010) (in Japanese)

[83] M. Liu, F. Gu, and Y. Zhang: "Ride comfort optimization of in-wheel-motor electric vehicles with in-wheel vibration absorbers", *J. Energies*, Vol. 10, No. 1647, pp. 1–21 (2017)

[84] X. Shao, F. Naghdy, and H. Du: "Reliable fuzzy H ∞ control for active suspension of in-wheel motor driven electric vehicles with dynamic damping", *J. Elsevier*, Vol. 87, pp. 365–383 (2017)

[85] E. Katsuyama and A. Omae: "Improvement of Ride Comfort by Unsprung Negative Skyhook Damper Control Using In-Wheel Motors", *SAE Int. J. Alt. Power.*, Vol. 5, No. 1, pp. 214–221 (2016)

[86] S. Ohno and K. Ito: "Unsprung vibration control for in-wheel-motor EV", *JSAE Annu. Congress (Autumn)*, No. 103, pp. 21–24 (2014) (in Japanese)

[87] A. Takesaki, M. Kawafuku, M. Iwasaki, and T. Fujii: "Vibration Suppression Control System for Electric Vehicle Considering Longitudinal Vibration", *Proc. of IEEJ Technical Meeting Record*, No. 97, pp. 7–12 (2010) (in Japanese)

[88] H. Fukudome: "Reduction of Longitudinal Vehicle Vibration Using In-Wheel Motors", *SAE Technical Paper*, 2016-01-1668 (2016)

[89] J. H. Montonen, N. Nevaranta, T. Lindh, J. Alho, P. Immonen, and O. Pyrhonen: "Experimental Identification and Parameter Estimation of the Mechanical Driveline of a Hybrid Bus", *IEEE Trans. on Ind. Electron.*, Vol. 65, No. 7, pp. 5921–5930 (2018)

[90] D. Tan, Q. Wang, and Y. Wu: "Modal Analysis of In-Wheel Motor-Driven Electric Vehicle Based on Bond Graph Theory", *J. Shock and Vibration*, No. 6459154 (2017)

[91] A. J Tuononen and A. Lajunen: "Modal analysis of different drivetrain configurations in electric vehicles", *J. Vibration and Control*, No. 1077546316635857 (2016)

[92] H. Fujimoto and Y. Hori: "Visual Servoing Based on Multirate Control and Dead-time Compensation", *J. Robotics Society of Japan*, Vol. 22, No. 6, pp. 780–787 (2004) (in Japanese)

[93] J. Luh, W. Fisher, and R. Paul: "Joint torque control by a direct feedback for industrial robots", *IEEE Trans. Ind. Electron.*, Vol. 28, No. 2, pp. 153–161 (1983)

[94] Y. Kuroki, Y. Kosaka, T. Takahashi, E. Niwa, H. Kaminaga, and Y. Nakamura: "Cr–N Alloy Thin–film Based Torque Sensors and Joint Torque Servo Systems for Compliant Robot Control", *IEEE International Conference on Robotics and Automation (ICRA–2013)*, pp. 4954–4959 (2013)

[95] S. Oh and K. Kong: "High-Precision Robust Force Control of a Series Elastic Actuator", *IEEE/ASME Trans. Mechatronics*, Vol. 22, No. 1, pp. 71–80 (2017)

[96] B. Na, J. Bae, and K. Kong: "Back-drivability recovery of a full lower extremity assistive robot", *Proc. of the 12th International Conference of IEEE on Control, Automation and Systems (ICCAS)*, pp. 1030–1034 (2012)

[97] P. Weiss, P. Zenker, and E. Maehle: "Feed-forward Friction and Inertia Compensation for Improving Backdrivability of Motors", *Proc. of the 12th International Conference of IEEE on Control, Automation, Robotics and Vision (ICARCV–2012)*, pp. 288–293 (2013)

[98] D K. Prasanga, E. Sariyildiz, and K. Ohnishi: "Compensation of Backlash for Geared Drive Systems and Thrust Wires Used in Teleoperation", *IEEJ J. Ind. Appl.*, Vol. 4, No. 5, pp. 514–525 (2015)

[99] K. Kaneko, T. Murakami, K. Ohnishi, and K. Komoriya: "Torque Control with Nonlinear Compensation for Harmonic Drive DC Motors", *Proc. of the 20th Annu. Conf. of IEEE Ind. Electron. Soc. (IECON)*, pp. 1022–1027 (1994)

[100] M. Odai and Y. Hori: "Speed control of 2-inertia system with gear backlash using gear torque compensator", *Proc. of the 5th Int. Workshop on Adv. Motion Control (AMC)*, pp. 234–239 (1998)

[101] I. Kolnik and G. Agranovich: "Backlash compensation for motion system with elastic transmission", *Proc. of the 27th Convention of Electrical and Electronics in Israel (IEEEI)*, pp. 1–5 (2012)

[102] M. Yang, C. Wang, D. Xu, W. Zheng, and X. Lang: "Shaft Torque Limiting Control Using Shaft Torque Compensator for Two-Inertia Elastic System With Backlash", *IEEE/ASME Trans. Mechatronics*, Vol. 21, No. 6, pp. 2902–2911 (2016)

[103] K. Kong, J. Bae, and M. Tomizuka: "A Compact Rotary Series Elastic Actuator for Human

Assistive Systems", *IEEE/ASME Trans. Mechatronics*, Vol. 17, No. 2, pp. 288–297 (2012)

[104] W. Roozing, J. Malzahn, N. Kashiri, D. G. Caldwell, and N. G. Tsagarakis: "On the Stiffness Selection for Torque-Controlled Series-Elastic Actuators", *IEEE Robotics and Automation Letters*, Vol. 2, No. 4, pp. 2255–2262 (2017)

[105] N. Paine, S. Oh, and L. Sentis: "Design and Control Considerations for High-Performance Series Elastic Actuator", *IEEE Trans. on Mechatronics*, Vol. 19, No. 3 (2014)

[106] S. Lee, Y. Yamada, K. Ichikawa, O. Matsumoto, K. Homma, and E. Ono: "Safety-Function Design for the Control System of a Human-Cooperative Robot Based on Functional Safety of Hardware and Software", *IEEE/ASME Trans. Mechatronics*, Vol. 19, No. 2, pp. 719–729 (2014)

[107] A. D. Wicke, J. v. Zitzewitz, A. Caprez, L. Lunenburger, and R. Riener: "Path Control: A Method for Patient-Cooperative Robot-Aided Gait Rehabilitation", *IEEE Trans. Neural Syst. Rehabil. Eng.*, Vol. 18, No. 1, pp. 38–48 (2010)

[108] H. Jamshidifar, S. Khosravani, B. Fidan, and A. Khajepour: "Vibration Decoupled Modeling and Robust Control of Redundant Cable-Driven Parallel Robots", *IEEE/ASME Trans. Mechatronics*, Vol. 23, No. 2, pp. 690–701 (2018)

[109] M. Schimmack, B. Haus, and P. Mercorelli: "An Extended Kalman Filter as an Observer in a Control Structure for Health Monitoring of a Metal-Polymer Hybrid Soft Actuator", *IEEE/ASME Trans. Mechatronics*, Vol. 23, No. 3, pp. 1477–1487 (2018)

[110] A. Calanca and P. Fiorini: "Understanding Environment-Adaptive Force Control of Series Elastic Actuators", *IEEE/ASME Trans. Mechatronics*, Vol. 23, No. 1, pp. 413–423 (2018)

[111] M. Omura, T. Shimono, and Y. Fujimoto: "Thrust Characteristics Improvement of a Circular Shaft Motor for Direct-Drive Applications", *IEEE Trans. Ind. Appl.*, Vol. 51, No. 5, pp. 3647–3655 (2015)

[112] A. Calanca, R. Muradore, and P. Fiorini: "A Review of Algorithms for Compliant Control of Stiff and Fixed-Compliance Robots", *IEEE/ASME Trans. Mechatronics*, Vol. 21, No. 2, pp. 613–624 (2016)

[113] H. Seki and Y. Hori: "Control of force sensorless power assist robot robust to environmental change", *Proc. of 2002 Annual Conference of IEE of Japan, Industry Applications Society*, Vol. 1, pp. 213–216 (2002) (in Japanese)

[114] K. Kobayashi, S. Oh, S. Inatama, and Y. Hori: "A 2DOF Intelligent control Approach for Train Doors Using Environmental Stiffness Estimation", *Proc. of IEE of Japan Technical Meeting Record*, IIC–09–116, pp. 25–29 (2009) (in Japanese)

[115] S. Shigeto, H. Fujimoto, Y. Hori, M. Otsuki, and T. Hashimoto: "Fundamental Research on Reduction of Impact Forces Using Actively Controlled Landing Gear in Lunar/Planetary Landers",

Trans. IEE of Japan. IA, Vol–D. 133, No. 3, pp. 335–341 (2013) (in Japanese)

[116] S. Oh and Y. Hori: "Experimental Study on Impedance and Impact Force Control by Position Feedback Control", *Proc. of IEE of Japan Technical Meeting Record*, IIC–09–117, pp. 31–36 (2009) (in Japanese)

[117] H. Seki and Y. Hori: "Control of sensorless power assist robot using variable impedance", *Proc. of 2001 Annual Conference of IEE of Japan, Industry Applications Society*, Vol. 1, pp. 601–604 (2001) (in Japanese)

[118] S. Katsura, Y. Matsumoto, and K. Ohnishi: "Modeling of Force Sensing and Validation of Disturbance Observer for Force Control", *IEEE Trans. Ind. Electron.*, Vol. 54, No. 1, pp. 530–538 (2007)

[119] T. Murakami, F. Yu, and K. Ohnishi: "Torque sensorless control in multidegree-of-freedom manipulator", *IEEE Trans. Ind. Electron.*, Vol. 40, No. 2, pp. 259–265 (1993)

[120] Y. Ohba, S. Katsura, and K. Ohishi: "Sensor-less Force Control for Machine Tool using Reaction Observer", *Proc. of IEE of Japan Technical Meeting Record*, IIC–06–86, pp. 133–138 (2006) (in Japanese)

[121] M. Matsuoka, T. Murakami, and K. Ohnishi: "Vibration suppression and disturbance rejection control of a flexible link arm", *Proc. of the Annu. Conf. of IEEE Ind. Electron. Soc. (IECON)*, pp. 1260–1265 (1995)

[122] J. Suzuki, T. Murakami, and K. Ohnishi: "Position and force control of flexible manipulator with position sensitive device", *Proc. of the 7th Int. Workshop on Advanced Motion Control (AMC)*, pp. 414–419 (2002)

[123] H. Zhang, S. Ahmad, and G. Liu: "Torque Estimation for Robotic Joint With Harmonic Drive Transmission Based on Position Measurements", *IEEE Trans. Robotics*, Vol. 31, No. 2, pp. 322–330 (2015)

[124] E. Sariyildiz, G. Chen, and H. Yu: "An Acceleration-Based Robust Motion Controller Design for a Novel Series Elastic Actuator", *IEEE Trans. Ind. Electron.*, Vol. 63, No. 3, pp. 1900–1910 (2016)

[125] C. Mitsantisuk, M. Nandapaya, K. Ohishi, and S. Katsura: "Parameter estimation of flexible robot using multi-encoder based on disturbance observer", *Proc. of the Annu. Conf. of IEEE Ind. Electron. Soc. (IECON)*, pp. 4424–4429 (2012)

[126] J. Lee, C. Lee, N. Tsagarakis, and S. Oh: "Residual-Based External Torque Estimation in Series Elastic Actuators Over a Wide Stiffness Range: Frequency Domain Approach", *IEEE Robot. Autom. Lett.*, Vol. 3 No. 3, pp. 1442–1449 (2018)

[127] H. Kobayashi, S. Katsura, and K. Ohnishi, "An Analysis of Parameter Variations of Disturbance

Observer for Motion Control", *IEEE Trans. Ind. Electron.*, Vol. 54, No. 6, pp. 3413–3421 (2007)

Publications

Journal papers

1. 山田翔太, 藤本博志，堀洋一，「高分解能エンコーダの適用による駆動側情報を用いない 2 慣性系の制振制御法」, 電気学会論文誌 D, 一般社団法人電気学会，Vol. 135, No. 3, pp. 212–219 (2015)
2. Shota Yamada and Hiroshi Fujimoto, “Precise Joint Torque Control Method for Two-inertia System with Backlash Using Load-side Encoder”, IEEJ Journal of Industry Applications, Vol. 8, No. 1, pp. 75–83 (2019)

Journal papers under review

1. Shota Yamada and Hiroshi Fujimoto, “Position-based High Backdrivable Control Using Load-side Encoder and Backlash”, IEEE/ASME Transactions on Mechatronics, (Under review)
2. Shota Yamada, Thomas Beauduin, Hiroshi Fujimoto, Takeshi Kanou, and Etsuo Katsuyama, “Active model-based suppression of secondary ride for electric vehicles with in-wheel motors”, IEEE Transactions on Vehicular Technology, (Under review)

Journal papers to be submitted

1. Shota Yamada and Hiroshi Fujimoto, “Minimum Variance estimation of Load-Side External Torque with Robustness against Modeling and Measurement Errors”, IEEE Transactions on Industrial Electronics, (Under preparation)

Coauthor journal papers

1. Michael Ruderman, Shota Yamada, and Hiroshi Fujimoto, “Backlash Identification in Two-Mass Systems by Delayed Relay Feedback”, Journal of Dynamic Systems, Measurement and Control, (Accepted)

Refereed conference papers

1. Shota Yamada and Hiroshi Fujimoto, “Vibration Suppression Control for a Two-Inertia System using Load-Side High-Order State Variables Obtained by a High-Resolution Encoder”, The 40th annual conference of the IEEE Industrial Electronics Society (IECON2014), pp. 2897–2903, Dallas, Texas, Oct. 2014
2. Shota Yamada, Kenji Inukai, Hiroshi Fujimoto, Kenji Omata, Yuki Takeda, and Susumu Makinouchi, “Joint torque control for two-inertia system with encoders on drive and load sides”, IEEE international conference on Industrial Informatics (INDIN2015), pp. 396–401, Cambridge, England, Jul. 2015
3. Shota Yamada, Kenji Inukai, and Hiroshi Fujimoto, “Proposal of Self Resonance Cancellation Control without Using Drive-Side Information”, The 41st annual conference of the IEEE Industrial Electronics Society (IECON2015), pp. 783–788, Yokohama, Japan, Oct. 2015
4. Shota Yamada and Hiroshi Fujimoto, “Joint Torque Control for Backlash Compensation in Two-Inertia System”, 2016 IEEE International Symposium on Industrial Electronics (ISIE2016), pp. 1138–1143, San Jose, America, Jun. 2016
5. Shota Yamada and Hiroshi Fujimoto, “Proposal of High BackDrivable Control Using Load-Side Encoder and Backlash”, The 42nd Annual Conference of the IEEE Industrial Electronics Society (IECON2016), pp. 6429–6434, Florence, Italy, Oct. 2016
6. Shota Yamada and Hiroshi Fujimoto, “Human-Machine Interactive Control for Geared Mechatronic Systems by Using Load-side Encoder”, The 3rd IEEJ int. workshop on Sensing, Actuation, Motion Control, and Optimization (SAMCON2017), Nagaoka, Japan, Mar. 2017
7. Shota Yamada, Thomas Beauduin, Hiroshi Fujimoto, Takeshi Kanou, and Etsuo Katsuyama, “Model-Based Longitudinal Vibration Suppression Control for Electric Vehicles with Geared In-Wheel Motors”, IEEE Int. Conf. Advanced Intelligent Mechatronics (AIM2017), pp. 517–522, Munich, Germany, Jul. 2017
8. Shota Yamada and Hiroshi Fujimoto, “Design of Load-side External Force Observer with a Load-side Encoder Considering Modeling Errors”, The 43rd annual conference of the IEEE Industrial Electronics Society (IECON2017), pp. 7589–7595, Beijing, China, Oct. 2017
9. Shota Yamada, Michael Ruderman, and Hiroshi Fujimoto, “Piecewise Affine (PWA) Modeling and Switched Damping Control of Two-Inertia Systems with Backlash”, The 15th International Workshop on Advanced Motion Control (AMC2018), pp. 479–484, Tokyo, Japan, Mar. 2018
10. Shota Yamada and Hiroshi Fujimoto, “Proposal of State-Dependent Minimum Variance Esti-

mation of Load-Side External Torque Considering Modeling and Measurement Errors”, 2018 IEEE International Symposium on Industrial Electronics (ISIE2018), pp. 1069–1074, Cairns, Australia, Jun. 2018

11. Shota Yamada and Hiroshi Fujimoto, “Joint Torque Control for Backlash Compensation in Two-Inertia System”, The 2018 American Control Conference (ACC2018), pp. 5238-5243, Milwaukee, America, Jun. 2018
12. Shota Yamada and Hiroshi Fujimoto, “Minimum Variance Estimation of Load-side External Torque Using Load-side Encoder and Torque Sensor”, The SICE Annual Conference 2018 (SICE 2018), pp. 737–742, Nara, Japan, Sep. 2018

Domestic conference papers

1. 山田翔太, 藤本博志，堀洋一,「高分解能エンコーダと負荷側状態変数を用いた 2 慣性系の制振制御」, 平成 26 年産業計測制御/メカトロニクス制御合同研究会, IIC–14–140, MEC–14–128, pp. 107–112, 東京, 2014 年 3 月
2. 山田翔太, 犬飼健二，藤本博志，小俣健二，武田勇樹，牧野内進,「負荷側エンコーダを用いた 2 慣性系における軸トルク制御の提案」, 平成 26 年メカトロニクス制御研究会/精密サーボシステムと制御技術, MEC–14–157, pp. 57–62, 東京, 2014 年 9 月
3. 山田翔太, 犬飼健二，藤本博志，小俣健二，武田勇樹，牧野内進,「負荷側情報のみを用いた自己共振相殺制御の提案」, 平成 27 年メカトロニクス制御研究会/精密サーボシステムと制御技術, MEC–15–024, pp. 65–70, 東京, 2015 年 9 月
4. 山田翔太，藤本博志,「負荷側エンコーダ情報及びバックラッシを利用した位置制御に基づく高バックドライバビリティ制御の提案」，平成 28 年メカトロニクス制御研究会/精密サーボシステムと制御技術，MEC–16–025, pp. 45–50, 東京, 2016 年 9 月
5. 山田翔太，トーマスベドウィン，藤本博志，狩野岳史，勝山悦男,「インホイールモータ車両の実験モード解析に基づく高帯域前後制振制御」，自動車技術会 2017 年秋季大会，大阪，2017 年 10 月
6. 山田翔太，トーマスベドウィン，藤本博志，狩野岳史，勝山悦男,「セカンダリーライド帯域の乗り心地及び運動性能改善に向けたインホイールモータ車両の実験モード解析及び高帯域前後制振制御」，自動車技術会 2019 年春季大会，神奈川，2019 年 5 月，（投稿準備中）

Coauthor conference papers

1. Michael Ruderman, Shota Yamada, Hiroshi Fujimoto, and Valentin Ivanov, “Examples of actuator uncertainties in environmental systems of mechatronic systems (SoMS)”, The 3rd

IEEJ int. workshop on Sensing, Actuation, Motion Control, and Optimization (SAMCON), Nagaoka, Japan, Mar. 2017

2. Thomas Beauduin, Shota Yamada, Hiroshi Fujimoto, Takeshi Kanou, and Etsuo Katsuyama, “Control-Oriented Modeling and Experimental Modal Analysis of Electric Vehicles with Geared In-Wheel Motor”, IEEE Int. Conf. Advanced Intelligent Mechatronics (AIM2017), pp. 541–546, Munich, Germany, Jul. 2017

Others

1. 特願 2014-175641,「制御装置」, 藤本博志, 山田翔太, 犬飼健二, 2014 年 8 月
2. 平成 26 年度東京大学工学部長賞
3. 平成 26 年度電気学会東京支部 電気学術奨励賞
4. 平成 26 年度東京大学工学部電気電子工学科優秀卒業論文賞
5. Best Presentation in session MR–Motion control for High-Precision Systems in The 40th Annual Conference of the IEEE Industrial Electronics Society, (IECON2014), Dallas, Texas, Oct. 2014
6. 平成 27 年度原島博学術奨励賞
7. 平成 28 年度メカトロニクス制御技術委員会 優秀論文発表賞
8. Best poster presentation award in IECON 2017 Pre-conference workshop by TC Motion control and TC Sensor and actuator